An underwater photograph showing a rocky seabed. A large, billowing plume of fine sediment or sand is being released from the base of a rocky slope, moving towards the viewer. The water is clear, and the lighting is bright, highlighting the texture of the rocks and the density of the sediment plume.

Interaction between Liquefying Submerged Slope and Submerging Water Mass

Interaction between Liquefying Submerged Slope and Submerging Water Mass

By

Abhishek Gupta

in partial fulfilment of the requirements for the degree of

Master of Science
in Civil Engineering

at the Delft University of Technology,
to be defended publicly on Monday March 25, 2019 at 3 PM.

Student number:	4619064	
Supervisor:	Prof. Dr. F. Molenkamp	TU Delft, Geo-Engineering
Thesis committee:	Prof. Dr. M.A. Hicks (Chair)	TU Delft, Geo-Engineering
	Asst. Prof. Dr. A. Askarinejad	TU Delft, Geo-Engineering
	Asst. Prof. Dr. R. J. Labeur	TU Delft, Hydraulic Engineering

Front page image is from Getty images, Credits: L. J. Sandoval

An electronic version of this thesis is available at <http://repository.tudelft.nl/>.

Abstract

The thesis presents a numerical study on dredging induced undrained instability and subsequent static liquefaction of submarine landslides. For the study, a pre-existing hydro-dynamic uncoupled submarine slope numerical model, developed by Molenkamp (1999), has been modified to incorporate a fully hydro-dynamic coupled interaction between submerging water mass and submarine slope. The modified model is able to simulate transient quasi-static and dynamic phenomena up-till and including the immediate post-liquefaction behavior of submerged slopes of loose undrained homogenous fine sands in a 2 dimensional Updated Lagrangian (UL) finite element (FE) frame of work. To simulate soil behavior under dredge loading applications the model incorporates a Monot soil constitutive model and for submerging water behavior a Lagrangian expression of Navier stokes for nearly-incompressible visco-elastic, irrotational, fluid model.

The study primarily addresses the effect of dynamics of submerging water on the liquefying submerged slope. The research findings suggest that the dynamic motion of submerging water barely affects the occurrence of instability. However, it may decrease the rate of post-instability liquefied flow as compared to the commonly sorted uncoupled scenario, where dynamics of submerging water mass is ignored and only constant hydrostatic pressure heads due to water level is considered at the slope interface. Moreover, the findings suggest that about 50% of the loss in the potential energy of soil is consumed by the potential energy of the submerging water at the very initial stages of post-instability and that the contribution of kinetic energy of water amounts to mere 3.4%.

Next, as a secondary issue, the study also provides a valuable insight into the effect of the liquefying slope on the motion of the submerging water mass. The findings show a surface impulse wave formation post-instability, moving along the direction of landslide. Moreover, it shows a development of a distinct circular motion of fluid along the slope interface. Other than this, the thesis also attempts to provide some similarities and differences between the current findings and the published conventional research studies which make use of basic slide shapes such as viscous or rigid sliding wedge blocks.

Finally, the thesis also addresses some numerical shortcomings such as the hour-glass effect, the shake-down by the procedure to define the “initial state” effect etc., and thereby providing necessary recommendations useful for future computational modelling work.

Keywords: Submarine landslide, liquefaction, hydro-dynamic coupling, Updated Lagrangian, finite element method, Monot soil model, Navier stokes, instability, energy, surface impulse wave, water motion, hour-glass effect.

Acknowledgement

The successful completion of the research work presented in this thesis, would have not been achieved without the contribution of several people. Firstly, I would like to express my heartfelt thankfulness to my supervisor Prof. Dr. F. Molenkamp. His continuous patient support, valuable insights, recommendations and thorough reviewing of any given content have aided me throughout the research work and during the writing of this thesis. His attitude, vast knowledge and passion for soil mechanics not just kept me motivated during the study, but inspired for life. I could not have hoped for a better supervisor for my master thesis.

I am also very thankful to my thesis external committee member Asst. Prof. Dr. R. J. Labeur, who took a special interest in this research work. His valuable insights, comments and hard questions from a hydraulic engineering perspective, helped me to reach more depth of this interdisciplinary research.

Further, I like express my sincere thanks to the rest of my thesis committee members: Prof. Dr. M.A. Hicks and Asst. Prof. Dr. A. Askarinejad, for their timely valuable suggestions, and encouragements.

I also like to express my special gratitude to Arash Maghsoudloo (PhD student), who was kind enough to take his time off from his busy schedule on numerous occasion, whenever asked for, to help me on the various aspect of this research work.

Last but not the least; I am also very grateful to my family and friends for their emotional support throughout the thick and thin of my master studies.

Abhishek Gupta

Delft, March 2019

Contents

Abstract	iii
Acknowledgement.....	v
List of Figures	xi
List of Tables.....	xvii
List of common abbreviations	xix
1	1
Introduction	1
1.1 General research background	1
1.2 Problem description.....	3
1.3 Research aim and corresponding questions	5
1.4 Research approach.....	6
1.5 Outline	8
2.....	9
Literature Review	9
2.1 Flow slides: A Geotechnical perspective.....	9
2.1.1 Static liquefaction and other soil mechanics relevant theory	9
2.1.2 Flow slide patterns: real events and experimental works	12
2.1.3 Flow slide computational works.....	23
2.2 Landslide induced waves: An Ocean and Coastal engineering perspective.....	30
2.2.1 Submarine landslide and induced wave feature.....	30
2.2.2 Wave studies experimental and computational works.....	32
2.3 Concluding remarks on literature studies	38
3.....	39
Theoretical Approach & Numerical Modelling.....	39
3.1 Existing model Finite Element programming framework	39
3.1.1 Introduction to residual, stresses and loads used in the program.....	39
3.1.2 Discretization in the time domain by Crank-Nicolson method and Newton Raphson Iteration Scheme	42
3.2 Soil Model and Characteristics.....	43
3.2.1 Introduction to Existing Monot Soil Model.....	43
3.2.2 Monot model Characteristic Parameter Values	44
3.3 Fluid Model and Formulation for the Existing FEM Framework	46
3.3.1 Introduction to Fluid Model and Governing equations	46
3.3.2 Weak formulation and numerical boundary conditions.....	48

3.3.3	Residual nodal vector	49
3.3.4	Newton-Raphson procedure and Time Discretization.....	50
3.3.5	Fluid characteristics.....	52
3.4	Energy Terms Implementation	52
3.4.1	Formulation of Various Forms of Energy	53
3.5	Geometry and Mesh	57
3.5.1	Problem Structure.....	57
3.5.2	Mesh: Elements, size and Layers	58
3.5.3	Surface Boundary conditions.....	62
3.6	Phases & Loading Conditions	63
3.6.1	Phase 1(A) & 1(B): Initial, K_0 state.....	64
3.6.2	Phase 2(A) and 2(B): Initial state with drained unloading	67
3.6.3	Phase 2(C): Fluid blocks activation and optimization.....	68
3.6.4	Phase 3(A), 3(B) and 3(C): Hydrostatic transition and simulation of dredging	69
3.7	Execution.....	75
3.7.1	Libraries.....	75
3.7.2	Parameter θ , Time increment, Loading time and Accuracy	75
3.7.3	Phase executional parameters	81
3.7.4	Phase execution	81
3.7.5	Overview of code functioning	84
3.8	Fluid tank test	87
3.8.1	Wave and fluid characteristics.....	87
3.8.2	Computed test geometry and meshing.....	87
3.8.3	Computed initial wave loading.....	88
3.8.4	Fluid tank test phase execution.....	88
3.8.5	Fluid tank test results.....	90
4.....		93
Results and Discussion.....		93
4.1	Introduction to results and discussion	93
4.2	Case A results: Old mesh with no fluid blocks	93
4.2.1	Phase 1(A): Initial K_0 state	93
4.2.2	Phase 2(A): Initial state with drained unloading	96
4.2.3	Phase 3(A): Hydrostatic transition and simulation of dredging	99
4.3	Case B results: New mesh with restrained fluid blocks	107
4.3.1	Phase 1(B): Initial K_0 state.....	107
4.3.2	Phase 2(B): Initial state with drained unloading.....	110

4.3.3	Phase 3(B): Hydrostatic transition and simulation of dredging.....	113
4.4	Case C results: New mesh with activated fluid blocks.....	121
4.4.1	Phase 2(C): Fluid blocks activation and optimization.....	121
4.4.2	Phase 3(C): Hydrostatic transition and simulation of dredging.....	126
5	141
Conclusion	141
5.1	Primary research conclusions: Effect of submerging water on liquefying slope	141
5.2	Secondary research conclusions: Submerging water motion due to liquefying slope.....	142
5.3	Tertiary research conclusions: Limitation and recommendations	143
References	147
Appendix (A)	– Overview of structure F.E program MODIFIED_DYN_MLK4.95.....	153
Appendix (B)	– Link to program related data files	156
Appendix (C)	– Discretization of saturated soil	157
Appendix (D)	– Phase 2(A) shake down effect on Phase 3(A)	161
Appendix (E)	– Phase 2(C): Activation of fluid material blocks optimization	162
Appendix (F)	– Phase 3(C): Other Results.....	164
Appendix (G)	- Some characteristics of hour-glass eigenmodes of plane 4-node finite elements	166

List of Figures

Figure 1.1: Features of submarine landslides (M.A. Hampton and H. J.Lee, 1996).....	1
Figure 1.2: Classification of submarine mass movement proposed by I.S.S.M.G.E (TC-11) committee (J. Locat, 2000).....	2
Figure 1.3: Tsunami wave swept over 10m harbor wall at Taro, Iwate, Japan during 2011 Tsunami. (Image source: http://www.sciencemag.org/news/2014/09/underwater-landslide-may-have-doubled-2011-japanese-tsunami).....	3
Figure 1.4: (a) Underwater rigid sliding block (Cremonesi et.al., 2011); (b) Semi-elliptical rigid body sliding down an underwater incline ($\alpha = 45^\circ$). Slide motion is left to right (Abadie et.al., 2006)	5
Figure 2.1: Characteristics of Monotonic undrained triaxial compression tests with axial displacement control of dense and loose sands (a) Deviatoric stress vs axial strain, (b) Effective stress Path (a and b, modified from Chu et al., 2015), (c) Excess pore water pressures (modified from Andersen and Schjetne, 2013).....	10
Figure 2.2: Instability loose sands (Chu et. al., 2015).....	11
Figure 2.3: Rotation of principal effective stresses along the potential slip surface characterized by angle α (Jager, 2018)	12
Figure 2.4: Type of Submarine slide; (a) Translational slide, (b) Rotational slide (Modified from, USGS: fact sheet- 2004-3072).....	13
Figure 2.5: Retrogressive Zeeland submarine slide, mechanism after Koppejan et. al., (1948)	14
Figure 2.6: Large Flume tank experiment at Delft soil mechanics lab (Groot et. al., 2018); (a) Experiment setup, (b) Retrogressive flow slide failure, (c) Pore water pressure vs time.....	15
Figure 2.7: Stromboli landslide (2002); (a) Different slides observed, (b) Profile of main slides- slip with pre- and postslide morphology (Boldini et. al., 2005).....	16
Figure 2.8: Liquefaction in Brutus tank, starting at time 11:06:53.2; a) $t = 0$ s, b) $t = 4$ s, c) $t = 6.2$ s d) 10.5s (Molenkamp and Os, 1987)	17
Figure 2.9: liquefaction tank with pore water pressure transducers: BP1, BP2 and BP3. (Jager, 2018)	18
Figure 2.10: Liquefaction failure of sand, time starting just before failure initiation; a) $t_1 = 0$ s, b) $t_2 = 4$ s, c) $t_3 = 8$ s and d) $t_4 = 12$ s. (Jager, 2018)	18
Figure 2.11: Pore water pressures in total time scale with marked failure time frames of figure 2.10. (Jager, 2018).....	19
Figure 2.12: Centrifuge Experimental setup (PPT – pore water pressure transducers, LDT – longitudinal displacement transducers, units in mm), referred from Byrne et. al., (2000).....	20
Figure 2.13: Result of Centrifuge Experiment; (a) Pore pressure during loading, (b) surface settlements during loading, (c) deformation field due to first surcharge of 60 kPa (modified from Byrne et. al., 2000)	20
Figure 2.14: Evolution of Breach failure event at the Amity Point study site on 21/1/2014 (Beinssen et.al., 2014).....	21
Figure 2.15: Overview of (a) the slope failure area and (b) the Laurentian Fan showing the cable breaks that occurred in the sea because of the turbid soil flows (yellow lines); the red dots indicate instantaneous cable breaks and the white dots delayed cable breaks. The red star indicates the earthquake epicenter. The presumed main failure area (pink dotted area) and area of local sediment failure (black dotted area). The image contains bathymetry. (c) Newly identified fault scarps, including rotational failure and translational failure head scarps. (Løvholt et. al., 2018)	22
Figure 2.16: Sensitive clay failure mechanism; retrogressive sliding (Hunter and Fell, 2001)	23
Figure 2.17: Simulated Storegga slide by Løvholt et. al. (2017); slide profile at different times	23

Figure 2.18: Results from study by Molenkamp (1999); (a) Initial effective stress state after unloading of assumed horizontal layers to achieve the cut type of soil conditions. Maximum effective principal stress is -280 kPa (Compressive), (b) Nodal displacement vectors at end of dynamic loading calculation ($t=22.571$ s). The maximum vector length represents 0.093 m, (c) Percentage Ratio of mobilized and failure deviatoric stress contours.	24
Figure 2.19: Problem Geometry (Jiang et. al., 2015)	25
Figure 2.20: Type of submarine failure computed based on MH dissociation zone (Jiang et. al., 2015)	25
Figure 2.21: Flow Type of submarine failure, computed Displacement vs Time (Jiang et. al., 2015)	26
Figure 2.22: Submarine failure, computed velocity of fluid and pore water vs Time (Jiang et. al., 2015).....	26
Figure 2.23: Work by Bandara and Soga (2015); a) Problem Geometry, b) deviatoric shear strain variation, (c) Pore water pressure (Pa), d)Vertical effective stress variation (Pa).....	29
Figure 2.24: Landslide classification for impulse wave generation. (Fritz, 2002)	30
Figure 2.25: (a) Failure pattern using a retrogressive block model and a remolding debris flow model superimposed in gray. The retrogressive slide blocks fail one by one, blocks 1 and 2 are moving parallel to the slope, blocks 3 and 4 are at rest. The slide material is mobilized more rapidly in the debris flow model, and several “blocks” may fail at the same time, (b) Trænadjupet Slide progression in the debris flow model, (c) Trænadjupet Slide progression using the retrogressive block model. (Løvholt et. al., 2017).	32
Figure 2.26: Experimental setup (Heinrich, 1992).....	33
Figure 2.27: Surface wave propagation in time; a) $t= 0.5$ s, b) $t=1$ s, c) $t=1.5$ s (Heinrich, 1992).....	33
Figure 2.28: Experimental setup (Cremonesi et. al., 2011).....	34
Figure 2.29: Rigid slides at different time steps; a) $t= 0.25$ s, b) $t= 0.5$ s, c) $t= 0.75$ s and d) $t= 1$ s (Cremonesi et. al., 2011)	34
Figure 2.30: Surface wave profiles at different times for both experimental and computed work; a) $t = 0.5$ s, b) $t = 1$ s	34
Figure 2.31: Submarine granular flow slide; a) experimental setup at $t= 0.8$ sec b) computed flow slide at $t= 0.8$ sec (Rzadkiewicz et. al., 1997).....	35
Figure 2.32: Assumed slide geometry after Heinrich (1992) by Abadie et. al.(2010)	36
Figure 2.33: Surface waves with stream flowlines (note flowlines are smoothed in air space above water level); a) at $t= 0.5$ s, b) 1s (Abadie et. al., 2010)	36
Figure 2.34: Various interfaces and velocity vectors for 3 slide viscosity cases; a) $t= 1.7$ s, $\mu = 5000$ Pa.s, b) $t= 1.9$ s, $\mu = 100$ Pa.s, c) $t= 1.9$ s, $\mu = 1$ Pa.s (Abadie et al., 2008).....	37
Figure 3.1: Principal effective stress space - (a) 4 fundamental stress state zones; (b) Increment in stress state and yield surface expansion (modified from Molenkamp, 1980).	44
Figure 3.2: Problem Structure (modified from- Molenkamp, 2018).	57
Figure 3.3: Mesh for Case A; (a) Node numbering with element size and origin; (b) Surface element numbering (modified from, Molenkamp 1999).....	58
Figure 3.4: Mesh for Case B & C; (a) Node numbering with element size and origin; (b) Surface element numbering (modified from, Molenkamp 2018).	59
Figure 3.5: Mesh of Case A with Material Block numbers.....	62
Figure 3.6: Mesh of Case B & C with Material Block numbers	62
Figure 3.7: Problem Geometry with assumed ground level and the resulting equilibrium externally applied traction forces	66
Figure 3.8: Problem Geometry with ground level in Phase-1 and in Phase-2 with respective unloading traction loads.	68
Figure 3.9: Problem Geometry with unloading traction loads.	69

Figure 3.10: Problem Geometry during initiation of dynamic Phase 3(A), 3(B) and 3(C), along with artificially induced intergranular stresses.....	71
Figure 3.11: Illustration of unbalance load applied during Phase 2(A) & (B).....	76
Figure 3.12: Illustration of unbalance load applied during Phase 3(A), (B) & (C).....	78
Figure 3.13: Flow Chart to execute analysis – a) Case A; b) Cases B & C	82
Figure 3.14: Flowchart for code functioning.....	86
Figure 3.15: Fluid tank test geometry and meshing with surface elements numbering	88
Figure 3.16: Fluid tank test geometry with indicative initial upper layer level in updated mesh (in red), assumed water level (in blue) and applied traction loading (in Green arrows). *The figure is unscaled.	89
Figure 3.17: Fluid tank test, phase execution flowchart.....	90
Figure 3.18: Fluid tank test, horizontally and vertically combined particle displacements contour at T= 1.75 s: (a) exact solution, (b) computed solution for ‘Phase 2(FT)_1’ i.e. 0.04 s time step and 0.005 allowable error. (Range of legend: - 0.0011 to 0.0011m)	90
Figure 3.19: Narrow channel time series of piezo-metric level η / A at (x, y) = (0, 10 m).....	91
Figure 4.1: Follower type of nodal loads (assumed water level + soil level) for phase 1(A).....	94
Figure 4.2: In-plane effective stress tensor for phase 1(A)	95
Figure 4.3: Normal effective stress on plane of deformation for phase 1(A) [Value Ranges: -270 kPa to 0 kPa].....	95
Figure 4.4: Pore water pressure for phase 1(A) [Value Ranges: -290 kPa to -20 kPa].....	96
Figure 4.5: Follower type of nodal loads (assumed water level only) for phase 2(A)	96
Figure 4.6: In-plane effective stress tensor for phase 2(A)	97
Figure 4.7: Normal effective stress on plane of deformation for phase 2(A) [Value Ranges: -259 kPa to 0 kPa].....	98
Figure 4.8: Nodal displacement for phase 2(A)	98
Figure 4.9: Pore water pressure for phase 2(A) [Value Ranges: -290 kPa to -20 kPa]	99
Figure 4.10: Combined nodal loads due to dredged part of soil on non-dredge boundaries; phase 3(A)	100
Figure 4.11: Horizontal displacement at a node midway to the slope surface for phase 3(A).....	100
Figure 4.12: Different time steps used in phase 2(A) vs Phase 3(A) failure response (instability point)	101
Figure 4.13: In plane effective stress tensor for phase 3(A).....	102
Figure 4.14: Normal effective stress on plane of deformation for phase 3(A) [Value Ranges: -259 kPa to 0 kPa].....	103
Figure 4.15: Ratio of mobilized and failure deviatoric stress Phase 3(A) [Value Ranges: 0% to 100%]	103
Figure 4.16: Excess pore pressure Phase 3(A) [Value Ranges: -290 kPa to 240 kPa].....	104
Figure 4.17: In-plane strain tensors phase 3(A)	105
Figure 4.18: Nodal displacements for Phase 3(A).....	105
Figure 4.19: Energy transitions Phase 3(A)	106
Figure 4.20: Follower type of nodal loads (assumed water level + soil level) for phase 1(B).....	107
Figure 4.21: In-plane effective stress tensor for phase 1(B).....	108
Figure 4.22: Normal effective stress on plane of deformation for phase 1(B) [Value Ranges: -280 kPa to 0 kPa].....	109
Figure 4.23: Pore water pressure for phase 1(B) [Value Ranges: -300 kPa to 0 kPa].....	109
Figure 4.24: Follower type of nodal loads (assumed water level only) for phase 2(B)	110
Figure 4.25: In-plane effective stress tensor for phase 2(B).....	111

Figure 4.26: Normal effective stress on plane of deformation for phase 2(B) [Value Ranges: -252 kPa to 0 kPa].....	111
Figure 4.27: Nodal displacements Phase 2(B)	112
Figure 4.28: Pore pressure Phase 2(B) [Value Ranges: -300 kPa to 0 kPa].....	113
Figure 4.29: Combined nodal loads due to dredged part of soil on non-dredge boundaries; phase 3(B)	113
Figure 4.30: Horizontal displacement at a node midway to the slope surface for phase 3(B)	114
Figure 4.31: In-plane effective stress tensor for phase 3(B).....	115
Figure 4.32: Normal effective stress on plane of deformation for phase 3(B) [Value Ranges: -252 kPa to 0 kPa].....	115
Figure 4.33: Ratio of mobilized and failure deviatoric stress Phase 3(B) [Value Ranges: 0% to 100%]	116
Figure 4.34: Excess pore pressure Phase 3(B) [Value Ranges: -190 kPa to 120 kPa].....	117
Figure 4.35: In-plane strain tensors phase 3(B).....	117
Figure 4.36: In-plane strain tensors phase 3(B), only soil region.....	118
Figure 4.37: Nodal displacements Phase 3(B)	119
Figure 4.38: Nodal displacements Phase 3(B), only soil region	119
Figure 4.39: Energy transitions Phase 3(B).....	120
Figure 4.40: Deviatoric stress state difference in soil domain between phase 2(B) and 2(C).....	122
Figure 4.41: In plane effective stress tensor for phase 2(C).....	124
Figure 4.42: Normal effective stress on plane of deformation for phase 2(C) [Value Ranges: -252 kPa to 0 kPa].....	124
Figure 4.43: Nodal displacements Phase 2(C)	125
Figure 4.44: Pore pressure Phase 2(C) [Value Ranges: -300 kPa to 0 kPa].....	125
Figure 4.45: Horizontal displacement at a node midway to the slope surface for phase 3(C)	126
Figure 4.46: In-plane effective stress tensor for phase 3(C).....	127
Figure 4.47: Normal effective stress on plane of deformation for phase 3(C) [Value Ranges: -252 kPa to 0 kPa].....	128
Figure 4.48: Ratio of mobilized and failure deviatoric stress Phase 3(C) [Value Ranges: 0% to 100%]	128
Figure 4.49: Excess pore pressure Phase 3(C) [Value Ranges: -160 kPa to 130 kPa].....	129
Figure 4.50: In-plane strain tensors phase 3(C) (*without excessive strained point).....	130
Figure 4.51: In-plane strain tensors phase 3(C), only soil region.....	130
Figure 4.52: Nodal displacements Phase 3(C), only soil region	132
Figure 4.53: Nodal displacements Phase 3(C) with marked circular formations	132
Figure 4.54: Impulse wave generation with time for Phase 3(C).....	135
Figure 4.55: Displacement normal to interface surface vs displacements normal to free water surface, at t = 1.5s.	136
Figure 4.56: Change in water elevation head at the interface w.r.t initial rest position.	137
Figure 4.57: Energy transitions Phase 3(C); a) all forms of energy contribution, b) magnified plot for kinetic energies contribution	138
Figure D1: Shake down affect in Phase 2(A), for horizontal displacement in mid-slope surface node	161
Figure E1: Nodal displacements phase 3(C) for 0.001 s time sets in phase 2(C)	162
Figure E2: Mobilized strength phase 3(C) for 0.001 s time sets in phase 2(C)	162
Figure E3: Nodal displacements phase 3(C) for 0.01 s time with zero initial nodal velocities	163
Figure E4: Mobilized strength phase 3(C) for 0.001 s time with zero initial nodal velocities.....	163
Figure F1: In Plain Strain tensors with excessively high strain point for Phase 3(C).....	164

Figure F2: Nodal displacement at dredged soil region filled with water for Phase 3(C)	164
Figure F3: Magnified Nodal displacement for Phase 3(C)	165
Figure J1: Illustration of two 4-node elements with spurious hour-glass eigenmodes (interpreted from Molenkamp et. al., 2000a).....	166
Figure J2: Illustration of 4-node element with fifth central node, showing the hour-glass related eigenmodes (interpreted from Molenkamp et. al., 2000a).....	167

List of Tables

Table 1.1: Thesis outline	8
Table 3.1: Monot model parameter values for loose sand.....	45
Table 3.2: Fluid material behaviour parameter values	52
Table 3.3: Direct contact surface elements (<i>DC</i>) and Dredge layer contact elements (<i>DL</i>).....	60
Table 3.4: Mesh boundary conditions	63
Table 3.5: Phases implemented for different cases.....	63
Table 3.6: Applied tractions along direct contact boundary for Phase 1(A) and 1(B).	66
Table 3.7: Applied tractions along direct contact boundary for Phase 2(A) and 2(B)	68
Table 3.8: Applied traction along direct contact boundary for Phase 2(C)	69
Table 3.9: List of libraries used in program “Modified_ Dyn_ mlk4.f95”	75
Table 3.10: Phase executional input Parameters	81
Table 3.11: Applied traction along the Upper free boundary surface with reference to 10.001 m water level.	88
Table 4.1: Key discussion points of different case sections	93
Table 4.2: Time sets vs calculated maximum nodal displacements in Phase 2(C) and time of failure in Phase 3(C)	121
Table B1: Program related various data files list.....	156

List of common abbreviations

ALE	Arbitrary Lagrangian-Eulerian
ALWERR	Allowable error
CFD	Computational fluid dynamics
DEM	Discrete Element Method
DNS	Direct numerical simulation
DC	Direct contact surface elements
DL	Dredge Layer contact elements
DTIMLD	Time step of loading
DEPSALLOW	Allowable strain increment
EPP	Excess pore pressure
EPK0	Ratio of effective vertical stress vs horizontal effective stress
EPOT, EPOT_S, EPOT_W	Total, soil and water potential energy.
EINT, EINT_S, EINT_W	Total, soil and water internal energy
ERAD	Radiated energy
EKIN, EKIN_S, EKIN_W	Total, soil and water kinetic energy
FEM	Finite element method
FOLL	Follower type boundary loads
FWORK	Follower type load energy
GMODW, GMODVSC	Elastic and viscous shear modulus water
GRAV	Gravitational force
I.S.S.M.G.E	International society for soil mechanics and geotechnical engineering
INTLD	Internal stress forces
INERT	Inertial forces
ITERS	Current iteration step
ITS	Number of Iterations allowed
KMODW, KMODVSC	Elastic and viscous bulk modulus water
LOAD	External load
MPM	Material point method
MH	Methane hydrates
MNR	Modified Newton Raphson
MAXDIS	Maximum allowable displacement
NS	Navier Stokes
NMATSOIL	Number of soil material
PLIC	Piecewise-linear interface calculation
PFEM	Particle finite element method
PA	Atmospheric pressure
RHOWET, RHODRY	Wet and dry density of material
RERR	Relative error of convergence
RERRB	Lowest relative error of convergence
SPH	Smooth particle hydrodynamics
TL	Total Lagrangian
TIMLD	Total time of loading
UL	Updated Lagrangian
VOF	Volume of fluid method
VBFC	Viscous boundary forces
w.r.t	With respect to
WGHT	Gravitational forces
WORK	External load energy

***Note on the usage of uncommon mathematical symbol in the report:**

\int_{Γ} → represents the surface integral

1

Introduction

1.1 General research background

Sandy Soil Slopes are very commonly observed in submarine environment, be it naturally presented such as continental slopes or artificially formed in the process of offshore land reclamation. In civil engineering terminology slopes are regarded as soil formations which fill the gap between two different elevations in ground surface. Considering triggers such as earthquakes and increasing human activities e.g. building of coastal and offshore structures, trenching, dredging, placement of submarine pipelines etc., submarine slopes nowadays have become more critical to landslides than ever, and hence an area of research interest.

The typical features associated with submarine landslide are generally of two types: a rupture surface and a displaced mass of sediment or rocks. Figure 1.1 depicts a more general practical condition that might get created post-failure (Hampton and Lee, 1996). Here the main scarp is where the rupture or slip surface initiates, crown crack may appear as a minor tensile cracks owing to certain adhesion in the soil because of maybe naturally presented clayey type of soil material or maybe due to suction/cavitation in the soil. Further the minor scarp can be linked to heterogeneity of the soil with the patches of strong and weak zones. The right-side of the figure depicts the total displaced mass from the upslope.

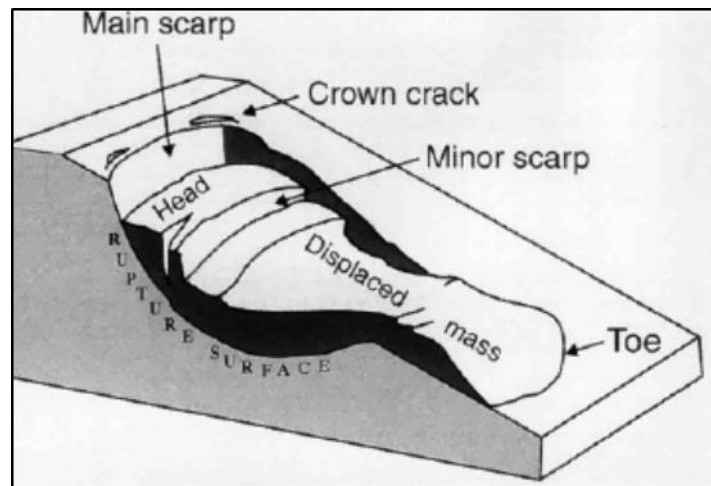


Figure 1.1: Features of submarine landslides (M.A. Hampton and H. J.Lee, 1996).

As per the classification of submarine mass movement proposed by I.S.S.M.G.E (TC-11), which can be referred in figure 1.2, one of the most common phenomena associated with soil sloped submarine landslides are sandy or muddy flow slides (Locat, 2000). In this kind of failure the slide area usually gets emptied and the failed mass may get deposited many hundreds of kilometers from its source (Locat, 1996).

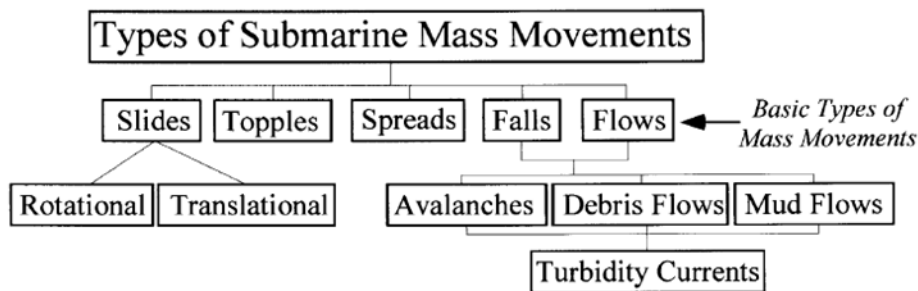


Figure 1.2: Classification of submarine mass movement proposed by I.S.S.M.G.E (TC-11) committee (J. Locat, 2000)

This type of soil slope failures is usually associated to the phenomena known as *Liquefaction*. In a full saturated undrained soil condition, *Liquefaction* occurs when due to the external loading/stresses in a soil-fluid skeleton, the pore water pressure increases in the soil up-to a point where the mean effective stress approaches zero (Mienert, 2009; Maghsoudloo et. al., 2017). In case of dense sand deposited formations such failure is triggered due to seismic motions such as earthquakes (ex. Fine et.al, 2005), also refers to as *Cyclic Liquefaction*. Whereas in case of slopes that are composed of loose fine and silty sands, the liquefaction is triggered due to monotonic loading (known as *Static Liquefaction*) such as gradual sediment depositions on sloping seabeds by waves, volcanic activities etc. (Sterling and Strohbeck, 1975; Chiocci et. al., 2008). Apart from aforementioned sandy flow slide (soil composed of sands or sand and silts), the failure phenomena have also been associated to quick clays. Although liquefaction not being its fundamental mechanics; this has been credited to the sensitivity of the clays and there minerology, but they too flow on sudden disruptions (Jager, 2018). However compared to sandy flow slides such cases have been recorded seldomly, in 25 case studies done by Edgers and Karlsrud (1982) on submarine flow landslides only 1 was directly associated to quick clays: the Sokkelvik, Norway 1959. The other such case and the biggest in history of quick clay flow slide is Resa, Norway 1978 (Gregersen, 1981). In addition to its seldom occurrence these flow slides, unlike the liquefaction flow slides, mostly occur above water (Jager, 2018), although their thin failure zones are fully water saturated.

Nevertheless the consequences of flow landslides in general are devastating, leading to huge property and structural damage. For example, Nerlerk Berm failure in Canada (1983), which failed due to static liquefaction when the height of the artificially constructed island reached 26 m, which originally was designed to be raised up to 36 m from a water depth of 44 m and the monetary losses of such construction failure was over \$100 million (Jager, 2018; Hicks and Onisiphorou, 2005).

Apart from the direct consequences, tsunamis are another major aspect of such failures. Several events of tsunamis have been observed all over the world throughout history. However due to lack of sufficient quantitative comparisons of different methods of tsunami generation, the adequate discrimination of their sources from coastline inundation data was difficult and inaccurate (Yalciner et. al., 2001) and hence given this fact, mostly tsunamis have only been associated to earthquake failures and tectonic movements. Mainly recent studies have shown the importance of submarine landslides in formation of large waves, e.g. two different case studies done on tsunami's: 1) Northern Papua New Guinea in 1998 (Tappin, 2017), where wave heights of 10–15m were experienced along a 25 km stretch of coastline. Several villages were wiped out and over 2200 people died. 2) Tohoku Japan in 2011 (Tappin et.al., 2014), where similar to former case tsunami recorded 10–15m of wave heights with run ups of up to 20m. Human losses of over 18000 (including missing) were reported. In both of

these, authors through numerical simulations and previous geographical survey data's have concluded that along with earthquakes, landslides were the major probable contributors.



Figure 1.3: Tsunami wave swept over 10m harbor wall at Taro, Iwate, Japan during 2011 Tsunami. (Image source: <http://www.sciencemag.org/news/2014/09/underwater-landslide-may-have-doubled-2011-japanese-tsunami>)

Above examples among many others, suggest that most tsunami's that are associated to flow landslides have mostly been triggered due to earthquakes. However, the event such as Stromboli 2002 submarine landslide which lead to the tsunamigenic waves with maximum run up of 10m, have been caused by static liquefaction of soil. In this case volcanic lava eruption and thereby its gradual deposition over the sea bed led to the liquefaction failure of the soil slope (Chiocci et. al, 2008).

Today, both the aspects of submarine landslide i.e. liquefaction flow slides and subsequent wave formations are an important research topic for both Ocean and Geomechanic engineering.

1.2 Problem description

In an initially hydrostatic submarine sandy-slope conditions, the phenomena of a *soil-slope mass movement*, triggered due to external non-wave type loadings such as: earthquake or dredging, which subsequently leads to *liquefaction slope failure* and also the *overlying water mass dissipation*, involves a dynamical coupling between the soil slope and overlying water. This coupling in geotechnical perspective, although less researched, but can be deduced in terms of soil stress state behavior at different phases of progressive slope failure: 1) Pre-liquefaction up-till the occurrence of practically undrained instability, 2) Post-instability liquefied flow 3) Post-liquefaction. It is to be noted that; the onset of liquefaction here is defined in terms of reaching an instantaneous undrained global instability state of a slope, thereafter which the failure becomes rapid or flow like. In theory, this soil behavior is understood at an elementary/local soil-stress state behavior level, where the onset of liquefaction or instability is defined when the soil intergranular stress-state passes its peak deviatoric stress. Whereas, full liquefaction refers to a point in local intergranular stress state where the mean effective stress reaches a minimum level with a minor deviatoric stress, due to pore pressure buildup (refer section 2.1.1).

1. *Pre-liquefaction up-till the occurrence of practically undrained instability* – At this stage for rapid type of loadings i.e. earthquake or dredging, the sandy soils are commonly treated as undrained with an assumption that the loading time is negligible with respect to consolidation

time. Thus, it signifies that there is no exchange or flow of water at the slope-water interface. Additionally, undrained response is controlled by the soil-skeleton response and pore fluid stiffness. The tendency of sand to change volume during loading; positive or negative dilatancy, is constrained by the pore fluid and therefore results in pore pressure changes (Atigh and Byrne, 2003). Hence, under this soil condition at the interface the overlaying water mass will act as a secondary set of external load to the soil-fluid skeleton.

Further, the strains/displacement increment response in soil during this stage is considered to be small and gradual, as the soil stress-state remains within the elasto-plastic strain limits (ex. refer figure 2.1). However, even this small displacement response in soil itself can cause a disturbance in overlaying water mass, which in turn will make the external load due to overlaying water mass at interface dynamic. Thus, under such circumstance both the primary loading i.e. earthquake or dredging and secondary dynamic load due to overlaying water mass will influence the local stress-state development and principal stress-state rotation within the soil and thus the initial global instability of the slope and therefore the onset of liquefaction.

2. *Post-instability liquefied flow* – During this phase, the soil behavior is associated with strain softening, where the soil strength is rapidly reduced and pore-pressure increases, leading to rapid strain increments. Experimental findings suggest this process to be spontaneous, where soil achieves full liquefaction in few seconds (Jafarian et. al., 2013, Jaeger, 2018). Thus at this phase the soil is treated as undrained and therefore the loading application due to dynamic motion of overlaying water mass at slope water interface will be similar to previous phase. However at this phase the dynamic water loading will impact the stress state development of soil under strain softening. Additionally, considering the rapid strains increments in soil the induced disturbance to the overlaying water mass will become more dynamic in nature.

Apart, from the loading aspect in reality, the interaction of rapid incremental strains/displacements of failing soil slope with overlaying fluid might also develop turbidity currents (Lowe, 1976). In occurrence of such events the part of soil slope will no longer remain liquefied or undrained instead suspended within the water mass, thus signifying exchange of soil-water mass at the interface.

3. *Post liquefaction* – Apart from the suspension of granular soil in turbid flow, experiments shows past the peak liquefaction stage soil tends towards stabilization, hence gradually dissipating excess pore pressure and achieving relatively denser state (ex. Jager, 2018 and Groot et. al, 2018). Considering soil shows drained behavior at this phase, the coupling between soil slope and overlaying water mass might become more complex. As in this case the overlaying water mass will not just act as an external dynamic loading directing the end of liquefied flow but will also be involve in diffusive process of excess pore pressures.

Present computational researches, involving submarine landslide are mostly very limited in terms of slope and free water coupling, especially in case of triggered liquefaction flow slide. Broadly, they are usually divided in two, based on the targeted mechanical aspects of submarine landslides: a) Motion of overlaying water after landslide and b) triggering or instability of landslide. For example research studies carried out by Abadie et.al. (2006), Cremonesi et.al. (2011) and Grilli and Watts (2005), fall under the former category, where they study the process of wave formation and propagation by using different numerical models such as Particle finite element, fully nonlinear potential flow, PLIC-VOF etc., and by considering simpler landslide geometries such as: a rigid or viscous sliding wedge (modelled as an incompressible or compressible viscous fluid) over a slope.

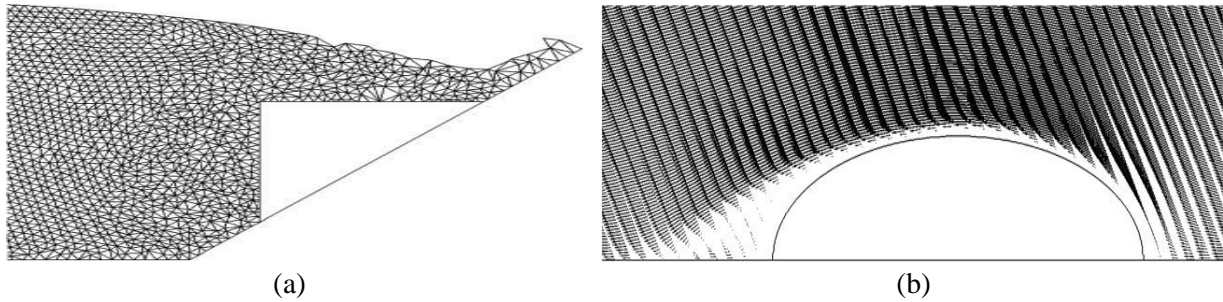


Figure 1.4: (a) Underwater rigid sliding block (Cremonesi et.al., 2011); (b) Semi-elliptical rigid body sliding down an underwater incline ($\alpha = 45^\circ$). Slide motion is left to right (Abadie et.al., 2006)

However, these studies might somewhat simulate the effect of rock sliding or partially incorporate the effect of liquefied soil-slope failure by considering a viscous or deforming wedge (refer figure 1.4), but what these studies mainly lack is to account for geotechnical aspects, particularly in case of *flow type/liquefied soil-slope failure in sands*. Hence, failing to capture more realistic slope deformations due to soil liquefaction related factors such as stress state development, material rotation and pore water pressure generations etc.

On the other hand, studies such as by Molenkamp (1999) or Azizian and Popescu (2005), which usually accounts for external triggers mechanism such as dredging or earthquake, mainly emphasize on the instability and liquefaction of submarine slope failures. Considering the source of external loading to be non-wave type, these studies commonly assumes constant hydrostatic pressure at seabed due to submerging water level head. Thus, overlooks the dynamic interaction between overlaying water mass and soil slope.

Hence viewing at these past researches, in order to study the influence of submerging water (initially at rest) on liquefying slope for non-wave type of primary loading and simultaneously the effect of liquefying slope on the dispersion of submerging water, this thesis is an attempt to develop a numerically coupled submarine slope model with *Dredging induced liquefaction mechanism*. It is to be noted that the study focus lies within the earliest phase of the post instability slope behaviour, thus covering the initial phase of strain softening behavior of soil. Development of granular suspended flow/turbidity and post liquefaction flow is beyond the scope of this research.

1.3 Research aim and corresponding questions

1. The *Primary aim* of the research is to evaluate the fully coupled effect of submerging water mass on dredge induced liquefying slope and thereby compare it with the usually considered case in geotechnical studies, which assumes constant hydrostatic pressures heads at soil slope surface due to submerging water level and thus ignores the dynamics involved. Thereby, the main research questions in relative terms to constant hydrostatic pressure head case that will be answered are as follow:
 - a. How does the coupled submerging water mass motion affect the occurrence of slope instability?
 - b. How does the coupled submerging water mass motion affect the development of liquefied flow post-instability behavior?
 - c. What are the differences in terms of energy transitions?
2. Further, the *Secondary aim* is to evaluate the effect of the liquefying slope on the motion of the submerging water mass. Additionally, considering the realistic liquefied-flow slide simulation, an attempt has been made to compare the dissipation of submerging water in the

developed numerical model with the existing literatures that assumes basic landslide shapes. Thus the research questions this will be covered are:

- a. How does the induced motion of overlaying water mass looks like at the earliest phase of the post-instability slope?
 - b. How similar or different is the induced motion pattern of numerical model vs literatures?
3. Finally, the *Tertiary aim* of the study is to explore the limitations of applied model and recommend the potential improvements for future works.

1.4 Research approach

The presented research essentially is an extension to the numerical model: ‘Dyn_mlk4.f95’, developed by Molenkamp (1999). This model was created to simulate transient quasi-static and dynamic phenomena involved with dredging-induced liquefaction of submerged slopes of loose homogenous fine sands in 2 dimensional Updated Lagrangian (UL), Finite element (FE) frame of work. In order to simulate soil behavior under the dredge loading applications the model incorporates a double strain hardening Monot soil model (Molenkamp, 1980). However, as a shortcoming this model does not include submerging water interaction, but rather assumes constant hydrostatic pressure heads at the slope surface. Thus concerning this limitation under the current research work a new model: ‘Modified_Dyn_mlk4.f95’ is developed with three major amendments to the previous model: ‘Dyn_mlk4.F95’, while keeping the soil model and properties the same. Amendments are as follow:

1. *Anticipated improved dredging mechanism*, in order to better simulate soil behavior under dredging and to compliment the numerical hydrodynamic coupling of slope and overlaying water.
2. *New mesh* of uniform bilinear quadrilaterals subdivided into four 3 node elements, to incorporate fluid layer. This type of element arrangements has been anticipated to prevent spurious modes and locking (Pastor et. al., 1999)
3. *Fluid behavior model and algorithms related to hydrodynamic coupling* of soil slope with submerging water.

It is to be noted that at the current level of research work, it was opted not to change the numerical approach of the previous model (i.e. Updated Lagrangian) for the aforementioned modifications. Thus, to implement the fluid behavior, *Lagrangian expression of Navier stokes for nearly-incompressible visco-elastic, irrotational fluid* was used. Although, it is known that UL limits the maximum extent of the flow due to the loss of numerical accuracy with increasing displacement, rotations and distortion of the finite elements, but for the current scope of work i.e. the very initial phase of post-instability, this approach is expected to work fine. Further a time step limitation based on the element size and shear wave velocity, was implemented in the previous model (Molenkamp, 1998) and thus is used in the current modification. This limitation ensures sufficient controllability of accuracy of simulated shear wave propagation with respect to the analytical wave solution, in soils. Additionally this restriction warrants the program to stop well before too severe mesh distortions occurs.

Next, the opted soil slope *geometry* was kept similar to the original work by Molenkamp (1999) with an additional shallow submerging water layer. This choice of geometry and the external loading i.e. dredging, was selected considering primarily the artificially constructed underwater slopes such as: submerged trenches, berms (ex. Nerlerk Berm, Wanatowski et. al., 2010) etc. Additionally in the selection due consideration to the current available experimental facilities at soil mechanics lab of TU Delft was also given. Experimental setup such as large Static Liquefaction Tank (SLT) is currently

equipped to execute such dredge type of induced slope failure for future validation works. It is worth mentioning that although the selected geometry is *not in the order of tsunamigenic flow slide*, the results are expected to provide valuable insight on the mechanisms of submerging water, especially at the slope interface, considering relatively realistic slope failure simulation.

Apart from this, in the current modified numerical model for simplicity the interaction between soil slope and submerging water considers following assumptions/limitations:

1. No interface hydraulic slip plane.
2. Interface nodes are solved, sharing both fluid and soil properties, thus same displacements and normal stress are considered at interface for both fluid and soil.
3. Additionally, no spin and vorticity for fluid material modelling was considered. Although, considering that the focus of study lies within the limited range of liquefied flow, it is not expected to have large fluid flow progression, where strong vorticity might be created.

Further, for *accuracy check* both soil model and fluid model are separately viewed. This is possible to do since the simulated situation is undrained, thus submerged water acts as an external load to soil – pore water skeleton and vice-versa. In the case of soil, as mentioned earlier, the accuracy in current modified model has been inherited from the previous model with respect to analytical shear wave propagation. For testing the dissipative mechanism of the submerging water due to external disturbance, a separate fluid tank simulation test is executed.

Finally, three test scenarios were analyzed; hereafter refer to as *Case A*, *Case B* and *Case C*. Out of these three tests the first test (*Case A*) was considered to be as a pilot test, who mainly complies with the previous model considerations. Hence, it consists of previous model mesh and numerically uncoupled setting i.e. constant hydrostatic pressure heads at soil slope surface, due to submerging water level. The major purpose of this test was to check the influence of newly modified dredge mechanism on the outcomes with respect to previous model simulated results. Further, also to evaluate the influence of different mesh refinement on the outcomes with respect to the new mesh models (i.e. *Case B* and *Case C*). Thus, this case mostly helps to better judge the limitations of the modified model and therefore to provide further recommendations accordingly, for future works. Hence, this case contributes to the *tertiary research aim* (refer section 1.3).

The other two cases i.e. *Case B* and *C* (a new mesh models), are the main scenarios that are analyzed in order to achieve the research goals. Here, *Case C* was modelled as a fully coupled soil slope and submerging water interaction model. Whereas, *Case B* is used as a comparative test, performed in order accomplish the *primary aim*. This case uses similar setting as in *Case C*, however the model is treated as uncoupled and assumes constant hydrostatic pressure heads at soil slope surface, due to submerging water level.

As per Author's best knowledge this is the first time such a coupled interaction of submarine landslide work has been carried out. Considering the interdisciplinary nature of this work, the results are expected to provide valuable insights that will be useful in both Geomechanical and Ocean engineering, submarine landslide related studies.

1.5 Outline

The outline of this thesis is presented in table 1.1.

Table 1.1: Thesis outline

Chapters	Overview
Chapter 1	Includes thesis motivation , aims, research questions and detailed overview on approach
Chapter 2	Includes literature studies based on both Geotechnical and ocean engineering perspective. Literatures on: Static liquefaction, flow slide patterns computational and experimental studies, submarine slide induce wave features, experimental and computational work.
Chapter 3	Section 3.1, 3.2, 3.3 and 3.4: Includes theory on numerical framework, Monot soil model, fluid model, and energy implementation, respectively. Section 3.5, 3.6 and 3.7: Includes methodology i.e. problem geometry, loading phases and execution Section 3.8: Includes fluid model verification test.
Chapter 4	Includes result and discussion of various implemented Cases A, B and C as discussed in previous section 1.4.
Chapter 5	Provides final conclusions asper the research questions. Summaries limitations and thereby provides recommendations for future work.

2

Literature Review

2.1 Flow slides: A Geotechnical perspective

This section details the geotechnical perspective of liquefaction flow slides with main focus on submarine statically triggered slides in loose sands. Thereby discussing both localized and global mechanical aspects based on real events and experimental studies. However where deemed necessary, some aspects of cyclic loading and different soil types are discussed, in order to have a broader view on the subject. Further this section also details the current computational methods, used for simulating flow slides in geotechnical engineering.

2.1.1 Static liquefaction and other soil mechanics relevant theory

Static Liquefaction – In Eckersley (1990) the term liquefaction has been defined as an apparent rapid solid-fluid transformations and consequent flow of soil to very gentle slopes (1° - 4°). The studies shows that young, loose fine grained sands with low plasticity are usually associated with static liquefaction in undrained or drained saturated water flow conditions (Eckersley – 1990, Lade and Yamamuro – 2011, Beddoe and Take – 2015). This behavior is in contrast to dense sands which under undrained conditions and monotonic loading have experimentally shown dilatant behavior (Chu et al., 2015). Additionally, it is noted that soil slopes even when under drained saturated conditions with water flow comply with the necessary requirement of liquefaction i.e. soil should experiences shear stress that is greater than or equal to those required to initiate liquefaction under undrained conditions (Kramer and Seed, 1988). Since, Eckersley (1990) has shown in his experiments that even in drained ground water flow conditions at a time when the failure is triggered the soil experiences high excess pore pressures, thus representing apparent undrained condition and liquefaction of a thin water-saturated soil layer.

Moving on, the liquefaction flow slides in reality have been associated to a wide variety of triggering mechanisms which may be associated to naturally occurring or human activities. One such early example of naturally occurring flow slides in submarine environment is of Zeeland, south western part of the Netherlands, first published in Koppejan et al., (1948). Here the flow slides occurred due to scouring of the soil mass along the toe combined with the occurrence of spring tides (see figure 2.5). Another, example of submarine liquefaction flow landslide is at Puget Sound northwestern coast of U.S in 1985; this is a special case where the flow slide has been triggered due to the combination of both man made activity, namely dredging, and naturally occurring tidal movements (Kraft et al., 1992).

In general it can be said that there always will be some kind of initiation or triggering mechanism involved in the activation of the flow slides. Therefore it is more important to understand the mechanics within it. Experimental studies listed below in section 2.1.2 for flow liquefaction slides in loose sands, overall show that high excess pore pressures are observed along the slope, while the triggering of instability takes place, leading to subsequent liquefaction. To improve the understanding

of this generally observed mechanism or behavior of loose sands further, typical characteristic of soils from elementary tests such as undrained triaxial tests can be referred to from figure 2.1. In here e_0 represents the initial void ratio of the soil and e_{cr} represents the critical state void ratio.

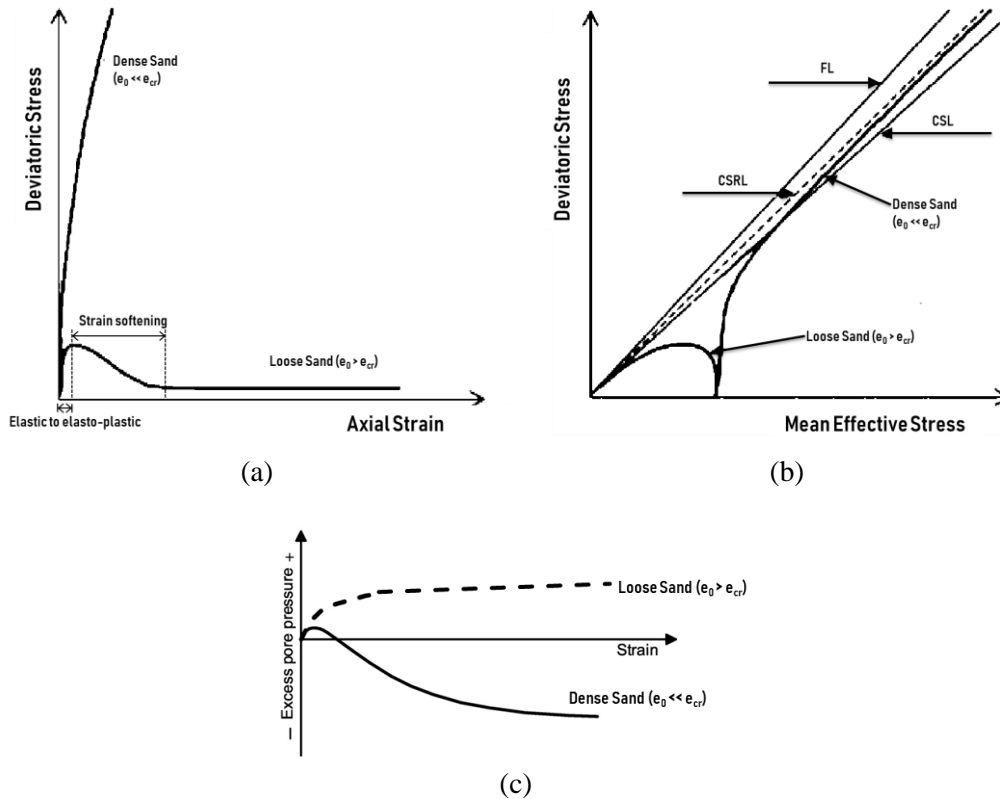


Figure 2.1: Characteristics of Monotonic undrained triaxial compression tests with axial displacement control of dense and loose sands (a) Deviatoric stress vs axial strain, (b) Effective stress Path (a and b, modified from Chu et al., 2015), (c) Excess pore water pressures (modified from Andersen and Schjetne, 2013)

The above figure gives a closer look of a soil element state during the application of loading for dense and loose sands. It can be observed that in both cases the pore water pressures play a critical role and have a contrasting behavior. In case of very dense sands during the initial loading phase the pore water pressure increases and thus indicating contractive behavior of the soil, however with further loading the excess pore pressure decreases drastically, leading to rapidly increasing excess pore water suction and strain hardening behavior, due to a tendency to dilate. This turning point for dense sands in literature has been associated to the change in soil particle arrangements or orientations which may include relatively more closer grains contact points from previous state at macro-level and the formation of metastable holes (Nasser and Takahashi, 1983). It is to be noted that this same dense sand in cyclic loading may still lead to its liquefaction, since as soon as the reversal in direction of the shear loading takes place the soil particles micro structure drastically loses its granular contact points and thus losing its strength (Guzman et. al., 1988). More on cyclic loading behavior of dense sands can be referred to from Castro (1969). For monotonic undrained compressive loading the dense sands show increasing strain hardening behavior. The corresponding effective stress path, shown in figure 2.1(b), causes the soil state to approach a constant stress ratio line. In this case the peak and critical states cannot be determined for the soil and such stress-state behavior is referred to as non-flow condition (Chu et al., 2015).

Undrained triaxial compression of loose sands with “axial displacement control” induces contraction of the granular skeleton, increasing deviatoric stress (see figure 2.1(a)) with accumulation

of pore water pressure as shown in figure 2.1(c). This process continues till a limit stability state is reached as represented by highest deviatoric stress point in case of figure 2.1(a) and 2.1(b), during this period the soil stress state moves from elastic to elasto-plastic behaviour. Any subsequent increase in pore water pressure due to loading leads to a progressive rapid reduction of the deviatoric stress as shown in 2.1(a). In, general the reduction of the deviatoric stress after its peak has been attained is referred to as strain softening and this thereby has been linked to liquefaction (Castro, 1969). Additionally, after peak point, excess pore water pressure increases dramatically throughout the strain softening of soil (Jafarian et. al., 2013). This nature of rapid increase in pore water pressure has often been used in the experimental studies as criteria for identification of the onset of liquefaction (ex. Jager, 2018 and Groot et. al, 2018).

Ultimately, the state when strain softening leads to complete reduction of deviatoric stress, such that soil reaches its residual strength as shown in figure 2.1(a), is classified as complete liquefaction. During this state of soil in undrained condition the pore water pressure becomes constant (Jafarian et. al., 2013). Apart from this, an intermediate case with medium loose sand will show a limited liquefaction where the soil stress state gets recovered (increase in deviatoric stress) after showing a certain extent of soil softening behavior, Castro (1969).

Furthermore, noting that the effective stress path from figure 2.1 (c) or 2.2 of loose sand, reaches its instability, represented by the peak deviatoric stress, defining the instability line, well before both the critical state line and the drained failure line. This observation implies that, considering that the instability is imposed due to drainage constraints rather than caused by bifurcation, this leads to a diffusive type of instability in soil instead of a localized shear band type failure that occurs above the critical state line (Jager, 2018). The zone of potential instability for undrained triaxial compression tests is defined between the instability line and the critical state line as shown in figure 2.2. This zone specifies the instability condition for loose sand under undrained conditions (Chu et. al, 2015). Moreover this zone of instability is stress point dependent rather than stress path dependent, implying that no matter what the trigger mechanism is to bring the soil into its instable state, further generation of excess pore pressure will lead to liquefaction (Jager, 2018).

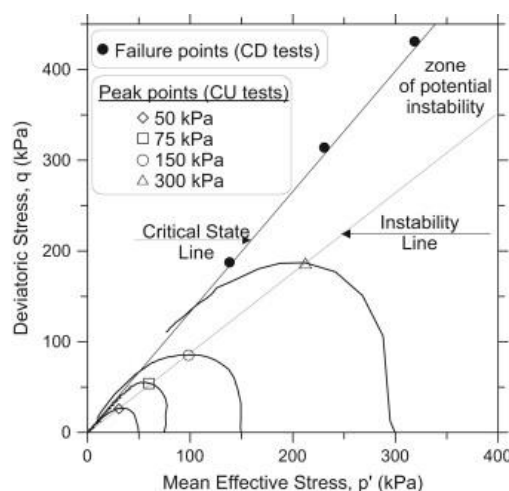


Figure 2.2: Instability loose sands (Chu et. al., 2015)

Potential slip surface pre application of trigger loading – In submarine sand slopes, apart from loading, several aspects such as: the process of sand deposition, its geometry (including shape of surface of deposits), ageing and the pre-history of loading all influence the formation of a potential

further lead to a change in inward movements at the top and outward movement at the bottom of the rupture surface (refer, figure 2.17 description).

Next, observing figure 2.4(b), it can be seen that the soil in slump type of slide moves along the rotational slip surface; moving down and inward along the direction of slope at the top and moving up and outward at the end of slip surface. It should be noted that in case of a liquefaction flow of sand or quick clays, since the collapse is initially diffusive rather than local, the whole soil mass will flow like a viscous fluid along this rupture zone instead of producing tension cracks, which may be the case in stiff clays.

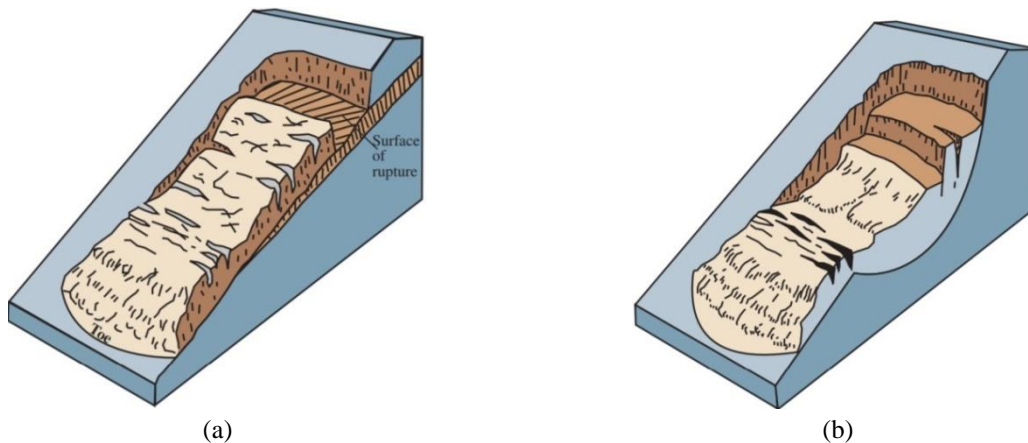


Figure 2.4: Type of Submarine slide; (a) Translational slide, (b) Rotational slide (Modified from, USGS: fact sheet- 2004-3072)

Moreover these flow slides are further characterized based on their failure progression as retrogressive or non-retrogressive spontaneous complete failures (Jager 2018), see figures 2.5 and 2.8 for example. The latter one has been more closely associated to complete liquefaction (Jager, 2018).

Next, considering different types of soil deposits prone to flow type of failures, such as: sensitive clays, loose and dense sands, author here does not choose to classify them based of type of slide. Since, it has been observed that each of this type of soils, depending on its anisotropic characteristics and varying bedding layer geology, may involve various slide characteristics. Thus, instead here several examples from each of the soil type are discussed, specifically focusing on static liquefaction of loose sands.

- Loose Sand: Zeeland slides are possibly the oldest examples of static liquefaction flow slide observed in Netherlands. They have been first published by Koppejan et. al., (1948). Figure 2.5 can be referred to for series of slides occurring in Zeeland based on mechanism after Kopejan et. al., (1948). The figure depicts a typical retrogressive slide with compound or rotational motion. Study suggests that the lower part of the slope, which forms a gentle slope profile of an angle of 3° to 4° after failure, is due to flow liquefaction. However, the later part of slope generates steeper profiles, failing more conventionally, involving the formation of shear bands (Jager 2018).

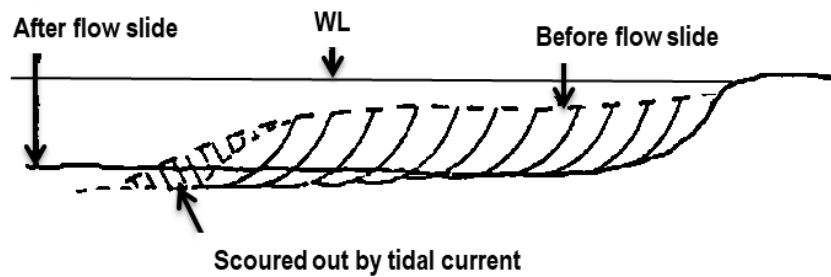


Figure 2.5: Retrogressive Zeeland submarine slide, mechanism after Koppejan et. al., (1948)

Experimentally this type of retrogression in loose sand has also been studied in Delft soil mechanics lab. The research was carried out for the design of the storm surge barrier in Oosterschelde estuary during the period 1973–1977 (Groot et. al, 2018). For this study a large and small size of flume tanks were used. However, here only the tests with the large tank are discussed. In these experiments loosely packed sand slopes were created by application of the fluidization method. Moreover the slopes considered was very steep 2V:1H and the triggers were induced by opening the rotating gates, supporting the soil slope. The experimental setup can be referred to from figure 2.6(a), which also shows the positions of the pore water pressure transducers.

In this study about 38 tests were performed out of which initially 13 were used to develop a satisfactory test setup, following 13 for studying the general behavior of loose sands and finally 12 to determine the critical relative density for the occurrence of flow slides. Nonetheless most of the experiments show a retrogressive liquefaction mechanism, one such experimental result can be referred to from figure 2.6(b) and 2.6(c), showing retrogressive slides at different times and pore water pressure development throughout the test, at different positions. From this test result it was concluded by Groot et. al., (2018), that all the slides occurred as a retrogressive flow slides, for which the whole bulk mass flowed out without the occurrence of any successive localized shear bands. However as stated in Jager (2018), it remains unclear whether the measured excess pore water pressure represents complete liquefaction or limited liquefaction. Nonetheless with the propagation of the deformation in time, in general, also a propagating peak in excess pore water can be observed (see figure 2.6(c)). Moreover the nature of the slide can also be observed, from figure 2.6(b), showing that during the early phase of the slide the flow is more a translational and during the later one turns progressively to a more rotational type.

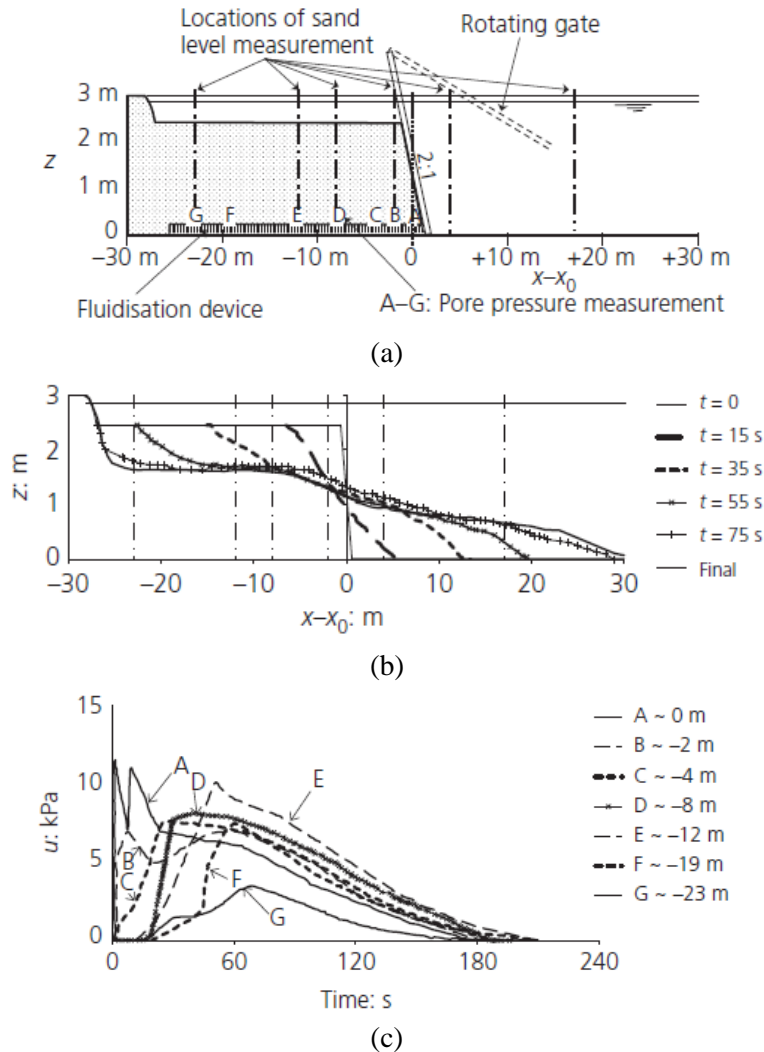


Figure 2.6: Large Flume tank experiment at Delft soil mechanics lab (Groot et. al., 2018); (a) Experiment setup, (b) Retrogressive flow slide failure, (c) Pore water pressure vs time.

Next, *non-retrogressive spontaneous liquefaction flow slide* has also been reported in a submarine landslide at Stromboli Volcano (Italy) in 2002. Here the series of submarine and subaerial slides have led to the formation of two tsunami waves with a maximum run up of 10m (Boldini et. al., 2005, Chiocci et. al, 2008). Figure 2.7(a) can be seen, for all the types of large slides observed in the area. The main triggering mechanism was the lava eruption which started 2 days prior to the first occurring deep-seated large sub-aerial landslide α , however no tsunami was reported after this failure. In fact, the disintegration of this slide mass led to the formation of large blocks β and γ . Finally, this progressive disintegration of α slide and the deposition of the masses above the submarine slope τ , was hypothesized to be the main cause of its static liquefaction. This thereby generates the first tsunami and then led to the subsequent second tsunami, due to sub-aerial γ and β destabilized blocks failure (Chiocci et. al, 2008, Bodini et. al, 2005).

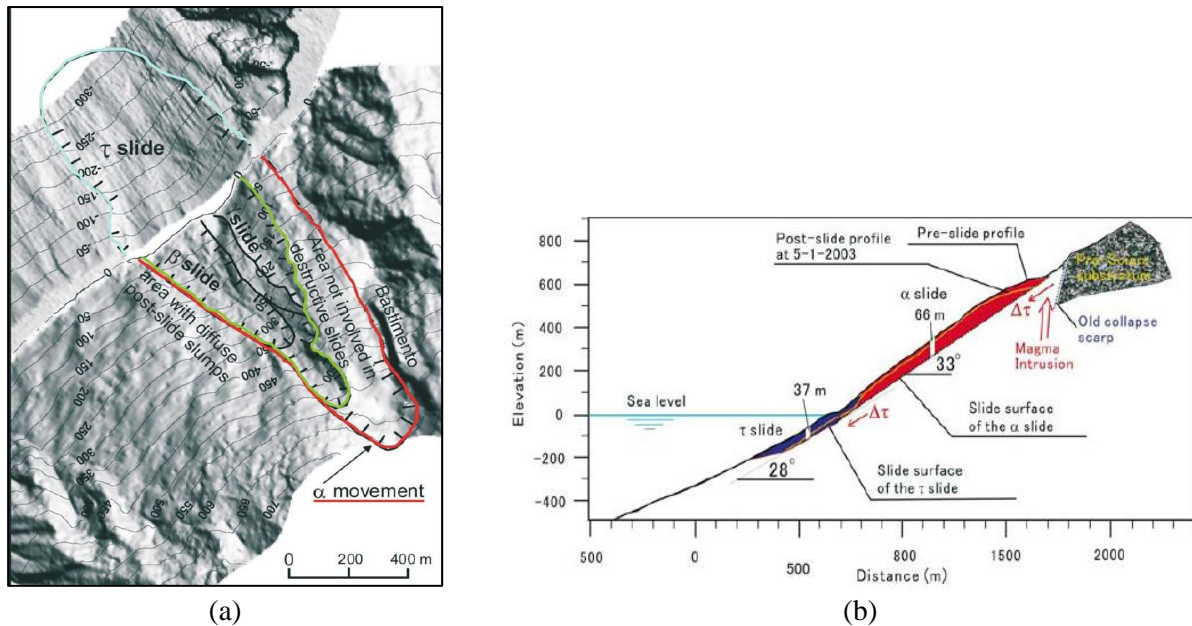


Figure 2.7: Stromboli landslide (2002); (a) Different slides observed, (b) Profile of main slides- slip with pre- and postslide morphology (Boldini et. al., 2005)

Bodini et. al, (2005) conducted undrained ring shear tests on the soil samples from the site, after which he concluded the sands to be medium dense rather than loose, with high crushability and low shear strength. The stress path and excess pore water pressure results in fact shows a dilatant behavior at first (during initially loadings) and thereby sudden liquefaction after reaching certain limit, indicating crushing of soil grains. It should be noted that the samples obtained for testing may not have represented the exact soil conditions due to several reasons: 1) samples are not exactly from location of τ slide rather near shore regions, 2) sampling is done after the event, on stabilized layers, 3) soil samples were segregated before testing which might also hamper the quality of results. There is a possibility that the actual submarine slide consisted of more loosely and finely graded sands, as Chiocci et. al, (2008) has mentioned that the submarine slide τ apron deposit was reported to have young and loose volcanoclastic debris with low shear strength.

Boldini et. al., (2005) also shows the profile view of submarine slide τ with averaged slope angle of 28° (see figure 2.7(b)), thus the slide here is considered as translational flow slide, occurring in a weak zone (probably due to heterogeneity in bedding layer). Additionally, it can be observed that the rupture surface at the end merges with the original slope in conical/sloping fashion for τ slide.

This type of underwater spontaneous non-retrogressive flow slide, has also been experimentally produced in Delft soil mechanics lab. The first such early experiment was conducted by Molenkamp and Os in Brutus tank in 1986 (Molenkamp and Os, 1987) and the second relatively new experiments conducted by Jager in large liquefaction tank in period between 2010- 2018 (Jager, 2018). In these cases, due to maintained homogeneity of the soil, the whole soil slope collapsed rather than a limited region collapse shown in figure 2.6(b).

In the first experimental work (Molenkamp and Os, 1987), the objective was to verify the capability to simulate and predict the initiation of static liquefaction and subsequent flow in the loose sandy soil by means of the constitutive model: Monot double-strain hardening model, developed by Molenkamp (1980). For this experiment the *Brutus tanks* was setup

which had an internal size of 2m by 1m by 1m (LxBxH). A loose sand profile was prepared by cut method, where firstly, through fluidization a sand bed up to the height of 0.73m was created and then through dredging, a slope of 1v:1.7h and height of 0.44m was achieved. In order to observe the excess pore water pressures and deformations in the soil, pore pressure gauges and gap sensor were placed at the bottom as shown in figure 2.8.

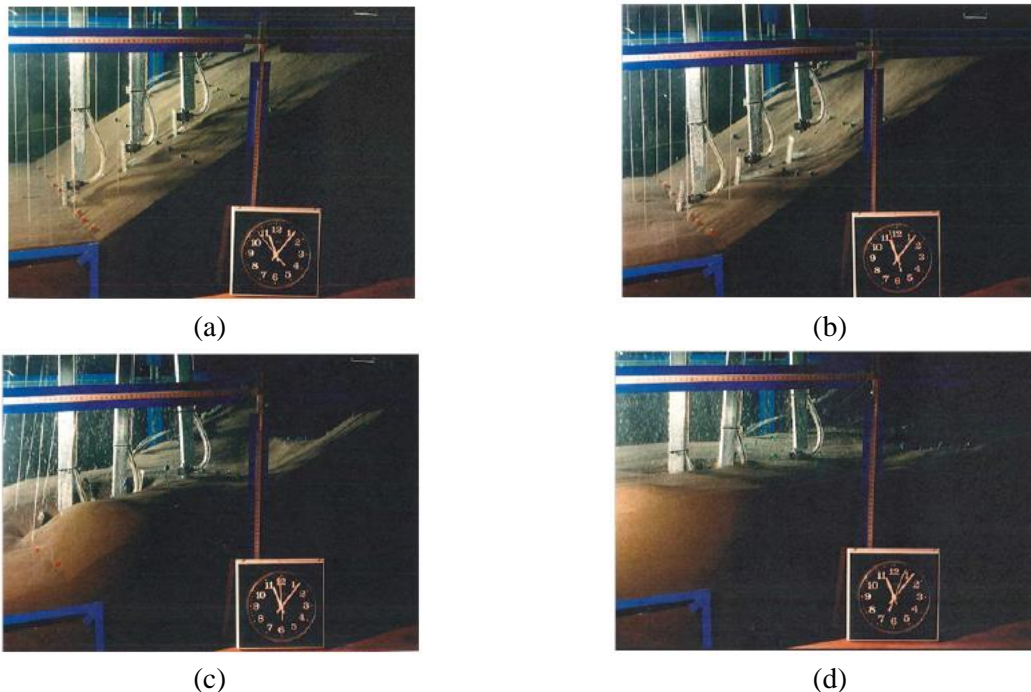


Figure 2.8: Liquefaction in Brutus tank, starting at time 11:06:53.2; a) $t=0$ s, b) $t=4$ s, c) $t=6.2$ s d) 10.5s (Molenkamp and Os, 1987)

After the final setup, a trigger mechanism by a sudden single pulse discharge through the fluidization system was used. As a result with increasing discharge in the system the excess pore water pressure in the system increased. This increase in pore pressure thereby led to sudden liquefaction of the slope marked by a corresponding pore pressure increase that amounted for full liquefaction. As soon as the liquefaction had been initiated the pore water pressure started changing and the slope deforming. By the end of the experiment marked by the time $t=10$ sec, the soil became static and the sand bed appeared to have leveled horizontally, representing complete collapse as shown in figure 2.8(d). The whole progression of collapse happened really fast as can be seen through the pictures taken of the tank at different time frames, through figure 2.8., thus the deformation rates could not be measured accurately. Further, it is also important to note that because of the way the measuring gauges were placed, as can be seen from figure 2.8(c), interference of the slope deformation occurred. Nevertheless it was concluded that the slope failed by liquefaction of the homogenous very loose sand.

Next, de Jager in his PhD work at Delft University, setup a *large liquefaction tank* of dimension 5m by 2m by 2m (LxBxH) (see figure 2.9), where he performed series of several liquefaction tests with varying densities and varying ageing period, in total about 32 tests were performed (Jager, 2018). The objective in broader sense is to establish a large test setup which can effectively simulate field conditions under 1g gravity loading, so that it can be used for evaluating the capabilities of numerical FE models with constitutive soil models based on a global behavior rather than just only element testing. A second objective is to evaluate the

detailed mechanism involved with loose sands static liquefaction. Besides observing the well-known phenomena of static liquefaction in his tests i.e. practically horizontal slopes after soil liquefaction, one of his main findings suggests that, static liquefaction of loose sands can be triggered at relatively gentle slopes, ranging between 1v:8h and 1v:10h.

The soil profile in the test setup was created and controlled through the fluidization method to produce profiles with a range of soil densities. Further, the underwater soil bed was created with horizontal layers, filling the tank up about 0.5m height by sand and another about 0.5m with water. Additionally, similar to all other physical experiments Jager too used pore water pressure as the variable to measure the extent of liquefaction. For this purpose 3 pore water pressure transducer were placed at the bottom of the bed, as shown in figure 2.9.

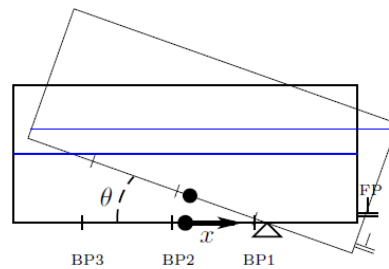


Figure 2.9: liquefaction tank with pore water pressure transducers: BP1, BP2 and BP3. (Jager, 2018)

After providing several resting period so that the sediments could settle after fluidization, finally a trigger mechanism was activated which was achieved by gradual and slowly tilting the liquefaction tank to the highest achievable rotation of 10° . While tilting a brief pause was provided at 5° rotation, before achieving the ultimate rotation angle, so to observe any movement within the lower limits itself.

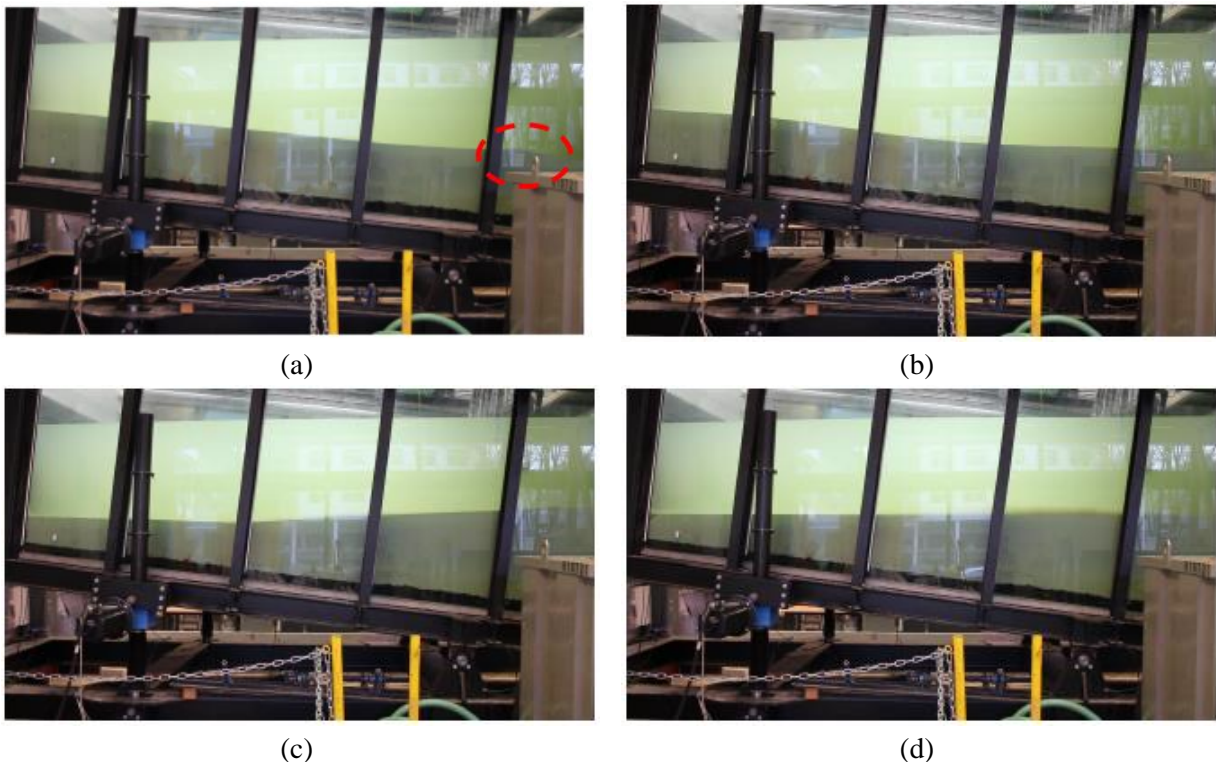


Figure 2.10: Liquefaction failure of sand, time starting just before failure initiation; a) $t_1=0$ s, b) $t_2=4$ s, c) $t_3=8$ s and d) $t_4=12$ s. (Jager, 2018)

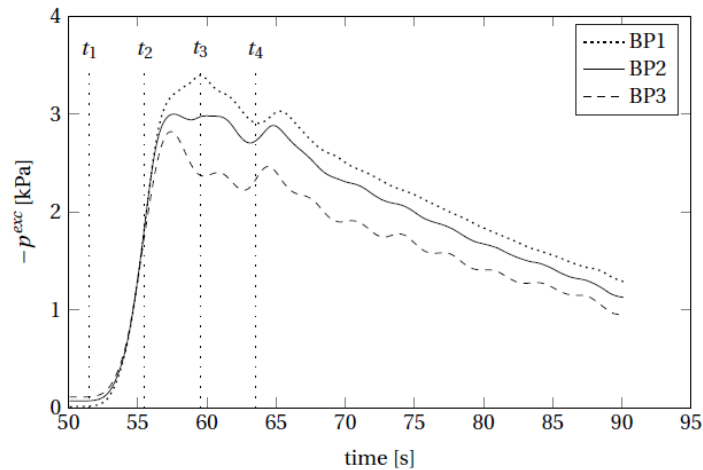


Figure 2.11: Pore water pressures in total time scale with marked failure time frames of figure 2.10. (Jager, 2018)

Figures 2.10 and 2.11 shows the typical behavior of the loose sand layer in the liquefaction tank, illustrating the captured soil failure at different time frames and pore water pressures, respectively. Figure 2.10(a) ($t_1=0$ s), depicts the sand bed just before it start moving. Here a first sign of failure is observed with the crest formed by the sediment material near the lower end of the tank. Next in figure 2.10(b) ($t_2=4$ s), a proper wave in a soil surface bed can be observed forming an arch shape in the middle of the tank. Figure 2.10(c) at $t_3=8$ sec, shows the effect of boundary condition as the soil wave is reflected from the lower end of the tank. This signifies the generation of inertial energy by moving soil mass down the slope. Finally at $t_4=12$ sec in figure 2.10(d), Jager (2018) reported that the soil reaches it stationary situation, where the soil surface gets almost horizontally levelled. However he also reported, as can be seen in figure 2.10(d), a small surficial wave travelling towards the bottom part of the slope. This wave was reflected earlier at the upper end of the tank.

In general from figure 2.10, one important observation is that the surficial soil movement travels in the form of waves, also suggesting that the overall movement of soil is not exactly translational. Particularly, the motion between figures 2.10(b), 2.10(c) and 2.10(d) probably suggests that the soil from the upper crest region of figure 2.1(b) moves down and rightward towards the mid thin arc formation and the soil at the lower part of the tank moves up and rightward.

Next, figure 2.11 shows the excess pore pressures generated throughout the time. It is to be noted that the x axis here represents the total time of testing, starting from 0.5 sec before the execution of tilting. In this figure the point where the pore-pressures start to increase progressively, practically represents the initiation of liquefaction. It can be seen that at around t_2 and t_3 , the pore water pressure transducers show the peak values representing the highest degree of liquefaction attained at these points. Next the pore pressures start dissipating and the soil begins to get consolidated. The average peak pore pressure noted in this test was about 3kPa, which was below the maximum value of the pore pressure corresponding to full liquefaction i.e. 4.45 kPa, calculated empirical in Jager (2018). This observation was reported to be consistent with other tests as well, by Jager(2018), even though the soil surface layer became horizontal at the end of liquefaction.

Other than the aforementioned translational and retrogressive type of failure events, it is possible that loose sand slope might fail as a *deep-seated rotational flow type*. One of the

centrifugal test experiments conducted under the *Canadian Liquefaction Experiment* research program can be used as a good reference. The objective of the study was to create and verify the numerical behavioral model for predicting liquefaction phenomena through both this test and also another field experiment (Byrne et. al., 2000). However, here this study has been used to show how a different triggering mechanism and pre-stress conditions than in previously stated experimental studies, can influence the failure type pattern.

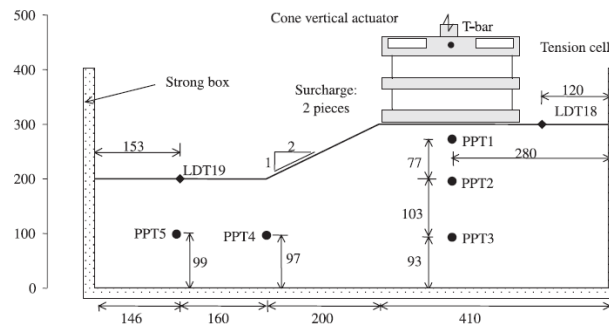


Figure 2.12: Centrifuge Experimental setup (PPT – pore water pressure transducers, LDT – longitudinal displacement transducers, units in mm), referred from Byrne et. al., (2000)

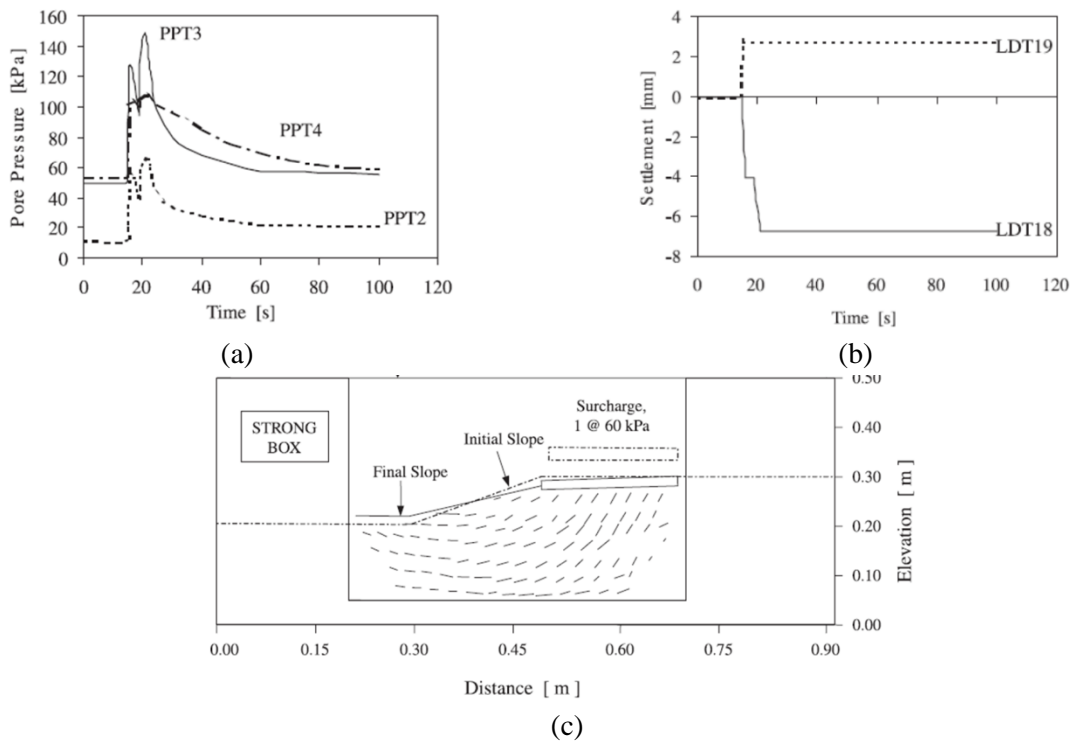


Figure 2.13: Result of Centrifuge Experiment; (a) Pore pressure during loading, (b) surface settlements during loading, (c) deformation field due to first surcharge of 60 kPa (modified from Byrne et. al., 2000)

The geometry and soil profile of the centrifuge experiment are indicated in figure 2.12. Here an underwater embankment of 5m height was setup on a 10 m deep foundation, all made up of loosely packed sands. As a part of initiation, the setup was subjected to an initial loading of 50g acceleration, brought in by a total of 5 increments with sufficient time intervals within each increment so to have drained condition. The final relative density obtained after

spinning was 29%. It is to be noted that for a scaled response of the pore water pressure dissipation under 50g acceleration, canola oil is used. Further, after the initiation stage under 50g acceleration, about 60kPa of loading was applied twice with an interval of about 2.6 sec between each loading.

Results of the experiment are illustrated in figure 2.13. From figure 2.13(a) it was observed that the transducers just below the loading i.e. PPT2 and PPT3 experience sudden increase in excess pore pressure, followed by rapid dissipation in both load applications. Thus both the measurements show pulse type formation with two peaks. However, the excess pore pressure reading by the transducer below the toe (PPT4), shows first a rapid increase under first load application, but hardly any dissipation thereafter. Finally with the 2nd pulse loading hardly any increment in pore pressure was observed. Similarly, complimentary behavior was observed in surface settlement recorders (see figure 2.13(b)), which at the embankment surface (LDT18) show a sharp increase in settlement with each load application. However the recorder at the toe surface does not show any increment after the 2nd loading. Nonetheless, the soil liquefies and a deep seated rotational flow failure was observed, see figure 2.13(c).

- **Dense Sand:** In densely packed water saturated sand, soil slope retrogressive collapse under static loading conditions have also been observed. The mechanics involved behind such failures are different than that of static liquefaction in loose sands and referred to as Breaching (Berg et. al., 2002). This type of failure has mainly been confined to very steep subaqueous slopes that are composed of densely packed sand and it fails as a thin surficial layer of sediment retrogressively (Berg et. al., 2002, Beinssen et.al.,2014). Moreover, on the contrary to liquefaction, where the collapse is very rapid the breaching collapse take time as can be seen in figure 2.14. In this case when dense sands are subjected to initial temporary loading, due to the increase in shear stresses they show dilative behavior, resulting in suction in the pores and thus make steep slopes initially stable. However, gradually as the inflow of the water reduces the suction, the grains located at boundaries of the slope lose their stability and thus collapse (Peelen, 2016).

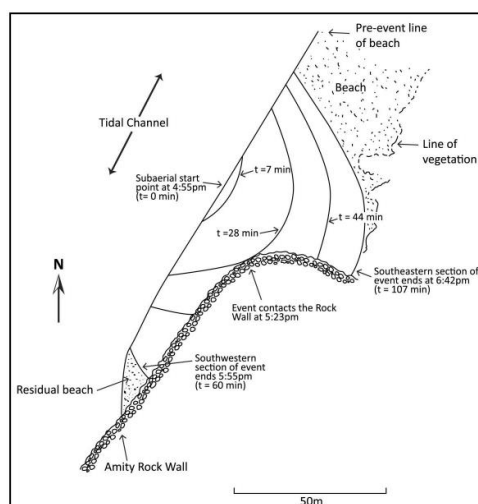


Figure 2.14: Evolution of Breach failure event at the Amity Point study site on 21/1/2014 (Beinssen et.al., 2014).

Example of such retrogressive failure has been recorded in 1983 at the bank of a 10-m-deep channel in the Dutch Wadden Sea (refer, Berg et. al., 2002). Another ex. is at Amity point, Australia in 2014. Figure 2.14 shows the retrogressive development of the failure.

Further apart from, static failure for increasing monotonic loading, the dense sand can experience liquefaction under the application of cyclic loading. Several cases of such sand slope failures in the submarine environment under earthquake loading have been recorded in history. One such incident is of the Grand Bank landslide in 1929 near Newfoundland, which got triggered by a preceding earthquake of $M=7.2$ (Fine et al., 2005). This landslide was so destructive that it is considered as a primary source of the Tsunami, which has been discussed in section 2.2. The displaced slope failure mass was considered to be of about 200 Km^3 , which ran as a mud and sand flow reaching up to 1000 km eastward from the source (Fine et al., 2005). With the initial available geological and morphological survey data, it was interpreted that several shallow translational landslides were triggered within the source region that later on merged and flowed as a viscous fluid, and the primary reason of the failure was considered to be soil liquefaction (Fine et al., 2005). However, with the availability of new precise seismic reflection data, it has been suggested that apart from translational slope failure, the landslide source region can also have experienced a large rotational type failure (Løvholt et al., 2018). Figure 2.15 can be seen for the details.

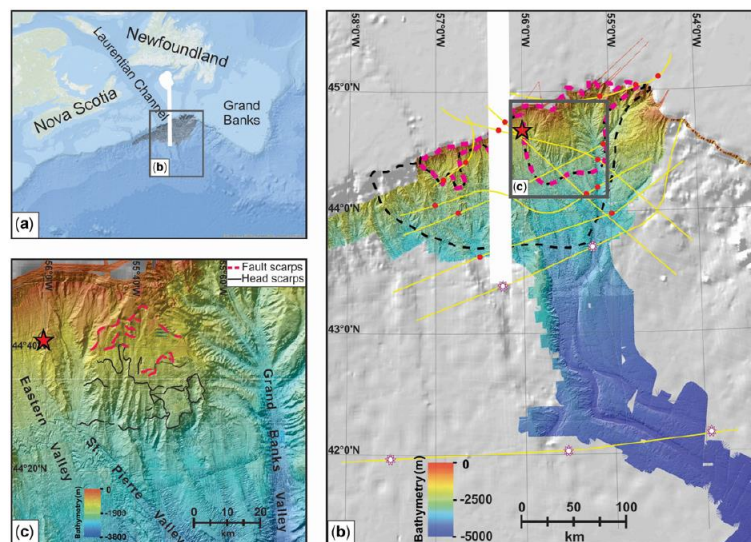


Figure 2.15: Overview of (a) the slope failure area and (b) the Laurentian Fan showing the cable breaks that occurred in the sea because of the turbid soil flows (yellow lines); the red dots indicate instantaneous cable breaks and the white dots delayed cable breaks. The red star indicates the earthquake epicenter. The presumed main failure area (pink dotted area) and area of local sediment failure (black dotted area). The image contains bathymetry. (c) Newly identified fault scarps, including rotational failure and translational failure head scarps. (Løvholt et al., 2018)

- **Sensitive Clays:** In sensitive clays literatures suggests that the most common type of failure is of retrogressive failure with rotational sliding or slumps of limited size type as shown in figure 2.16. However, translational slides have also been observed, which are mostly confined within Scandinavian regions (Hunter and Fell, 2001). Example, Rissa slide, which is considered as translation slide, has been well document in Gregersen (1981).

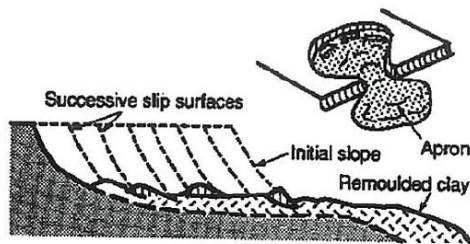


Figure 2.16: Sensitive clay failure mechanism; retrogressive sliding (Hunter and Fell, 2001)

Another example is of Storegga slide near Norway, which is considered as one of the ancient submarine landslides (about 8000 years ago), that resulted in a major Tsunami (Løvholt et. al., 2017). Løvholt et. al. (2017) simulated the slide using a remolding debris flow model to predict the tsunami waves (see figure 2.17). This has been explained in more detail in section 2.2.

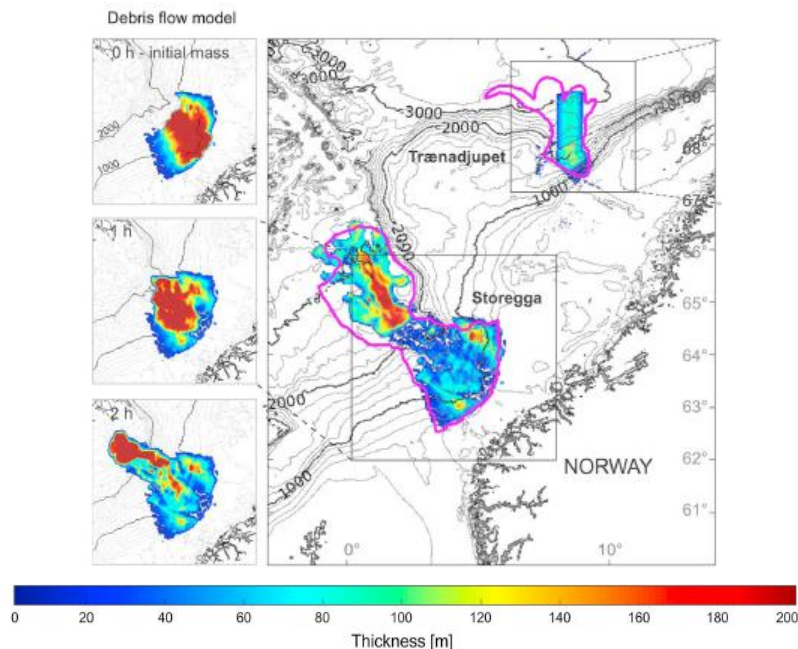


Figure 2.17: Simulated Storegga slide by Løvholt et. al. (2017); slide profile at different times

2.1.3 Flow slide computational works

Primarily this section details two main case studies: 1.) Original work by Molenkamp (1999), of which this thesis is an extension. 2.) A coupled water and submarine slope instability model by Jiang et. al. (2015) which focuses on studying the effect of thermal hydraulic coupling of dissociative methane hydrates layers on sub-aqueous slope instabilities. Apart from this, a brief comparison between commonly used Numerical methods in soil mechanics for simulating large deformation is discussed.

Submarine Slope failure work by Molenkamp (1999) – As stated before this work involves a 2D, 3 node finite element mesh with updated Lagrangian frame work, which studies the dynamic analysis of a dredging induced flow slide on a submarine slope. The details of the geometry are described later in section 3.5 and figure 3.2. The highlight of this work was an application of an overlaying fluid mass as represented the hydrostatic water pressure, expressed in terms of the surficial nodal loads. The slope

failure was triggered by artificially simulating dredging of a soil block below the toe, see figure 3.2. Here, the artificial dredging was achieved by gradually reducing the buoyant weight of the soil block (uniformly) to zero within ramp loading time of 100 s. Further the activation and initiation of soil geometry involved first a horizontal layer with an initial effective stress state defined by $K_0 = 1$, where K_0 is the coefficient of the lateral effective stress at rest. Subsequently the slope was created by virtual dredging, involving the removal of the buoyant weight of the upper part on the later slope surface interface. Since similar initiation steps are applied in current extinction work, more details on this can be found in section 3.6. Figure 2.18, shows some pictures from the paper by Molenkamp (1999).

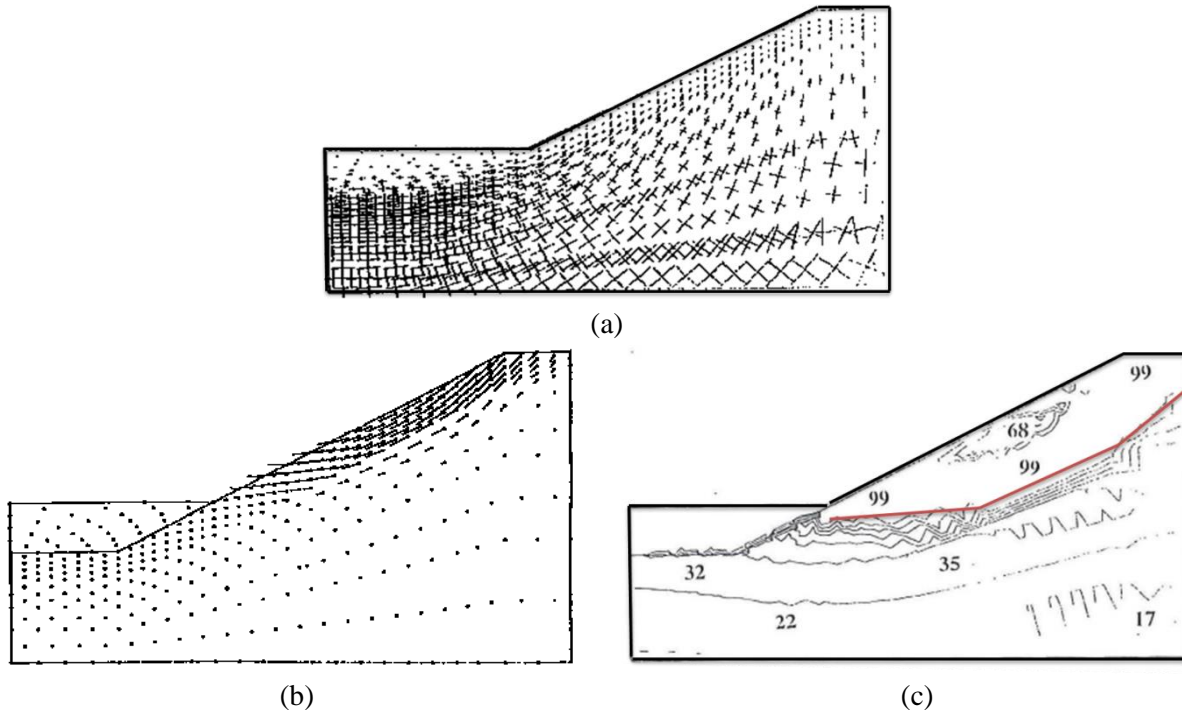


Figure 2.18: Results from study by Molenkamp (1999); (a) Initial effective stress state after unloading of assumed horizontal layers to achieve the cut type of soil conditions. Maximum effective principal stress is -280 kPa (Compressive), (b) Nodal displacement vectors at end of dynamic loading calculation ($t=22.571$ s). The maximum vector length represents 0.093 m, (c) Percentage Ratio of mobilized and failure deviatoric stress contours.

From figure 2.18(a), it was observed that after unloading of the initial horizontal layer to produce the cut type of soil effective stress states, with the effective principal stress tensor rotated to align themselves along with the direction of shear, this imitates the mechanism as shown in figure 2.3. Further the overall in-plane effective stresses were reduced from the initial condition resulting in a severe reduction of the near surface stress tensors. After the application of dynamic loading during the dredging phase, it was observed that the slope fails after about 22 s of load application and the calculation ends after 22.571s due to a numerical restriction in remaining accuracy set in the model.

Figures 2.18(b) and 2.18 (c), show the displacement mechanism and the extent of soil slope collapse due to liquefaction. Moreover, the rupture surface seems to be slightly curvy, but it still illustrates features closer to a (thick) translational flow type slide rather than a rotational one. The rupture surface can basically be divided into three parts (see, figure 2.18(c)): two sloping edges and middle part parallel to the slope. It can be observe that this formed rupture zone is clearly influenced by the principal effective stress tensor rotation at the initiation stage (see, figure 2.18(a)) and the artificial trigger mechanism to simulate dredging.

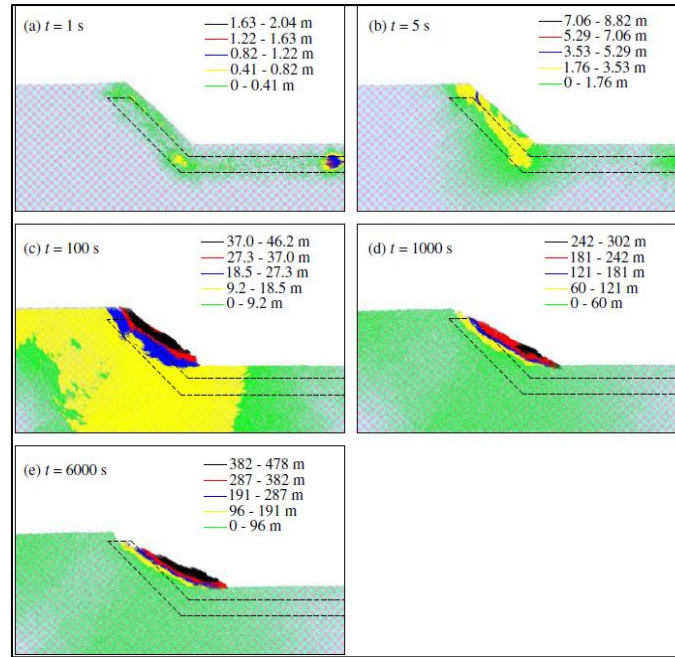


Figure 2.21: Flow Type of submarine failure, computed Displacement vs Time (Jiang et. al., 2015)

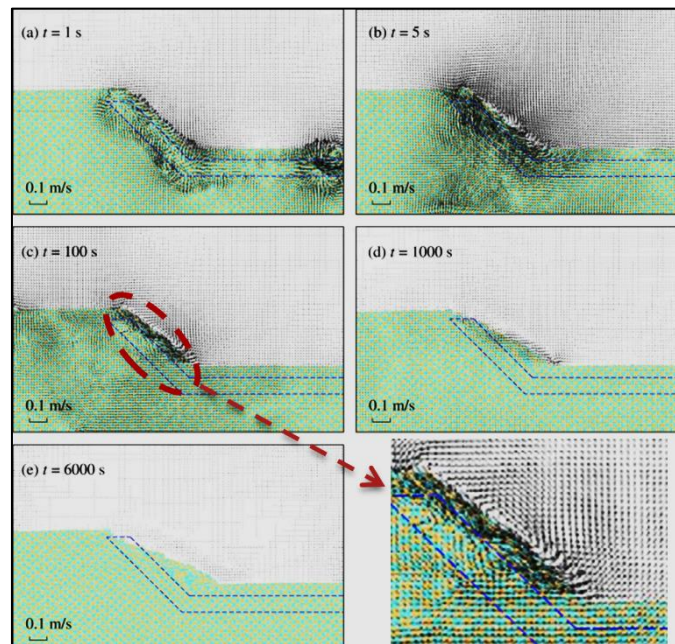


Figure 2.22: Submarine failure, computed velocity of fluid and pore water vs Time (Jiang et. al., 2015)

Soon after the dissociation of the MH layer the slope starts failing, the displacements in the soil particles along the slope can be seen from figure 2.21(a). The failure here seems to be of dispersed type near the slope, indeed indicating a flow type failure and liquefaction in the loose sand soil. Moreover observing the progression of soil mass flow, it can be observed that till time = 5 s in figure 2.21, the obtained displacements are quite small with respect to the scale of the problem geometry (see figure 2.19). It is only after $t = 100$ sec (refer figure 2.21(c)), that a full fledged shear zone formation and deformation in the geometry can effectively be seen. From this figure, one can also make out similarities with the displacement pattern observed under the study done by Molenkamp (1999), see

figure 2.18(b). Finally at $t= 6000$ sec in figure 2.20(e), the soil in the study was reported to attain a stable position. A clear displaced soil mass from the initial geometry of the slope; forming a gentler slope, can be observed from this figure.

Considering the current scope of the work, the most relevant aspect of this study is to look at the simulated interaction between flow type slope failure and submerging water. However, the results reported by Jiang et. al. (2015) concerns the computed, overlaying fluid velocity and pore water velocity of the system, rather than soil particle velocity. Nonetheless, this will still give a fair idea of the submerging water movements. In the figure 2.22, the direction of the arrows represents the direction of sea water and pore water, and the vector length is in proportional to the magnitude of the velocity. At the initiation of the landslide after hydrate dissociation, water in the dissociation zone flows outwards due to excess pore pressure generation (Figure 2.22(a)). During the onset of the landslide (Figure 2.22(b) and 2.22(c)), the sea water has been reported to show circulation near the vicinity of the slope. To be precise the magnified region of figure 2.22(c), clearly shows such circular formation near the mid slope region. Moreover in this figure, at the slope crest surface the, sea water seems to move inward as the soil is displaced down and at the toe it seems to move up and outward/rightward. Beyond the vortex formation the sea water near the mid slope region, seems to move up towards the crest of the slope. Further, during the sliding process (figure 2.22(d)), it was reported that the flow mainly distributes around the landslide body, mostly moving outward, resulting from the water–grain interaction. Finally, when the landslide is terminated (Figure 2.22(e)), the flow ends too, indicating that the water flow during the landslide is mainly driven by the movement of the body itself. Apart from the observations made by Jiang et. al. (2015), it can be inferred that for the flow type of failure ending at the toe, the onset stage of the slide (figure 2.22(b) and 2.22(c)) will be more crucial for surface wave generation than the other stages. Since, as per figure 2.22, the highest amount of velocity (implying energy) is being transferred from the landslide to the water body, at these stages.

Numerical methods in soil mechanics for large deformations- Under mesh type approaches, the two basic types of frame work that's have been conventionally used for modelling the problem in soil mechanics are Lagrangian and Eulerian mesh formulations. However both have their own advantages and disadvantages, especially when concerning a large deformation analysis in soil mechanics.

- Lagrangian mesh: In this case the Lagrangian coordinates of nodes move with the material. Making (material) coordinates of material points suitable for describing the material history in terms of anisotropic instantaneous stress strain and orientation, which thereby makes this approach easy to use for materials with history-dependent characteristics. Further as the boundary nodes remain in contact with the boundary, it makes it easy to define boundary and interface conditions. However, this approach in case of large deformations is known to suffer from severe mesh distortion and entanglement. This issue can be resolved through re-meshing techniques (Qui et. al.- 2011, Davim -2017)

The Lagrangian approach has further been divided into two types: the Total Lagrangian (TL) and Updated Lagrangian (UL) approach. The fundamental difference between these two approaches is in the way they deal with the static and kinematic variables. In TL approach these quantities correspond to the initial mesh configuration, whereas in UL they corresponds to the last calculated mesh configuration (Mohammadi, 2013).

- Eulerian mesh: In this approach the movement of a continuum is specified as a function of the spatial coordinate and time. In contrast to the Lagrangian formulation, here the mesh remains undistorted and thereby traces and allow the material to move freely within the mesh. The

advantage of such numerical approach is it can be used for fluid type motion since it is free from element distortions. However, the material point changes with time, at a given element quadrature point, thus making this approach difficult when engaging with time history depended problems. Moreover, due to the independent movement of materials, it poses difficulties in modeling of the interfaces, and in case of two or more materials this may lead to numerical diffusion. It is also difficult to apply boundary conditions, since boundaries of the Eulerian mesh nodes and the material do not coincide. Further, the Eulerian domain needs to be modeled larger to avoid body motions outside the mesh (Qiu- 2002, Konkol - 2014).

- Other More Advanced Approaches – In addition to the above mentioned conventional methods, several other advance numerical approaches have been developed with primary objective to overcome the aforementioned disadvantages and thus to achieve more accuracy. To name the few: Arbitrary Lagrangian and Eulerian (ALE), Smoothed particle hydrodynamics (SPH) and Material point method (MPM) are some commonly used approaches.

ALE – This is one of the most renowned approaches used in Geotechnics for large deformation analysis, due to its capability of incorporating the best features from te both the Lagrangian and Eulerian approaches and thus overcoming their known disadvantages. Overall the ALE method involves 3 sequential steps: a) The material nodes are moved to new positions b) Re-meshing to best-fit the material point, as per their newly displaced positioning in the previous step. c) Transferring data of the current solution from old mesh to newly modified one. Even though, this method overcomes most of the disadvantages from conventional Eulerian and Lagrangian approaches, due to its nature of repetitive re-meshing, in case of large deformation problems it becomes computationally expensive. Moreover the quality of the result is highly sensitive to the algorithm written for modifying the mesh and the data transferring (Gadala and Wang, 1998, Konkol – 2014).

SPH – This is a widely used meshless method for fluid modelling working on a Lagrangian backed framework (Steinmetz and Muller, 1992). However in the recent past it has been extended for the use in solid mechanics due to its capability of simulate large distortions by Libersky and Petschek (1990, 1993). In this approach the problem geometry is replaced by a set of particles and each particle possesses individual material properties, which moves according to balance equations. The SPH uses a kernel function to establish a relation and influence of neighboring particles with the set range. It uses field functions and their derivates at particles whose values are approximated by using kernel function at each time (Konkol – 2014). Even though this method is widely used, it still possesses limitations in case of geotechnical studies. Firstly tensile instability is a well-known problem in SPH (Konkol – 2014). Moreover, it may result into loss of consistency and accuracy due to insufficient neighboring particles at the boundary interfaces. Further, it allows particle penetration which may be unwanted in some cases (ex. soil-structure interfaces) (Bandara and Soga, 2015). It is to be noted that this feature might be useful in studying cloud formation phenomena (e.g. sediment dispersion in water), because of submarine landslide studies.

MPM – This method have been developed in recent past by Sulsky et al. (1993). In the MPM continuum is discretized as a set of Lagrangian material points within a fixed Eulerian mesh, which is used to solve the equation of momentum conservation (Konkol – 2014). In each time step firstly, the state variables (e.g. velocity, acceleration) are mapped onto the nodes of the background mesh. Secondly, a FEM analysis is undertaken, where the mesh is allowed to update its position along with the material points. Finally, the mesh is reset, with the material points remaining in their updated positions (Vardon et. al., 2017). Due to the

presence of a background grid this method has an advantage of applying straightforward boundary conditions. Also particle penetration between the interfaces is avoided. The main benefit of this method as compared to other advance approaches is the simpler application of boundary conditions; here the boundary conditions can be directly applied to grid nodes as in the finite elements methods (Bandara and Soga, 2015). This method recently has been widely researched for its application on large deformation problems in soil mechanics (ex. Bandara and Soga, 2015, Bhandari et. al., 2016 etc.). However one main disadvantage of MPM method is that it is computationally more expensive in terms of storage and run time, than other conventional methods. Further, another issue is that although stress calculations seem globally correct, stress oscillations occurs locally, this happens when material point starts to move and cross cells (Pruijn, 2016).

To show the capabilities of MPM for simulating large deformations, the study by Bandara and Soga (2015) is discussed here very briefly. Bandara and Soga, formulated a numerically intensive model in MPM to solve fully coupled dynamic problems that undergo large deformations in saturated soils. The main feature of the work was the use two Lagrangian material points to represent soil and water. The problem geometry concerned with the study is shown in figure 2.23(a).

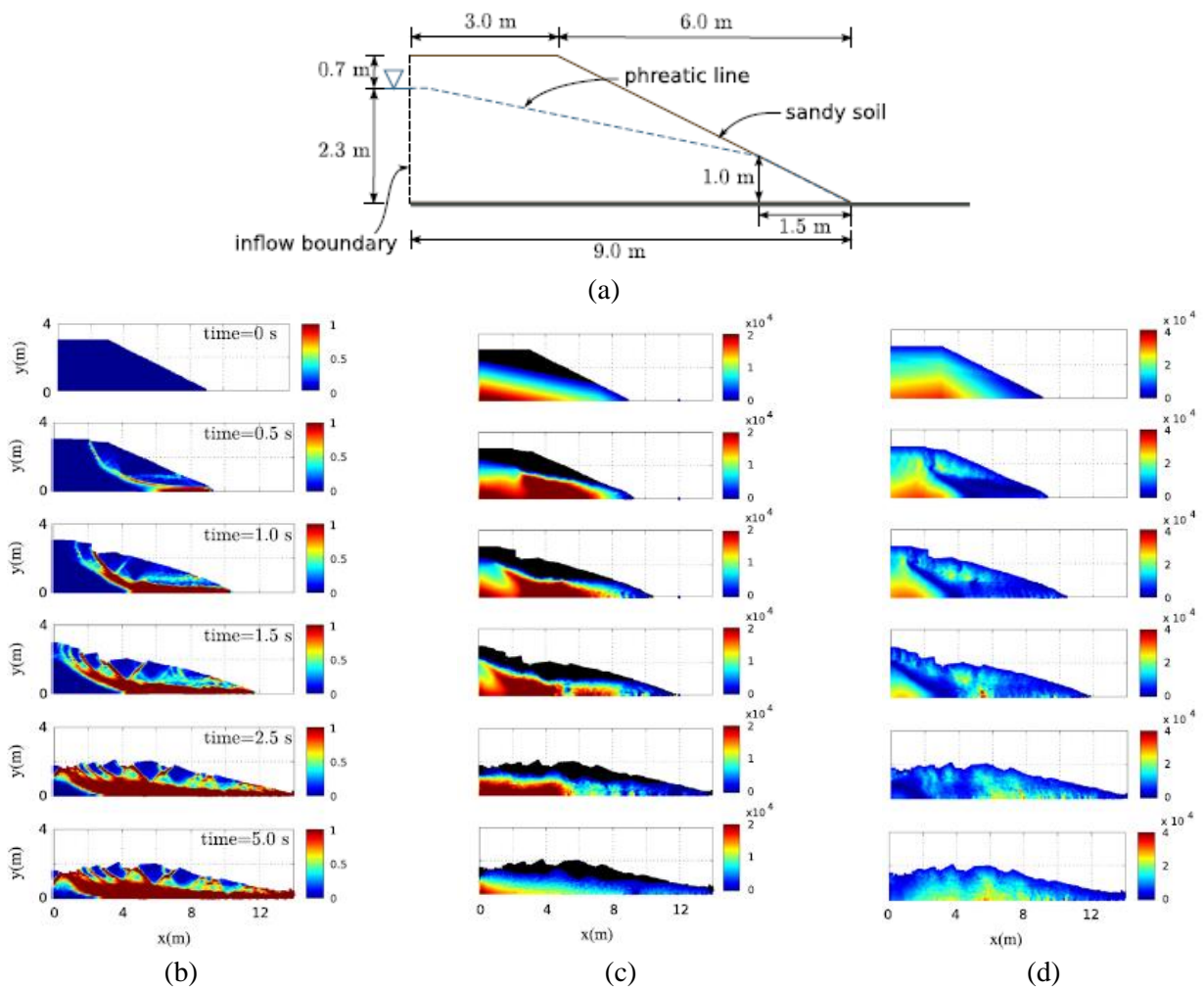


Figure 2.23: Work by Bandara and Soga (2015); a) Problem Geometry, b) deviatoric shear strain variation, (c) Pore water pressure (Pa), d) Vertical effective stress variation (Pa).

In total two scenarios were considered in this study, however only one is detailed here. The Soil was considered as loose sand modelled using Mohr-Coloumb with strain softening and hardening behavior. Further soil above the phreatic level was considered as partially saturated with defined matric suction values. As a trigger mechanism a constant water discharge was maintained by controlling inflow and outflow boundary conditions.

Result for change in deviatoric shear strain, pore water generation and vertical effective stress, throughout time can be seen from figure 2.23. It was reported that the initial shear failure has resulted in high excess pore pressures along the shear bands, which therefore results in zero mean effective stresses in the saturated region. Moreover with time several shear bands were developed and spread towards the levee, thereby resulting in progressive failure of the soil. Further, the unsaturated soil that lies above the saturated region shows discontinuous failure mechanisms, and the resulting soil blocks tend to flow above the saturated region. This, therefore results in higher excess pore pressures and further instability. At the end of the rapid slope failure, the excess pore pressure gradually dissipates and the effective stresses increased.

Though this not being a submarine landslide literature study, it still provides a good indication on the current capabilities of models used in geotechnical engineering. It shows how complex scenarios (such as: soil conditions, loadings etc.) can effectively be handled and further, their ability to capture complex features of a slope failure, post failure and deposition stages.

2.2 Landslide induced waves: An Ocean and Coastal engineering perspective

In this section it is attempted to provide an idea through literature, how submarine landslides are treated in Oceanic and Coastal engineering for modelling induced waves. Also the generated wave features are discussed, especially during the initial stages of submarine failure.

2.2.1 Submarine landslide and induced wave feature

In regard to wave generation, 3 types of landslides are categorized depending upon the initial slide position, such as: subaerial, partially submerged and subaqueous (Fritz, 2002), see figure 2.24. However, the current section will only focuses on submarine type of slides.

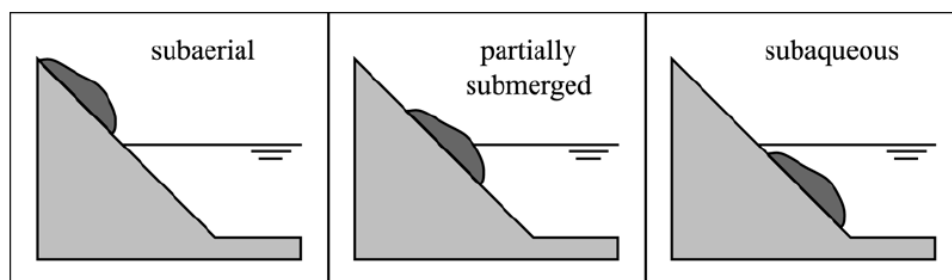


Figure 2.24: Landslide classification for impulse wave generation. (Fritz, 2002)

In the recent past, studies such as: Ugamak slide in 1946 (Fryer and Watts, 2001), Grand Banks slide in 1929 (Fine et. al., 2005), Papua New Guinea (1998) (Tappin, et al., 1999, Synolakis et. al., 2002) suggest that tsunamis may originate due to the dual impact of earthquakes and shallow water submarine landslides, rather than earthquakes being the only source. In fact in some cases the submarine landslides are more prominent factor or may be the only factor for ex. Stromboli slide

(Italy) in 2002 (Chiocci et. al, 2008). Literature suggests that submarine landslides account for roughly 10 % of tsunamis observed in oceans (Kajiura, 1990).

The waves produced by such events are known as impulse waves. Impulse waves are classified as gravity water waves generated by an impulsive disturbance of the water body (Fritz, 2002). It should be noted that, although earthquake and submarine landslides both results in tsunamis, the impulsive waves generated by submarine landslides typically possess different features than the waves produced by earthquakes. Tsunamis generated by submarine landslides often have very large run-up heights close to the source area, but have more limited far-field effects than earthquake tsunamis (Harbitz et. al., 2006). A large earthquake can produce far field wave energy directivity as if radial spreading from a very long line source, but only an submarine landslide can produce both near-field and far-field wave energy directivity along its axis of failure (Watts, 2001).

Further within the class of submarine landslides, studies have shown that usually flow slides is the most common type of slides have mass destructive capabilities (Hunter and Fell, 2001), example: 1994 Skagway - Alaska tsunami, 1929 Grand Banks tsunami etc. This is unexpected, as it is known from previous sections, that flow slides have been divided into more complex mechanisms such as retrogression and complete rapid collapse. It is not until very recently that, researchers modelling waves due to landslides have started giving weightage to the dynamics of flow slides and their subsequent effect on tsunami wave production. Study by (Harbitz et. al., 2006) suggests that, retrogressive landslide behavior normally reduces associated tsunami heights, but retrogression might increase the height of the landward propagating waves due to time lags between releases of individual elements of the total released mass. Further it suggested that a retrogressive submarine landslide with short time lags may lead to both shorter wave components originating from individual blocks and a longer total wavelength from superposition compared to rigid or complete rapid collapse slides.

Another study, done by Løvholt et. al., (2017), evaluated the effects of the dynamics and mechanism involved in submarine slides with respect to wave formation. For this the researchers opted two of the largest submarine landslides in Norwegian region; Storegga slide and Trænadjupet slide. The former one has been reported to cause tsunami and the latter one does not. They considered two different types of advanced submarine slide models: a) visco-plastic debris flow model, including remolding effects, thus mimicking the complex phenomena such as multistage failure and rapid retrogressive collapse, b) Retrogressive block model based on energy balance approach. Each of the submarine slides was simulated using both such models. Further the planes of sliding were approximated from real scar depth data and the motions of the slides were controlled through managing their velocities co-relation with base friction terms.

Figure 2.25 (a) illustrates the difference between both types of submarine slide models and figure 2.25 (b) and (c) shows progression of Trænadjupet slide in case debris flow and retrogressive block failure model, respectively.

The results from the study were compared with the known information of waves produced and lateral spreads of the flow deposit. It was observed that the debris flow model for Storegga slide case produce similar results with literature and Trænadjupet slide significantly over predicts the wave height. However, on the other hand retrogressive failure gives reasonable outcomes for Trænadjupet slide.

With the results observed it was finally, concluded that the retrogressive failure in itself is insufficient of producing tsunami ways and most probably cause of tsunami due to flow slide is indeed rapid collapse type failure (Løvholt et. al., 2017).

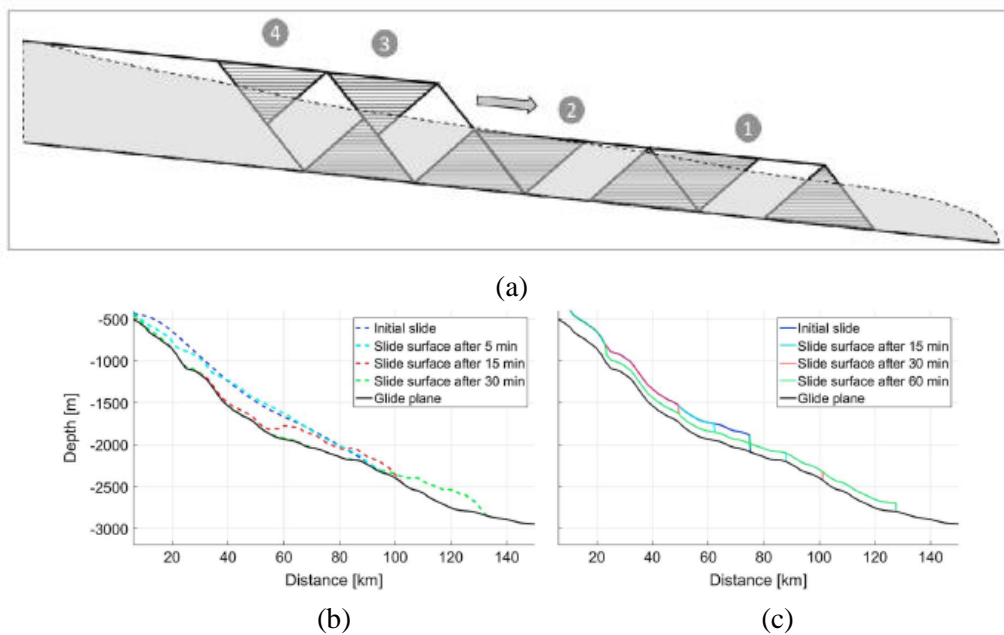


Figure 2.25: (a) Failure pattern using a retrogressive block model and a remolding debris flow model superimposed in gray. The retrogressive slide blocks fail one by one, blocks 1 and 2 are moving parallel to the slope, blocks 3 and 4 are at rest. The slide material is mobilized more rapidly in the debris flow model, and several “blocks” may fail at the same time, (b) Trænadjupet Slide progression in the debris flow model, (c) Trænadjupet Slide progression using the retrogressive block model. (Løvholm et. al., 2017).

2.2.2 Wave studies experimental and computational works

Several physical and computational works have been carried out by researcher for modelling the landslide generated impulsive waves. In these studies, since the focus is on the wave generation and overall water movement, landslides were usually treated with simple models such as: triangular wedge block, semi elliptical rigid block, deformable/viscous block (or granular slides experimentally) etc. and these blocks were usually allowed to slide through an inclined surface (Henrich -1992, Rzadkiewicz et. al., 1997, Grilli and Watts – 2005, Abadie et. al., -2010, Løvholm et. al.- 2018). Owing to the similarity in approaches, only few of the important works have been reviewed hereafter.

Experimental and computation work by *Heinrich (1992)* in this area is one of the early and most detailed work. He experimentally performed submarine and subaerial landslides in the laboratory in order to validate a modification to hydrodynamic program Nasa-Vof2D for simulating generation, propagation, and run-up on the shore of water waves created by landslides. Nasa-Vof2D, is a nonlinear Eulerian code, which solves the complete incompressible Navier-Stokes equations by a finite difference method. The modification includes making the fluid domain boundaries (i.e., the bathymetry) time-dependent. The problem geometry consists of a triangular wedge shaped box of $0.5 \times 0.5 \text{ m}^2$ cross-section, sliding over a 45° inclined surface (see figure 2.26). The water height was considered to be 1m from the bottom of surface of the setup. For numerical modelling a similar geometry was considered and for controlling the motion of slide the velocity measured experimentally was used as an input.

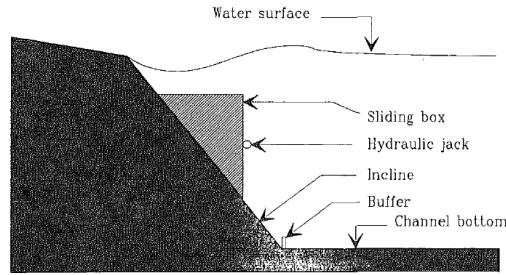


Figure 2.26: Experimental setup (Heinrich, 1992)

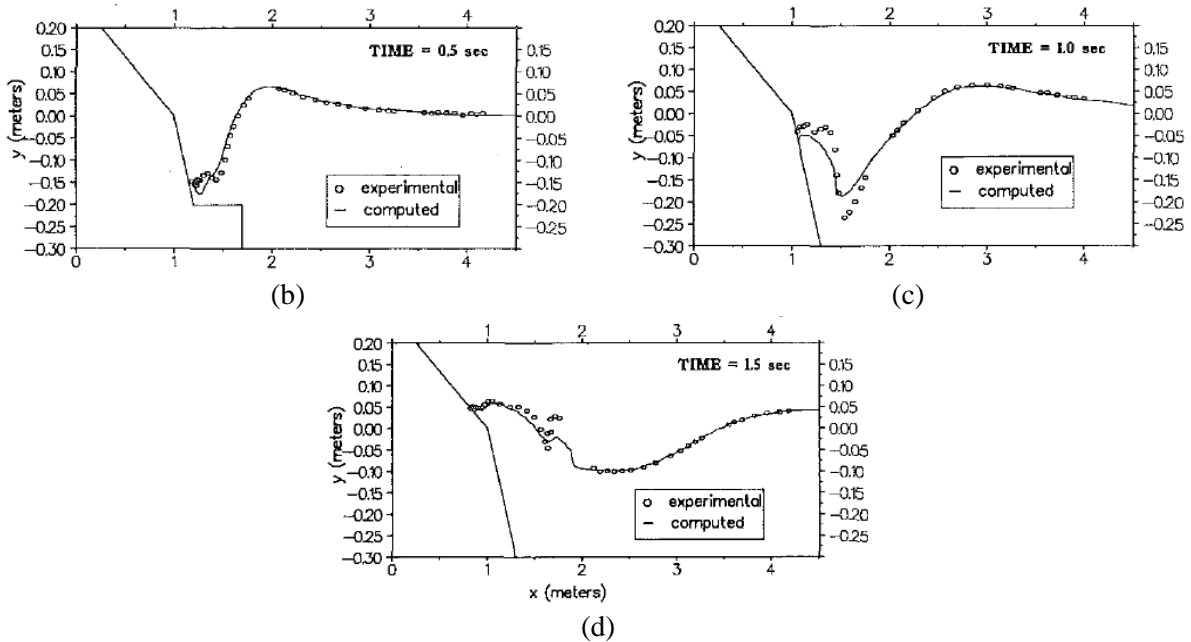


Figure 2.27: Surface wave propagation in time; a) $t=0.5$ s, b) $t=1$ s, c) $t=1.5$ s (Heinrich, 1992)

Figure 2.27 can be referred for the experimental and computed results at the wave generation phase. It was observed; that the result obtained by the numerical model was quite similar to the experimental work. Few discrepancies until $t=1$ sec, were reported owing to the numerical model insufficiency in modelling realistic turbulent behavior. However later at $t=1.5$, numerically the produced wave seemed to propagate faster than in the experiment. This has been reasoned because of the energy dissipation in reality due to turbulence in flow.

Apart from this a general comment on the features of the wave can be made. It can be observed that at $t=0.5$ sec, a primary wave has been developed. It has a long elongated crest at far field and deep trough at just above the landslide box source. After that, at $t=1$ sec, a secondary wave can also be seen near the landslide source position. It should also be noted, that this type of simplistic slide may approximate a rock fall or avalanche, but it would not represent a realistic flow slide pattern (refer section 2.1.2). Nonetheless, it still gives some insight on typical surface wave features due to simple block type submarine failures.

Next, similar to Heinrich (1992), *Cremonesi et al.*, (2011) conducted a rigid block slide experiment. However, instead of using the Eulerian formulation, researchers rather opted for full Lagrangian frame work owing to its capability to model the evolving free surface, in the particle finite element method (PFEM), with re-meshing codes. The landslide and the water basin were modeled as a continuum, incompressible, non-homogeneous fluid, where the material property of the rigid landslide

was controlled through its viscosity. Furthermore the slide motion was controlled by prescribed slide velocity throughout the time. Experimental setup can be referred from figure 2.28.

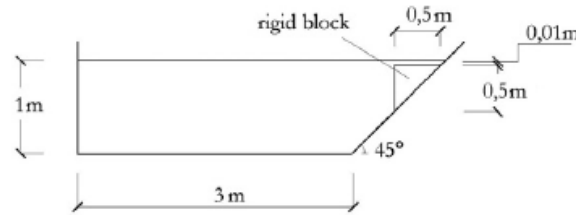


Figure 2.28: Experimental setup (Cremonesi et. al., 2011)

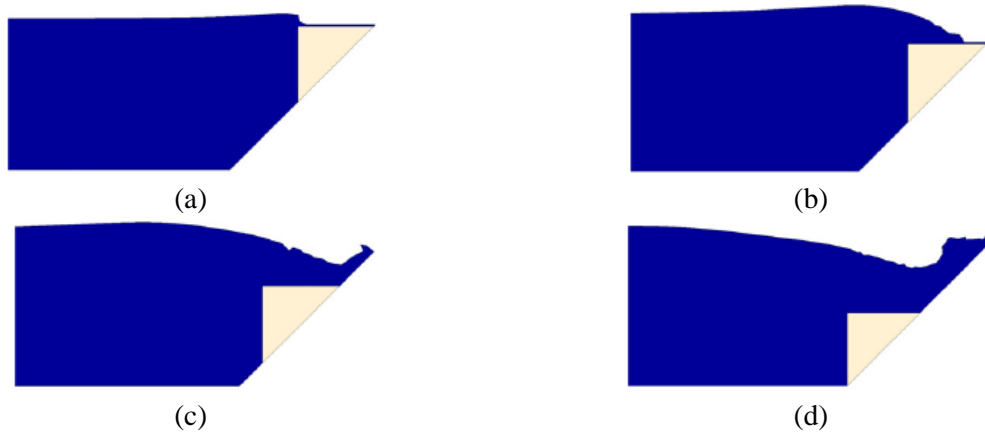


Figure 2.29: Rigid slides at different time steps; a) $t = 0.25s$, b) $t = 0.5s$, c) $t = 0.75s$ and d) $t = 1s$ (Cremonesi et. al., 2011)

The surface water elevation profile from figure 2.29 and 2.30 can be observed at different times. The results produced computationally show well in agreement with the experimental results.

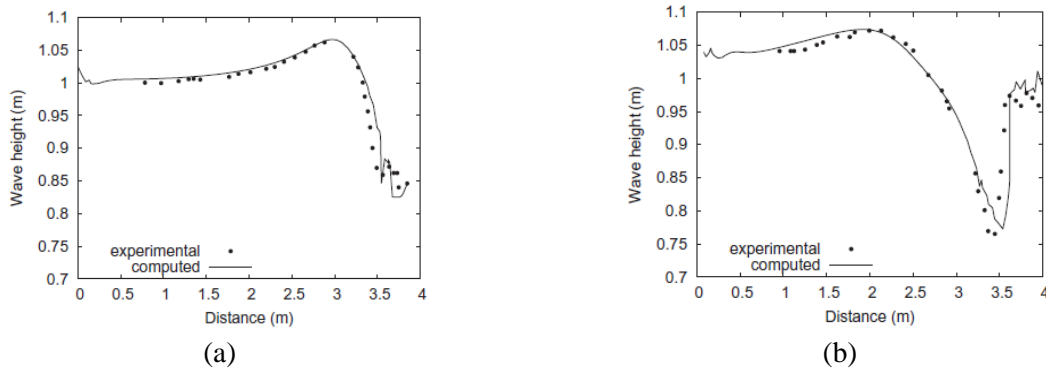


Figure 2.30: Surface wave profiles at different times for both experimental and computed work; a) $t = 0.5 s$, b) $t = 1 s$

Further, looking at figure 2.30, it can be observed that the surface waves developed here are quite comparable to Heinrich's (1992) produced results in figure 2.27. At the initiation of the slide at $t=0.5s$ (figure 2.30(a)) a premature primary wave can be observed with elongated fully developed crest at far field and deep partially developed trough, near the source. At the slide progress at $t=1s$ the primary wave seems to be fully matured with distinct crest and trough visible, also experimentally a secondary wave is hinted in the figure 2.30(b).

Other than rigid block slides, researchers have experimented and computed granular slides as well so to simulate submarine flow type translational slides. One such work has been conducted by *Rzadkiewicz et al. (1997)*. Researchers here conducted laboratory experiments by sliding lumps of

granular sands underwater. Moreover, in order to compute such a slide, in a Nasa-Vof2D model the rheology from fully solid to Newtonian fluid was included by a 2D diffusion model describing the mechanical behavior of sediments by a Bingham law. The numerical parameters, such as the plastic viscosity, the friction, diffusion coefficients etc., were calibrated based on the results of the laboratory experiments. Figure 2.31 illustrates the experimental and numerical results for same time period of slide progression. The computed wave results were reported to be comparable with those produced in experiments.

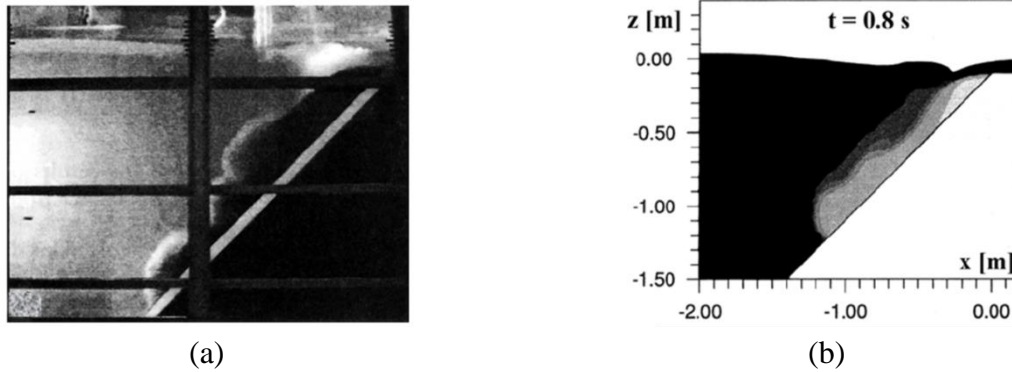


Figure 2.31: Submarine granular flow slide; a) experimental setup at $t = 0.8$ sec b) computed flow slide at $t = 0.8$ sec (Rzadkiewicz et. al., 1997)

It is to be noted that these types of slides are quite commonly used in other computational research works as well (ex. Grilli and Watts- 2005, Abadie et. al.- 2010), where a landslide is modeled as a visco-plastic deformable substance in order to simulate translational flow slides induced waves. However, such approximations of translational slides may differ from realistic slides at generation phase. Especially when considering a case, where the soil mass flows along the slope beyond the rupture zone i.e. when the rupture surface tail ends before the slope toe. Since, as discussed in section 2.1.2 and 2.1.3 (or see figure 2.7 and 2.21), in this scenario, a typical translational flow type slide during the initial failure stages will show slightly up and outward along the slope movement, near the tail regions of the rupture zone. Whereas, down and inward along the slope movement, at the top region of the rupture zone.

This feature is clearly missing in the figure 2.31, mainly due to the straight sloping slide bottom considered. In this case any kind of curving or upward dispersed movement (cloud formation) is purely due to interaction between sliding mass and water (ex. diffusion). Thus, considering its limitation in simulating a realistic generation phase of the slide, it can be commented that this type of slide may represent sub-aerial granular slide or even submarine slide mass flow after it exists the rupture zone

Other computational work can also be referred to for deforming granular slides, such as: *Abadie et. al.,(2010)*. A new advanced model (Thetis), based on Direct Numerical Simulation (DNS) of Navier Stokes equations, was developed in this work. Water, air, and slide are treated as fluids, whose interfaces are tracked using the volume of fluid (VOF) method. Both rigid block slide and deforming slide were computed. However, here only the deforming slide case is discussed. In case of a deforming slide, the initial geometry can be referred to from figure 2.32. The slide material is computed with a lower viscosity value so to attain deformation in slide while it's being in motion. Moreover, in this case the slide moves over the porous medium on the bottom, and progressively slows down due to the zero velocity condition, which is implicitly imposed on the slide.

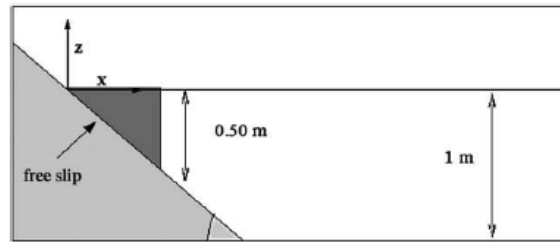


Figure 2.32: Assumed slide geometry after Heinrich (1992) by Abadie et. al.,(2010)

Figure 2.33, illustrates the progression in surface wave elevations and stream flowlines for water movements, induced due to deforming slide motion at initial stages. This figure shows that as soon as the slide is set into motion it loses its initial shape and becomes thinner with bulbous front, see figure 2.33(a). It was further reported, that the free surface elevation is qualitatively similar to that of the rigid case. Thus, a typical primary wave during the initial stage (figure 2.33(a)) and secondary wave during the mid-progression stage (2.33(b)) can be observed. However, it was reported that the second wave is less steep than for the rigid case, due to the thinning of the slide geometry.

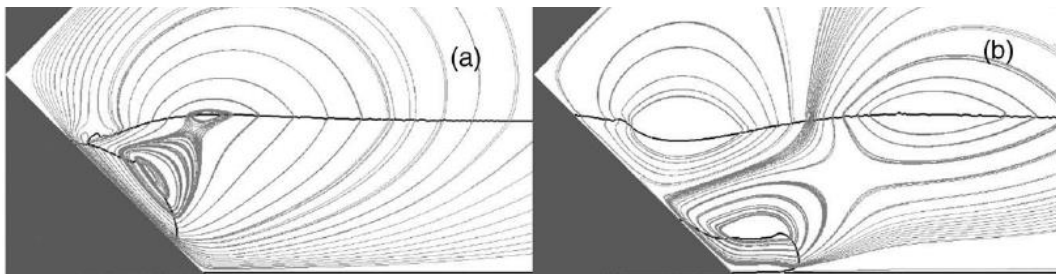


Figure 2.33: Surface waves with stream flowlines (note flowlines are smoothed in air space above water level); a) at $t = 0.5$ s, b) 1s (Abadie et. al., 2010)

Considering that this slide typically demonstrates a translational flow slide progression, it can be compared with the flow slide from figure 2.22, which involves a full scale soil model coupling with the overlying fluid mass. It can be observed that in the current case no full circular formation of submerging water adjacent to the sliding soil mass can be seen, in contrast to what was visible in the figure 2.22. This further shows that the lack of simulating realistic flow slide features during the slide generation stage by these idealized deforming translational slide models, may affect the overlying water mass movements.

Similar to the above study, Abadie et al., (2008) can also be referred to for comparing overlying water mass vector movements due to deforming slides with varying viscosity (μ), see figure 2.34). In here landslide generated waves are studied using a numerical model based on Navier-Stokes equations, with a VOF algorithm to track the interfaces. In this case the generation of waves due to partially submerged landslides was studied. A slope inclination for slides was opted to be 26.6 deg. Similar to other literatures such as (Grilli and Watts- 2005) an idealized semi-elliptical slide geometry was assumed, with length $L = 1$ m and thickness $T = 0.2$ m. The slide is initially at rest and partly submerged, with its center of mass located at $d/L = -0.048$ below the still water level.

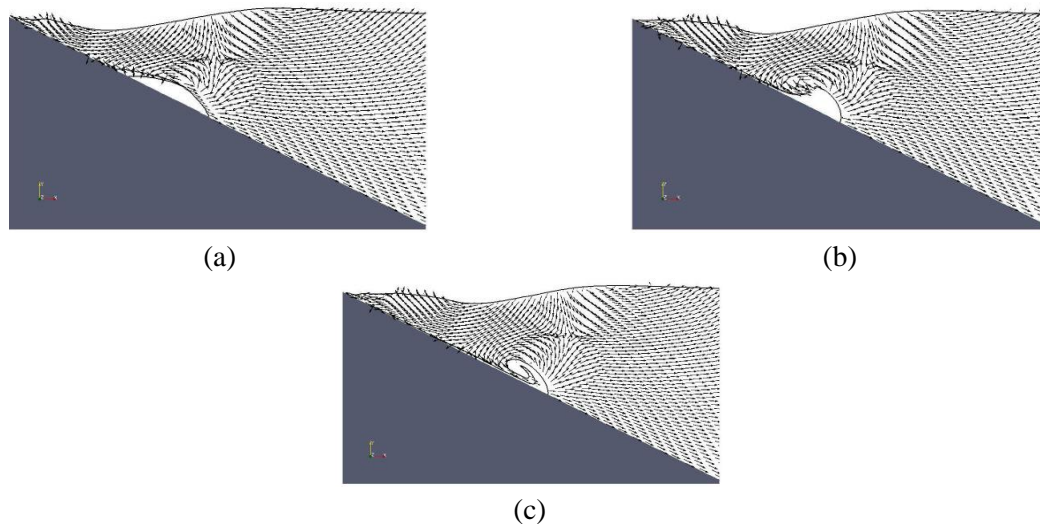


Figure 2.34: Various interfaces and velocity vectors for 3 slide viscosity cases; a) $t = 1.7s$, $\mu = 5000Pa.s$, b) $t = 1.9s$, $\mu = 100Pa.s$, c) $t = 1.9s$, $\mu = 1Pa.s$ (Abadie et al., 2008)

Although figure 2.34, shows different shapes of the deformed soil mass due to assumed different slide viscosity, their shape still does not represent, the typical translational flow slide feature, as discussed earlier. Thus the overlaying water mass movements, neighboring the soil mass body, though different in all scenarios, still do not show full circular formation along the deformed slope of soil mass as if in case of figure 2.22.

Other than these conventional studies, advanced *site specific research* works have also been conducted, such as: Watts et. al. (2003), Løvholt et. al. (2017) and Løvholt et. al.(2018). It is to be noted that, considering the smaller relevancy of such studies for the current work, this writer does not intend to go into detail about each of these works, rather just providing a general overview.

The objective of those studies is usually to post-fit their simulation with acquired site specific data about the landslide and resulting wave formations. They usually apply advance models such as Geowave (Watts et. al., 2003), incorporate 3D ocean morphology, and may simulate effects due to dual phenomena such as earthquake and submarine slides combined. However, even than the studies such as Watts et. al. (2003), Løvholt et. al. (2018) tend to over simplify landslides as either just translational or rotational. Thereby, using idealized 3D slide geometries such as semi ellipsoids sliding over approximated straight inclined plane or rotational plane. Dimensions of these semi ellipsoid, slides are approximated based on realistic landslide data. Considering these over simplifications, it can be still argued that even these works may not be able to simulate realistic wave feature at initial stages, which thereby effect the overlaying water mass movements.

2.3 Concluding remarks on literature studies

Following conclusions can be made after comparison between geotechnical and ocean engineering perspective on submarine landslides and induced wave motions:

- Type of soil, pre-loading history, ageing, geometry of slope, bedding layer surface geometry and the process of soil deposition will all influence the shape and type of slope failure.
- With a change in shape of a submarine slide also the overlaying water mass movement changes.
- Submarine flow slide models currently used for studying induced wave propagation are over generalized and may not represent realistic failure, especially during the initial stages. On the other hand geotechnics based slope models can provide more variation within the generalized type of slides and thus can produce more realistic failures and thereby water mass movements.
- Soil is often modeled as a visco-plastic fluid by using the Bingham law or by the Herschel Bulkley model in case of submarine flow slide induced waves. However, considering the mechanics involved with complete liquefaction, the soil under loading changes its state from elasto-plastic to plastic. This change of state can still govern the initial movement of the slide. Geotechnics based soil models are capable to simulate such behavior and therefore can provide better definitions.
- Submarine failure controlling parameters in geotechnics such as: pre-stress history and loading or triggering mechanisms are more reliable and realistic comparative to velocity control.
- Physical modelling in geotechnics is capable of generating wide varieties of submarine slides and simulating more field conditions. Thus these can provide more valuable insights on overlaying water mass movements than the conventionally used laboratory experiments.
- Apart from generalized slope failures, Geotechnics based 2D computational models are capable enough to simulate complex multi-staged failures based on soil properties, their initial stress-states and triggering mechanisms.
- Coupled modelling of overlaying fluid mass with soil-slope profiles, will be numerically more expensive and demanding compared to current simpler models. In this case numerical methods such as ALE or MPM are expected to provide better simulations than by means of the other discussed approaches.

3

Theoretical Approach & Numerical Modelling

3.1 Existing model Finite Element programming framework

The existing model finite element framework here refers to the previous program: ‘Dyn_mlk4.f95’, developed by Molenkamp (1999). It is to be noted that for the current extension work to the previous model, the general mathematical framework has been kept unchanged, which therefore can be understood in this section. Moreover, considering this the fluid model, as an extension to the previous work, has also been formulated in a similar compatible frame of work (section 3.3).

3.1.1 Introduction to residual, stresses and loads used in the program

The existing frame work was based on updated Lagrangian approach. The variables used in the calculations were displacement, velocity and acceleration. Referring to the report by Molenkamp (1998), the numerical frame work represented by eq. (3.3), has been derived from the discretization of the equation of conservation of linear momentum (LM) of saturated bulk of soil mass (Refer appendix C for the full derivation). This discretization can be expressed in terms of the nodal residual vector f_k^{p-r} in index notation as shown in eq. (3.1).

$$LM \text{ soil bulk} \rightarrow \sigma_{ji,j}^* + p_{,j} + \rho b_i - (1-n)\rho_s \ddot{u}_i - n\rho_f (\ddot{u}_i + \dot{v}_i|_{\dot{u}}) = 0$$

Discretization,

$$\begin{aligned} \Rightarrow f_k^{p-r} = & \int_{s_{0r}} N^p \bar{\tau}_k^{(n)} \left| \hat{G} \right| ds + \int_{V_0} N^p \rho b_k \left| \hat{F} \right| dv - \int_{V_0} B_{kij}^p R_{jk}^{rT} \left(\sigma_{kl}^o + \Delta \tilde{\sigma}_{kl}^c \right) R_{li}^r \left| \hat{F} \right| dv \\ & - \int_{s_{0v}} N^p C_{jk} N^q \left| \hat{G} \right| ds \dot{u}_k - \int_{V_0} N^p \rho N^q \left| \hat{F} \right| dv \ddot{u}_k \approx 0 \end{aligned} \quad (3.1)$$

where,

ρ_s - average density of the minerals composing the grains

ρ_f - average density of the fluid filling the pores, namely for air-saturated dry soil it is pore air and for saturated soil it is water.

n - porosity of solid skeleton.

$\rho = (1-n)\rho_s + n\rho_f$ - saturated bulk density of soil

\ddot{u}_i - average acceleration vector of the soil skeleton

$v_i|_{ii}$ - relative average velocity vector of the pore fluid with respect to the soil skeleton

$\sigma_{ij,j}^*$ - average intergranular stress tensor (continuum mechanics: tension positive).

p - average pore fluid stress (continuum mechanics: tension positive).

$\sigma_{ji,j} = \sigma_{ji,j}^* + p_{,j}$ - total internal stress of soil bulk

b_i - body force vector per unit of mass ($b = -g\delta_{iv}$) due to gravity

N^p - is the nodal shape function of node number p

$|\hat{G}|$ - is ratio of the local boundary surface area at the end and the begin of the considered deformation increment. This quantity helps to change the surface integration and define it in terms of current state (S_0) than rather the new state (S). When expressed in tensor format it can be written as:

$$|\hat{G}| = \frac{\det(\hat{F})}{\sqrt{n \cdot \hat{F} \cdot \hat{F}^T \cdot n}} = \frac{\sqrt{N \cdot \hat{F}^{-1} \cdot (\hat{F}^{-1})^T \cdot N}}{\det(\hat{F}^{-1})} \quad (3.2)$$

Here, the incremental deformation gradient tensor \hat{F} expresses the incremental deformation at the end with respect to the begin of the time increment Δt and unit normal vectors n and N are defined at the end and the begin respectively. Similar to $|\hat{G}|$, the determinant $|\hat{F}|$ of the incremental deformation gradient \hat{F} defines the volumetric integration in terms of current state volume (V_0) rather than new state volume (V).

$\bar{\tau}_k^{(n)}$ - is the applied traction load on co-moving boundary surface S_{0t}

B_{kij}^p - strain-nodal displacement components

\hat{R}_{jk} - incremental material rotation rate

σ_{kl}^0 - total stress at the current state

$\Delta \tilde{\sigma}_{kl}$ - components of co-rotational stress increment

C_{ji} - is the applied viscous damping matrix at the boundary S_{0v}

\hat{u}_k - is the nodal displacement vector in Cartesian direction k

The existing numerical frame work in comparable format to eq. (3.1), symbolically can be written as:

$$f_k^{p-r} = F_k^{p-t} + F_k^{p-f} + F_k^{p-g} - L_k^p - C_{jk}^{p-b} \dot{u}_k - M_{jk}^p \ddot{u}_k \approx 0 \quad (3.3)$$

In (3.4) the first nodal load vector is comparable to first term of (3.1), thus with the traction \bar{T}_k^t inducing incremental deformations, and the nodal shape function N^p of node number p and boundary surface of S_{0t}^* it can be expressed as:

$$F_k^{p-t} = \int_{S_{0t}^*} N^p \bar{T}_k^t \left| \hat{G} \right| ds \quad (3.4)$$

In the numerical implementation in program 'Dyn_mlk4.f95', the nodal load vectors F_k^{p-t} due to prescribed traction \bar{T}_k^t is indicated by the name: LOAD. Thus it can be expressed as:

$$\text{LOAD} \Leftrightarrow F_k^{p-t} \quad (3.5)$$

The second nodal load vector F_k^{p-f} is due to constant, so-called follower type traction \bar{T}_k^f on the follower type of boundaries, on which the traction remains constant during deformation. This again is comparable to the 1st term of (3.1) and expressed namely as:

$$F_k^{p-f} = \int_{S_{0t}^*} N^p \bar{T}_k^f \left| \hat{G} \right| ds \quad (3.6)$$

In the numerical implementation in the program, the nodal load vector F_k^{p-f} due to follower type traction \bar{T}_k^f is indicated by the name: FOLLD and thus expressed as:

$$\text{FOLLD} \Leftrightarrow F_k^{p-f} \quad (3.7)$$

It is to be noted that this FOLLD type of loading in the program is used to apply constant traction loads on the nodes. Further, depending on the phases as discussed in section 3.6, this may represent virtual loads at slope interface either due to assumed constant hydrostatic water level and soil level or just because of the constant water level.

The fourth nodal load vector F_k^{p-g} is due to gravity (g_k) which is comparable to 2nd term of (3.1) and thus expressed as:

$$F_k^{p-g} = \int_{V_o} N^p \rho g_k \left| \hat{F} \right| dv \quad (3.8)$$

In the numerical implementation in the program the nodal load vector F_k^{p-g} is indicated by the name: WGHT and thus expressed as:

$$\text{WGHT} \Leftrightarrow F_k^{p-g} \quad (3.9)$$

The internal nodal force vector L_k^p due to due to total internal stress σ_{kl} , is comparable to 3rd term of (3.1) and thus expressed by:

$$L_k^p = \int_{V_o} B_{kij}^p R_{jk}^{rT} \left(\sigma_{kl}^o + \Delta \tilde{\sigma}_{kl}^c \right) R_{jk}^r \left| \hat{F} \right| dv \quad (3.10)$$

In the numerical implementation in the program the nodal load vector L_k^p due to total internal stress σ_{kl} is indicated by the name: INTLD and thus expressed as:

$$\text{INTLD} \Leftrightarrow L_k^p \quad (3.11)$$

The nodal force vector $C_{ij}^{pq-b} \dot{u}_k^q$ due to the transmitting boundary is comparable to 4th term of (3.1) and thus reads as:

$$C_{ij}^{pq-b} \dot{u}_k^q = - \int_{s_{0v}} N^p C_{jk} N^q \left| \hat{G} \right| ds \hat{u}_k^q \quad (3.12)$$

In the numerical implementation in the program the nodal load vector $C_{ij}^{pq-b} \dot{u}_k^q$ due to the viscous boundary force is indicated by the name: VBFRC and thus expressed as:

$$\text{VBFRC} \Leftrightarrow C_{ij}^{pq-b} \dot{u}_k^q \quad (3.13)$$

in which \dot{u}_k^q represents the nodal velocity of node q in Cartesian direction k.

Finally, the nodal inertial force vector $M_{jk}^{pq} \ddot{u}_k^q$ in (3.3) is comparable to 5th term of (3.1) and expressed by

$$M_{jk}^{pq} \ddot{u}_k^q = \int_{V_o} N^p \rho N^q \left| \hat{F} \right| dv \ddot{u}_k^q \quad (3.14)$$

in which \ddot{u}_j^m is the nodal acceleration of node m in direction j.

In the numerical implementation in the program the nodal load vector $M_{jk}^{pq} \ddot{u}_k^q$ due to the inertial forces is indicated by the name: INERT and thus expressed as:

$$\text{INERT} \Leftrightarrow M_{jk}^{pq} \ddot{u}_k^q \quad (3.15)$$

3.1.2 Discretization in the time domain by Crank-Nicolson method and Newton Raphson Iteration Scheme

In this program the incremental solution is obtained by the application of the Crank-Nicolson method and for the iteration steps the Newton Raphson scheme has been incorporated. In the Crank-Nicolson method the solution vector \dot{u}_1^{n+1} in terms of nodal velocity at the end of the time increment Δt and at the end of the n -th Newton-Raphson iteration step is related to the solution vector u_1^{n+1} of the nodal displacement at the end of the time increment Δt and at the end of the n -th Newton-Raphson iteration step and the vectors at the begin of the time increment $u|_0$ of nodal displacement and $\dot{u}|_0$ of nodal velocity, namely:

$$\dot{u}_1^{n+1} = \frac{1}{\theta \Delta t} \left(u_1^{n+1} - u|_0 \right) - \frac{(1-\theta)}{\theta} \dot{u}|_0 \quad (3.16)$$

Secondly, in the Crank-Nicolson method the second time rates $\ddot{u}|_0$ and \ddot{u}_1^{n+1} at the begin and end of the time increment respectively are never calculated. Nevertheless, the following expression of the second time rate at the intermediate time $\ddot{u}|_\theta^{n+1}$ can be expressed by

$$\ddot{u}|_\theta^{n+1} = \frac{1}{\theta \Delta t^2} \left(u_1^{n+1} - u|_0 \right) - \frac{1}{\theta \Delta t} \dot{u}|_0 \quad (3.17)$$

The residual vector $f^r|_\theta^n$ at the intermediate time and at the end of the n -th Newton Raphson iteration step is interpolated between both the residual vectors $f^r|_0$ at the begin of the time increment and $f^r|_1^n$ at the end of the time increment. This dependence is expressed by:

$$f^r|_{\theta}^n = \theta f^r|_1^n + (1-\theta) f^r|_0^n \quad (3.18)$$

In the n -th Newton-Raphson iteration step for the Crank-Nicolson calculation of the solution for a time step, in principle the expression of the zero value of the first order Taylor series approximation of $f^r|_{\theta}^{n+1}$ is applied, namely:

$$f^r|_{\theta}^{n+1} \approx f^r|_{\theta}^n + \frac{df^r}{du}|_{\theta}^n (u|_{\theta}^{n+1} - u|_{\theta}^n) = f^r|_{\theta}^n + k|_{\theta}^n (u|_{\theta}^{n+1} - u|_{\theta}^n) = 0 \rightarrow k|_{\theta}^n (u|_{\theta}^n - u|_{\theta}^{n+1}) = f^r|_{\theta}^n \quad (3.19)$$

where, the quantity $k|_{\theta}^n = \partial f^r / \partial u|_{\theta}^n$ is the first order derivative (tangent) and $(u|_{\theta}^n - u|_{\theta}^{n+1})$ is the resulting weighted corrective increment of the global freedom vector containing the free variables.

In the numerical implementation both the residual vectors $f^r|_0$ at the begin of the time increment and $f^r|_1^n$ at the end of the time increment and at the end of the n -th Newton-Raphson iteration step are expressed by respectively:

$$\begin{aligned} f^r|_0 &= \text{LOAD0+FOLLD+WGHT0-INTLD0-INERT-VBRFC0} \\ f^r|_1^n &= \text{LOAD1+FOLLD+WGHT1-INTLD1-INERT-VBRFC1} \end{aligned} \quad (3.20)$$

while, in the first iteration step the following approximations are applied, namely:

$$\text{WGHT1} \approx \text{WGHT0}; \quad \text{INTLD1} \approx \text{INTLD0}; \quad \text{VBRFC1} \approx \text{VBRFC0} \quad (3.21)$$

The Newton-Raphson scheme as described in equation (3.19) leads to:

$$\left(\theta \mathbf{K} + \frac{\mathbf{C}}{\Delta t} + \frac{\mathbf{M}}{\theta \Delta t^2} \right) (\Delta u|_{\theta}^n - \Delta u|_{\theta}^{n+1}) = \theta f^r|_1^n + (1-\theta) f^r|_0^n \quad (3.22)$$

where, \mathbf{K} is global tangent stiffness matrix, \mathbf{C} is the global viscosity matrix and \mathbf{M} is the global mass matrix. As a whole, the expression in the first bracket in the above equation, which includes all the stiffness terms, is referred to as Global stiffness matrix (k).

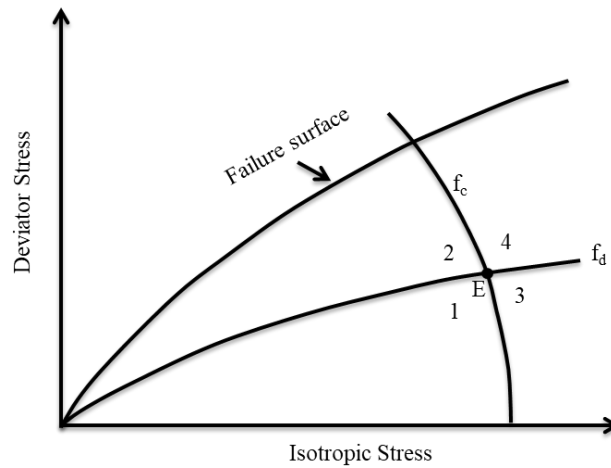
3.2 Soil Model and Characteristics

3.2.1 Introduction to Existing Monot Soil Model

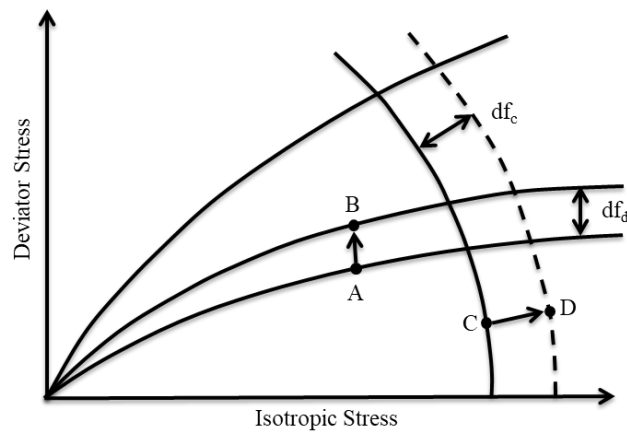
As stated before, the soil in the current study will be modeled as loose sand. For this the soil behavior model used in the modified program remains unchanged to what has been used by Molenkamp (1999) in his original work. The model is known as Monot and it is a double strain hardening Elasto-plastic model developed by Molenkamp (1980) for simulating sands.

Briefly describing this model, the most distinct feature that it had at the time of its development, was its capability to describe both the deviatoric strain and dilatancy for monotonic deviatoric loading and the volumetric compression for isotropic loading. Consequently, this model lacks the critical state theory and is not suitable for cyclic loading. Although, even than this model produces reasonable results for loose sands and monotonic loading, as proven in Molenkamp (1980) and Hicks (1995). Thus, this model can still be used for the current study, since the analysis involves

loose sand with dredge type of ramp loading and limited post-instability monotonic deformation (refer section 3.6 and 3.7).



(a)



(b)

Figure 3.1: Principal effective stress space - (a) 4 fundamental stress state zones; (b) Increment in stress state and yield surface expansion (modified from Molenkamp, 1980).

Further, figure 3.1(a) can be applied for the principal effective stress space illustration of the model. From that figure it can be observed that the principal effective stress space has been divided into 4 zones by two isotropic yield surfaces: a) $F_d(\sigma_{ij}, f_d) = 0$, yield surface of deviatoric model; b) $F_c(\sigma_{ij}, f_c) = 0$, yield surface of compressive model. Moreover, the effective stress state change and the subsequent expansion of yield surfaces can be apprehended through figure 3.1(b). Here if the change in yield surface f_d from A to point B is such that it increases the deviatoric yield surface i.e. $df_d = f_{db} - f_{da} > 0$, then this signifies the plastic increment $d\epsilon^d$ due to increase in deviatoric stress. Similarly, if the change in yield surface f_c from C to D is such that it increases the compressive yield surface i.e. $df_c = f_{cD} - f_{cC} > 0$, then this signifies the increase in plastic strain increment $d\epsilon^c$ due to compressive stresses. Further, along with these plastic strain increments in the model, elastic strain increment $d\epsilon^e$ occurs for any change in effective stress. Therefore with the aforementioned details, changing stress starting at intersection point of the yield surface i.e. point E in figure 3.1 (a), following strain increments occur in the 4 stress state zones:

- $1 \rightarrow d\varepsilon^e$
- $2 \rightarrow d\varepsilon^e + d\varepsilon^d$
- $3 \rightarrow d\varepsilon^e + d\varepsilon^c$
- $4 \rightarrow d\varepsilon^e + d\varepsilon^c + d\varepsilon^d$

3.2.2 Monot model Characteristic Parameter Values

Table 3.1 can be followed from below to refer the model parameter values set in order to simulate loose sands. These calibrated parameters remain unchanged from the original work by Molenkamp (1999) and these have been further referred from the work by Hicks (1995); on optimized parameter calibration of this soil model.

Table 3.1: Monot model parameter values for loose sand

Characteristic Behaviour	Parameters with respective variable array names used in modified program	Values
Density	ρ_s (RHOWET)	2 kN/m ³
	ρ_d (RHODRY)	1 kN/m ³
Ratio of vertical stress vs horizontal stress	K_0 (EPK0)	1
Non-linear elastic model	V	0.12
	AA	0.0011
	AP	0.42
Compressive plastic model	BB	0.0023
	BP	0.26
Deviatoric plastic model failure surface	COH	0
	CC	0.5656
	CP	1
Yeild surface	DP	0.6
Dilatancy	FIMU	30
	FICV	30
	SCV	1
	VGC	0
	VGP	1
	NU	0
Hardening	EE	0.07
	EP	2.6
	LB	0.3
	CN	7
	PARCI	0
	PARDI	0
Shear strain in pi-plane	CG	0.8
Volumetric strain in pi-plane	CV	0.8
Plastic potential in pi-plane	RT	0.3
Bulk modulus of pore water	KWN (Drained)	0 kN/m ²
	KWN (Undrained)	4.E6 kN/m ²
Cavitation coefficient for pore water	CAVCF [#]	1

[#] Activates the possibility of cavitation in pore water if the pore pressure reduces to below atmospheric pressure

3.3 Fluid Model and Formulation for the Existing FEM Framework

3.3.1 Introduction to Fluid Model and Governing equations

One of the main parts of this thesis is to implement a fluid behavior model in the existing program's FEM framework. To model the overlaying water mass, the governing equations, concerning the conservation of mass and momentum, are of *Lagrangian expressions of Navier-Stokes* in case of *nearly-incompressible or partially compressible (elastic compressibility) isotropic linear viscous (irrotational) flows*. However, other forms such as Eulerian expressions of Navier-Stokes are commonly used for modelling fluid material (e.g. Zienkiewicz and Taylor, 1991 and, Smith and Griffiths (2004)). But since the existing frame work for soil mechanics involves Lagrangian formulations, the same is used to model the water mass. Additionally, the Lagrangian form has an advantage over the Eulerian form for the type of problem in hand, in which the evolution of the free water surface has to be simulated, due to slope failure.

Further, for modelling the fluid material two principal assumptions are used, namely: (a) the problem is isothermal, and (b) the variation of fluid density (ρ_f) with isotropic fluid stress (p^f) is very small. Therefore with these assumptions the governing equations: (3.23) to (3.27) are recalled from the lecture notes by Molenkamp, (2017), where (3.23) represents the field equation of the law of conservation of linear momentum of a single phase fluid material in index format and (3.24), represents the law of mass conservation.

$$\sigma_{ij,i}^f + \rho_f b_j - \rho_f \ddot{u}_j = 0 \quad (3.23)$$

$$\dot{\rho}_f + \rho_f \dot{u}_{i,i} = 0 \quad (3.24)$$

where, $\dot{\rho}_f$ is the rate of change of fluid density, σ_{ij}^f is a fluid stress component, u_j is the displacement vector of fluid and, $b_j = -g\delta_{3j}$ is the body load vector components, where g is the acceleration of gravity and the corresponding upward Cartesian direction is represented by unit vector e_3 .

As per the above stated lecture notes, the elastic compressibility at constant temperature can be represented as (isotropic fluid stress (p^f), being positive in tension):

$$\dot{p}^f = -K^w \frac{\dot{\rho}_f}{\rho_f} \Rightarrow p^f = K^w \varepsilon_{vol} \quad (3.25)$$

where, K^w is bulk modulus of elasticity of water and ε_{vol} is its volumetric strain.

Moreover, the stress component (σ_{ij}^f), in case of compressible isotropic linear viscous fluid, which is independent of the rate of volume changes (bulk viscosity modulus = 0), can be represented as:

$$\sigma_{ij}^f = p^f \delta_{ij} + 2G^v \left(\delta_{ik} \delta_{jl} - \frac{1}{3} \delta_{ij} \delta_{kl} \right) \dot{\varepsilon}_{kl} \quad (3.26)$$

where, G^v is a shear dynamic viscosity term and $\dot{\varepsilon}_{kl}$ is a strain rate. Subsequently the stress rate can be written as:

$$\dot{\sigma}_{ij}^f = \dot{p}^f \delta_{ij} + 2G^v \left(\delta_{ik} \delta_{jl} - \frac{1}{3} \delta_{ij} \delta_{kl} \right) \dot{\varepsilon}_{kl} \quad (3.27)$$

Further, eq. (3.26) according to (3.25) can be rewritten as:

$$\sigma_{ij}^f = K^w \varepsilon_{vol} \delta_{ij} + 2G^v \left(\delta_{ik} \delta_{jl} - \frac{1}{3} \delta_{ij} \delta_{kl} \right) \dot{\varepsilon}_{kl} \quad (3.28)$$

From the above eq. (3.28) it can be observed, that the first part i.e. $K^w \varepsilon_{vol} \delta_{ij}$ represents the isotropic linear elastic term of the stress and the second part i.e. $2G^v \left(\delta_{ik} \delta_{jl} - \delta_{ij} \delta_{kl} / 3 \right) \dot{\varepsilon}_{kl}$ represents the deviatoric viscous part of the stress.

The elastic isotropic part of the above equation can be compared to the standard equation for the isotropic linear elastic stress-strain relation. In index format this can be represented as:

$$\sigma_{ij}^f = K^w \varepsilon_{vol} \delta_{ij} + 2G^w \varepsilon'_{ij} = \left(\left(K^w - \frac{2}{3} G^w \right) \delta_{ij} \delta_{kl} + 2G^w \delta_{ik} \delta_{jl} \right) \varepsilon_{kl} = D_{ijkl} \varepsilon_{kl} \quad (3.29)$$

in which for fluids the elastic shear modulus G^w is zero and ε'_{ij} is the deviatoric strain.

Moreover, in the matrix format the above relation is represented by:

$$\begin{Bmatrix} \sigma_{11} \\ \sigma_{22} \\ \sigma_{33} \\ \sigma_{12} \\ \sigma_{23} \\ \sigma_{31} \end{Bmatrix} = \begin{bmatrix} K^w + \frac{4}{3} G^w & K^w - \frac{2}{3} G^w & K^w - \frac{2}{3} G^w & 0 & 0 & 0 \\ K^w - \frac{2}{3} G^w & K^w + \frac{4}{3} G^w & K^w - \frac{2}{3} G^w & 0 & 0 & 0 \\ K^w - \frac{2}{3} G^w & K^w - \frac{2}{3} G^w & K^w + \frac{4}{3} G^w & 0 & 0 & 0 \\ 0 & 0 & 0 & G^w & 0 & 0 \\ 0 & 0 & 0 & 0 & G^w & 0 \\ 0 & 0 & 0 & 0 & 0 & G^w \end{bmatrix} \begin{Bmatrix} \varepsilon_{11} \\ \varepsilon_{22} \\ \varepsilon_{33} \\ 2\varepsilon_{12} \\ 2\varepsilon_{23} \\ 2\varepsilon_{31} \end{Bmatrix} \quad (3.30)$$

where the matrix with K^w and G^w or in index format D_{ijkl} in eq. (3.29) represent the stiffness matrix of isotropic linear elastic stress-strain relation of a solid material.

Further, similar to the elastic part of fluid stress, the second part of eq. (3.28) i.e. the deviatoric viscous stress part of the fluid is also comparable with eq. (3.29) and eq. (3.30) by replacing the terms K^w , G^w and ε_{kl} , by bulk viscosity modulus (K^v), shear viscosity (G^v) and strain rate ($\dot{\varepsilon}_{kl}$), respectively and thereby setting $K^v = 0$.

This aforementioned comparison enables to form both the linear elastic isotropic and viscous deviatoric stiffness matrix of fluid material via using one standard subroutine; 'FRMDGK', in the program 'Modified_Dyn_mlk4.f95'. The function of this subroutine in the program is to call for the formation of the stiffness matrix represented by eq. (3.29) or (3.30). Therefore, using the subroutine and setting $G^w = 0$ and $K^v = 0$, both the formerly mentioned stiffness matrices can be formed, respectively.

Finally, with the above governing equations, the following sub-sections detail the *Spatial Discretization* of law of conservation of linear momentum (eq. 3.23); the steps followed for this are referred to Molenkamp (2009).

3.3.2 Weak formulation and numerical boundary conditions

The finite element discretization of the fluid model can be followed from below. However, it should be noted that no interface hydraulic slip plane was considered in the current work. Additionally, interface nodes are solved, sharing both fluid and soil properties, thus same displacements and normal stress are considered at interface are for both fluid and soil.

Law of Conservation of Linear Momentum:

In addition to the equation (3.23), the following boundary conditions can be applied:

- at the part of the boundary S_t with prescribed traction vector $\bar{t}^{(n)}(t)$:

$$t_j^{(n)} - \bar{t}_j^{(n)} = 0 \quad (3.31)$$

- at the part of the boundary S_u with prescribed displacement vector $\bar{u}(t)$:

$$u_j - \bar{u}_j = 0 \quad (3.32)$$

Note that the total boundary surface S is the sum of boundaries S_t and S_u , namely:

$$S = S_t + S_u \quad (3.33)$$

Next, (3.34) represents the first of 3 steps combined, in order to arrive at the weak formulation, as stated in the notes by Molenkamp, (2017). In here, using Galerkin's approach, the field equations (3.23) and the boundary conditions (3.31) and (3.32) were first multiplied by dimensionless weight functions $N^p(x)$ and $M^p(x)$ respectively and subsequently integrated over volume v and surfaces of the new state for which they are valid. Finally, they were added together while equating the sum to be zero.

$$\int_v N^p (\sigma_{ij,i}^f + \rho_f b_j - \rho_f \ddot{u}_j) dv + \int_{s_t} M^p (t_j^{(n)} - \bar{t}_j^{(n)}) ds + \int_{s_u} M^p \eta (u_j - \bar{u}_j) ds = 0 \quad (3.34)$$

where η has been used just to equalize the dimensions of all terms which have been eliminated in later steps.

Further expanding the above equation and applying the divergence theorem and the spatial partial differentiation to the stress term σ_{ij}^f gives:

$$\begin{aligned} & -\int_v N_{,i}^p \sigma_{ij}^f dv + \left[\int_s N^p \sigma_{ij}^f n_i ds + \int_v N^p (\rho_f b_j - \rho_f \ddot{u}_j) dv + \int_{s_t} M^p (t_j^{(n)} - \bar{t}_j^{(n)}) ds \right. \\ & \left. + \int_{s_u} M^p \eta (u_j - \bar{u}_j) ds \right] = 0 \end{aligned} \quad (3.35)$$

where, vector n_i is the outward unit normal vector on the boundary surface s .

Since, $\sigma_{ij}^f n_i = t_j^{(n)}$ and $M^p(x) = -N^p(x)$, the equation (3.35) can be rewritten as:

$$\begin{aligned} & -\int_v N_{,i}^p \sigma_{ij}^f dv + \left[\int_s N^p t_j^{(n)} ds + \int_v N^p (\rho_f b_j - \rho_f \ddot{u}_j) dv - \int_{s_t} N^p t_j^{(n)} ds + \int_{s_t} N^p \bar{t}_j^{(n)} ds \right. \\ & \left. - \int_{s_u} N^p \eta (u_j - \bar{u}_j) ds \right] = 0 \end{aligned} \quad (3.36)$$

The above can be further elaborated to:

$$-\int_v N_{,i}^p \sigma_{ij}^f dv + \int_v N^p (\rho_f b_j - \rho_f \ddot{u}_j) dv + \int_{s_u} N^p t_j^{(n)} ds + \int_{s_t} N^p \bar{t}_j^{(n)} ds - \int_{s_u} N^p \eta (u_j - \bar{u}_j) ds = 0 \quad (3.37)$$

where, third term in above equation has been obtained through the subtraction of second and fourth term of eq.(3.36) via using the relation between boundary surface as shown in eq. (3.35).

Reversing the sign of (3.37) and rewriting leads to:

$$\int_v N_{,i}^p \sigma_{ij}^f dv - \int_v N^p (\rho_f b_j - \rho_f \ddot{u}_j) dv - \int_{s_u} N^p t_j^{(n)} ds - \int_{s_t} N^p \bar{t}_j^{(n)} ds + \int_{s_u} N^p \eta (u_j - \bar{u}_j) ds = 0 \quad (3.38)$$

Considering the fact that in order to discretize the above equation, thereby using the displacement vector u_j as the nodal variable and taking the dimensionless shape function equal to previously introduce weight function ($N^q(x) = N^p(x)$), the local displacement can be replaced as the sum of the weighted nodal displacement i.e. $u_i = N^p \hat{u}_i^p$. Here, \hat{u}_i^p is the nodal displacement of node p in the direction of the unit base vector e_i .

Moving on, it can be said in such case that the boundary condition of (3.32) on the boundary surface S_u with prescribed displacement \bar{u}_j will be satisfied automatically, by which the integral with the unknown scalar η can be omitted. Consequently, on boundary surface S_u no further solution will be needed and therefore the integral with traction $t_j^{(n)}$ can also be omitted, thereby reducing (3.38) to:

$$\int_v N_{,i}^p \sigma_{ij}^f dv - \int_v N^p (\rho_f b_j - \rho_f \ddot{u}_j) dv - \int_{s_t} N^p \bar{t}_j^{(n)} ds = 0 \quad (3.39)$$

Now, since the terms in (3.41) are integrated on the basis of new state quantities; volume v and boundary surface s are unknown. Therefore it is opted to transform (3.39) into the current state where volume V_0 and boundary surface S_0 are known. Leading to the resulting equation:

$$\int_{v_0} N_{,i}^p \sigma_{ij}^f \left| \hat{F} \right| dv - \int_{v_0} N^p (\rho_f b_j - \rho_f \ddot{u}_j) \left| \hat{F} \right| dv - \int_{s_{0t}} N^p \bar{t}_j^{(n)} \left| \hat{G} \right| ds = 0 \quad (3.40)$$

Where, $s \rightarrow S_0$, $s_t \rightarrow S_{0t}$, $dv \rightarrow \left| \hat{F} \right| dv$ and $ds \rightarrow \left| \hat{G} \right| ds$.

3.3.3 Residual nodal vector

As per the notes by Molenkamp, (2017), in the finite element method, for small strain and material rotation, the strain increments ε_{ij} can be expressed in terms of the small local incremental displacement components u_k and the corresponding nodal displacement component \hat{u}_k^p as follows:

$$\varepsilon_{ij} = \frac{1}{2} \left(\frac{\partial u_i}{\partial x_j} + \frac{\partial u_j}{\partial x_i} \right) = \frac{1}{2} (N_{,j}^p \hat{u}_i^p + N_{,i}^p \hat{u}_j^p) = \frac{1}{2} (N_{,j}^p \delta_{ik} + N_{,i}^p \delta_{jk}) \hat{u}_k^p = B_{ijk}^p \hat{u}_k^p = \hat{u}_k^p B_{kij}^{pT} \quad (3.41)$$

where, B_{ijk}^p contains the strain-nodal displacement components B_{ijk} of node p .

Next considering the first term of equation (3.41), multiplying it by δ_{kj} and reformulating it as:

$$\delta_{kj}(N_{,i}^p \sigma_{ij}^f) = \frac{1}{2}(\delta_{kj}N_{,i}^p \sigma_{ij}^f + \delta_{ki}N_{,j}^p \sigma_{ij}^f) = \frac{1}{2}(\delta_{kj}N_{,i}^p + \delta_{ki}N_{,j}^p) \sigma_{ij}^f = B_{kij}^{pT} \sigma_{ij}^f \quad (3.42)$$

With above consideration multiplying the whole equation (3.40) by δ_{kj} , results in:

$$\begin{aligned} \int_{v_0} \delta_{kj} N_{,i}^p \sigma_{ij}^f |\hat{F}| dv - \int_{v_0} \delta_{kj} N^p (\rho_f b_j - \rho_f \ddot{u}_j) |\hat{F}| dv - \int_{s_{0r}} \delta_{kj} N^p \bar{t}_j^{(n)} |\hat{G}| ds = 0 \\ \Rightarrow \int_{v_0} B_{kij}^{pT} \sigma_{ij}^f |\hat{F}| dv - \int_{v_0} N^p (\rho_f b_k - \rho_f \ddot{u}_k) |\hat{F}| dv - \int_{s_{0r}} N^p \bar{t}_k^{(n)} |\hat{G}| ds = 0 \end{aligned} \quad (3.43)$$

Finally now in order to satisfy the need of an iterative process to approach zero by above equation, it has been equated to non-zero quantity f_k^{p-lmf} , as shown in (3.44), which is a residual nodal force in Cartesian direction k on node p.

$$f_k^{p-lmf} = \int_{v_0} B_{kij}^{pT} \sigma_{ij}^f |\hat{F}| dv - \int_{v_0} N^p (\rho_f b_k - \rho_f \ddot{u}_k) |\hat{F}| dv - \int_{s_{0r}} N^p \bar{t}_k^{(n)} |\hat{G}| ds \quad (3.44)$$

3.3.4 Newton-Raphson procedure and Time Discretization

As per the notes by Molenkamp, (2017), the formulation of a Newton-Raphson iteration step for (3.45) can be derived by substituting in (3.44) for the stress components σ_{ij}^f at the new state the following approximation:

$$\sigma_{ij}^{f(n+1)} \approx \sigma_{ij}^{f(n)} + \dot{\sigma}_{ij}^f \Delta t \approx \sigma_{ij}^{f(n)} + \left(\dot{p}^f \delta_{ij} + 2G^v \left(\delta_{ir} \delta_{js} - \frac{1}{3} \delta_{ij} \delta_{rs} \right) \ddot{\epsilon}_{rs} \right) \Delta t \quad (3.45)$$

The isotropic fluid stress increment \dot{p}^f can be written as (satisfying the conservation of the mass continuity condition):

$$\dot{p}^f = K^w \delta_{rs} \dot{\epsilon}_{rs} \quad (3.46)$$

Therefore substituting (3.46) in (3.45) gives:

$$\sigma_{ij}^{f(n+1)} \approx \sigma_{ij}^{f(n)} + \dot{\sigma}_{ij}^f \Delta t \approx \sigma_{ij}^{f(n)} + K^w \delta_{ij} \delta_{rs} \dot{\epsilon}_{rs} \Delta t + 2G^v \left(\delta_{ir} \delta_{js} - \frac{1}{3} \delta_{ij} \delta_{rs} \right) \ddot{\epsilon}_{rs} \Delta t \quad (3.47)$$

The above can be rewritten as:

$$\sigma_{ij}^{f(n+1)} \approx \sigma_{ij}^{f(n)} + D_{ijrs} \dot{\epsilon}_{rs} \Delta t + T_{ijrs} \ddot{\epsilon}_{rs} \Delta t \quad (3.48)$$

where D_{ijrs} contains the elastic stiffness components and T_{ijrs} contains the dynamic viscosity components.

Next for small increments of time t, strain and strain rate, the following expressions are acceptable:

$$\Delta \epsilon_{rs} = \dot{\epsilon}_{rs} \Delta t, \quad \Delta \dot{\epsilon}_{rs} = \ddot{\epsilon}_{rs} \Delta t \quad (3.49)$$

Further, the increments of strain and strain rate, according to eq. (3.41), can be represented as:

$$\Delta \varepsilon_{rs} = B_{rsm}^q \hat{u}_m^q, \quad \Delta \dot{\varepsilon}_{rs} = B_{rsm}^q \dot{\hat{u}}_m^q \quad (3.50)$$

Therefore, substituting (3.48) in (3.44), while accounting for (3.49) gives:

$$\begin{aligned} f_k^{p-lmf} = & \int_{v_0} B_{kij}^{pT} \sigma_{ij}^{f(0)} |\hat{F}| dv + \int_{v_0} B_{kij}^{pT} D_{ijrs} B_{rsm}^q |\hat{F}| dv \hat{u}_m^q + \int_{v_0} B_{kij}^{pT} T_{ijrs} B_{rsm}^q |\hat{F}| dv \dot{\hat{u}}_m^q \\ & - \int_{v_0} N^p (\rho_f b_k) |\hat{F}| dv + \int_{v_0} N^p \rho_f N^q |\hat{F}| dv \ddot{\hat{u}}_k^q - \int_{s_{0r}} N^p \bar{t}_k^{(n)} |\hat{G}| ds \end{aligned} \quad (3.51)$$

Next, comparing the above expression with eq. (3.3) in section 3.1.1 of existing formulation, the following could be observed about eq. (3.51):

- The first three terms of the equation represents the internal stress in fluid, thus:

$$\text{INTLD} \Leftrightarrow L_i^k = \int_{v_0} B_{kij}^{pT} \sigma_{ij}^{f(0)} |\hat{F}| dv + \int_{v_0} B_{kij}^{pT} D_{ijrs} B_{rsm}^q |\hat{F}| dv \hat{u}_m^q + \int_{v_0} B_{kij}^{pT} T_{ijrs} B_{rsm}^q |\hat{F}| dv \dot{\hat{u}}_m^q \quad (3.52)$$

- The fourth term of the equation represents the weight of fluid, thus:

$$\text{WGHT} \Leftrightarrow F_k^p = \int_{v_0} N^p (\rho_f b_k) |\hat{F}| dv \quad (3.53)$$

- The fifth term of the equation represents the inertial load, thus:

$$\text{INERT} \Leftrightarrow M^{pq} \ddot{\hat{u}}_k^q = \int_{v_0} N^p \rho_f N^q |\hat{F}| dv \ddot{\hat{u}}_k^q \quad (3.54)$$

- Finally, the sixth term of the equation represents the traction loading, thus:

$$\text{LOAD} \Leftrightarrow F_k^{p-n} = \int_{s_{0r}} N^p \bar{t}_k^{(n)} |\hat{G}| ds \quad (3.55)$$

Apart from these aforementioned different force terms for fluid material, other forces as stated in section 3.1.1 are deemed to be zero. Thus with these the residual unbalance force of fluid material can be represented in a similar fashion as shown in eq. (3.20).

Further, as it can be seen in eq. (3.51) the second and third terms are in Cartesian direction m of node q and fifth term, where local acceleration have been replaced by shape function N^q of node q and the nodal acceleration $\ddot{\hat{u}}_k^q$ of node q , is in Cartesian direction k . Therefore, in order to get the equivalent expression for tangential slope quantity 'k' as per the (3.22), equation (3.51) is differentiated with respect to nodal displacement of node r and Cartesian direction w as shown below:

$$\begin{aligned} df_k^{p-lmf} &= \frac{\partial f_k^{p-lmf}}{\partial \hat{u}_w^r} d\hat{u}_w^r \\ &= \int_{v_0} B_{kij}^{pT} D_{ijrs} B_{rsm}^q |\hat{F}| dv \delta_{rq} \delta_{mw} d\hat{u}_w^r + \int_{v_0} B_{kij}^{pT} T_{ijrs} B_{rsm}^q |\hat{F}| dv \frac{d}{dt} (\delta_{rq} \delta_{mw} d\hat{u}_w^r) \\ &\quad + \int_{v_0} N^p \rho_f N^q |\hat{F}| dv \frac{d^2}{dt^2} (\delta_{rq} \delta_{kw} d\hat{u}_w^r) \end{aligned} \quad (3.56)$$

Above equation can be compressed as:

$$\begin{aligned} df_k^{p_lmf} &= K_{km}^{pq} d\hat{u}_m^q + C_{km}^{pq} d\dot{\hat{u}}_m^q + M^{pq} \delta_{km} d\ddot{\hat{u}}_m^q \\ &= \int_{v_0} B_{ijk}^{pT} D_{ijrs} B_{rsm}^q \left| \hat{F} \right| dv d\hat{u}_m^q + \int_{v_0} B_{ijk}^{pT} T_{ijrs} B_{rsm}^q \left| \hat{F} \right| dv d\dot{\hat{u}}_m^q + \int_{v_0} N^p \rho_f N^q \left| \hat{F} \right| dv \delta_{km} d\ddot{\hat{u}}_m^q \end{aligned} \quad (3.57)$$

where, K_{km}^{pq} , C_{km}^{pq} and M^{pq} are the elastic component of stiffness matrix, the viscous component of stiffness matrix and the mass matrix, respectively.

Finally similar to eq.(3.22), the above expression for n-th Newton Raphson iteration step and with Crank Nicolson time stepping (θ method), can be elaborated as:

$$\left(\theta K_{km}^{pq} + \frac{C_{km}^{pq}}{\Delta t} + \frac{M^{pq}}{\theta \Delta t^2} \right) \left(\Delta \hat{u}_m^q \Big|_0^n - \Delta \hat{u}_m^q \Big|_0^{n+1} \right) = \theta f_k^{p_lmf} \Big|_1^n + (1-\theta) f_k^{p_lmf} \Big|_0^n \quad (3.58)$$

where, $f_k^{p_lmf} \Big|_0^n$ and $f_k^{p_lmf} \Big|_1^n$ represent the residual vector forces at the start of the time increment and at the end of the time increment, respectively and $\Delta \hat{u}_m^q \Big|_0^n$ and $\Delta \hat{u}_m^q \Big|_0^{n+1}$ represent the changes in displacement at n^{th} and $n+1^{\text{th}}$ iteration step, respectively.

3.3.5 Fluid characteristics

Below in table 3.2, the details of all fluid material behaviour parameters are given together with their corresponding reference name in program 'Modified_Dyn_mlk4.f95'.

Table 3.2: Fluid material behaviour parameter values

Characteristic Behaviour	Parameters with respective variable array names used in modified program	Values
Density	ρ_w (RHOWET)	1 kN/m ³
	ρ_d (RHODRY)	1 kN/m ³
Elastic bulk modulus	K^w (KMODW)	2.E6 kN/m ²
Elastic shear modulus	G^w (GMODW)	0 kN/m ²
Viscous bulk modulus	K^v (KMODVSC)	0 kN/m ²
Viscous shear modulus	G^v (GMODVSC)	1.002E-6 kN/m ²
Ratio of vertical stress vs horizontal stress	K_0 (EPK0)	1

It is worth mentioning that for the density of the fluid, the referrals used were as such that it requires minimal change in the model. Thus, here ρ_w represents the fluid density (ρ_f) and ρ_d value is set as such that it makes the buoyant density (ρ_{buoy}) equals to zero.

3.4 Energy Terms Implementation

Apart from the hydrodynamic coupling of the problem another important aspect of this work is to evaluate the energy transition in the whole system during dynamic failure. The loss of slope stability via transient quasi-static loading, involves the slope of passing through its limit resistance and ultimately reaching into a complete collapse state. This collapse phenomenon is dynamic in nature and with this dynamic instability it involves a transition of energies such as potential energy to kinetic

energy. With the problem in hand, it involves several different forms of energy and transition between those during failure, thus making it an important aspect of the behaviour to analyze. Further, the change in energies have also been evaluated in the old study by Molenkamp (1999), therefore what make this aspect even more important is to observe the difference between the forms of transition; as the virtual hydrostatic pressures (FOLLID type of loading) at soil surface has been replaced by the overlaying water mass.

Further, it is important to mention the fact that since the whole current numerical model has been worked out with the assumption of an isothermal condition, thus no coupling with respect to heat exchange has been applied. However, in reality the transfer of internal mechanical energy into thermal energy by irreversible deformation also occurs during such dynamic collapses. The study done by Jager (2018) has well expressed the involvement of such forms of energy, where internal energy is indeed shown as a combination of thermal and mechanical energies. Here in the current model the internal energy term only involves the internal stress terms, as shown later in this section. Moreover, the work done by Jager (2018) also looks upon macro level energy transition/transfer due to the interaction between the pore fluid and the soil skeleton; however this is beyond the scope of this study since here the interest is on global energy systems.

3.4.1 Formulation of Various Forms of Energy

The *conservation of internal energy at macro level* continuum in isothermal and undrained condition is expressed as follow (Jager, 2018):

$$\text{For soil bulk} \rightarrow (1-n)\rho_s \dot{e}_s + n\rho_f \dot{e}_f - \sigma_{ij} \dot{u}_{i,j} = 0 \quad (3.59)$$

$$\text{For submerging water} \rightarrow \rho_f \dot{e}_f - \sigma_{ij}^f \dot{u}_{i,j} = 0 \quad (3.60)$$

where,

- n - porosity of solid skeleton
- ρ_s - average density of the minerals composing the grains
- ρ_f - fluid density (water)
- e_s - specific internal energy of the minerals composing the particles forming the solid skeleton
- e_f - specific internal energy of the pore fluid
- σ_{ij} - total internal soil bulk stress (refer details of eq. 3.1)
- σ_{ij}^f - total fluid stress (water) as per eq. (3.26)
- \dot{u}_i - instantaneous velocity

The mechanical power balances: eq.(3.59) and (3.60), of the undrained saturated bulk and submerging water respectively, enables to express the following changes of global mechanical energy over the time interval $t_0 \rightarrow t$, namely:

Change of local material energy:

$$\text{For soil bulk} \rightarrow E_{mat}^s = \int_{t_0}^t \int_{V_s} (1-n)\rho_s \dot{e}_s + n\rho_f \dot{e}_f \, dv \, dt \quad (3.61)$$

$$\text{For submerging water} \rightarrow E_{mat}^f = \int_{t_0}^t \int_{V_w} \sigma_{ij}^f \dot{u}_{i,j} \, dv \, dt \quad (3.62)$$

Change of local stress-strain energy:

$$\text{For soil bulk} \rightarrow E_{mat}^s = \int_{t_0}^t \int_{V_s} \sigma_{ij} \dot{u}_{i,j} dv dt \quad (3.63)$$

$$\text{For submerging water} \rightarrow E_{mat}^f = \int_{t_0}^t \int_{V_w} \rho_f \dot{e}_f dv dt \quad (3.64)$$

involving the integration of the mechanical power terms over volumes V_s (bulk soil) and V_w (submerging water), and time, starting from the begin of dredging at time t_0 and extending to current time t .

Substituting the eq.(3.61) and eq.(3.63) in eq.(3.59) or eq.(3.62) and eq.(3.64) in eq.(3.60), summarizes the generalize form of the instantaneous energy state with respect to that at the start of dredging by:

$$E_{mat} - E_{sig} = 0 \quad (3.65)$$

The above expression demonstrates that for the isothermal and undrained condition, the product of stress and strain rate E_{sig} causes the local changes of the material energy E_{mat} . Moreover, it also demonstrated that the product of stress and strain rate E_{sig} of both soil and pore water causes the local changes of the material energy E_{mat} within both the minerals, composing the soil skeleton, and the pore water.

Next, for the *energy conservation of global system*, equations used in this section are referred and modified from the report by Molenkamp (1998). Referring to the same, the conservation of energy equation for the finite element mesh can be expressed in the rate form of nodal loads, as expressed in conservation of linear momentum eq. (3.3), and nodal velocities \dot{u}_i by:

$$\dot{u}_i F_i^{k-t} + \dot{u}_i F_i^{k-b} + \dot{u}_i F_i^{k-f} + \dot{u}_i F_i^{k-g} - \dot{u}_i L_i^k - \dot{u}_i C_{ij}^{k-b} \dot{u}_j - \dot{u}_i M_{ij}^k \ddot{u}_j = 0 \quad (3.66)$$

Where similar to before different force terms represents,

$F_i^{k-t} + F_i^{k-b}$	- Load: prescribed nodal external load
F_i^{k-f}	- FOLL: nodal follower load
F_i^{k-g}	- WGHT: nodal weight
L_i^k	- INTLD: nodal load due to internal stress
$C_{ij}^{k-b} \dot{u}_j$	- VBFRC: nodal viscous boundary force
$M_{ij}^k \ddot{u}_j$	- INERT: nodal inertial load

Further, with an aim to evaluate the energy transition between the overlaying water mass and the soil, the above expression can further be fabricated for the problem in hand. Thus, the terms in above equation involving nodal loads: F_i^{k-g} , L_i^k and $M_{ij}^k \ddot{u}_j$ can be split according to boundaries and volume of overlaying water mass (V_w) and saturated soil skeleton (V_s) as follow:

- *Nodal weight energy term*, from eq.(3.66) can be elaborated using eq.(3.8) and (3.53) namely:

$$\begin{aligned}\dot{u}_i F_i^{k-g} &= \int_{V_s} \dot{u}_i N^k \rho g_i \left| \hat{F} \right| dV + \int_{V_w} \dot{u}_i N^k \rho_f g_i \left| \hat{F} \right| dv \\ &= (\dot{u}_i F_i^{k-g})^s + (\dot{u}_i F_i^{k-g})^w\end{aligned}\quad (3.67)$$

- Similar to above using eq. (3.10) and (3.52), the *Internal load energy term* can be expressed as:

$$\begin{aligned}\dot{u}_i L_i^k &= \int_{V_s} \dot{u}_i B_{ikm}^k R_{kp}^{rT} \left(\sigma_{pq}^o + \Delta \tilde{\sigma}_{pq}^c \right) R_{qm}^r \left| \hat{F} \right| dV + \int_{V_w} \dot{u}_i B_{kij}^k T \sigma_{ij}^{f(0)} \left| \hat{F} \right| dv \\ &+ \int_{V_w} \dot{u}_i B_{kij}^k T D_{ijrs} B_{rsm}^q \left| \hat{F} \right| dv \hat{u}_m^q + \int_{V_w} \dot{u}_i B_{kij}^k T T_{ijrs} B_{rsm}^q \left| \hat{F} \right| dv \hat{u}_m^q \\ &= (\dot{u}_i L_i^k)^s + (\dot{u}_i L_i^k)^w\end{aligned}\quad (3.68)$$

- Finally, the *Inertial load energy* term via using eq. (3.14) and (3.54) can be expressed as:

$$\begin{aligned}\dot{u}_i M_{ij}^{km} \ddot{u}_j^m &= \int_{V_s} \dot{u}_i N^k \rho N^m \left| \hat{F} \right| dV \ddot{u}_j^m + \int_{V_w} \dot{u}_i N^k \rho_f N^m \left| \hat{F} \right| dv \ddot{u}_j^m \\ &= (\dot{u}_i M_{ij}^{km} \ddot{u}_j^m)^s + (\dot{u}_i M_{ij}^{km} \ddot{u}_j^m)^w\end{aligned}\quad (3.69)$$

It can be noted that in the above elaborations of the energy term, the viscous boundary force energy term has been excluded. This is because in the modified model no transmitting boundary has been defined so this energy term is irrelevant. However, it still exists in the framework of the program, therefore it has been opted to be mentioned in the main expression eq. (3.66).

Next, substituting eq. (3.67) to (3.69) in eq. (3.66) gives:

$$\begin{aligned}\dot{u}_i \bar{F}_i^{k-t} + \dot{u}_i \bar{F}_i^{k-b} + \dot{u}_i \bar{F}_i^{k-f} + (\dot{u}_i F_i^{k-g})^w + (\dot{u}_i F_i^{k-g})^s - (\dot{u}_i L_i^k)^w - (\dot{u}_i L_i^k)^s - \dot{u}_i C_{ij}^{k-b} \dot{u}_j \\ - (\dot{u}_i M_{ij}^{km} \ddot{u}_j^m)^w - (\dot{u}_i M_{ij}^{km} \ddot{u}_j^m)^s = 0\end{aligned}\quad (3.70)$$

Further, integration of the above equation over time interval Δt gives the energy conservation expression as:

$$\begin{aligned}\Delta u_i \bar{F}_i^{k-t} + \Delta u_i \bar{F}_i^{k-b} + \Delta u_i \bar{F}_i^{k-f} + (\Delta u_i \bar{F}_i^{k-g})^w + (\Delta u_i \bar{F}_i^{k-g})^s - (\Delta u_i \bar{L}_i^k)^w - (\Delta u_i \bar{L}_i^k)^s \\ - \Delta u_i C_{ij}^{k-b} \frac{\partial \bar{u}_j}{\partial t} - (\Delta u_i M_{ij}^k \frac{\partial^2 \bar{u}_j}{\partial t^2})^w - (\Delta u_i M_{ij}^k \frac{\partial^2 \bar{u}_j}{\partial t^2})^s = 0\end{aligned}\quad (3.71)$$

where, symbol [$\bar{\quad}$] above the vectors represent their average value during the time interval.

Ultimately with eq. (3.71), different terms in here can be associated to different forms of energy in the system, as follows:

- The first form of incremental energy is due to external loads i.e. first two terms of the equation. This type of energy in the modified program has been referred to as WORK and ideally this is the energy which should be equal to the combination of all the other energy terms, as they are internal energies of the system. Symbolically, it can be represented as:

$$\Delta W^k = \Delta u_i \bar{F}_i^{k-t} + \Delta u_i \bar{F}_i^{k-b}\quad (3.72)$$

- Next, the third term from the equation is an incremental energy due to follower type of traction loading, which in modified program is defined as FWORK. This energy has been associated

with Case A and Case B scenarios, where hydrostatic pressure on the direct contact surface of soil has been applied as follower type of traction loading. Symbolically this can be written as:

$$\Delta W^{k-f} = \Delta u_i \bar{F}_i^{k-f} \quad (3.73)$$

- Moving on, the fourth and fifth terms together in the equation, represents the total incremental potential energy due to nodal weight. This in the modified program has been defined as EPOT. Further in similar fashion, individually the fourth and fifth terms have been referred to as: EPOT_W (potential energy in water) and EPOT_S (potential energy in saturated soil skeleton), respectively. These can be represented as:

$$\begin{aligned} E_{pot} &= -\Delta u_i \bar{F}_i^{k-g} \\ \Delta E_{pot_w} &= -(\Delta u_i \bar{F}_i^{k-g})^w \\ \Delta E_{pot_s} &= -(\Delta u_i \bar{F}_i^{k-g})^s \end{aligned} \quad (3.74)$$

The minus sign in the above expression signifies that the potential energy is the negative value of work done by gravity.

- Similar to before, the sum of sixth and seventh term in the equation represents the total incremental internal energy due to internal stresses. This in the program has been referred to EINT. Moreover individually the incremental energy terms, as before, are referred to as: EINT_W and EINT_S, respectively. Symbolically these can be expressed as:

$$\begin{aligned} E_{int} &= \Delta u_i \bar{L}_i^k \\ \Delta E_{int_w} &= (\Delta u_i \bar{L}_i^k)^w \\ \Delta E_{int_s} &= (\Delta u_i \bar{L}_i^k)^s \end{aligned} \quad (3.75)$$

- The eighth term in the equation represents the incremental radiated energy due to absorption by viscous damping boundaries. However, as mentioned before since no viscous boundaries were considered in the current study this energy will be irrelevant for the model. Yet, this energy in the modified program referred to as ERAD and further symbolically can be represented as:

$$\Delta E_{rad} = \Delta u_i C_{ij}^{k-b} \frac{\partial \bar{u}_j}{\partial t} \quad (3.76)$$

- Finally, the ninth and tenth terms combined represent the total incremental kinetic energy due to inertial loading, referred to as EKIN in the modified program. Further, individually the incremental kinetic energy for water and saturated soil skeleton is referred to as EKIN_W and EKIN_S, respectively. Symbolically all the three quantities can be written as:

$$\begin{aligned} E_{kin} &= \Delta u_i M_{ij}^k \overline{\frac{\partial^2 u_j}{\partial t^2}} \\ \Delta E_{kin_w} &= (\Delta u_i M_{ij}^k \overline{\frac{\partial^2 u_j}{\partial t^2}})^w \\ \Delta E_{kin_s} &= (\Delta u_i M_{ij}^k \overline{\frac{\partial^2 u_j}{\partial t^2}})^s \end{aligned} \quad (3.77)$$

Substituting, the eq. (3.72) to (3.77) in (3.71), give the final expression to be as:

$$\Delta W^k + \Delta W^{k-f} - \Delta E_{pot_w} - \Delta E_{pot_s} - \Delta E_{int_w} - \Delta E_{int_s} - \Delta E_{rad} - \Delta E_{kin_s} - \Delta E_{kin_w} = 0 \quad (3.78)$$

Thus with this expression, the external supplied work to the system is subdivided into changes of follower type of energy, potential energies, internal energies, radiated energy and kinetic energies.

3.5 Geometry and Mesh

3.5.1 Problem Structure

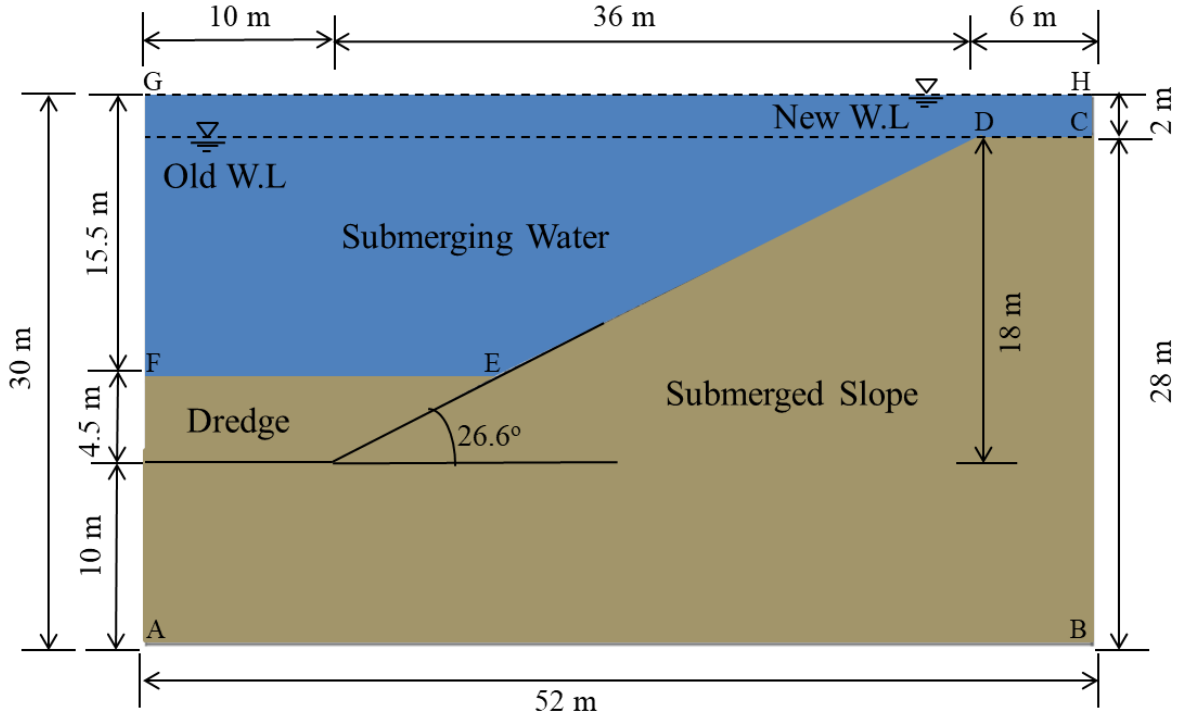


Figure 3.2: Problem Structure (modified from- Molenkamp, 2018).

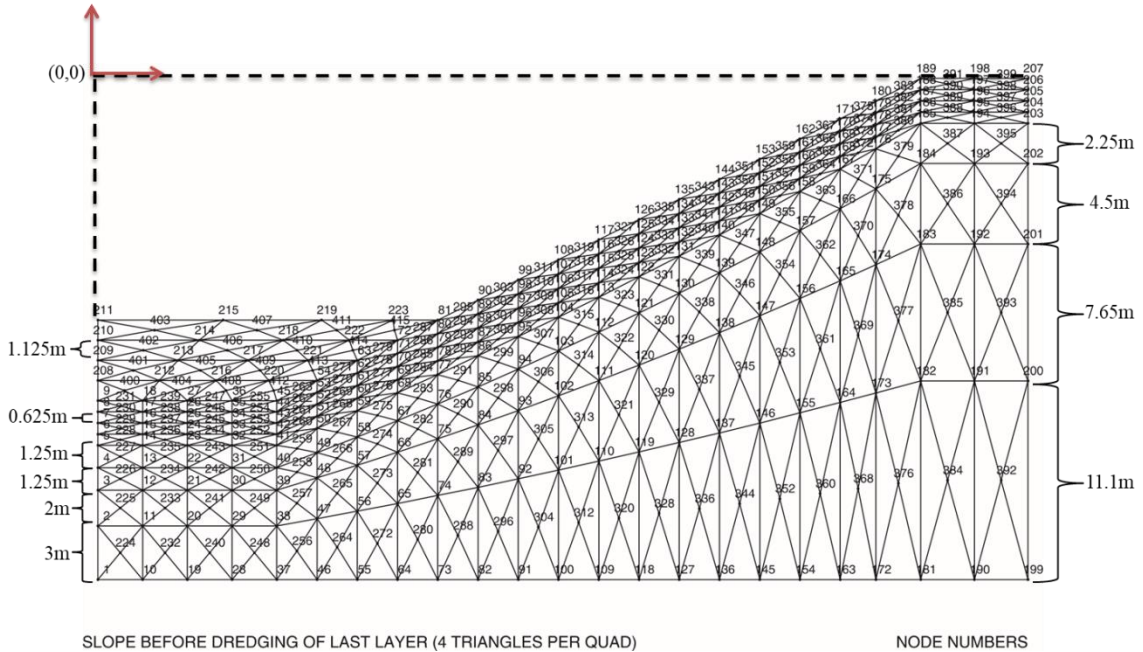
Note: here after in the description the problem geometry is in reference to the considered mesh geometries in the test scenarios. As stated before in section 1.4, the *soil slope geometry* was kept similar to the previous work by Molenkamp (1999), the area ‘ABCDEF’ represents the same. Further, it is to be noted that in the previous model the constant hydrostatic pressure loads applied at the interface, was by assuming the water level that coincides with the upper soil level (represented by Old W.L line in fig. 3.2). However, for the current scenarios the water level has been raised by 2m (represented by New W.L line in fig. 3.2). This has been done so to keep the soil structure completely submerged under shallow water and also with an assumption that it will produce more prominent water movements immediate to the post-instability.

Therefore with these considerations, the pilot test i.e. Case A, uses the geometry similar to the previous model (Molenkamp, 1999), represented by area ‘ABCDEF’, with virtually applied constant hydrostatic pressure loads at the interface (slope surface) as per ‘new water level’. Figure 3.3, can also be referred to visualize this geometry.

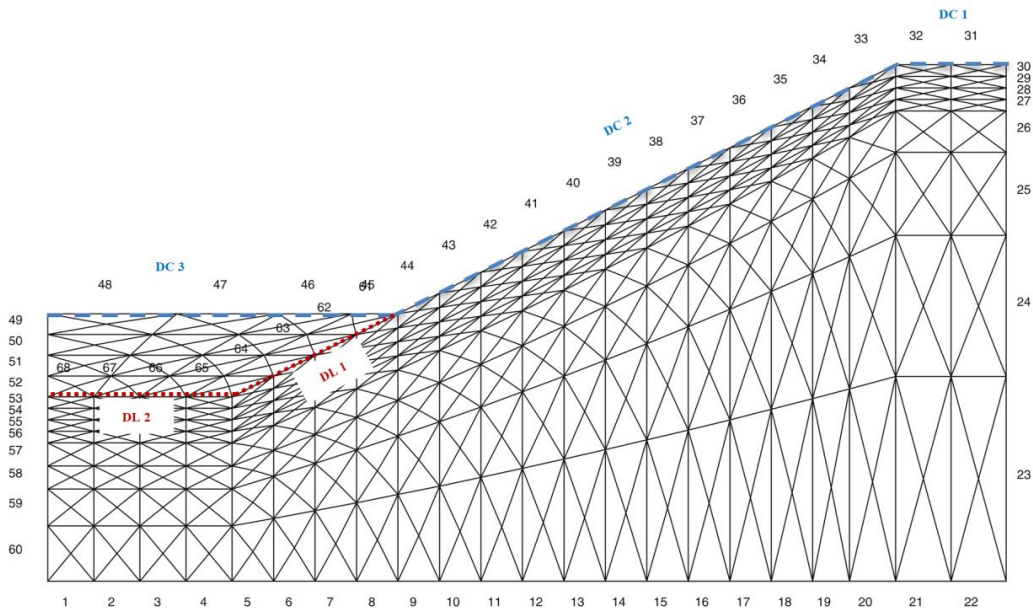
Next, Case B and Case C uses a full problem geometry that is with the inclusion of water layers as finite elements, represented by area ‘ABHG’. Figure 3.4, can be referred for further visualization. However, it is to be noted that considering that Case B, is also an uncoupled scenario

which considers constant hydrostatic pressure loads at the interface as per ‘new water level’, the fluid finite element layers are kept ‘restrained or inactive’ in this case.

3.5.2 Mesh: Elements, size and Layers



(a)

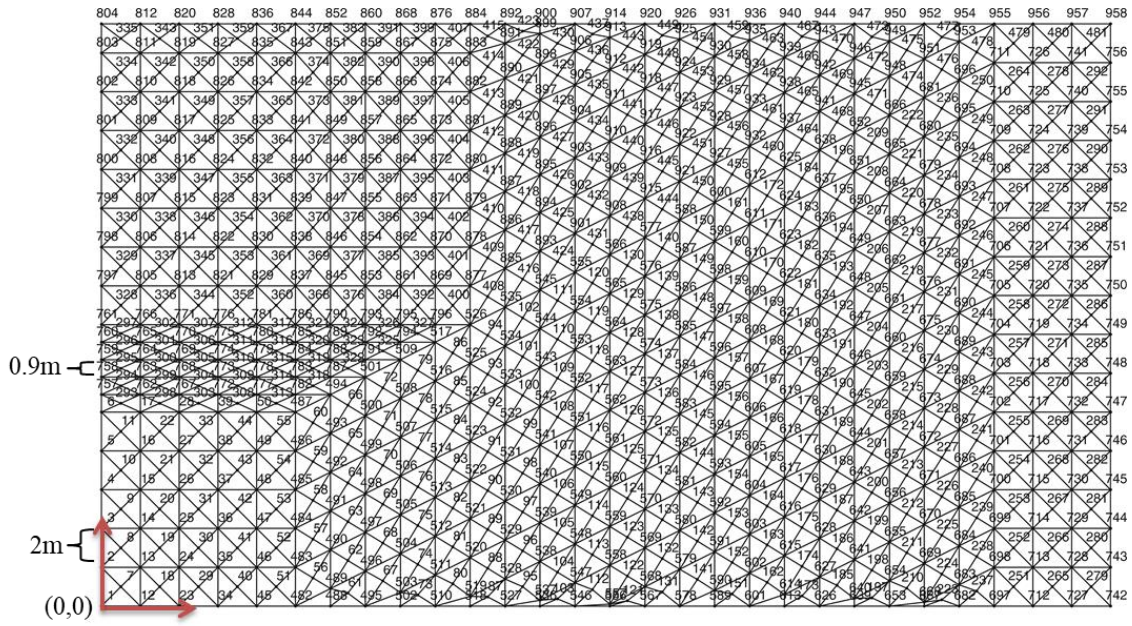


(b) Surface elements

Figure 3.3: Mesh for Case A; (a) Node numbering with element size and origin; (b) Surface element numbering (modified from, Molenkamp 1999).

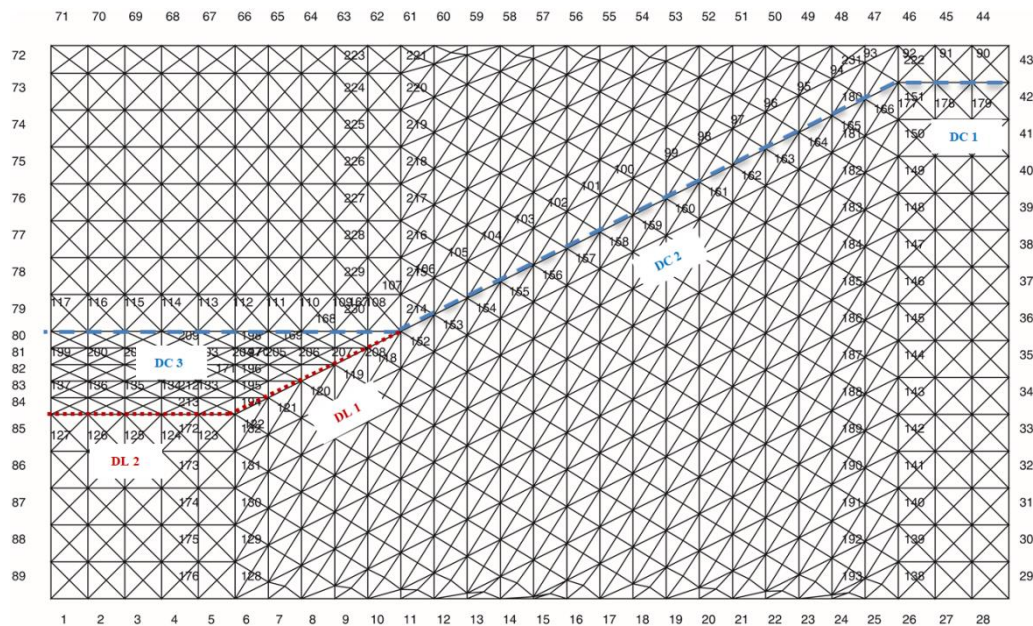
The mesh of the original work, with number of nodes and number of surface elements, is shown in above figure 3.3. This has been referred from Molenkamp (1999) and also used for the Case A scenario. Further, the new mesh for the extension to the original work is depicted in figure 3.4. This has been directly referred from the report by Molenkamp (2018). The program developed by Molenkamp in order to generate the new mesh is named as ‘MESH_GEN3.F95’. Further this mesh, as

is used for Case B and Case C scenarios. Link to the data files for both the meshes are detailed in Appendix B.



MESH OF 4 TRIANGLES PER SQUARE NODE NUMBERS

(a)



MESH OF 4 TRIANGLES PER SQUARE SURFACE ELEMENT NUMBERS

(b)

Figure 3.4: Mesh for Case B & C; (a) Node numbering with element size and origin; (b) Surface element numbering (modified from, Molenkamp 2018).

From the figures 3.3 (b) and 3.4 (b) the boundary surface elements count can easily be observed as they are in continuation, starting from left bottom corner and going anti-clockwise from that point forward. However, the direct contact surface element numbering, separating the fluid layer from soil layer and the dredge contact layer are difficult to visualize; especially for figure 3.4(b). Therefore, for this table 3.3 can be followed.

Table 3.3: Direct contact surface elements (*DC*) and Dredge layer contact elements (*DL*)

Contact Surface	Mesh Case A (Surface element numbers)	Mesh Case B & C (Surface element numbers)
DC 1	31 – 32	90 – 92
DC 2	33 – 44	93 – 107
DC 3	45 – 48	108 – 117
DL 1	62 – 64	118 – 122
DL 2	65 – 68	123 – 127

Elements – From both the figures 3.3 and 3.4, it can be observe that these meshes have been developed by subdividing a quadrilateral element into 4 triangular 3 nodal elements. In general, this type of low order FEM's are beneficial because of their simplicity and low computation cost. Additionally, such elemental arrangement is said to prevent spurious modes and locking in the numerical analysis (Pastor et. al., 1999). Following are the more elaborated reasoning on choosing such elements and their arrangement:

- The problem in hand is of “*quasi-static phenomena*”, where the slope structure fails due to gradual static unloading that leads to the static liquefaction. The progression to this type of failure in slopes is accompanied by induced slow static deformation and pore water flow, because of which the intergranular stress state gradually approaches a state of slope instability. Immediately following this instability state the soil particles experience relatively fast motion and large strains, which practically leads to the undrained behavior of water-saturated sand. This undrained behaviour is especially more pronounced in case of low permeable fine sands where the relative motion of pore water gets restricted compared to the soil skeleton during the small time increment of the post-instability deformation. Further, since due to the incompressible nature of pore water and 100% saturation of the soil system, during this occurrence the rate of volume change of the soil elements approaches zero and therefore the undrained soil becomes practically incompressible. Thus, for appropriate numerical quantification of such undrained dynamic behavior and the subsequent dynamic phase with developing liquefied flow, the same type of small finite elements are required throughout the finite element mesh (Molenkamp, 2018).
- Further, from the literature it has been found that the standard quadrilateral finite elements possess comparatively higher risk of *locking*, when full spatial integration over the finite elements containing incompressible material is applied (e.g. Babuška, 1973, Brezzi, 1974, Pastor et.al., 1999). This locking phenomenon, further leads to freezing of the deviatoric deformation of the affected elements and thus severely degrades the numerical accuracy.

On the other hand dividing a bigger quadrilateral element into 4 smaller quadrilaterals may provide higher accuracy in terms of displacements, as it interpolates the data to higher order. However, still 3 node linear triangular elements were opted for subdivision, since owing to higher risk of shear locking in former case (Molenkamp, 2018).

- Literature suggests that the adapted 3 node linear triangular elements arrangement have been found to provide an excellent definition for shocks and discontinuities in Fluid Dynamics (Pastor et.al., 1999).
- In addition to all the above, considering that at the initiation of instability, shock waves will be initiated through soil and water, radiating away from the suddenly severely deforming soil region. In order to handle this phenomenon in the numerical simulation and considering

that their maximum velocity of propagation depends mainly on the large stiffness of water an uniform element size has been chosen for the *new mesh* (refer to figure 3.4).

Element Size – It is to be noted this sub-section covers some general aspects of the opted element size with respect to the computational soil mechanics theory. However, since the finite element meshes used were pre-defined at the start of this research work, more details on how the accuracy is maintained in the program for the *soil domain* through time step restrictions with respect to the pre-fixed element size can be followed from section 3.7.2. Further, for *fluid domain* a separate compatibility test with respect to the opted mesh and time step configuration has been executed, which can be referred from section 3.8.

As a general rule, in soil mechanics, for the size of the element Δx , it should be small enough that it can simulate the expected largest natural frequency of the applied loading. Along with this size Δx , the parameter of the velocity of shear wave propagation (c) of the material defines the largest natural frequency of the finite element model. Thus ideally, the target is that this frequency should complement the loading frequency. Stating this, the criteria for Δx can be written as (Molenkamp, 1998):

$$\Delta x_{\max} = \frac{\pi c}{\omega_{\max}} \quad (3.79)$$

Where, ω_{\max} is highest circular frequency of loading.

In practice, usually ω_{\max} in case of cyclic loading is known, thus with the known shear wave velocity of the material a first approximation of element size can be easily made. However the case in hand where the dredge loading is simulated as ramp type (static: gradual increments) with very small load increments, ω_{\max} of vibration is usually low compare to cyclic loading, thus based on this the element size can be taken relatively coarser. Section, 3.7.2 which details the time steps and time of ramp loading, can be referred for circular loading frequency (ω_{\max}) and thereby for calculation to check on eq. 3.79 for the meshes.

Further, even though a loading frequency is low, it is important to consider the fact that with the loading the soil enters into a plasticity zone and with increase in plasticity the shear wave velocity (c) decreases (reaching zero at pure plastic state) and therefore the required element size decreases too (Molenkamp, 1998). Keeping this factor in mind it can be seen from the mesh of the original work (refer, figure 3.3), that Molenkamp has refined the elements in the zone where there is a possibility of observing a slope failure and hence a higher development of plasticity. Further, conversely the probable zones that do not interfere with the dynamic instability of the problem were kept very coarse. However, for the extension work the mesh has been mainly kept uniformly coarser (refer figure 3.4). This has been done considering the fact that in the new mesh the elements have already been increased because of the addition of the fluid layer. Therefore refining the problem will come with the cost of higher computation time. Thus for simplicity this the mesh was predominantly kept coarser, only the part which will be dredged or unloaded was kept fine so to have more precise calculation in that zone. Additionally, as stated before that, the program already includes a time step restriction which ensures sufficient controllability of the accuracy in the analysis (refer to section 3.7.2 for more details).

Although, considering that a minimum bar is set for accuracy, there is still a possibility that Old mesh test scenario (Case A) might produce relatively higher accurate result than New mesh test scenarios (Case B & C). Further, considering once the soil enters to plasticity zone the maximum

element size criteria will keep decreasing as per eq. (3.79) and with the accuracy restrictions in the model, it is possible that the analysis with the test scenarios using new mesh might stop early than old mesh test scenarios. In the current study these difference will judged later by comparing Case A (i.e. old mesh uncoupled test) and Case B (i.e. new mesh uncoupled test) results.

Layers –

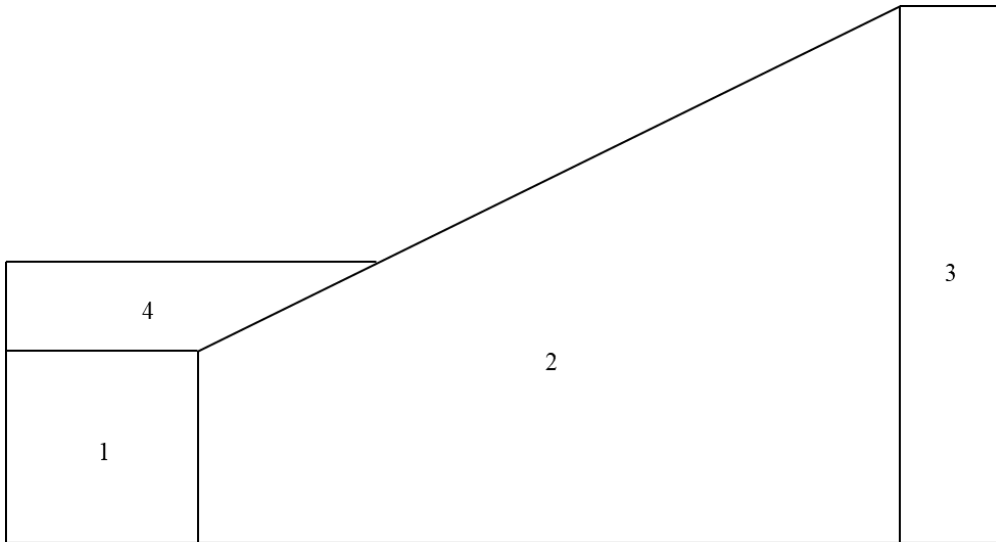


Figure 3.5: Mesh of Case A with Material Block numbers

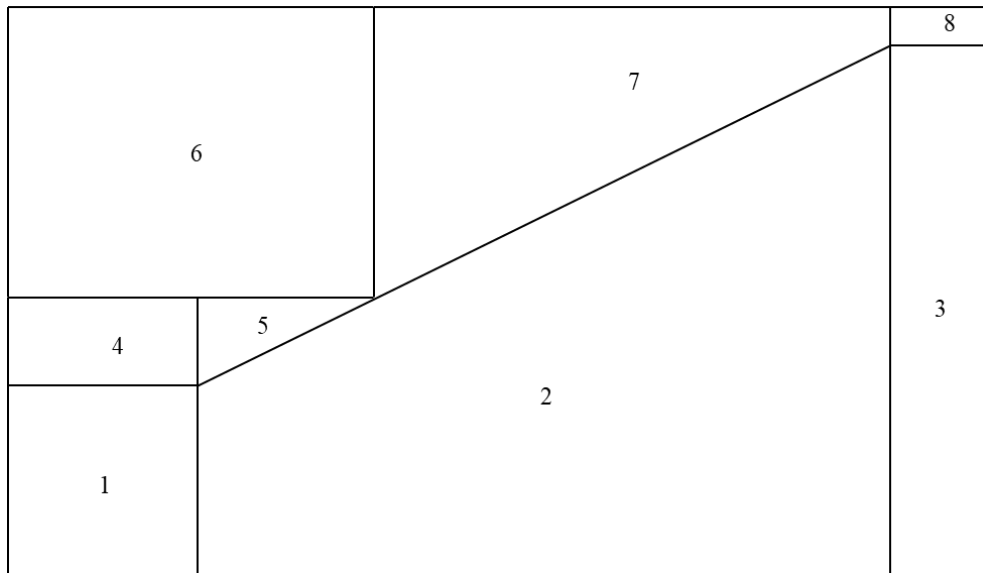


Figure 3.6: Mesh of Case B & C with Material Block numbers

Figures 3.5 and 3.6, show the total number of material blocks considered for the mesh of case A and the mesh of Cases B & C, respectively. From figure 3.5, it can be clearly observed that the number of material blocks used for Case A mesh is 4 i.e. from the original work. In this mesh all the blocks represent the same type of soil model i.e. double strain hardening Monot model with similar characteristics (refer to section 3.2 for more detail on the soil model and it characteristics) until the dredging induced dynamic loading phase is reached. At the start of this dynamic loading phase the 4th

material block, which is a dredge layer, is changed into a fluid material model layer (refer, section 3.6 for details on loading mechanism).

Similarly, for Cases B & C mesh, from figure 3.6 it can be observed that the total material block numbers implemented are 8, out of which 6 – 8 are blocks filled with fluid material model (refer section 3.3.5 for fluid characteristics filled in these layers), 1 – 3 blocks with Monot soil model and lastly 4 and 5 are the dredge blocks, which before dynamic loading is filled with Monot soil model and afterwards with fluid material model.

3.5.3 Surface Boundary conditions

Table 3.4 can be followed for the applied surface boundary conditions. It can be noted the bottom layer boundary is considered as rough, thus restricted for any kind of movements in x (horizontal) and y (vertical) direction. Next, upper layer boundary was kept free for movements in both x and y direction, whereas both the vertical wall boundaries were restricted to move in x direction but allowed to move in y direction.

Table 3.4: Mesh boundary conditions

Boundary	Surface Elements		x axis	y axis	Remarks
	Mesh Case A	Mesh Case B & C			
Bottom	1 – 22	1 – 28	0	0	0 → Restrained 1 → Free
Right	23 – 30	29 – 43	0	1	
Top	31 – 48	44 – 71	1	1	
Left	49 – 60	72 – 89	0	1	

3.6 Phases & Loading Conditions

In order to successfully evaluate the three cases: A, B and C as discussed earlier; several phases were incorporated, in order to keep the analyses consistent with the original study by Molenkamp (1999). According to this original work, three phases were ran for the analyses, where Phase 1 is the K_0 phase, Phase 2 is the drained unloading phase and finally, Phase 3 is dynamic dredge loading phase. Using similar approach for the current study, table 3.5 can be followed for the phases implemented in each Case.

Table 3.5: Phases implemented for different cases

Cases	Initial K_0 state	Initial state with drained unloading	Fluid Blocks Activation (Drained)	Hydrostatic transition and simulation of dredging
Case A Old mesh with water level	Phase 1(A)	Phase 2(A)		Phase 3(A)
Case B New mesh with restrained fluid blocks	Phase 1(B)	Phase 2(B)		Phase 3(B)
Case C New mesh with Active fluid blocks	-	-	Phase 3(C)	Phase 3(C)

From the above table it should be noted that the approach used in *Case C*, where fluidic layers were restrained for the initial two phases and thereby activated on the subsequent phase, was decided, based on the reasoning that fluid material being low mass density and in addition having very low viscosity, makes it highly prone to large displacements with slight change in loading conditions. Thus

during the application of *drained unloading Phase* directly with incorporated activated fluid layers it was found that the fluid material goes through large, and unwanted displacements. Moreover, to reach this solution several assumptions had to be made to overcome pre-existing numerical limitation of allowable accuracy in the model and additionally time steps had to be significantly reduced, making it impossible to reach the complete loading convergence in reasonable time. One alternative solution attempt involved increasing the viscosity of the fluid by 10^9 or 10^{12} only for the drained unloading phase, and thereby run the dynamic loading phase with realistic viscosity value. In this way, still higher displacements in the fluid material and the normal effective stress state were generated in the soil, showing the higher discrepancies in comparison with Case B phase 2(B) results (restrained fluid layers with new mesh, drained unloading case). These results have been compared since the aim is to produce similar stress state in soil domain in both the cases before the dredging is initiated, so to have reasonable comparison. Further, since the aim is to initiate the dredging phase analysis with submerging water being at rest initially, thus any movement in the fluid and their subsequent effect in the soil stress state prior to the dredging phase is unwanted.

Therefore, to avoid all the mentioned complex approaches, it was decided to reach a drained unloading state of soil in a more straight forward way, thus considering a restrained fluid layer during this phase (Phase 2(B)) and fluid layer activation in the subsequent phase (Phase 2(C)). This approach hence also reduces the higher risk of losing numerical accuracy.

3.6.1 Phase 1(A) & 1(B): Initial, K_0 state

The loading condition used for these phases were the same, although the phases 1(A) and Phase 1(B) differ in terms of mesh and therefore the resulting input data files (refer to link and table B1 in appendix B). Further, this phase, as discussed earlier, acts as K_0 phase, thus it fulfills the purpose of activating the soil layers in the program. Moreover, an activation key is used in the code under the variable name ‘TYPCHANG’ and when the value of this variable is set equal to 2; it activates the calculation of the quantities at the start of current calculation phase. In general, the significance of this key in the model is, that it is used to calculate various quantities based upon any type of predefined changes in soil or water conditions at the start of the calculation of the respective phase, thus before the MNR (Modified Newton Raphson) iteration process.

The soil layers are treated as drained and it produces the initial spatial distributions of both the intergranular stress tensor σ^* and the scalar isotropic pore fluid stress p , before any loading is applied. These initial spatial distributions in the old and modified program, both are approximated by representative quantities at the integration points of the finite element mesh.

Further, the intergranular stress tensor σ^* is obtained by starting from a homogeneous horizontal soil layer with a thickness z . Consequently in that particular case the intergranular stress tensor σ^* at level x_3^{co} with respect to the level of the upper surface of the layer can be expressed in terms of the principal vertical and horizontal intergranular stresses. The principal vertical normal intergranular stress reads:

$$\sigma_{33}^* = - \left| x_3^{co} \right| \rho_{buoy} g \quad (3.80)$$

where, $\rho_{buoy} g$ is the buoyant soil weight.

It is to be noted that the sign conventions opted here are in terms of continuum mechanics with tension and stretching being positive and vice versa compression being negative. Next, the principal horizontal normal intergranular stresses $\sigma_{11}^* = \sigma_{22}^*$ are expressed by:

$$\sigma_{11}^* = \sigma_{22}^* = K_0 \sigma_{33}^* = -|x_3^{co}| K_0 \rho_{buoy} g \quad (3.81)$$

where, K_0 is the ratio of the horizontal and vertical principal intergranular stresses.

Consequently for the matrix of stress tensor components σ_{ij}^* with respect to Cartesian triad $(\mathbf{e}_1, \mathbf{e}_2, \mathbf{e}_3)$ of unit base vectors, unit vector \mathbf{e}_3 being vertically upward, follows:

$$\sigma_{ij}^* = \begin{bmatrix} \sigma_{11}^* & 0 & 0 \\ 0 & \sigma_{22}^* & 0 \\ 0 & 0 & \sigma_{33}^* \end{bmatrix} \quad (3.82)$$

The hydrostatic pore fluid stress at level x_3^{wo} below the water table is expressed by:

$$p = -|x_3^{wo}| \rho_f g \quad (3.83)$$

The combined total traction components $\tau_k^{(n)}$ on a boundary surface due to both types of stresses is expressed by:

$$\tau_i^{(n)} = \sigma_{ij}^{(n)*} n_j + p n_i \quad (3.84)$$

where, the unit outward normal vector $\mathbf{n} = n_k \mathbf{e}_k$ on the boundary surface occurs.

The nodal force components $F_i^{k-\tau}$ due to the combined total traction components $\tau_k^{(n)}$ follow from the substitution of (3.84) in the first term of (3.1), leading to:

$$F_i^{k-\tau} = \iint_{S_{0\tau}} N^k \bar{\tau}_i^{(n)} |\hat{G}| dS = \iint_{S_{0\tau}} N^k \left(\sigma_{ij}^{(n)*} n_j + p n_i \right) |\hat{G}| dS \quad (3.85)$$

The intergranular stress state in the submerged slope starts from the assumption that the initial soil layer was horizontal with its upper surface, coinciding with the horizontal plane through the current crest level shown as ‘G.L phase 1’ line in figure 3.7. In that layer the vertical intergranular stress σ_{33}^* was defined by the buoyant weight and the horizontal intergranular stress σ_{11}^* and σ_{22}^* being defined by stress ratio $K_0 = 1$. This has been done so that a consolidated intergranular stress state can be generated in a subsequent phase: Phase 2(A) or Phase 2(B), by removal of the assumed soil layer over the slope surface. Additionally, the pore fluid stress p in the submerging water layer with the horizontal water surface level illustrated as W.L line in figure 3.7, is considered hydrostatic as described by eq.(3.83).

Therefore with these assumptions in order to attain global equilibrium with above mentioned formulations, an additional traction boundary at upper surface of soil slope is required, thus the direct contact section boundary surfaces which is indicated in figure 3.7 with initials DC. The traction stresses should correspond to the nodal in plane forces as per eq. (3.85). Thus with given ρ_{buoy} of soil, ρ_f of water, soil level x_3^{co} with respect to soil upper surface and water level x_3^{wo} with respect to upper surface of water, the expression (3.85) can be rewritten according to substitution of (3.80), (3.81) and (3.83) as:

$$F_1^{k_\tau} = -|x_3^{co}| \rho_{buoy} g K_0 \int_{S_{0r}} N^k n_1 |\hat{G}| dS - |x_3^{wo}| \rho_f g \int_{S_{0r}} N^k n_1 |\hat{G}| dS$$

$$F_3^{k_\tau} = -|x_3^{co}| \rho_{buoy} g \int_{S_{0r}} N^k n_3 |\hat{G}| dS - |x_3^{wo}| \rho_f g \int_{S_{0r}} N^k n_3 |\hat{G}| dS$$
(3.86)

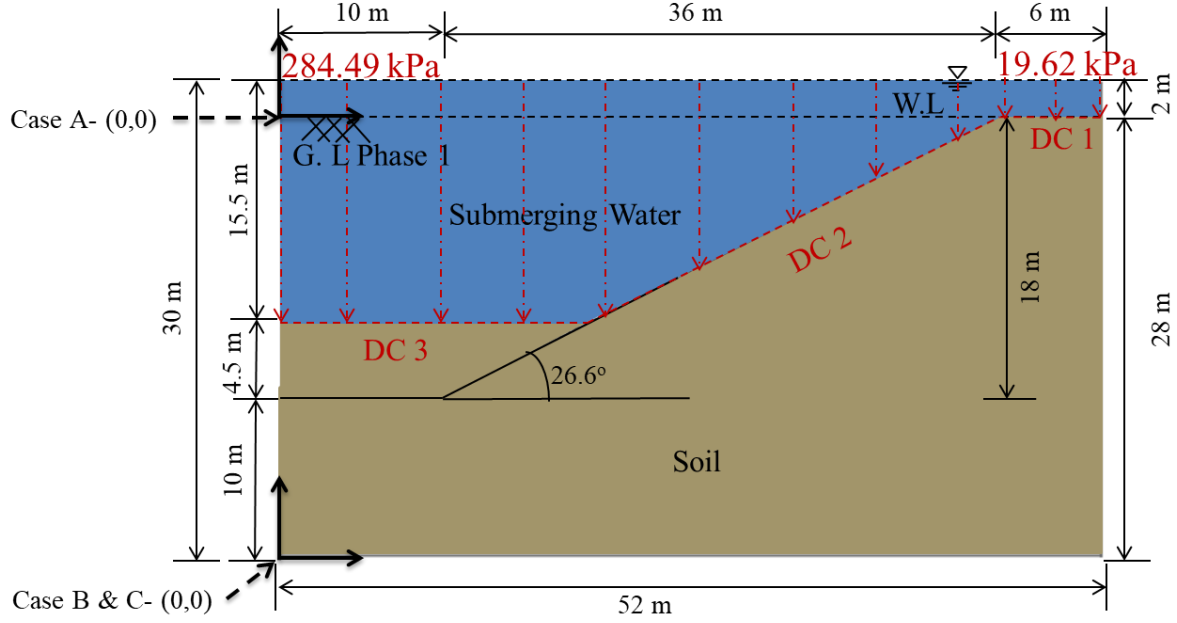


Figure 3.7: Problem Geometry with assumed ground level and the resulting equilibrium externally applied traction forces

Therefore, with eq. (3.84) and thereby substitution of the parameter values taken from section 3.2.2 and 3.3.5 for soil and fluid material respectively, and the local gravitational acceleration $g = 9.81 \text{ [m/s]}$, σ_{33} can be expressed for the current problem geometry (referred to figure 3.7) as:

$$\sigma_{33} = \sigma_{33}^* + p = -\rho_{buoy} g |x_3^{co}| - \rho_f g |x_3^{wo}|$$
(3.87)

Finally through eq. (3.69), upper and lower limits of the total vertical stress σ_{33} were calculated on the three contact boundaries. Table 3.6 and also figure 3.7 details the same.

Table 3.6: Applied tractions along direct contact boundary for Phase 1(A) and 1(B).

Boundary	Upper Limit	Lower Limit	Upper Limit	Lower Limit	Upper Limit	Lower Limit
	$ x_3^{co} $ [m]	$ x_3^{co} $ [m]	$ x_3^{wo} $ [m]	$ x_3^{wo} $ [m]	(σ_{33}) [kN/m ²]*	(σ_{33}) [kN/m ²]*
DC 1	0	0	2	2	19.62	19.62
DC 2	13.5	0	15.5	2	284.49	19.62
DC 3	13.5	13.5	15.5	15.5	284.49	284.49

*Note: The values for inputting in data files are considered positive since the considered sequencing of the surface elements inverse the sign conventions for these applied tractions.

Corresponding nodal forces according to eq.(3.86) are stored in modified program under the name of nodal vector FOLLDND, indicated as ‘follower type of load’, which implies that these nodal loads remain constant during later motion of the boundary surfaces. Additionally, the corresponding name of the boundary sections used for these types of loads in the program is FSECT.

3.6.2 Phase 2(A) and 2(B): Initial state with drained unloading

Similar to previous phases, these particular phases also have the same loading conditions and they differ based on type of mesh and input data file (refer to link and table B1 in appendix B.). Moreover, these are still accounted as a kind of initiation state phases, before dynamic loading starts.

The objective of these phases, as stated before, is to bring the soil material into a more consolidated form, thus drained conditions are applied. Moreover, as a continuation to Phase-1 in order to get the final soil profile to be pre-stressed, the loading induced due to previous assumption i.e. soil crest level is considered to be along ‘GL Phase 1’ line as illustrated in figure 3.8, now will be removed to reach soil crest level of ‘GL Phase 2’ line as shown in figure 3.8.

Further, since there is no kind of pre activation of material before the beginning of applied unloading for this phase analysis, ‘TYPCHANG = 0’ is set, which signifies that there will be no prior stress calculation or activation applied to the materials, before the start of MNR iteration.

Moreover in here, with the reference to the removal of assumed soil layer level, the nodal forces representing the effects of the buoyant weight on the soil skeleton are removed, inducing redistribution of the intergranular stress field and corresponding deformation of the soil skeleton. To control this process the reduction of these nodal forces in the numerical code is applied in sufficiently small time steps (refer section 3.7.2), for each of which M-N-R iteration process is applied, for maintaining static equilibrium.

In fact this reduction of the nodal forces along the upper boundary according to eq. (3.86) involves only its first terms, representing the effects of the buoyant weight and the related intergranular stresses. Consequently the second terms remain, representing the effects of the hydrostatic pore fluid stress on the submerged slope. Consequently for this phase the following additional nodal forces need to be applied, namely

$$\begin{aligned} F_1^{k,\tau^*} &= -|x_3^{co}| \rho_{buoy} g K_0 \int_{S_{0r}} N^k n_1 \hat{G} dS \\ F_3^{k,\tau^*} &= -|x_3^{co}| \rho_{buoy} g \int_{S_{0r}} N^k n_3 \hat{G} dS \end{aligned} \quad (3.88)$$

It should be noted that the signs of the terms in (3.88) are opposite to the corresponding terms in (3.68).

Moreover considering eq.(3.88) and eq.(3.87), the upper and lower limits of the additional vertical intergranular stresses σ_{33}^* , along the direct contact boundaries can be expressed as :

$$\sigma_{33}^* = -\rho_{buoy} g |x_3^{co}| \quad (3.89)$$

Thus, with above equation the upper and lower limits of the countering vertical intergranular stresses (σ_{33}^*) at three contact surface boundaries are calculated as shown in table 3.7 and further physically represented in figure 3.8.

Subsequently, to maintain the equilibrium, the nodal forces representing the effects of the hydrostatic pore fluid stress on the submerged slope are removed. However, the traction forces applied through activated fluid blocks at the direct contact boundary of submerged slope are the same. These virtually induced hydrostatic nodal forces at the direct contact boundaries, applied in Phase-1, can be represented by the second part of eq. (3.86). Therefore for the removal of the same, additional nodal forces can be applied and be expressed as below:

$$F_1^{k,\tau^s} = -|x_3^{wo}| \rho_f g \int_{S_{0r}} N^k n_1 \hat{G} dS$$

$$F_3^{k,\tau^s} = -|x_3^{wo}| \rho_f g \int_{S_{0r}} N^k n_1 \hat{G} dS$$
(3.90)

Hence, similarly to previous phases, with above expression and second part of eq. (3.87), the upper and lower limit of additionally applied vertical hydrostatic stress (σ_{33}) at direct contact boundaries can be represented as:

$$\sigma_{33} = -p = -\rho_f g |x_3^{wo}|$$
(3.91)

Therefore with above expression the limits calculated are as shown in below table 3.8 and depicted in figure 3.9.

Table 3.8: Applied traction along direct contact boundary for Phase 2(C)

Boundary	Upper Limit $ x_3^{wo} $ [m]	Lower Limit $ x_3^{wo} $ [m]	Upper Limit (σ_{33}) [kN/m ²]	Lower Limit (σ_{33}) [kN/m ²]
DC 1	2	2	-19.62	-19.62
DC 2	15.5	0	-152.055	-19.62
DC 3	15.5	15.5	-152.055	-152.055

*Note: The values for inputting in data files are considered negative since the modified program inverse the sign conventions for these applied tractions.

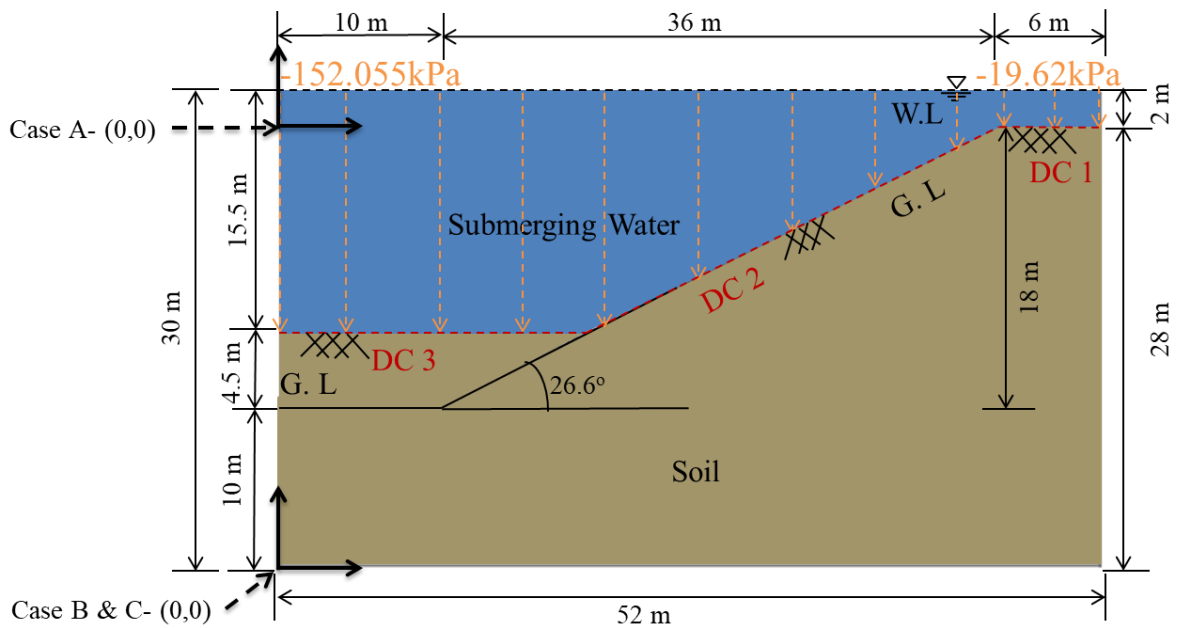


Figure 3.9: Problem Geometry with unloading traction loads.

From table 3.8, it can also be noticed that the extreme stress limits shown are basically the difference of Phase 1 and Phase 2, respective stresses. Therefore with addition of these all the assumed

virtual loading will be balance out. Further, these corresponding tractions, similar to Phase 2, are again stored under the name of nodal vector LOADSND and the corresponding type of boundaries section name as LSECT.

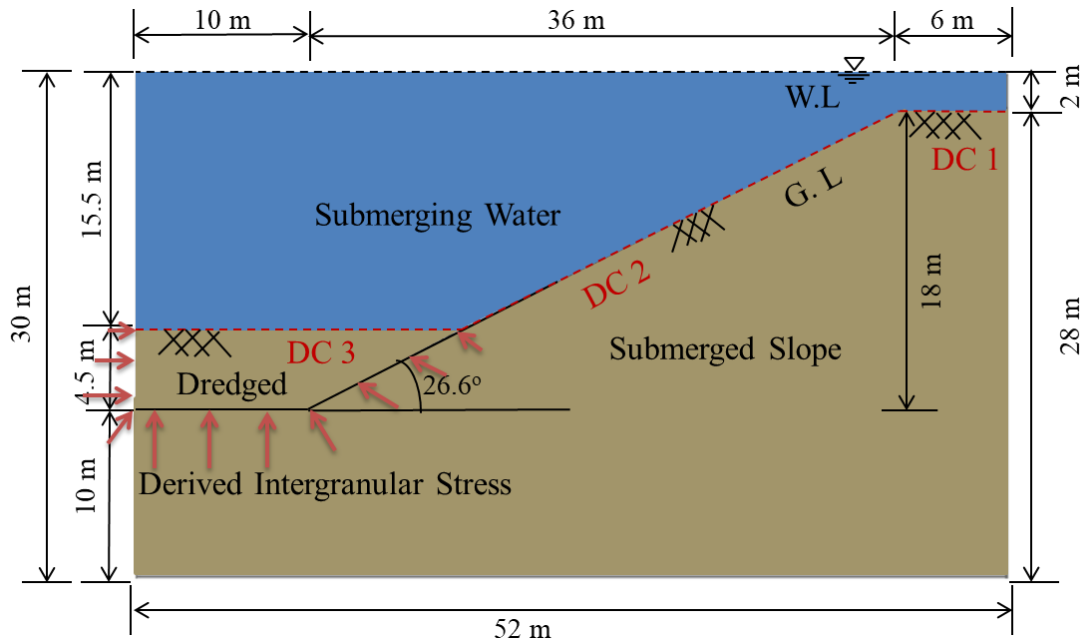
3.6.4 Phase 3(A), 3(B) and 3(C): Hydrostatic transition and simulation of dredging

These are the main dynamic loading phases for 3 respective Cases: A, B and C, where soil is treated as undrained. Similar to Phases 2(A) and 2(B), the loading condition used in these phases were the same, however they vary in terms of meshes and therefore resulting input files. Moreover, just like other phases, the activation key set for this phase is 'TYPCHANG = 4', which basically initiates the initial setup required to simulate the dredging in the problem before going into actual unloading calculations for dredging.

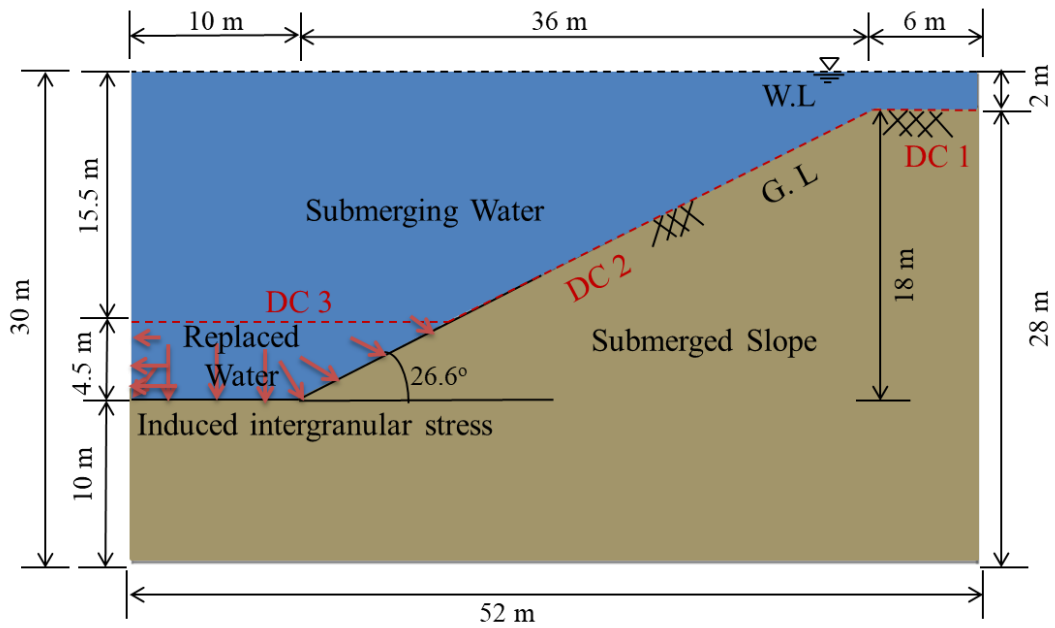
Further, this initial setup also concerns the loading mechanism, which as stated before has been changed in the modified program. This difference in loading mechanism is such that, the modified program is able to simulate dredging like conditions more precisely in the original program. To be more specific, the old approach simulates the removal of the dredge block (shown in figure 3.10) by gradually reducing the block's buoyant weight from soil to zero, representing water. Drawback of such approach is that since it uniformly reduces the buoyant weight of the dredged soil block, it therefore creates the possibility of slope failure even before the complete transition of a dredged soil block to fluid is reached, which was the case in Molenkamp (1999). Thus in this way it misses the replication of underwater dredging where the soil block is removed and simultaneously replaced by water. Further, it may produce conservative results as the full deformation of the slope is resisted at the toe and also the results produced within the dredge block maintain an ambiguity, since the material density in that part is in between that of the actual soil and the fluid.

In the new approach, the dredged drained soil block is removed first, under hydrostatic conditions, and replaced by water. Further, to maintain the equilibrium condition the traction force applied through intergranular stresses of the dredged soil block on the non-dredged surface is derived and thereby artificially induced on the surface after the removal of the soil block. This change of condition here and after has been referred to as hydrostatic transition of dredged soil block. Figure 3.10 can be followed for the visual representation. Moreover, in the modified code, this is the transition which gets initiated with the aforementioned activation key. Finally, once this step has been attained, the artificially induced intergranular stress on the non-dredged soil surface is uniformly reduced through time steps in order to active the slope failure. Section 3.7.2 can be further referred to for more detail on dynamic time stepping scheme. Thus, with this new approach, a dredged block will already have been converted into water, so the results post failure will be simulated relatively closer to the practical dredge conditions overcoming the ambiguity in the results faced with the previous approach. Further, it gives an added advantage to the modified program to simulate the water motion in the dredged zone as well.

It is worth mentioning the fact that even with these aforementioned advantages of the new approach, the results will still remain conservative. This is because the unloading of the artificially induced intergranular stresses occurs uniformly for the entire 4.5m by more than 10m block, which ideally would not represent the practical dredging process where the dredged layers will be relatively of smaller dimensions at a time. Thus this uniform unloading might lead to an early slope failure due to the absence of refraining soil layers, in compare to practical scenarios. One way to overcome this drawback could be by implementing static transition steps of the dredged block for smaller dimensions at a time, thus to simulate layer by layer dredging, however currently this is beyond the scope and objective of the study.



(a) Before hydrostatic transition of dredged block



(b) After hydrostatic transition of dredged block

Figure 3.10: Problem Geometry during initiation of dynamic Phase 3(A), 3(B) and 3(C), along with artificially induced intergranular stresses.

The eqs.(3.92) to (3.109) represents the mathematical derivation that has been worked out in order to have equilibrium conditions maintained during hydrostatic transition. Thus, this derivation also formulates the expression for the dredged intergranular traction force that are acting on the non-dredged surface.

For drained and undrained saturated soil the physical condition of the conservation of linear momentum of the bulk of the soil for the Lagrange formulation is expressed by

$$\rho \ddot{u} + n \rho_f \dot{v}|_{ii} - \nabla \cdot (\sigma^* + p I) - \rho b = 0 \quad (3.92)$$

where, the following quantities occur:

$$\rho = \rho_s (1 - n) + n \rho_f \text{ - volume weight of saturated soil} \quad (3.93)$$

ρ_s - average density of the minerals composing the grains

ρ_f - average density of the fluid filling the pores, namely for air-saturated dry soil it is pore air and

for saturated soil it is water.

n - porosity of solid skeleton.

\ddot{u} - average acceleration vector of the soil skeleton

$v|_{ii}$ - relative average velocity vector of the pore fluid with respect to the solid skeleton

σ^* - average intergranular stress tensor (continuum mechanics: tension positive).

p - average pore fluid stress (continuum mechanics: tension positive).

$\nabla \cdot$ - divergence vector operator

I - second order isotropic tensor

$$b = -g e_3 \text{ - body force vector per unit of mass:} \quad (3.94)$$

where, g is the downward vertical acceleration due to the earth's gravity and (e_1, e_2, e_3) is the Cartesian triad of unit base vectors, where e_3 is vertically upward.

For the hydrostatic case the corresponding physical condition of the conservation of linear momentum of water is expressed by

$$-\nabla p - \rho_f b = 0 \quad (3.95)$$

where, $\nabla p = \nabla \cdot (p I)$ is the gradient vector of the pore fluid stress.

Substituting eq. (3.95) in (3.92) gives for the conservation of linear momentum of the bulk of the saturated soil in the hydrostatic case as:

$$-\nabla \cdot (\sigma^* + p I) - \rho b + \nabla p + \rho_f b = 0 \quad (3.96)$$

which elaborates to:

$$\nabla \cdot \sigma^* = -(\rho - \rho_f) b = -(\rho_s - \rho_f)(1 - n) b = -\rho_{buoy} b \quad (3.97)$$

where, the buoyant density is expressed by :

$$\rho_{buoy} = (\rho_s - \rho_f)(1 - n) = \rho - \rho_f \quad (3.98)$$

relating the buoyant density ρ_{buoy} to both the mineral density ρ_s and the porosity n .

For the weak form of the integral of the conservation of linear momentum of the saturated bulk for finite element implementation, based on eq. (3.92), follows in terms of the index notation:

$$\begin{aligned}
 \int_v N^p \rho \ddot{u}_k dv + \int_v N^p n \rho_f \dot{v}_k \Big|_u dv + \int_v B_{kji}^p \sigma_{ji}^* dv + \int_v N_{,k}^p p dv + \\
 - \int_v N^p \rho b_k dv - \int_{s_\tau} N^p \bar{\tau}_k^{*(n)} ds - \int_{s_p} N^p \bar{p} n_k ds = 0
 \end{aligned} \tag{3.99}$$

Where,

N^p - shape function of finite element of node p

B_{kji}^p - components of strain-nodal displacement matrix of node p for displacement in Cartesian direction k and strain component in Cartesian directions j, i

$N_{,k}^p$ - partial derivative in Cartesian direction k of shape function of finite element of node p

$\bar{\tau}_k^{*(n)}$ - prescribed intergranular traction vector acting on the co-moving boundary surface s_τ of the solid skeleton

\bar{p} - prescribed isotropic pore fluid stress $\bar{p}(t)$ on the boundary s_p of the pore fluid

v - considered co-moving material volume of the solid skeleton

s_τ - part of co-moving boundary of the solid skeleton with prescribed intergranular traction vector $\bar{\tau}^{*(n)}(t)$

s_p - part of co-moving boundary of the solid skeleton with prescribed isotropic pore fluid stress $\bar{p}(t)$

Note that in eq. (3.99), also the effects of the boundary conditions concerning the conservation of the linear momentum affecting the solid skeleton and the pore fluid occur. These boundary conditions are specified by

- at the part of the co-moving boundary s_τ of the solid skeleton with outward normal unit vector n and prescribed intergranular traction vector $\bar{\tau}^{*(n)}(t)$:

$$\tau_i^{*(n)} - \bar{\tau}_i^{*(n)} = n_j \sigma_{ji}^* - \bar{\tau}_i^{*(n)} = 0 \tag{3.100}$$

- at the complementary part of the boundary $s_u = s - s_\tau$ with prescribed displacement vector $\bar{u}(t)$:

$$u_i - \bar{u}_i = 0 \tag{3.101}$$

- at the part of the boundary s_p with prescribed isotropic pore fluid stress $\bar{p}(t)$:

$$p - \bar{p} = 0 \tag{3.102}$$

- at the complementary part of the boundary $s_w = s - s_p$ of the pore fluid with outward unit normal vector $-n$ and prescribed pore fluid flux $\bar{w}^{(-n)}(t)$:

$$n_i w_i - \bar{w}^{(-n)} = 0 \tag{3.103}$$

Substituting eq. (3.95) and (3.97) in (3.99) leads for the conservation of linear momentum of the saturated bulk for the finite element implementation for the hydrostatic case to:

$$\int_v B_{kji}^p \sigma_{ji}^* dv + \int_v N_{,k}^p p dv - \int_v N^p \rho b_k dv - \int_{s_r} N^p \bar{\tau}_k^{*(n)} ds - \int_{s_p} N^p \bar{p} n_k ds = 0 \quad (3.104)$$

Next the boundary conditions before and after drained removal of a saturated bulk soil volume is considered, involving the drained replacement of the saturated bulk soil volume by water, all under hydrostatic conditions. To this end first consider the finite element formulation of the drained saturated bulk soil volume with the buoyant weight according to eq. (3.97) before dredging, leading to:

$$\int_v N^p \sigma_{ji,j}^* dv = - \int_v N_{,j}^p \sigma_{ji}^* dv + \int_{s_r} N^p \bar{\tau}_i^{*(n)} ds = - \int_v N^p \rho_{buoy} b_i dv \quad (3.105)$$

Then the first term of eq. (3.104) can be elaborated for hydrostatic equilibrium of the saturated bulk volume (before dredging) by substituting eq.(3.105), leading to:

$$\int_v B_{kji}^p \sigma_{ji}^* dv = \int_v \delta_{ki} N_{,j}^p \sigma_{ji}^* dv = \int_v N^p \rho_{buoy} b_k dv + \int_{s_r} N^p \bar{\tau}_k^{*(n)} ds \quad (3.106)$$

Finally from eq. (3.106) follows for the boundary integral of the intergranular traction force over the boundary area s in the hydrostatic case:

$$\int_{s_r} N^p \bar{\tau}_k^{*(n)} ds = \int_v B_{kji}^p \sigma_{ji}^* dv - \int_v N^p \rho_{buoy} b_k dv \quad (3.107)$$

The above describes the intergranular interaction force by the saturated bulk volume before dredging on the remaining non-dredged soil underneath.

Next consider the hydrostatic equilibrium of the water volume after dredging according to eq.(3.104) by substituting the intergranular traction force according to (3.107). Elimination of opposing terms and substituting the densities according to eq. (3.93) and (3.97) gives:

$$\int_v N_{,k}^p p dv - \int_v N^p \rho_f b_k dv - \int_{s_p} N^p \bar{p} n_k ds = 0 \quad (3.108)$$

Rearrangement of above equation enables to express the interaction force on the boundary surface s_p with prescribed hydrostatic pore pressure

$$\int_{s_p} N^p \bar{p} n_k ds = \int_v N_{,k}^p p dv - \int_v N^p \rho_f b_k dv \quad (3.109)$$

During the removal of the soil skeleton the dredged soil skeleton is replaced by water satisfying the initial hydrostatic condition. The resulting interaction force according to eq.(3.109) on the surface area of the remaining non-dredged soil underneath the dredged soil corresponds to the effect of the free hydrostatic water pressure on that surface area, thus without any effect of the dredged soil. Consequently, the interaction force eq.(3.109) by the water after dredging remains identical to the interaction force by the pore water before dredging due to eq.(3.107).

Furthermore, it can be concluded that for the saturated soil underneath the dredged region no changes occur if during the removal of the soil skeleton the interaction force eq.(3.107) by the soil skeleton is maintained artificially. In the modified program this artificially induced force has been ultimately stored under the variable name ‘‘LOADSB’’, which basically signifies; load at the begin of ramp loading. Subsequently ‘‘LOADSE’’ is the variable name used to store values for the load at the end of time loading, which for this case has been set to zero.

3.7 Execution

3.7.1 Libraries

The program “Modified_Dyn_mlk4.f95” uses the same set of libraries that has been used in original work; “Dyn_mlk4.f95” program by Molenkamp (1999). Although, it is worth mentioning that there have been few updates in the library by Molenkamp after the commencement of his original work. Considering this, in total 9 libraries have been implemented in the program, namely as listed in table 3.9.

Table 3.9: List of libraries used in program “Modified_Dyn_mlk4.f95”

No.	Libraries	Remarks
1.	MYKIND.f95	Portable definition of precision (16 decimal digits precision is used in the program)
2.	MAIN_F95.f95	Library by Smith and Griffth (2004) with later modifications by Molenkamp (2006)
3.	COMCONST.f95	Common constitutive subroutines by Molenkamp (2006)
4.	MLK_LB1.f95	Finite element subroutine by Molenkamp(2005)
5.	MISES.f95*	Library of subroutines for enhanced Von-Misses soil model by Molenkamp (1999)
6.	COULOMB.f95*	Library of subroutines for Mohr-Coulomb vertex soil model by Molenkamp (1999)
7.	MONOT.f95	Library of subroutine for primary Monot Model by Molenkamp (1980)
8.	MONOT2.f95*	Library of subroutines for secondary Monot model with different set of Parameters by Choobbastig (1997)
9.	ALTERNAT.f95*	Library of subroutines for Alternat model (Kinematic Elasto-Plastic model) by Molenkamp (1997)

*These libraries are implemented in the program though not used for the current work.

3.7.2 Parameter θ , Time increment, Loading time and Accuracy

Parameter θ , value in a numerical model governs the damping of the frequencies, thus it becomes important to optimize it so to damp out unwanted high frequencies generated in a model due to numerical inaccuracies. Additionally at the same time, care should be taken so to avoid excessive reduction of the natural frequencies. Considering this, the report by Molenkamp (1998) details a numerical solution of undamped oscillator by means of θ method, which was interpreted based on a calculated response of the analytical solution of the damped oscillator for the same initial conditions of unit displacement and zero velocity. Thereby with this interpreted results, the variation of the parameter θ was observed on the equivalent numerical damping (ζ) and the numerical distortion of Eigen frequencies, which were illustrated as a function of quantity ($\omega\Delta t$). It is to be noted, $\omega\Delta t$ is a dimensionless quantity which depends on the natural undamped frequency ω and on applied time step Δt in the numerical integration. This quantity represents the applied phase angle per time step. Further, the observation made in that work shows the following:

- $\zeta > 0$ for $\theta > 0.5$, signifying positive damping of vibration as calculated by numerical integration time steps.
- $\zeta = 0$ at $\theta = 0.5$, no damping
- $\zeta < 0$ at $\theta < 0.5$, signifies numerical integration increases the artificial vibration in the system.
- $\zeta \approx 0.4$, is maximum when $\omega\Delta t = 2$ and $\theta = 1$, which basically signifies very high artificial damping in the system and thus leading to substantial erroneous results.

- For θ between 0.3 and 0.7 the reduction of the natural frequency is of the order 0.8 at $\omega\Delta t = 2$ and for larger values of $\omega\Delta t$ the reduction is much more severe.

Therefore with the observations above, it was concluded in that study that in order to keep the damping smaller than 5% values between 0.5 and 0.55 must be chosen. Further to limit the reduction of the natural frequency to 80% the time step Δt must be selected such that $\omega\Delta t$ remains less than 2. Finally, therefore with these conclusions in the current work the value opted for θ is 0.51, which is also the same value that has been used in original work by Molenkamp (1999).

Time increment Δt and Loading time, have been considered separately and accordingly, for each type of loading. Further, below details can be followed for the values used at different phases:

- For Phase 1(A) and 1(B), which are initial K_0 states with restrained fluid layers, both time interval and loading time (DTIMLD and TIMLD respectively, reference in program) were opted to be the same since this was an equilibrium condition; hence the numerical calculations were required to be converged in 1 step. The time opted for these states were 1.E5 seconds which is the same used in original work by Molenkamp (1999). Additionally, using such large time step ensures no involvement of inertial mass as per eq.(3.22).
- Phase 2(A) and 2(B), as stated before these phases are still considered to be initiation states, yet involving unloading. However this unloading is considered to be of low impact in the system where the soil will still remain mainly in elastic state. Moreover, these are the phases to achieve an initial consolidated state of the soil, which is assumed to be attained slowly throughout a time period. Thus given that, the total time of loading (TIMLD) for these phases has been considered to be 1.E5 seconds. Further, to control the whole process relatively smaller time steps (DTIMLD) of 200 seconds has been opted, thus the total number of time steps for unloading involved were 500. This type of ramp loading is depicted in figure 3.11.

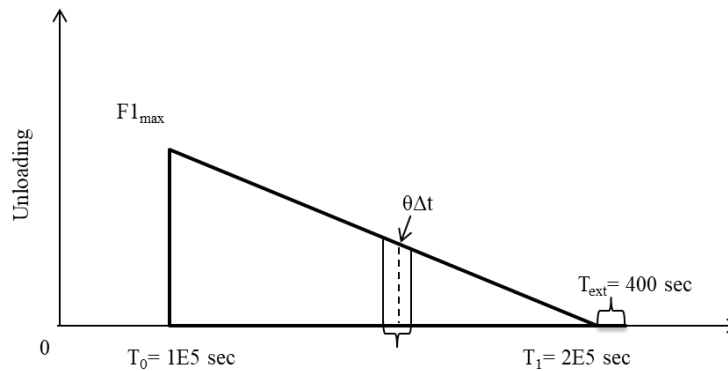


Figure 3.11: Illustration of unbalance load applied during Phase 2(A) & (B).

Here $F1_{\max}$ represents the total ramp unloading (refer section 3.6 for loadings), which is achieved in the system within the time frame of T_0 to T_1 . The T_0 represents the time spent in previous phase and subsequently T_1 , time at the end of the unloading. In addition to this, considering the θ method, at least 1 extra time steps is required in a problem so to achieve full unloading. Therefore, with this additional 2 steps were incorporated for this phase, making it 502 steps total.

Further, with Figure 3.11, the maximum circular frequency ω_{\max} of unloading can be calculated as (referred from Molenkamp, 1998):

$$\omega_{\max} = \frac{2\pi}{T_{\min}} = \frac{2}{\Delta t} = 0.01 \text{ rad/s} \quad (3.110)$$

Thus having such a low circular frequency of unloading along with shear wave velocity (c) under elastic condition, equals to 193.167 m/s (calculated through program), the maximum element size condition from eq. (3.79) can be calculated as:

$$\Delta x_{\max(\text{limit})} = \frac{\pi c}{\omega_{\max}} = \frac{\pi c \Delta t}{2} \approx 6 \times 10^4 \text{ m} \quad (3.111)$$

Comparing the above solution with the meshes from Case A, B & C (refer figure 3.3 and 3.4), it can be concluded that the maximum elements size $\Delta x_{\max(\text{mesh})}$ in all the meshes are small enough to simulate the natural frequency of unloading. Additionally, given that the shear wave velocity decreases with increasing plasticity, the difference between $\Delta x_{\max(\text{limit})}$ and $\Delta x_{\max(\text{mesh})}$ for all the opted meshes will be large enough that they can be considered well under the limits, even if the soil stress state starts initiating plasticity in the current phase.

In addition to this, in the modified program, limits has been set for maximum and minimum time steps based upon opted maximum element size of mesh and allowable strains, respectively. However, it is not of concern at this phase, as the soil is expected to remain mainly elastic with considerably low small incremental strains during the mentioned time interval. Though, these aforementioned aspects are important for dynamic loading phase and thus discussed later in this section.

- *Phase 2(C)*, just like Phases 1(A) and 1(B), is an equilibrium phase where fluid blocks get activated. Thus it is required to achieve numerical convergence in 1 step, this is done by setting the total time of loading (TIMLD) and time step (DTIMLD) again equal to 1E5 seconds. This large time step will ensure that the hydrostatic condition is maintained with no role of viscous shear stress or inertial mass as per eq.(3.58) on the system.
- *Phases 3(A), 3(B) and 3(C)*, as stated, are the main dynamic loading phases where the dredging begins. It will be noted below in this part, that the optimization of the time interval and element size has been done based on the soil response, since the priority during unloading was to maintain high accuracy in simulating shear wave propagation or frequency in the soil domain. Moreover, for fluid domain where pressure wave propagation is the critical criteria, a fluid tank test has been executed (refer to section 3.8) in order to evaluate the fluid response for the opted settings. Moving on, in order to simulate realistic dredging time, the total loading time (TIMLD) considered was 100 sec. Further, time step (DTIMLD) opted to be relatively smaller than Phase 2 i.e. 0.1 sec, thus using 1001 steps (+ 1 step, as per θ method) to reach the complete unloading. Further, figure 3.12 illustrates this type of ramp unloading. Here, $F2_{\max}$ represents the total unloading force (refer section 3.6.4), T3 is the total time at the beginning of the current phase and T4 total time at end of the unloading.

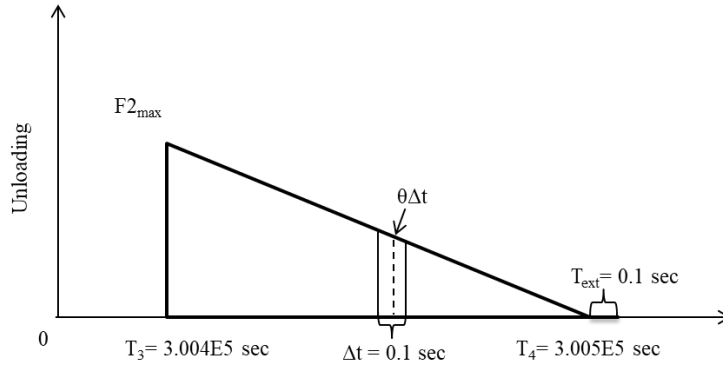


Figure 3.12: Illustration of unbalance load applied during Phase 3(A), (B) & (C)

With the mention loading time and interval, similar to Phase 2, the condition mentioned in eq. (3.79) can now be checked for element size as shown below:

The maximum circular frequency of unloading (ω_{\max}) is:

$$\omega_{\max} = \frac{2\pi}{T_{\min}} = \frac{2}{\Delta t} = 20 \text{ rad/s} \quad (3.112)$$

Therefore with this the solution to eq. (3.79) is shown in eq.(3.113). It is to be noted that for this calculation the soil response was assumed elastic, thus elastic shear wave propagation velocity ($c = 193.167\text{m/s}$) is used.

$$\Delta x_{\max(\text{limit})} = \frac{\pi c}{\omega_{\max}} = \frac{\pi c \Delta t}{2} \approx 30.34 \text{ m} \quad (3.113)$$

Similar to Phase 2, again comparing the above solution from the mesh element for all the cases (refers, figure 3.3 and 3.3) it can be said that the maximum element sizes opted $\Delta x_{\max(\text{mesh})}$ are small enough to incorporate the natural frequency of unloading at elastic response of the soil. Although, as discussed before in section 3.5.2 that, in and around the slope failure zone the soil transits its state from elastic to increasingly plastic, thereby causing decrease in shear wave velocity and thus leading to the reduction of $\Delta x_{\max(\text{limit})}$ as stated above, at the concerned failure region.

At the occurrence of global instability the global slope behaviour becomes dynamic, causing shock waves to propagate away from the collapsing soil region. For a realistic numerical simulation of this dynamic wave propagation in all directions uniformity of the elements of the mesh is essential, while the time step Δt and the element size Δx should be balanced relatively, as expressed by eq. (3.113), in order to achieve maximum accuracy for the applied numerical effort.

Soil domain accuracy – Molenkamp (1998) describes the time step limits so to simulate the frequencies accurately. These limits were used in the original program by Molenkamp (1999) and it have been directly implemented in the modified program as well.

In this, firstly, the minimum limit has been set for the time interval (Δt) for the given maximum element size of mesh used, refer eq.(3.114). This limit has been set such that it maintains the distorted frequency ratio of simulated frequency to 80%.

$$\frac{\Delta x_{\max(mesh)}}{c\Delta t_{\min(limit)}} < \frac{\pi}{2} \quad \text{so} \quad \Delta t_{\min(limit)} > \frac{2\Delta x_{\max(mesh)}}{\pi c} \quad (3.114)$$

In the program shear wave propagation (c) is calculated as:

$$c = \sqrt{\frac{G_s}{\rho_s}} \quad (3.115)$$

where, G_s is equal to shear modulus of soil at give stress state, this gets calculated internally in the program through Monot soil model algorithms. Moreover, ρ_s is the saturated density of soil.

It is to be noted that in eq. (3.114) the shear wave propagation velocity c provides a similar limitation to the maximum element size $\Delta x_{\max(limit)}$ as does in eq. (3.115). Thus with known $\Delta x_{\max(mesh)}$ and with the shear velocity c decreasing due to increasing plasticity in the soil the corresponding minimum time step $\Delta t_{\min(limit)}$ will increase.

Further, secondly, Molenkamp (1998) also describes the upper limit to the time step based on the strain attained per time interval. At this point, it is worth mentioning that the time interval ($\Delta t = 0.1$ sec) and thereby the number of steps i.e. 1001 to achieve the complete unloading was set as such that the strain increment per interval in the system remains small enough for the numerical implementation of the constitutive model to remain applicable specially under the limit stability state of slope. However, when instability in the slope occurs the maximum strain rates achieved in the system starts to increase with per time increment, thus this requires the reduction of the time interval so to have maximum strain achieved in the system within acceptable limits. This reduction is achieved in a way that if the time interval Δt^a at any step causes the achieved maximum modulus of strain increment $|\Delta \mathcal{E}_{\max}^a|$ to be more than that of allowable strain increment $|\Delta \mathcal{E}_{allow}|$ (value set can be referred from section 3.7.3) than the time interval for that steps get reduced as shown in eq.(3.116) and thus the calculation is repeated with the reduced time step Δt^b .

$$\Delta t^b = \frac{\Delta t^a |\Delta \mathcal{E}_{allow}|}{4 |\Delta \mathcal{E}_{\max}^a|} \quad (3.116)$$

From the above conditions it can be observed that in the program this will lead to a conflict with eq. (3.114), when the plasticity increases in the soil and eventually the static limit state of slope will be passed and lead to dynamic collapse motion. Once this state is achieved it requires the time step to be reduced considerably so to keep the allowable strain limit at check. However at the same time the minimum time step limit through eq. (3.114) will keep increasing. Another observation that can be made here is that the $x_{\max(mesh)}$ can be reduced so to run the analysis for comparatively larger strains. However, again this will cost for higher computational time, which was unwanted for the current work.

Moving on, both the original work by Molenkamp (1999) and the modified program implemented two additional limits on time interval so to optimize it in a way that fast calculations can be attained. Both these limits depends on the number of iterations required for convergence; Type-A, involves a decreasing time step, in case convergence in MNR iterations of the time step is too slow,

and Type-B, concerns an increasing time step, provided the convergence becomes faster after a certain amount of decrease through eq.(3.116) in the calculations.

Elaborating the Type-A limit, it has been set as such that if in any MNR iteration of a time step the relative error in the convergence condition mentioned in eq. (3.117) gets fulfilled the program will extrapolate the iteration required for the convergence $Its_{(conv)}$ based on eq.(3.118).

$$1E-5 < ALF = (RERR/RERRB) \times (1/(ITERS)) < 0.99999 \quad (3.117)$$

where, RERR is the relative error of convergence for the current MNR iteration step (ITERS) and RERRB is the lowest relative error of convergence calculated before the current MNR iteration step.

$$Its_{(conv)} = \text{Integer}(-(\log(RERR)-\log(ALWERR))/\log(|ALF|))+ITERS \quad (3.118)$$

where, ALWERR, refers to allowable error in MNR iteration convergence (refer, section 3.7.3)

Finally, if this $Its_{(conv)}$ is estimated to be more than the allowable number of MNR iterations $Its_{(allow)}$, that the calculation is repeated based on a new time step Δt^b which is calculated based on current time step Δt^a as shown in eq.(3.119).

$$\text{if } Its_{(conv)} > Its_{(allow)} \text{ then } \Delta t^b = \frac{\Delta t^a}{2} \quad (3.119)$$

Further, the Type-B condition has been implemented in programs in order to increase the time step. To this end an algorithm is used to judge $Its_{(conv)}$ for every time step and if it finds that after a certain dip in time step due to eq.(3.116), the $Its_{(conv)}$ for later time steps becomes faster then the program increases the time step. Eq.(3.120) provides the condition for judging the speed of convergence. If $Its_{(conv)}$ is less than 5 times the value of $Its_{(allow)}$ then the time step increment Δt is allowed to be increased.

$$Its_{(conv)} < 5 \times Its_{(allow)} \quad (3.120)$$

In such case the next incremental time step Δt^{b+1} is express as:

$$\Delta t^{b+1} = 1.5 \times \Delta t^a \quad (3.121)$$

3.7.3 Phase executional parameters

The main input parameters for the calculation processes of the various phases are collected in table 3.10. For more details about these and other parameters e.g. atmospheric pressure, ramp loading activation key etc., the input data files can be referred from the link and table B1 in appendix B.

Table 3.10: Phase executional input Parameters

Phases	ITS	ALWERR	THET	TIMLD	DTIMLD	STEP	MAXDIS *	DEPSALLOW *
Phase 1(A) & 1(B): Initial K0 state	100	0.001	0.51	1e ⁵ s	1e ⁵ s	1	0.05 m	0.01
Phase 2(A) & 2(B): Initial drained unloading state	100	0.001	0.51	1e ⁵ s	200 s	502	0.5 m	0.01
Phase 2(C): Fluid activation phase	100	0.001	0.51	1e ⁵ s	1e ⁵ s	1	0.05 m	0.01
Phase 3(A), 3(B) & 3(C): Dredging phase	100	0.005	0.51	100 s	0.1 s	1001	0.8 m	0.02

*The limits are set based on soil response in the program, thus excluding water.

Where, ITS – Max. no. of allowed MNR iteration
ALWERR – Allowable relative error
THET – Parameter θ
TIMLD – Total time of loading
DTIMLD – Time step

DEPSALLOW – Allowable strain increment
MAXDIS – Maximum allowable displacement
DEPSALLOW – Allowable max. strain increment
MAXDIS – Maximum allowable displacement

From the above table 3.10 it can be noted that the maximum allowable displacements in Phases 2(A) and 2(B) have been increased as compared to Phases 1(A), 1(B) and 2(C). This is due to the applied drained unloading in the former cases, which may lead to certain amounts of displacements in soil. However, it is not expected for the displacement in these phases to go up to 0.5m.

Further, since Phases 3(A), (B) and (C) are dynamic loading phases which are expected to produce large displacements and strains, the maximum displacement limit has been opted to be higher. Additionally, knowing that convergence of incremental loading might take longer times, the parameters such as: allowable error and strain increment have been slightly relaxed as compared to the earlier phases, so to attain faster convergence.

3.7.4 Phase execution

Run Analysis – Figure 3.13 illustrates the flow chart of steps and files executed in order to run the analysis by means of Modified_Dyn_mlk4.f95 for all Cases.

From the figure 3.13, it can be noticed that for the 1st phase of the analysis the modified program uses two sets of files as input: a) ‘.dat’ type file, which stores the data for the material parameters, loading and boundary conditions, b) ‘.msh’ type file, which stores the mesh file data. Following this phase of analysis the main output files that are generated and readily used are of; firstly, ‘.res’ type file, which stores all type of results of the analysis, such as nodal displacements, effective stress tensor, pore water pressure etc. Second important type of output file is ‘.rex’ file, in the program this has been referred to as restart file with output data. More, specifically this file contains all the relevant stress state data after the analysis, which therefore required as restart file for subsequent phases. In this way, step wise phase analysis can be carried out where for each new phase the stress state gets updated based on the previous phase results. Further, in order to execute the ‘.rex’ file for the

subsequent analysis as illustrated in the above figures, the file is needed to be converted in '.rin' file, which stands for restart input file in the code.

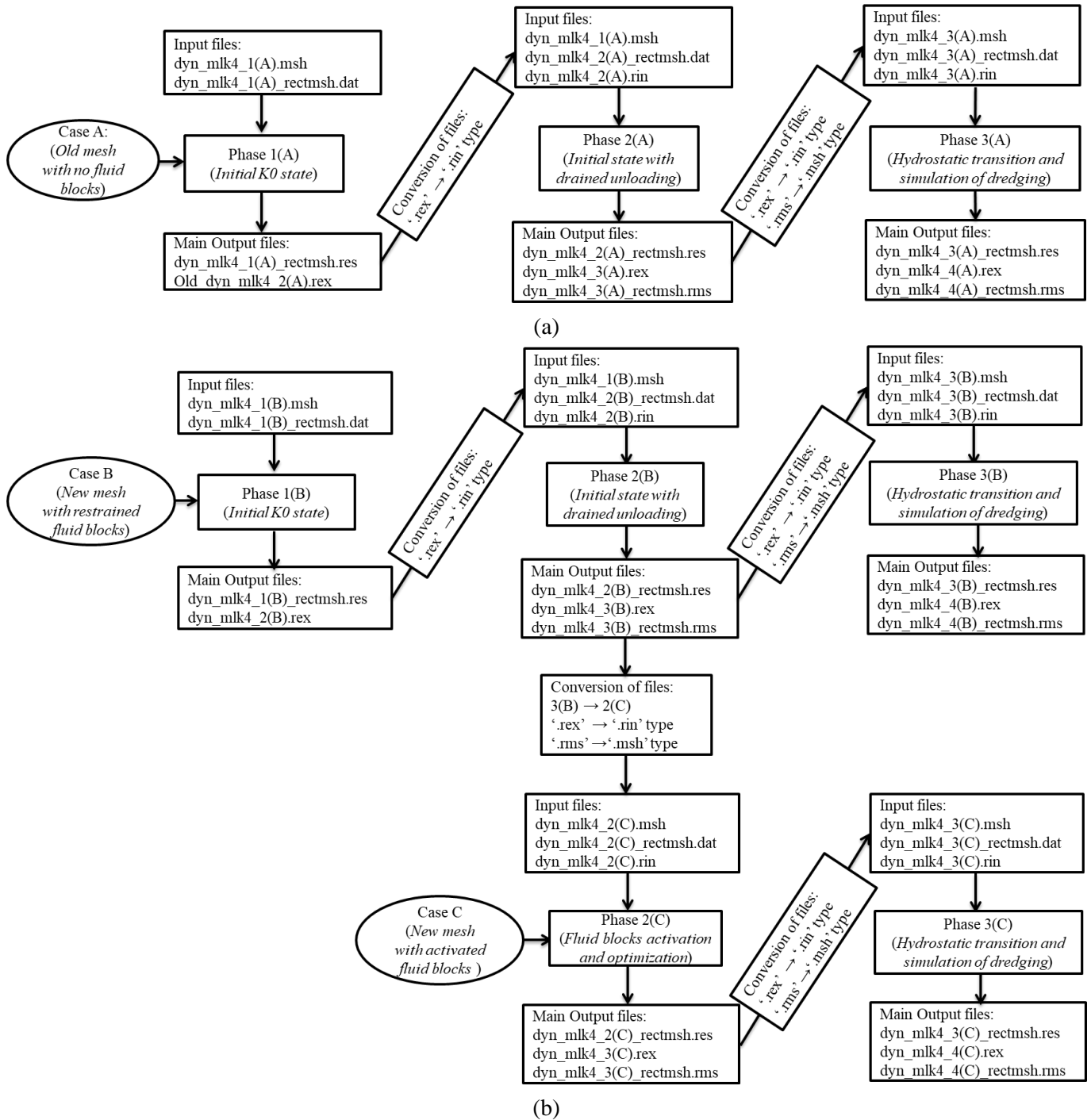


Figure 3.13: Flow Chart to execute analysis – a) Case A; b) Cases B & C

Moving on, the subsequent phases, 2(A) & 2(B) for cases A and B, are carried out in a similar fashion as phase-1. For this, the only addition to the input files is of '.rin' type file, in order to update the stress state before the calculation begins. Similarly, in the output files '.rms' type of file has been generated additionally to the result and restart output files. This, '.rms' type of file has been referred to as updated deform mesh in the program and it is used in similar fashion as the '.rex' file, since this contains the mesh data with updated displaced nodal data. Further, again similar to the '.rex' file this

file type is changed to '.msh' for subsequent phase calculations. Here it is important to mention that in case of aforementioned phases, the input mesh used was the same as used in phase 1. This is because phase -1 is a K_0 state, which does not involve any kind of deformation in the mesh. However, after phases 2(A) and 2(B), the following phases used updated meshes only, as the input file.

Saying this, phases 3(A) and 3(B) were run with a similar pattern as phases 2(A) and 2(B), respectively, the only difference as explained before is that these phases used an updated '.msh' type file obtained by converting the '.rms' file from the respective previous phases.

Finally, the execution steps of Case C can be observed from figure 3.13(b). It can be seen that the initial two phases of this case follow those from Case B i.e. phase 1(B) and 2(B). However, as mentioned before in section 3.6, this case involves an extra phase, which basically activates the fluid material blocks. This activation phase is represented by Phase 2(C) and moreover the analysis of this phase follows the same pattern as applied for phases 3(A) and 3(B), thus using updated mesh ('.msh' type file) and updated stress state file ('.rin' type file) follow from the Phase 2(B) analysis. Ultimately, Phase (3C) is also run using a similar pattern as applied in the previous phase, with updated mesh and stress state files.

It is to be noted that these data, mesh and the result files of all the phases can be referred from the link and table B1 in appendix B. Moreover, apart from output files illustrated in the figure 3.13, the program generates a wide variety of different output files and these are listed as below:

- '.sip' type file contains data of calculated stresses and strains at integration points.
- '.scr' type file, output scratch file for input and output meshes.
- '.dip' type file contains integration points data.
- '.mat' type file contains data for type of material behaviour and restraints of integration points.
- '.lay' type file contains layer numbers and restraints of elements.
- '.porp' type file, output initial isotropic pore fluid stress
- '.esig' type file, output in-plane components of initial effective stress tensor
- '.ensg' type file, output initial effective stress component normal to plane of deformation

Post Processing Results – In order to produce post-analysis graphic illustrations of results a program main_plt.f95 developed by Molenkamp (Version – 2001, undocumented) is used. Some notable features of this code have been used, namely:

- Plotting 2D finite element mesh, with surface element, element numbering, node numbering etc.
- Plotting 2D nodal vectors, such as nodal displacements, on a finite element mesh.
- Plotting 2D tensors at integration points of finite element mesh, such as effective stress tensor.

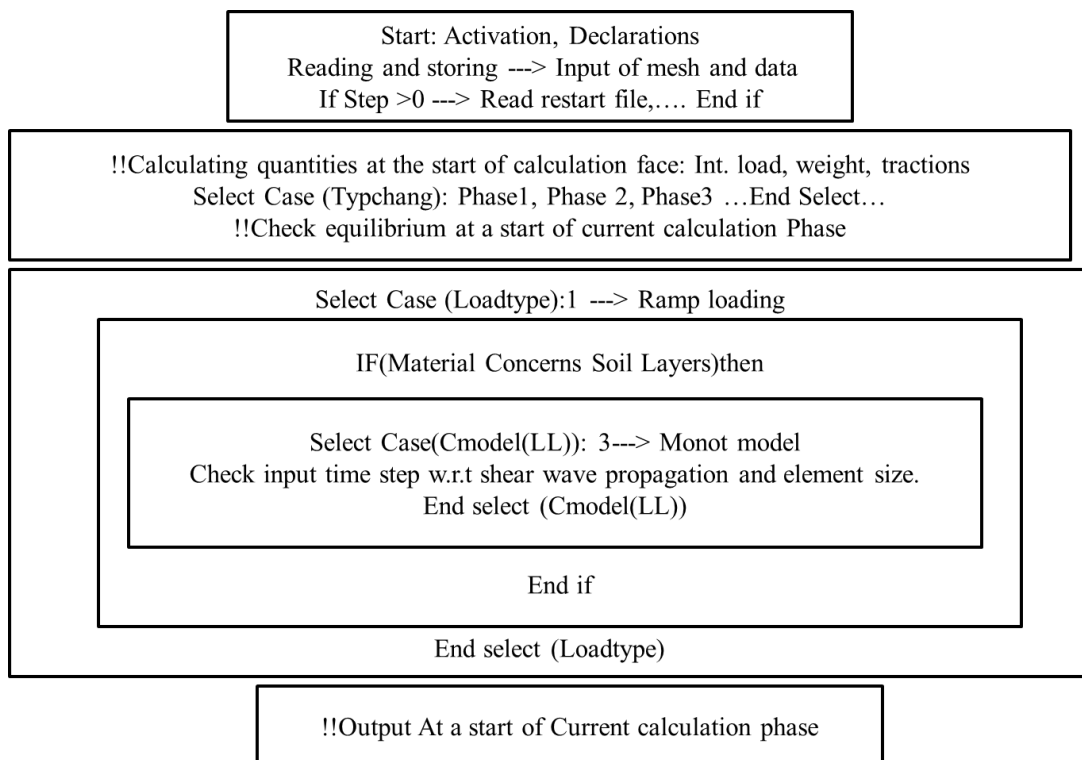
In order to use this program, for each type of result parameter plotting, the data are extracted from the result file '.res' type for the respective phase and then stored separately in '.dat' type of file. Further, apart from the result parameter data input file, this program also needs mesh file, '.msh' type, as an additional input. For the results illustrated and discussed in chapter 4, the mesh file used in these scenarios belong to the phase 1 analyses for all cases. Moreover, specifically for plotting contours of different scalar quantity the program requires another kind of file, which is of a '.mip' type file format. This type of file essential contains the mesh of integration points of the respective finite element meshes of the Cases analyzed. For the results illustrated in chapter 4, the integration point meshes of phase-1 finite element meshes, have been used.

Moreover, to generate above mentioned '.mip' file, another set of programs have been used and the whole process has been divided in two: Step –1 involves a program, known as Rev_msh.f95 developed by Molenkamp (1997, undocumented). The use of this program is to create a reverse order mesh file '.rev' type, for given finite element mesh file. This '.rev' mesh file thereafter is used in Step – 2, along with integration point file '.dip' in a program named as 'IP_mesh4.f95' to develop the final '.mip' type of integration points mesh file. The later program has been adapted from Smith (1998).

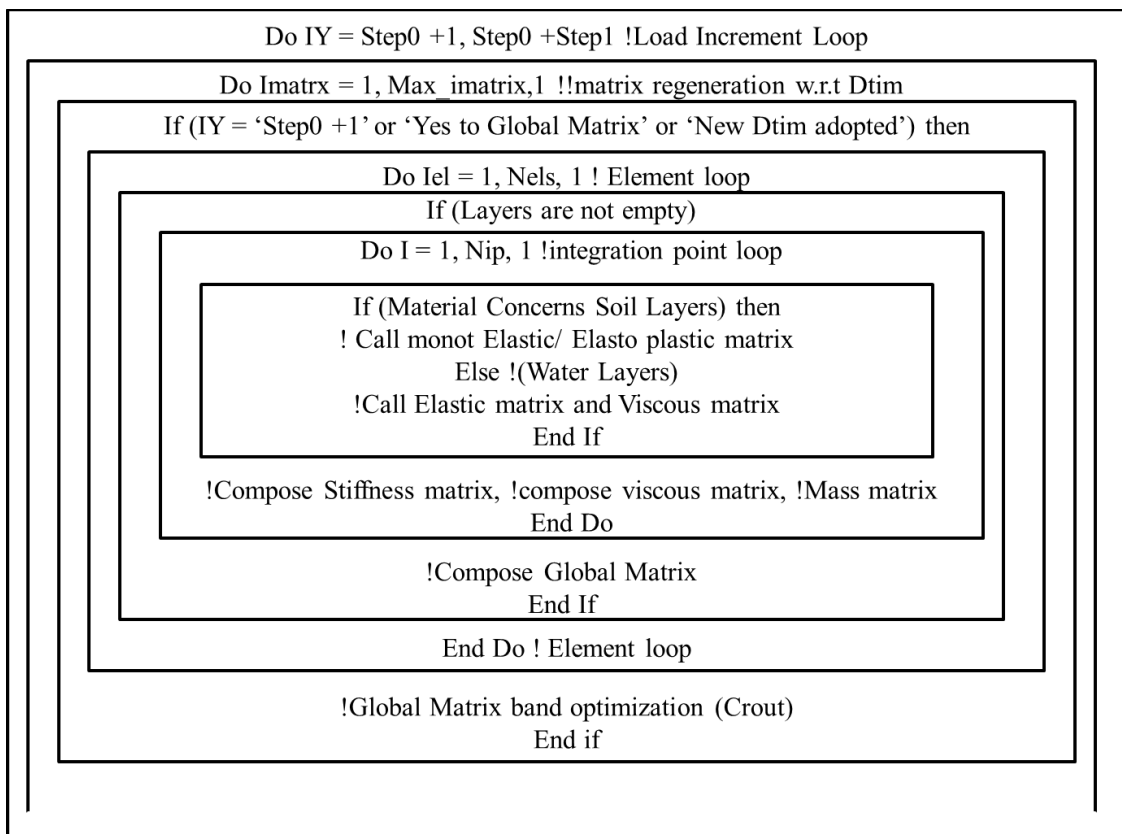
It is to be noted that in addition to 'main_plt.f95' program, for 2D colored counter plots of scalar quantities, a matlab code: 'triangulation_order3_contour', developed by Burkardt (2010) is used.

3.7.5 Overview of code functioning

Figure 3.14 shows a complete flowchart for code functioning, spread out over 3 pages.



(Contd...)



(See next page)

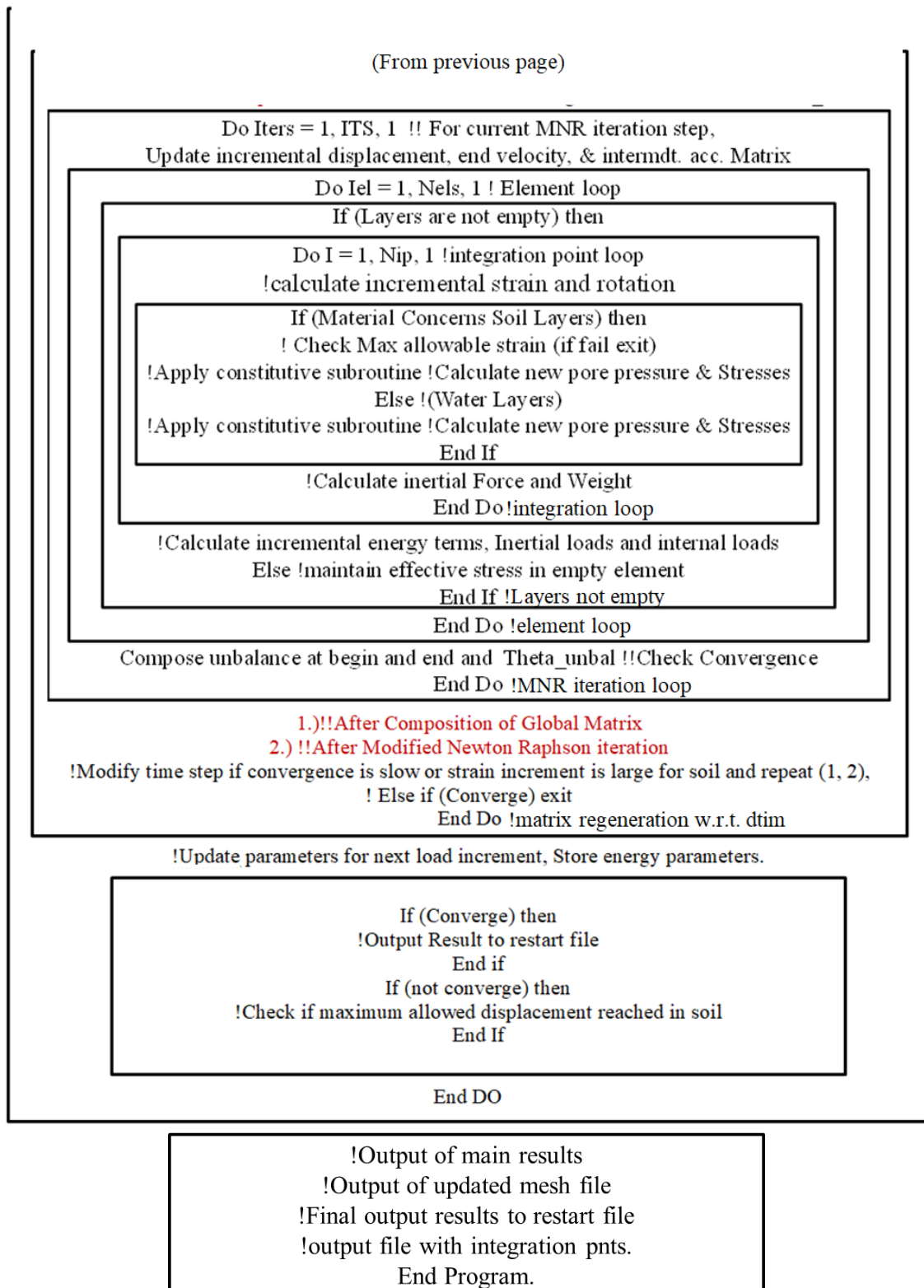


Figure 3.14: Flowchart for code functioning

3.8 Fluid tank test

In order to detect the dissipative mechanism of the numerical hydraulic model a narrow channel fluid tank test, referred from Labeur (2009), has been executed. This test is specifically used to analyze the kinematic free-surface boundary condition. The test considers the natural linear-wave mode in a basin with horizontal bottom and closed vertical walls. The practical applicability of such linearized wave mode in a basins a small wave involves the application of amplitude theory, in which the wave amplitude is assumed to be very small with respect to the wave length and depth of the basin, thus making convection and advection affects ignorable (Sorensen, 2006 and Varma, 2014).

Considering that the occurrence of natural wave modes in an enclosed basin is mainly influenced by the result of near-resonant forcing, thus numerically the accuracy of such wave mode simulation depends on the minimal artificial dissipation (Labeur, 2009).

For the closed basin with domain as: $(x, y) \in (0, L) \times (-d, 0)$, with smooth vertical side walls at $x=0$ & $x=L$, the undisturbed free surface at $y=0$ and bottom at $y=-d$, the solution to the natural wave mode in the basin for dynamic pressure head η_m is given by (Labeur, 2009):

$$\eta_m = A_m \frac{\cosh[k_m(y+d)]}{\cosh(k_m d)} \cos(k_m x) \cos(\omega_m t) \quad (3.122)$$

and the horizontal (ζ_m) and vertical (ξ_m) particle displacements are given by (Sorensen, 2006):

$$\zeta_m = -A_m \frac{\cosh[k_m(y+d)]}{\sinh(k_m d)} \sin(k_m x) \cos(\omega_m t) \quad (3.123)$$

$$\xi_m = -A_m \frac{\sinh[k_m(y+d)]}{\sinh(k_m d)} \cos(k_m x) \cos(\omega_m t) \quad (3.124)$$

where $m = 1, 2, 3, \dots$ denotes the wave mode, $k_m = m\pi / L$ is the associated wave number, ω_m is the eigen frequency and A_m is the maximum surface elevation. The solution represents a standing wave with constant amplitude. Further the frequency is related to the wave number via the dispersion relation:

$$\omega_m^2 = g k_m \tanh(k_m d) \quad (3.125)$$

3.8.1 Wave and fluid characteristics

Here the test concerns a mode $m = 1$ standing wave in a basin of dimension 10 by 10 meters filled with inviscid fluid material property having density of $\rho_f = 1000 \text{ kg/m}^3$. Considering the mode, wave number $k_1 = 0.314 \text{ rad/m}$ and natural frequency $\omega_1 = 1.751 \text{ rad/s}$ were used. Moreover, to remain consistent with the applicability of the analytical wave expression, amplitude (A_1) is opted to be very small with respect to the wave length and basin depth, i.e. 0.001m.

3.8.2 Computed test geometry and meshing

Figure 3.15 illustrates the test geometry with the meshing (refer to link and table B1 in appendix B, for the mesh files). The element arrangement and its coarseness have been kept similar to the one considered in the main submarine slope problem (see figure 3.4), i.e. a uniformly distributed bilinear quadrilaterals of 2m by 2m are subdivided into 4 linear 3 node triangular elements. Moreover, the boundary conditions used are in accordance with the analytical expression for particle displacements (i.e., eq. 3.123 and 3.124), thus are as follows:

- *Horizontal bottom layer boundary* – restrained in y direction and free in x direction
- *Vertical walls boundary* – restrained in x direction and free in y direction (see, figure 3.15).

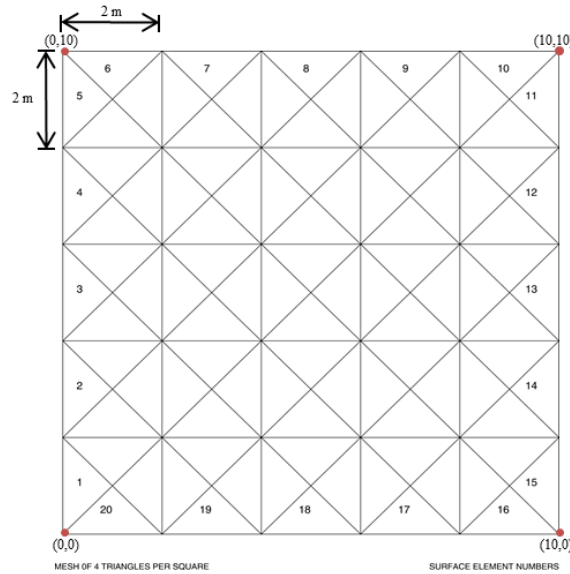


Figure 3.15: Fluid tank test geometry and meshing with surface elements numbering

3.8.3 Computed initial wave loading

In order to set an initial wave disturbance of amplitude $A_l = 0.001\text{m}$ in a computed geometry, the initial mesh co-ordinates at free surface boundary (water surface) was updated as per eq. (3.122) at $t = 0$ s. The new displaced mesh data can be referred from the link and table B1 in appendix B.

3.8.4 Fluid tank test phase execution

The test is conducted using similar phase approaches as detailed in section 3.6 for main submarine slope problem. In total 2 phases were run, details of which can be followed from below:

- *Phase I(FT): Initial K_0 state*, used for the material layers activation. In this phase an updated mesh with initial wave disturbance was used. Considering the application of updated mesh where the co-ordinate (0, 10) is been raised by 0.001m and co-ordinate (10, 10) by -0.001m, for hydrostatic stress calculation as per eq. (3.83) the water level was assumed to be at 10.001m. Therefore with this assumption in order to attain the global equilibrium an external traction boundary at upper surface is required. This traction stresses should correspond to the nodal in plane forces as per eq. (3.86). Moreover, through eq. (3.87), upper and lower limits of the total hydrostatic stress σ_{33} can be calculated on the upper free fluid surface. Table 3.11 and figure 3.16 details the same.

Table 3.11: Applied traction along the Upper free boundary surface with reference to 10.001 m water level.

Upper Limit $ x_3^{wo} $ [m]	Lower Limit $ x_3^{wo} $ [m]	Upper Limit (σ_{33}) [kN/m ²]*	Lower Limit (σ_{33}) [kN/m ²]*
0	0.002	0	-0.01962

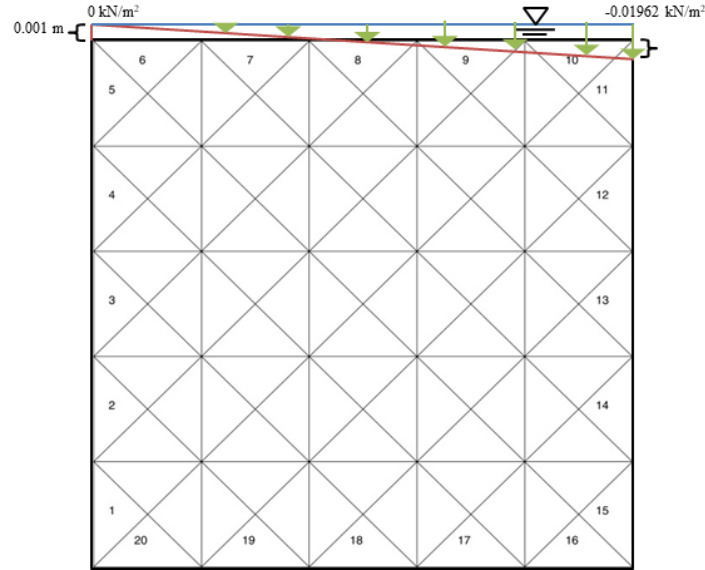


Figure 3.16: Fluid tank test geometry with indicative initial upper layer level in updated mesh (in red), assumed water level (in blue) and applied traction loading (in Green arrows). *The figure is unscaled.

- *Phase 2(FT): Unloading of traction loading*, at this phase the applied traction loading in Phase 1 is unloaded and thus the system is allowed to oscillate to an equilibrium position of a 10m water level.

Table 3.12 illustrates the controlling parameters used for both the phases. It is to be noted that two different sets of values of allowable error and time step were used for Phase 2, in order to evaluate the sensitivity of the numerical model.

Table 3.12: Fluid tank test controlling parameters

Phase	Max. iterations per time step (ITS)	Allowable error (ALWERR)	Theta (θ)	Time of loading [s] (TIMLD)	Time step (DTIMLD)	Total steps	Steps per cycle
Phase 1(FT)	100	1e-9	0.5	0.01	0.01	1	-
Phase 2(FT)_1*	100	0.005	0.5	0	0.04	275	90
Phase 2(FT)_2	100	1e-14	0.5	0	0.005	2200	718

* Controlling parameter values in proportion with that of dredging phase 3 of the main submarine slope model.

The first set of values complies with dredging phase 3 of the main submarine slope model. Thus, the allowable error opted here is the same as in dredging phase 3 i.e. 0.005. However, to select a time step, considering the relative dimensioning of submarine slope model and fluid tank test, it was proportionally reduced from 0.1s in dredging phase 3 to 0.04s in the current test. This proportionality has been done on the bases of natural wave frequencies, considering that the maximum water depth in the main submarine slope problem (d) is 15.5m and length (l) is 52 m, the highest natural frequency as per eq.(3.123) that will be possible for mode 1 natural wave is 0.659 rad/s. Hence, a time step of 0.1s for natural frequency of 0.659 rad/s will corresponds to 0.04 s time step for natural wave frequency of 1.751 rad/s in the current fluid tank test.

On the other hand, the second set opted in phase 2 i.e. Phase 2(FT)_2, uses considerably smaller time step i.e. 0.005s and demands high accuracy with allowable error equals to 1e-14.

Steps followed for phase execution, shown in figure 3.17, is of similar pattern used in main submarine slope problem (refer section 3.7.4).

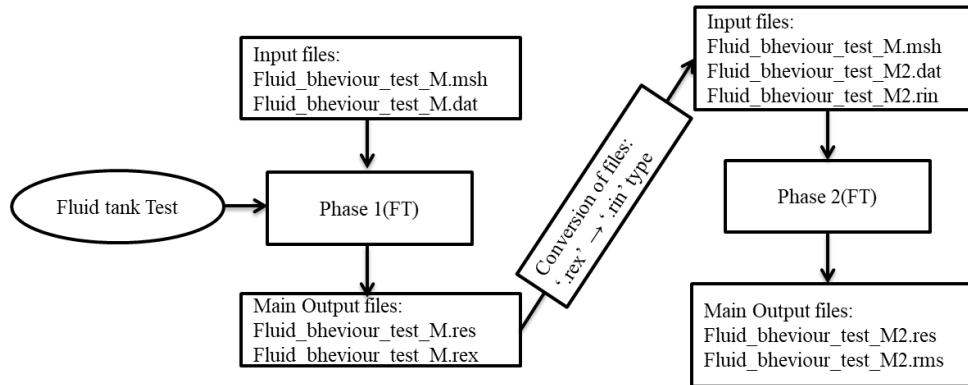


Figure 3.17: Fluid tank test, phase execution flowchart

3.8.5 Fluid tank test results

Considering that the numerical program for the main submarine slope model phase 3 dredge analyses with activated fluid layers ran for 1.5 sec (refer, section 4.3.2), the results of the fluid tank test in here mainly concerns same short duration of time range. Thus, figure 3.18 shows the exact and computed solutions of the particle displacements at $t = 1.76$ s. It is to be noted that since the model uses the Lagrangian approach, the particle displacements were the opted choice for the comparison of simulated vs analytical solution. Further, figure 3.18 consists of vector displacements, where vertical components were contoured over the horizontally displaced mesh. Moreover, the computed solution illustrated in the figure is for phase 2(FT)_1 range of controlling parameters (see, table 3.12).

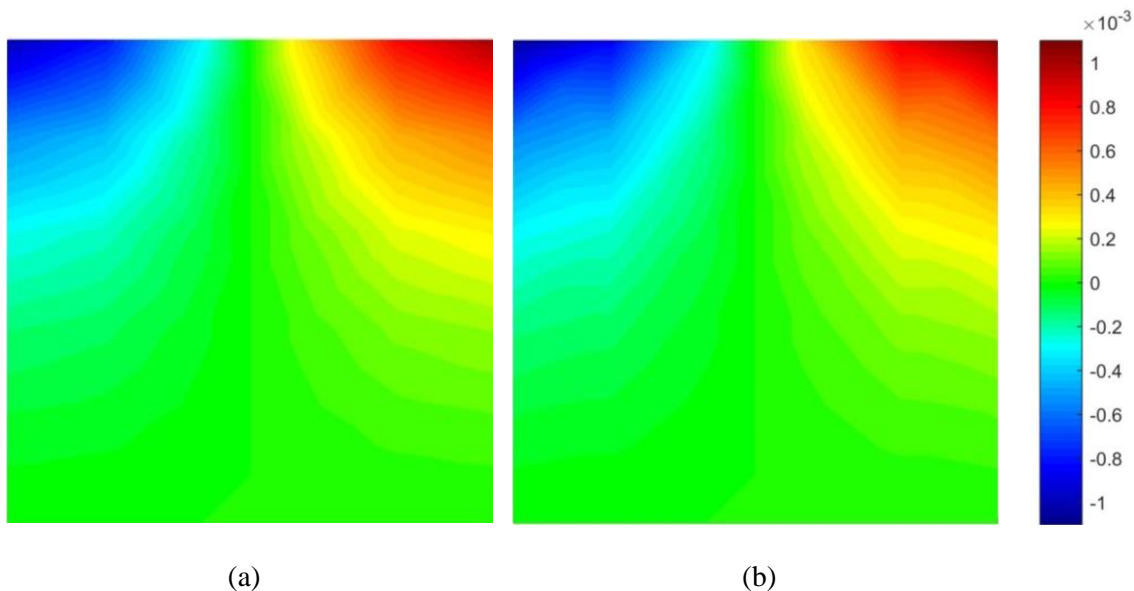


Figure 3.18: Fluid tank test, horizontally and vertically combined particle displacements contour at $T= 1.75$ s: (a) exact solution, (b) computed solution for 'Phase 2(FT)_1' i.e. 0.04 s time step and 0.005 allowable error. (Range of legend: - 0.0011 to 0.0011m)

Considering the coarseness of the mesh implemented, from the comparison of figure 3.18(a) and 3.18(b) it can be observed that the computed result is fairly similar to that of exact solution, even though some irregularities can be noticed in the fluid dissipation near the free water surface. This thus

indicates the need of further mesh refinement in order to achieve more smooth and accurate dissipation.

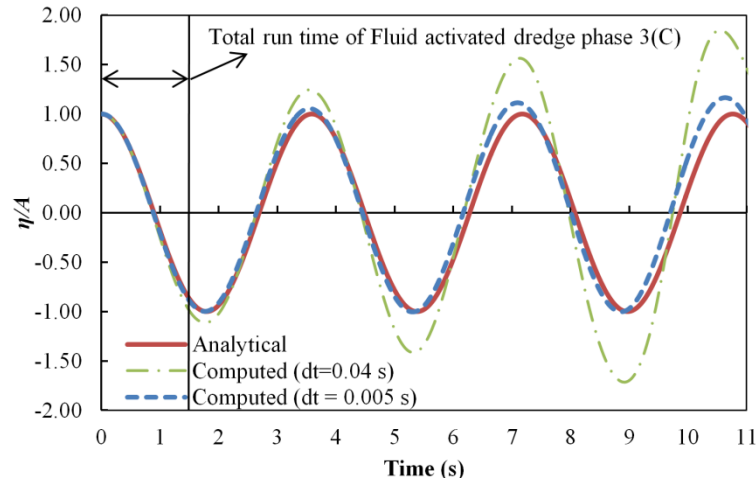


Figure 3.19: Narrow channel time series of piezo-metric level η / A at $(x, y) = (0, 10 \text{ m})$.

Further, time series of the exact and computed solution of dynamic pressure head or vertical displacement (same for the particular node) at piezo metric level (0, 10) are shown in figure 3.19. It can be observed from the figure that the computed solution using Phase 2(FT)_1 i.e. with numerical parameters that are in proportion to the one used in submarine slope model, gives fairly close results to the analytical solution for about 3 seconds of the analysis. The maximum amplitude incremental error within the range of 3 seconds is about 10% at $t = 1.76 \text{ s}$, and the phase error amounts to 1.8%. However, it can be observed that the computed solution for Phase 2(FT)_1, becomes highly destabilized for later time periods and thus shows high numerical excitation reaching up to 80% incremental error at $t = 10.5 \text{ s}$. On the other hand the computed solution, with second set of controlling parameters which uses considerably smaller time step and allowable error i.e. Phase 2(FT)_2, produces relatively accurate results, although even with this set a numerical excitation can be seen at the end of the analysis, thus indicating some numerical destabilization. Further, apart from these observations it was also noticed that using theta (θ) = 0.51 and viscosity of $1.002 \text{e-}6 \text{ kN/m}^2$, the values used in submarine slope model, shows negligible difference in computed results.

Overall, from the observations it can be concluded that the current implementation of the fluid model and set of controlling parameters used in the analysis, of the submarine slope will produce reasonable results, considering that the program runs for maximum of about 1.5 s. However, further investigation and improvement is needed for simulating wave propagation for later periods. Possible modification such as mesh refinements and reduce time step might work.

4

Results and Discussion

4.1 Introduction to results and discussion

General note: In this chapter, the results of any variable data set that are depicted on the submarine slope geometry are in reference to the initial undisturbed mesh co-ordinates. Further, most of these figures, other than those that are mentioned on nodes, are plotted at the integration point's mesh which thereby is overlapped over the slope geometry. It is to be noted that as per the current availability of post-processors the results at integration points are only *interpolated* and *not-extrapolated*. This limitation especially affects the appearance of contour plots of scalar quantities, where *the Grey colored boundary regions indicates "undefined value region"* (see ex., figure 4.3 or 4.4). Further, table 4.1 briefs the possible key discussion points attempted to be addressed simultaneously with the result observations of different cases.

Table 4.1: Key discussion points of different case sections

Sections	Cases	Key discussion points
4.2	Case A: Old mesh with no fluid blocks	<ul style="list-style-type: none">• Influence of new modified dredging mechanism on results with respect to previous model by Molenkamp (1999)
4.3	Case B: New mesh with restrained fluid blocks	<ul style="list-style-type: none">• Influence of new mesh on outcomes with respect to old mesh used in Case A
4.4	Case C: New mesh with activated fluid blocks	<ul style="list-style-type: none">• Influence of fully coupled hydrodynamic interaction with respect to Case B, which is uncoupled and assumes constant hydrostatic pressure heads at soil slope surface, due to submerging water level.• Induced motion of submerging water.

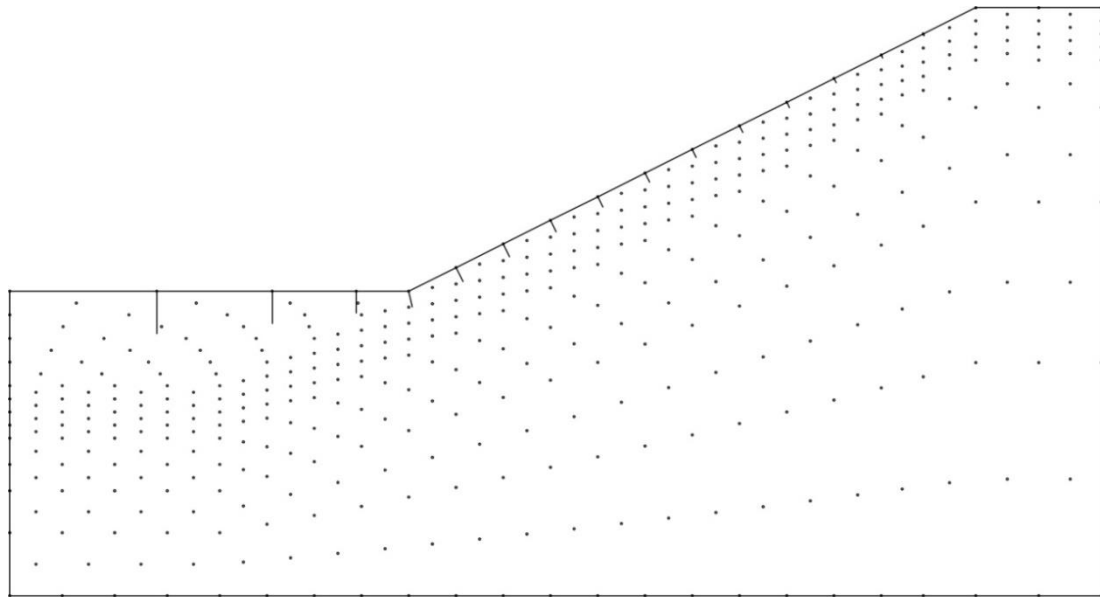
4.2 Case A results: Old mesh with no fluid blocks

4.2.1 Phase 1(A): Initial K0 state

Since this is a K0 phase and therefore does not involve any movement or external loading in the system, the results analyzed were based on three basic parameters: a) In plane effective stress tensors, b) Normal effective stress on plane of deformation and c) pore water pressure; figures 4.2 to 4.4 can be referred, respectively.

Figure 4.1 illustrates the nodal forces that have been calculated in the program at the slope surface due to the assumed water pressure level and horizontal soil level during the current phase analysis. This pressure is applied as follower type of traction loading at the free surface of soil layer, remaining constant during displacement as discussed in section 3.6. From this figure as expected, after the discretization of the applied follower type of traction load along the soil surface at the nodes, a gradual increment in nodal load as going downstream along the slope up until the toe, is observed. The maximum nodal load calculated is about 1800 kN (for unit width) which can be related to the longest

vector length in the figure, which corresponds to node number 215 (refer to figure 3.3 for node numbers). Moreover, it can be noted that the non-uniformity in nodal load distribution along the toe of the slope is due to the non-uniform distribution of the element size in the mesh. Also, it is worth mentioning that the nodal loads along the surface at the crest of the slope is less visible in the figure, since the values corresponding to these nodes are relatively small as compare to the maximum. The minimum value corresponds to the extreme right corner of the top surface i.e. node number 207, with a value of about 30 kN .



SLOPE BEFORE DREDGING OF LAST LAYER (4 TRIANGLES PER QUAD)
 NODAL LOAD BY FOLLOWER TYPE OF TRACTION AND APPLIED LOAD
 MAGNIFICATION FACTOR ON PAPER:1.0E+00

NODAL VECTORS
 MAXIMUM VECTOR LENGTH:1.8E+03
 REAL-SCALED MAGNIFICATION:8.7E+02

Figure 4.1: Follower type of nodal loads (assumed water level + soil level) for phase 1(A)

In figure 4.2 the stress tensors at the integration points of the problem geometry can be observed. The in-plane stresses in both principal axes are the same, representing isotropic conditions with $K_0 = 1$, as required. Further, it can be noted that the in-plane stresses are represented by a 45° rotational angle. It should be noted, that for an isotropic state any rotation will represent the same stress state. Further, the minimum and maximum stress levels in figure 4.2 are indicated in terms of kPa units. Moreover, from this figure it can be seen that the stress states observed is static and indeed K_0 . The straight line stress contours observed in figure 4.3 also support this observation. Moreover, from both figures (fig. 4.2 and 4.3), it can be observed that the stresses are smallest near the upper soil surface and maximum at the bottom, as expected. Additionally, the stress-state solution can be checked with the analytical solution using eq.(3.80), which suggests that for a point at the bottom the effective stress would be -274.68 kPa. This magnitude is consistent with the quantities shown in figures 4.2 and 4.3. The normal effective stress-state near the bottom in figure 4.3 is 270 kPa, which is reasonable considering the values calculated at integration points, which are slightly above the actual bottom of the problem geometry.

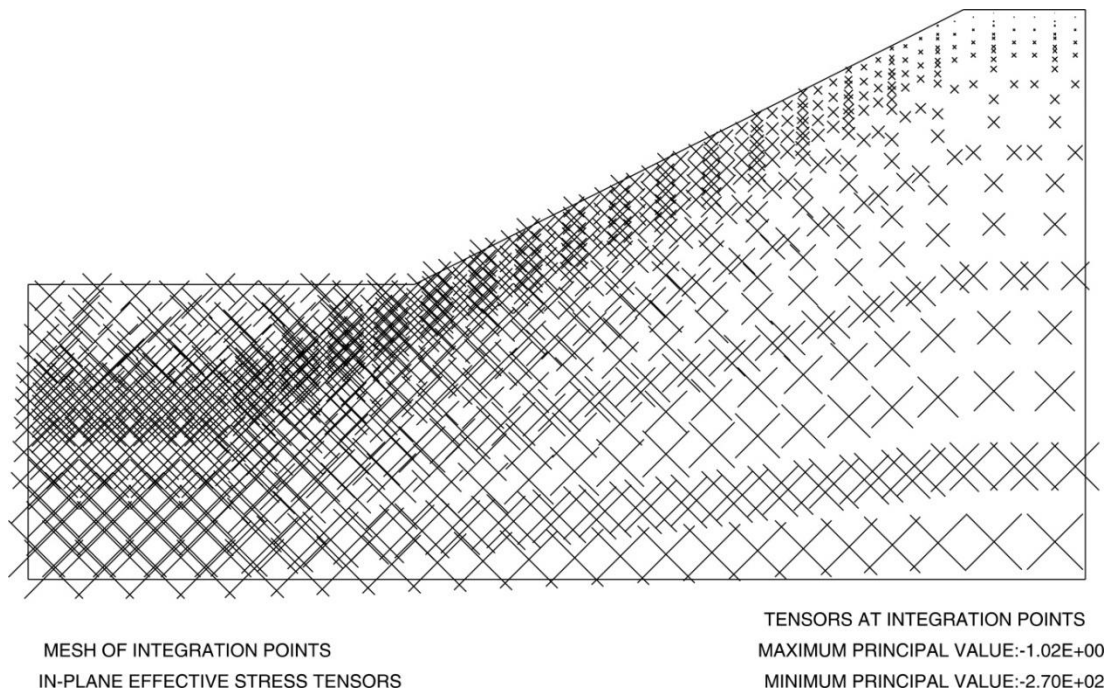


Figure 4.2: In-plane effective stress tensor for phase 1(A)

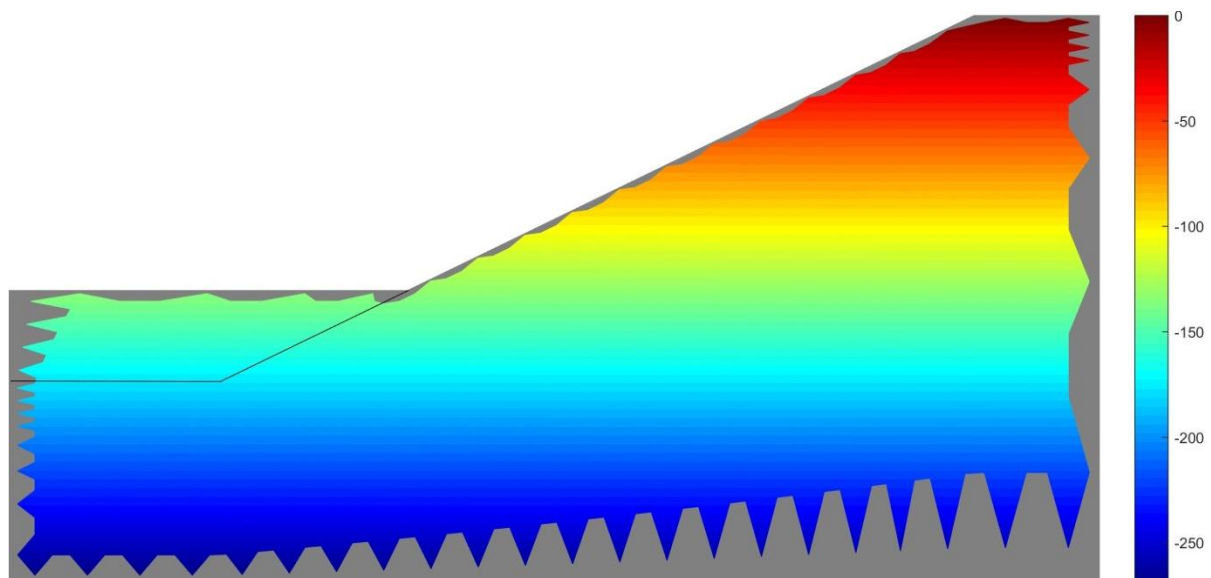


Figure 4.3: Normal effective stress on plane of deformation for phase 1(A) [Value Ranges: -270 kPa to 0 kPa]

Finally, figure 4.4 represents the pore water pressure calculated by the numerical model in this phase. From the contour pattern of pore water pressures observed it can be concluded that this is a hydrostatic drained phase analysis. Further, supporting the analytical solution from eq.(3.83), it can be observed that the pore pressures are minimum at the upper most layer of the slope, with values consistent with the applied 2m hydrostatic pressure condition on the top of the layer. Additionally, the pressures are maximum at the bottom part of the problem geometry. The contours of integration points here shows the pore water pressure to be around 290 kPa, which again is analytically reasonable considering the total depth of water assumed being 30m.

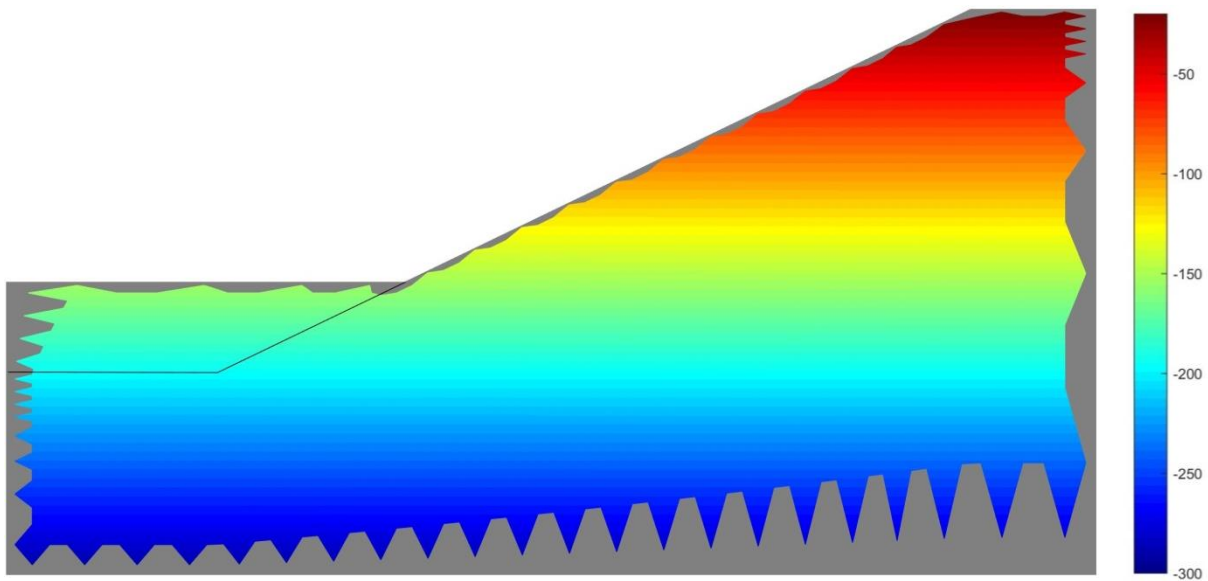
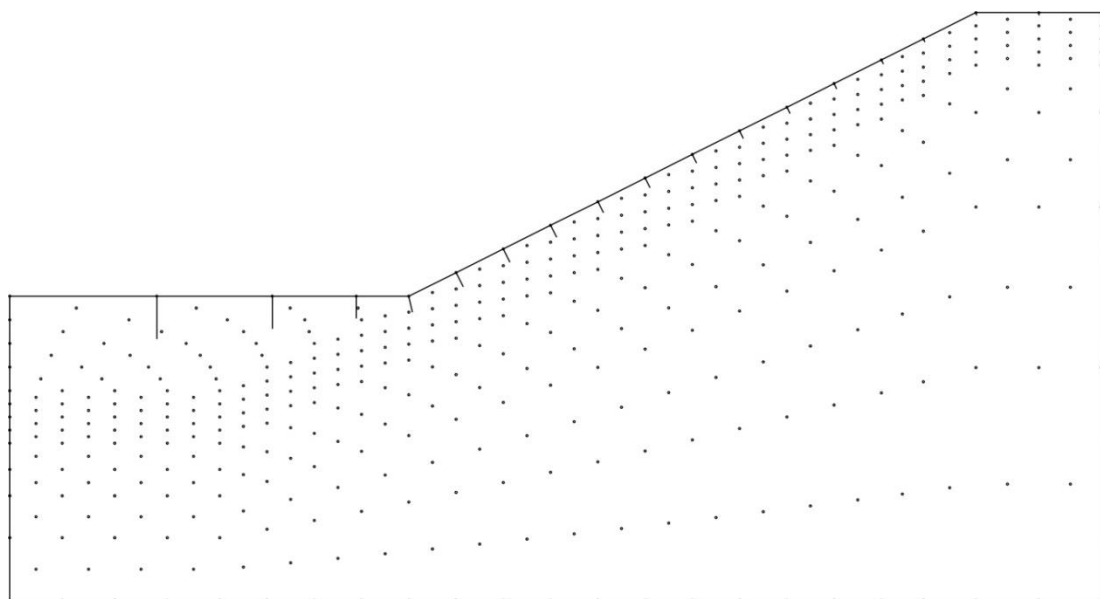


Figure 4.4: Pore water pressure for phase 1(A) [Value Ranges: -290 kPa to -20 kPa]

4.2.2 Phase 2(A): Initial state with drained unloading

In this phase the unloading of the virtually assumed initial horizontal soil layer above the slope surface is considered. Therefore starting from the quantities obtained in the previous phase an additional nodal displacement mode is analyzed.



SLOPE BEFORE DREDGING OF LAST LAYER (4 TRIANGLES PER QUAD)
 NODAL LOAD BY FOLLOWER TYPE OF TRACTION AND APPLIED LOAD
 MAGNIFICATION FACTOR ON PAPER:1.0E+00

NODAL VECTORS
 MAXIMUM VECTOR LENGTH:9.5E+02
 REAL-SCALED MAGNIFICATION:4.7E+02

Figure 4.5: Follower type of nodal loads (assumed water level only) for phase 2(A)

Figure 4.5, shows the nodal loads remaining after the removal of the virtual soil layer from the previous phase, as the follower type of loading. It can be observed from the vector lengths of the remaining nodal loads that these loads have been decreased. The maximum nodal load (represented by

longest vector length) equals 950 kN at the same nodal location as the previous phase i.e. node number 215. However, as expected, the nodal loads at the upper surface of the slope do not change since the assumed virtual loads at this boundary of the problem are only due to hydrostatic pressures of 2m of water. Thus the minimum value at node 207 remains about 30kN, which is similar as in the previous phase.

Next, figures 4.6 and 4.7, representing in plane effective stress tensor and normal effective stress contours, can be followed to observe the stress-state of the soil. From both figures it can be concluded that the overall mean effective stress has been relatively reduced, thus representing a unloaded soil state. This unloading especially impacted on the upper surfaces, as the reduction is relatively larger in that region. This observation is also supported by the nodal displacements illustrated in figure 4.8 which shows relatively higher displacements in the upper soil surface layers than in the bottom regions. Further, in figure 4.6, rotations in principal stress direction can be observed, aligning itself with direction of the displacements. Further, with the maximum principal effective tensor value of -278 kPa the pattern and the results observed at this phase are similar to what was presented by Molenkamp (1999) in his original work for the initial state (refer to figure 2.18).

Moreover, in the right mid-bottom region of figure 4.6 some unusual rotational pattern of the principal effective stress at the integration points can be observed. The same phenomenon is illustrated in the same regions in figure 4.7. These unusual patterns can be explained as due to the relative large finite elements in those regions in the concerned mesh (refer to figure 3.4). Also so-called “shear locking (Sun, 2006) may play a role. However, considering slope failure, these discrepancies occur in a region which is less relevant, thus these effects can be considered as acceptable. Also apart from this, in figure 4.7, the sharp zig-zag countering is observed instead of smooth curves due to coarseness of mesh.

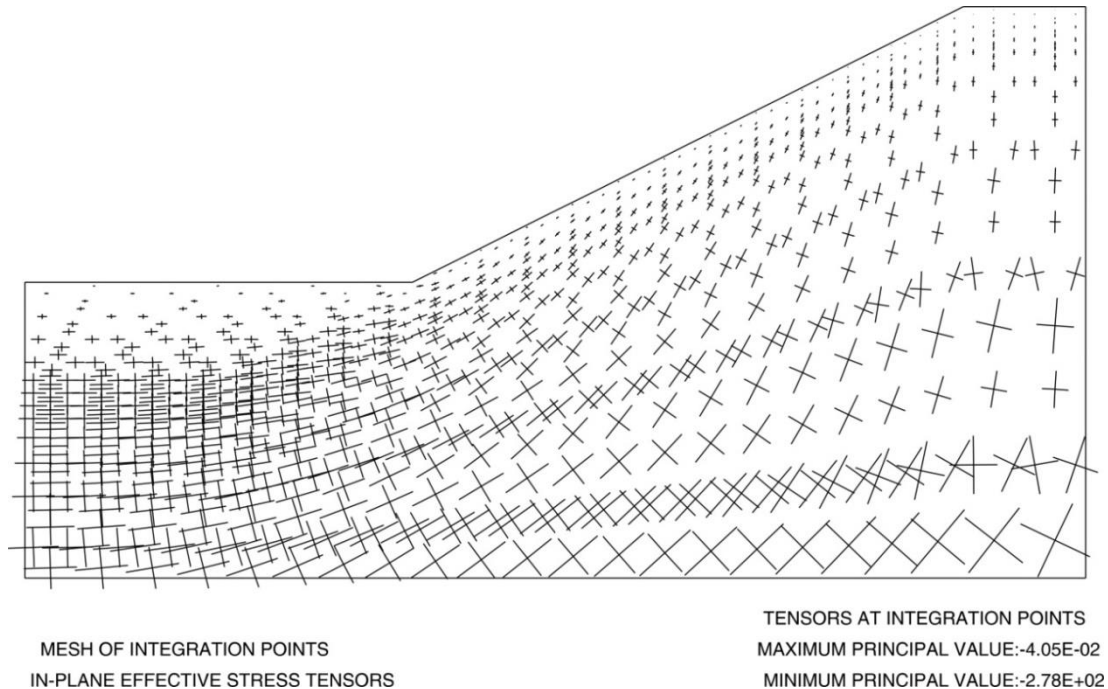


Figure 4.6: In-plane effective stress tensor for phase 2(A)

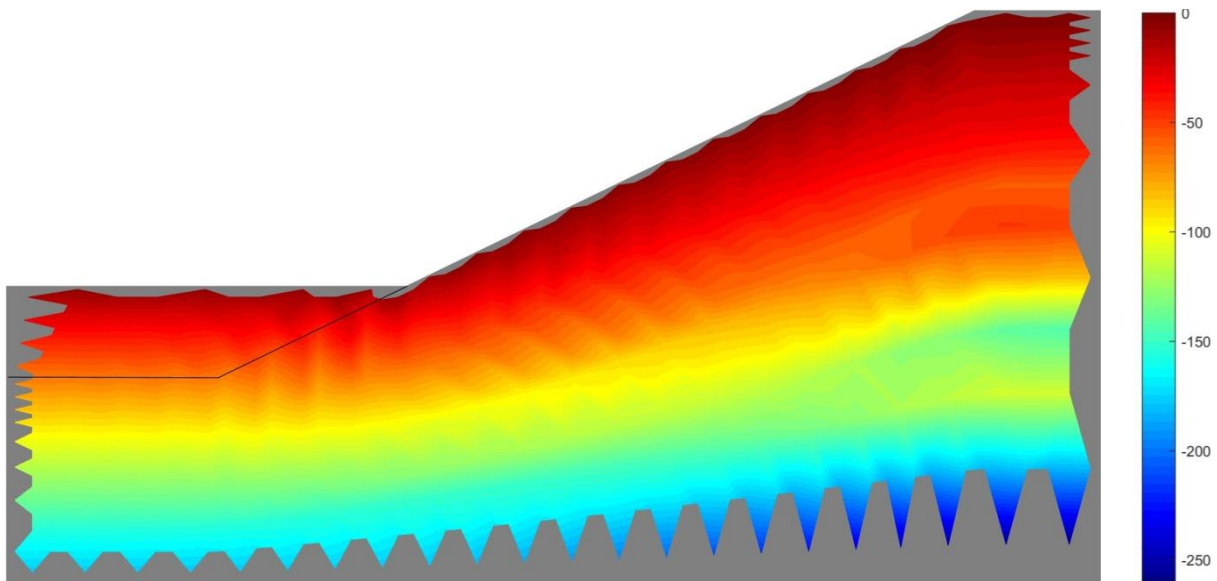
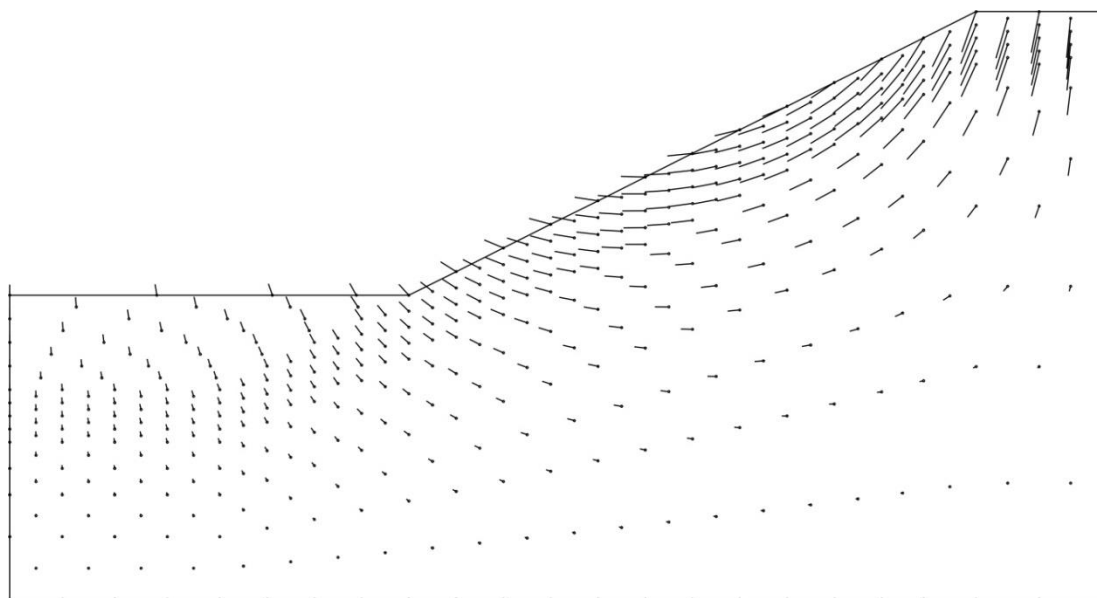


Figure 4.7: Normal effective stress on plane of deformation for phase 2(A) [Value Ranges: -259 kPa to 0 kPa]



SLOPE BEFORE DREDGING OF LAST LAYER (4 TRIANGLES PER QUAD)

NODAL DISPLACEMENTS IN LOADING PHASE

MAGNIFICATION FACTOR ON PAPER:1.0E+00

NODAL VECTORS

MAXIMUM VECTOR LENGTH:5.4E-02

REAL-SCALED MAGNIFICATION:2.6E-02

Figure 4.8: Nodal displacement for phase 2(A)

Observing figure 4.8 it can be seen, that the overall movement in the soil seems to be slightly displacing the soil materials to the left along the slope and thus moving down at the top of the slope surface and uplifting slightly at the bottom of the slope surface. Moreover, with the maximum displacement of 5.4 cm, represented by the longest vector length in the above figure, the overall displacement in the problem can still be considered as rather large, but not yet representing failure. However, contrary to previous expectations the majority of soil elements at this phase enter into a plastic state instead of remaining predominantly under elastic conditions. The Phase 2(A).mat file

addresses the soil material behavior state for each element (refer to link and table B1 in appendix B). The results in this file indicate that the effective stress state elements with maximum deformation entered into the 2nd zone of soil material behavior. This zone, as per section 3.2.1; theory on Monot soil model, represents the soil-state which accumulates both elastic and deviatoric plastic strains.

Moving on, figure 4.9 can be referred to for the results of the pore-water pressures generated. It can be observed that the hydrostatic condition is still maintained; the results being identical to that of Phase 1(A) see figure 4.4. This is expected since the analysis performed at this phase is for drained soil conditions.

Overall, given the fact that the hydrostatic condition is maintained, in addition to the results of in-plane effective stress tensors, which are comparable to what have been represented in the original work by Molenkamp (1999), the calculation at this phase can be considered as reasonable.

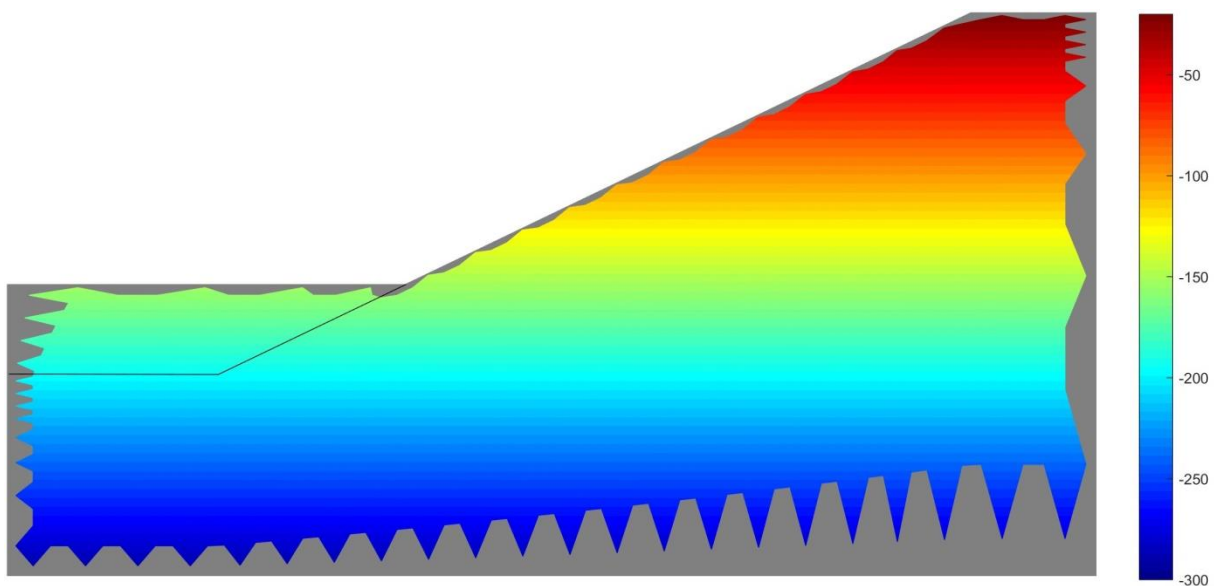


Figure 4.9: Pore water pressure for phase 2(A) [Value Ranges: -290 kPa to -20 kPa]

4.2.3 Phase 3(A): Hydrostatic transition and simulation of dredging

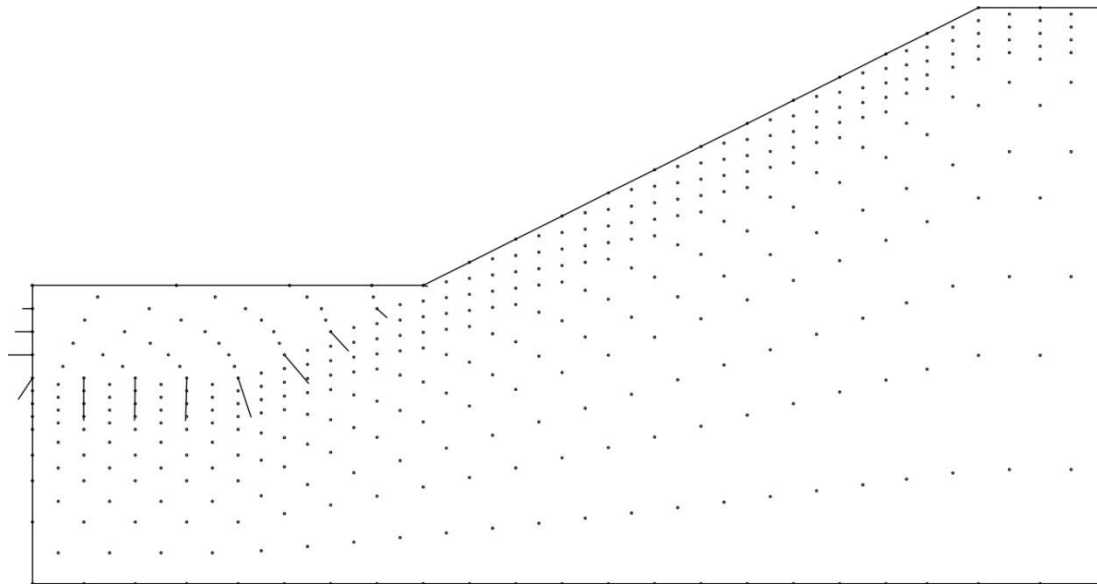
This being a dredge loading phase, where the slope failure occurs, the results analyzed in this section are based on several different quantities. Figure 4.10, shows the calculated nodal distribution of the artificially applied combined loading due to the intergranular traction forces by the dredged soil on to the non-dredged soil surface before the start of unloading. The maximum nodal load occurs at the bottom of the dredged surface.

The analysis of unloading of the above mentioned load (dredging), indicates that the slope failure occurs relatively quickly after about 1.5 sec of unloading. This observation is illustrated by means of figure 4.11 which shows the horizontal displacement of the node that is approximately at the middle of the slope surface (node: 135, see figure 3.3). Further due to the limitations related to accuracy as per eq.(3.114), the program is stopped after the end of 2 seconds.

Comparing this result with the original work by Molenkamp (1999), it can be noted that the failure occurs much earlier than according to the original work study, in which soil fails after about 22 seconds of unloading. This difference can mainly be attributed to the fact that the work by Molenkamp had a completely different unloading mechanism than developed in the current work. As it was also

observed that, even after using the old water level in the current model (as in original work, refer to figure 3.2) the time corresponding to instability remains the same

The above observation of different time responses further indicates that in the current analysis, involving uniformly unloading a large block of dredged material in one long unloading period underestimate the soil strength. To remain more realistic the layers should be smaller in size and thus enabling the remaining layers to be dredged to refrain the large soil deformation and hence to delay the failure. However, it is important to note that, given this drawback of the current unloading mechanism, it does not assure the accuracy of the old mechanism used in Molenkamp (1999), where the slope fails numerically when the remaining buoyant weight of the dredge soil approaches zero.



SLOPE BEFORE DREDGING OF LAST LAYER (4 TRIANGLES PER QUAD)
 COMBINED LOAD DUE TO DREDGING
 MAGNIFICATION FACTOR ON PAPER:1.0E+00
 NODAL VECTORS
 MAXIMUM VECTOR LENGTH:1.1E+02
 REAL-SCALED MAGNIFICATION:5.3E+01

Figure 4.10: Combined nodal loads due to dredged part of soil on non-dredge boundaries; phase 3(A)

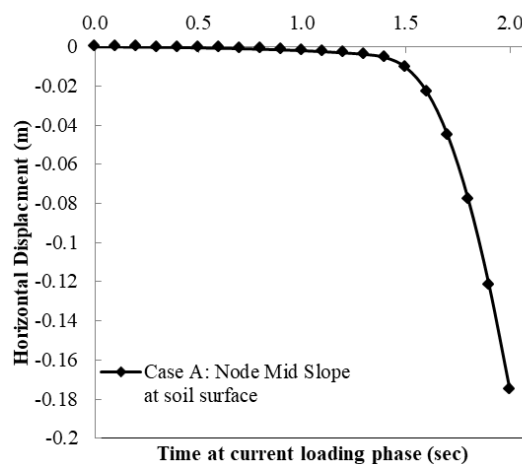


Figure 4.11: Horizontal displacement at a node midway to the slope surface for phase 3(A)

Apart from this it was observed that if the number of time steps in previous phase analysis (i.e. Phase (2A)) is increased beyond the time of loading for reaching the lower limit of ramp unloading (see figure 3.12), the failure time response in the current phase tends to get delayed a bit.

Figure 4.12, shows the slope failure time response with respect to different time steps implemented in previous Phase 2(A) analysis. From this figure it can be observed that the failure time increased to 4.6 seconds and becomes constant after 552 steps. This observation also signifies that the soil-stress state gets more strengthened after Phase 2(A) analysis, with increasing time steps beyond the time of loading.

This difference in the results occurred due to the numerical shake down of previous Phase 2(A) analysis. This is the state of numerical solution where reducing the remaining unbalanced residual error, even after achieving the full time of loading leads to considerable change in the numerical accuracy of the solution. However, after an extent the change becomes negligible and thus steady state solution is achieved. Figure D1 in appendix D, shows this transition of solution from shake down to steady state for previous Phase 2(A) analysis, in terms of horizontal displacement of a node.

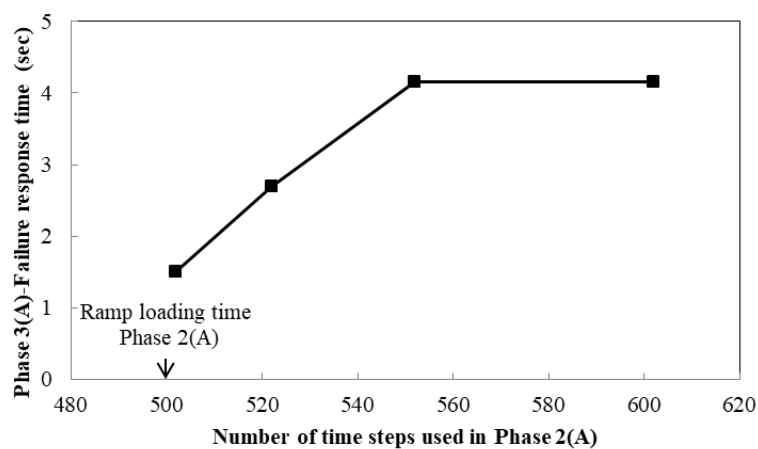


Figure 4.12: Different time steps used in phase 2(A) vs Phase 3(A) failure response (instability point)

The main purpose of this part of the analysis was to compare the outcome of the modified model with the original work by Molenkamp (1999) and therefore to conclude the differences more in all detail. Thus, with aforementioned observations it can be concluded that the differences in time of approaching failure were indeed mainly due to the change in mechanism of unloading, as discussed earlier.

However, for the current phase results, the use of originally considered 502 steps in previous phase 2(A) analysis were deemed acceptable. Since considering that the shake down affect is more critical in case of simulating realistic situations and here the model simulations are for the artificially created scenario, thus maintaining same level of error or inaccuracy in the solution will still be tolerable. Further, this will still allow to achieve the primary focus of study i.e., to evaluate the difference in the results in case of hydrodynamic coupling and also for enabling to maintain the consistency with the outcomes for the mesh used for Cases B and C.

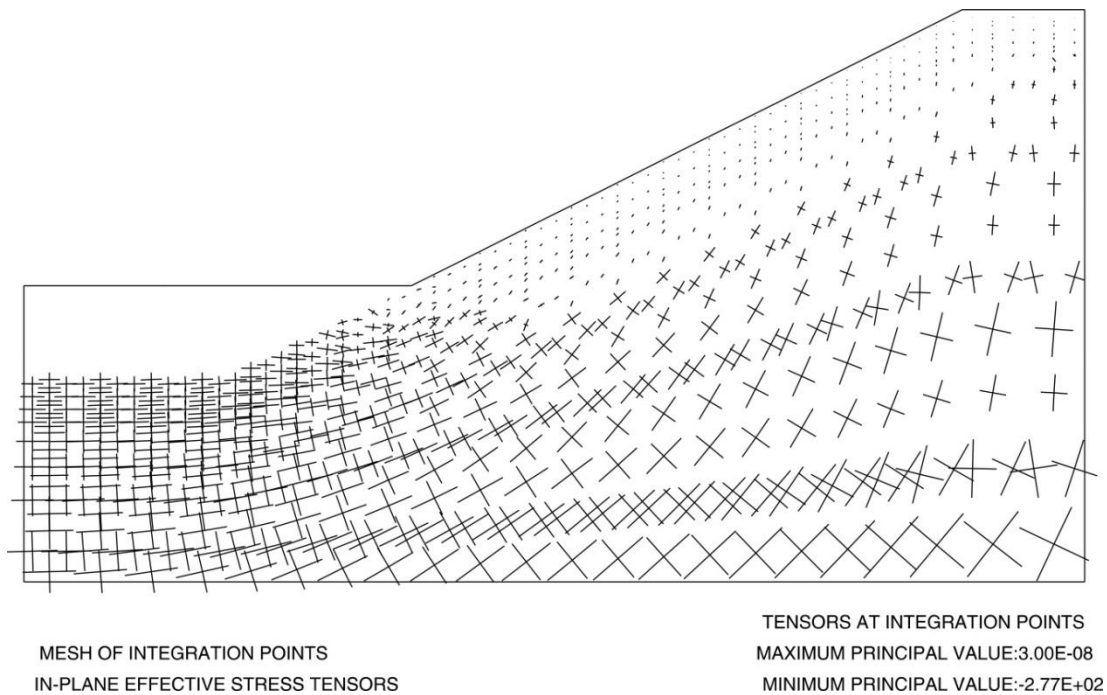


Figure 4.13: In plane effective stress tensor for phase 3(A)

Figures 4.13 and 4.14, illustrate the in-plane effective stress tensors and normal effective stresses respectively, after the end of the dredging analysis. From these figures, firstly, it can be observed that in the dredged part, which is considered to be filled with only water, no effective stresses are shown as expected. A complete loss of the effective stress tensors around slope surface region can be observed in figure 4.13, indicating a shear failure zone with soil liquefaction. However, the maximum compressive principal effective stress tensor remains the same as in Phase 2(A) i.e. -277 kPa. Similar, effects can be seen in figure 4.14, where the normal effective stresses have been drastically decreased around the slope surface due to liquefaction failure as compared to phase 2(A) results (see figure 4.7).

Further, to have a more clear insight on failure, figure 4.15 illustrates the ratio of mobilized deviatoric strength; this clearly depicts a shear failure zone with 100% of strength mobilized around the slope surface, also indicating the liquefaction of the soil. However, also a small patch of 80-98% partially mobilized strength can be observed at approximately the center of the slope surface. Moreover comparing this figure with result produced in original work by Molenkamp (1999) (see, figure 2.18), it can be said that, even though the shake down of the problem was ignored and additional 2 m higher water table has been considered in the current analysis, the patterns of mobilized shear strength in both the cases looks somewhat similar. This shows some level of consistency of the modified program with respect to the original program by Molenkamp (1999).

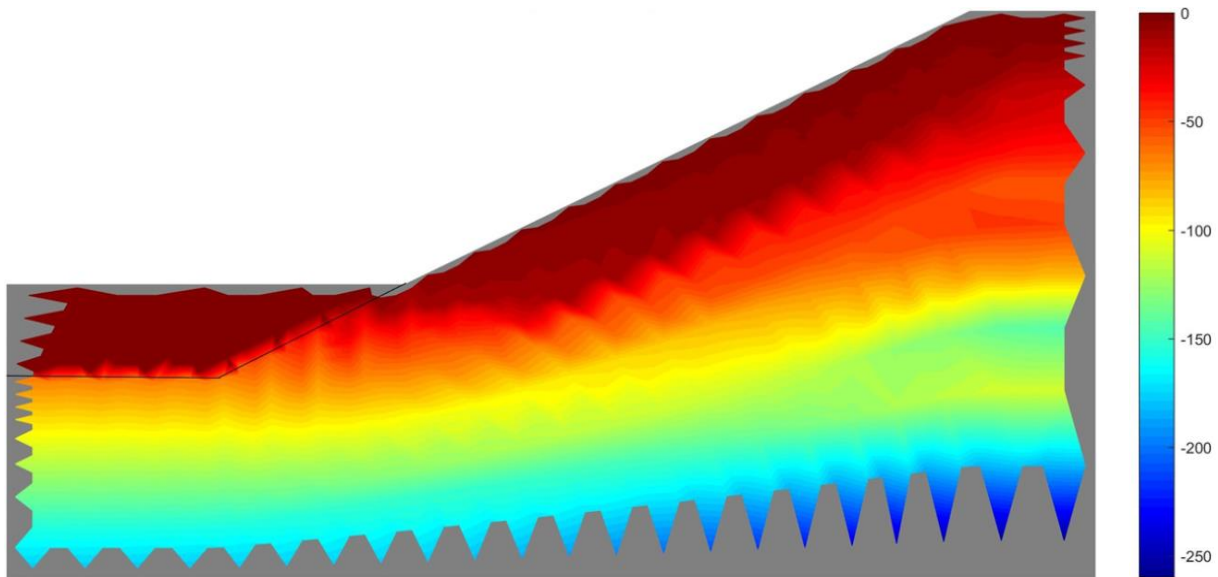


Figure 4.14: Normal effective stress on plane of deformation for phase 3(A) [Value Ranges: -259 kPa to 0 kPa]

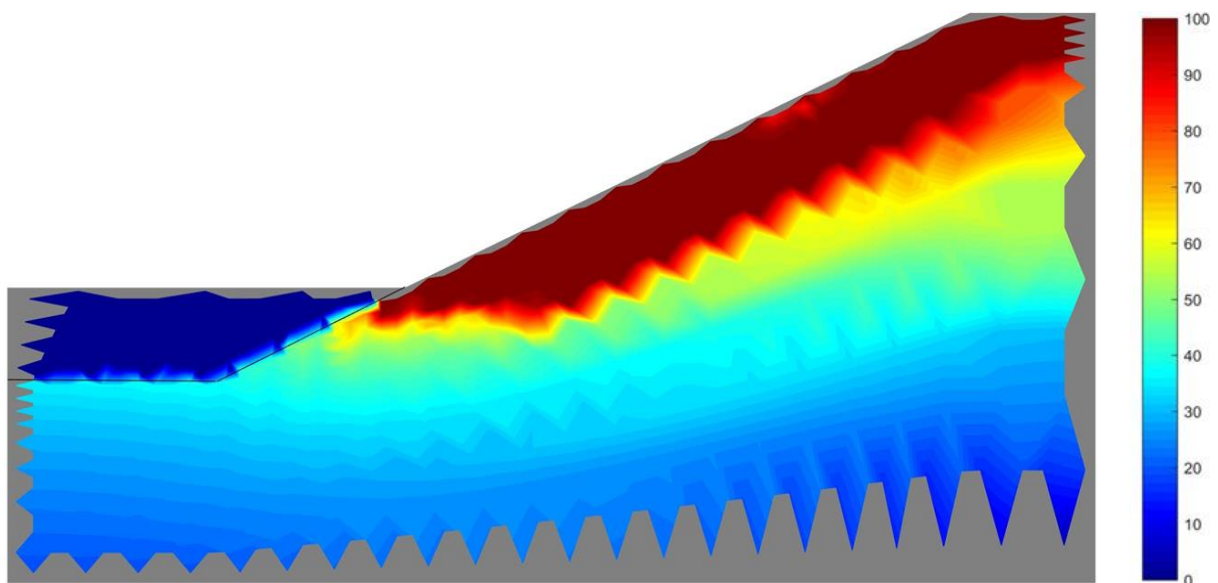


Figure 4.15: Ratio of mobilized and failure deviatoric stress Phase 3(A) [Value Ranges: 0% to 100%]

Next, figure 4.16 depicts the excess undrained pore pressure developed at the end of this phase. It can be seen that, the pressure field is mainly represented by negative excess pore pressure contours with maximum pressure being -290 kPa at the toe, suggesting contraction of the soil. However there are also some neighboring patches with positive excess pore pressures with maximum value of 240 kPa, occurring just slightly above the toe at the slope surface. These positive values suggest that locally pore water pressure is in tension, which suggests the dilatant behavior of the soil. However, this calculated strongly alternating undrained excess pore water pressure response in the wide shear zone, is due to the fact that very significant local contractions and dilations are occurring within the adjacent triangular finite elements. Considering there is no shear locking involved in this regions, it is probably occurring due to the finite element characteristics known as “hour glassing” (Sun, 2006). This is treatable by the numerical process known as “smoothing”. For the type of mesh

involved in the model, this can be done by averaging the excess pore pressure values of the triangular elements around the bilinear quadrilateral elements. However, doing this is beyond the scope of current work and thus has not been implemented, rather recommended for future works. Nevertheless, observing that the negative excess pore-pressure contours dominates the positive in figure 4.16; the average pore-pressure response of the flow slide can be expected to be contractive in nature.

Moreover, the excess pore pressure is zero in the dredge zone, which signifies no change in water pressure in that region. Thus the water pressure in the dredged part has been kept the same as shown in figure 4.9 (Phase 2A; pore water pressure).

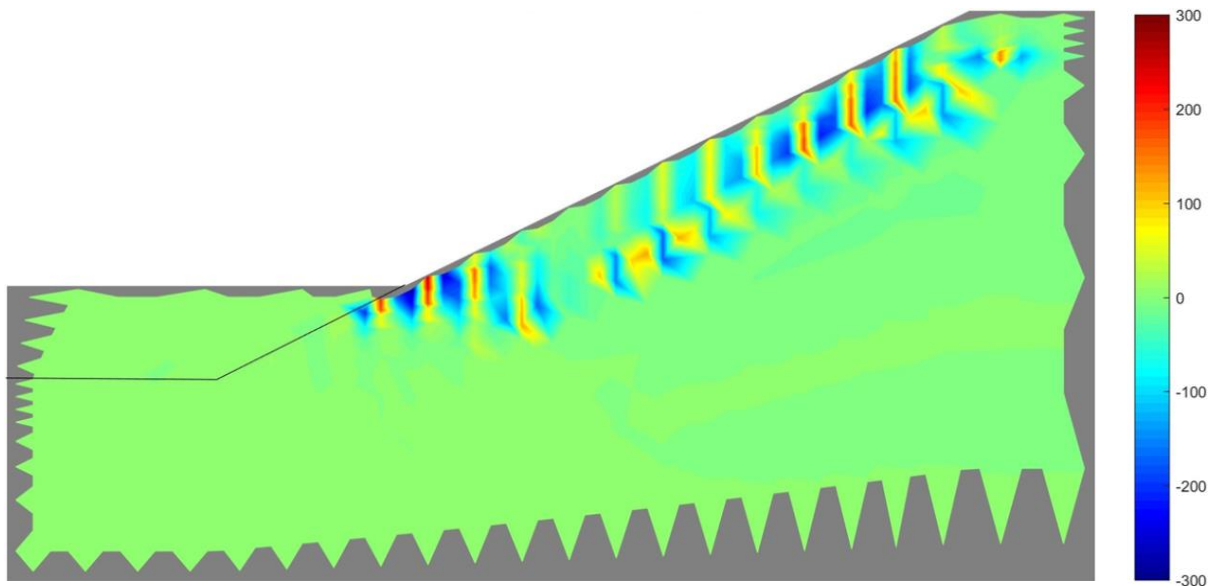
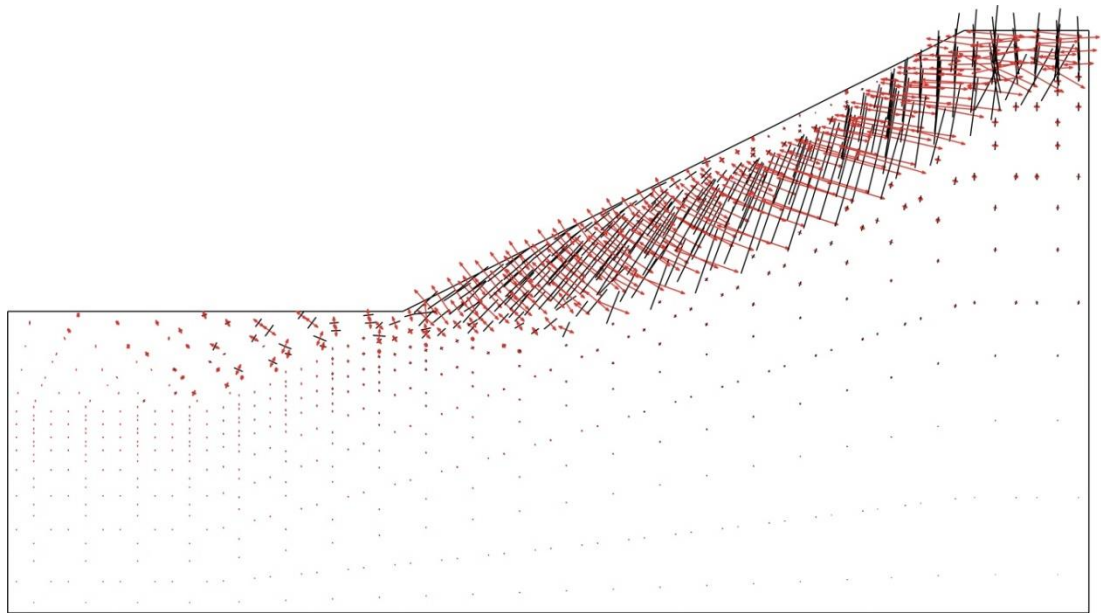


Figure 4.16: Excess pore pressure Phase 3(A) [Value Ranges: -290 kPa to 240 kPa]

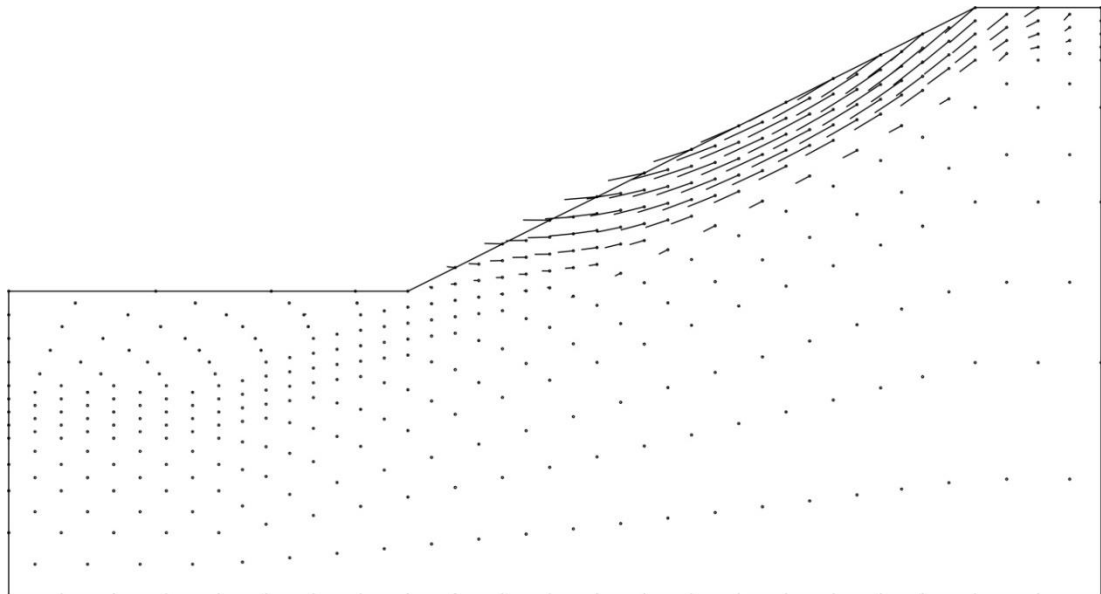
Figure 4.17 illustrates the in-plane strain tensors depicting the incremental deformations within the elements. Looking at the figure large strain tensors can be observed along the rupture zone, decreasing from there up towards the slope surface. The maximum positive tensile (red) principal strain value observed here is 0.0412 and the minimum compressible (black) principal strain is -4.24. Further, a small patch halfway the upper part of the slope surface can be observed, where the strain tensors are negligible, suggesting negligible deformations implies zero relative movements or shear. This was expected as this is the region in figure 4.15, showing a 80 – 98% ratio of the partially mobilized deviatoric stress, thus the soil in this region still retains some strength and therefore has not completely failed or collapsed/liquefied. Interestingly some small strain tensors can also be observed in the dredged water section, suggesting some relative movements of the water in these elements. However, these tensors may be influenced by the slope failure, following the type of deformation below it, therefore they are not relevant.



MESH OF INTEGRATION POINTS
IN-PLANE STRAIN TENSORS

TENSORS AT INTEGRATION POINTS
MAXIMUM PRINCIPAL VALUE:4.12E-02
MINIMUM PRINCIPAL VALUE:-4.24E-02

Figure 4.17: In-plane strain tensors phase 3(A)



SLOPE BEFORE DREDGING OF LAST LAYER (4 TRIANGLES PER QUAD)
NODAL DISPLACEMENTS IN LOADING PHASE
MAGNIFICATION FACTOR ON PAPER:1.0E+00

NODAL VECTORS
MAXIMUM VECTOR LENGTH:2.0E-01
REAL-SCALED MAGNIFICATION:9.7E-02

Figure 4.18: Nodal displacements for Phase 3(A)

The calculated nodal displacements are shown in figure 4.18. It can be seen that the maximum nodal displacement is about 20 cm. The nodal displacement vectors halfway the slope are almost parallel with the slope surface, decreasing in magnitude with increasing distance to the slope surface. This observation is consistent with the earlier description of the wide rupture zone rather than a single rupture plane. Moreover, the results pattern closely resembles the original work by Molenkamp, 1999

(refer to figure 2.18) indicating translational type of flow failure, even though the maximum displacements are different in both cases. Additionally, it should be noted that some nodes of the dredged fluid region show displacements as evident in figure 4.17 of strain tensors, however due to their relatively smaller displacements they are less visible in above figure.

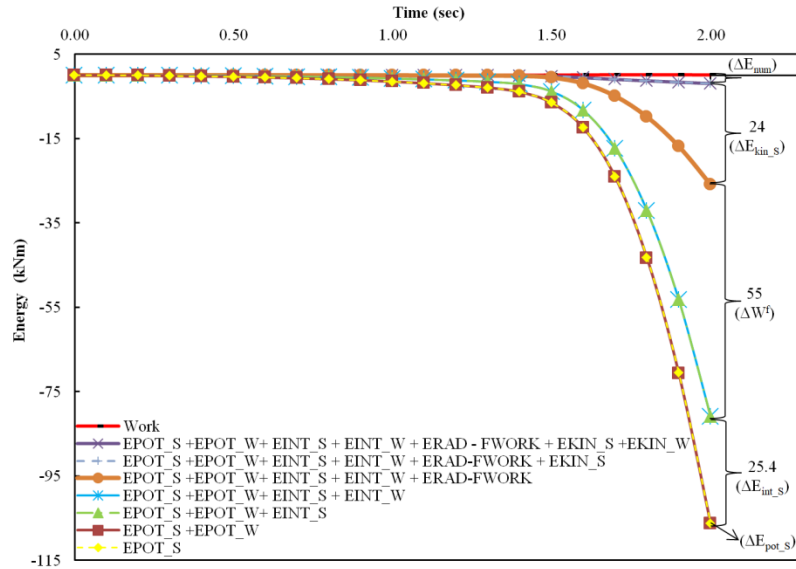


Figure 4.19: Energy transitions Phase 3(A)

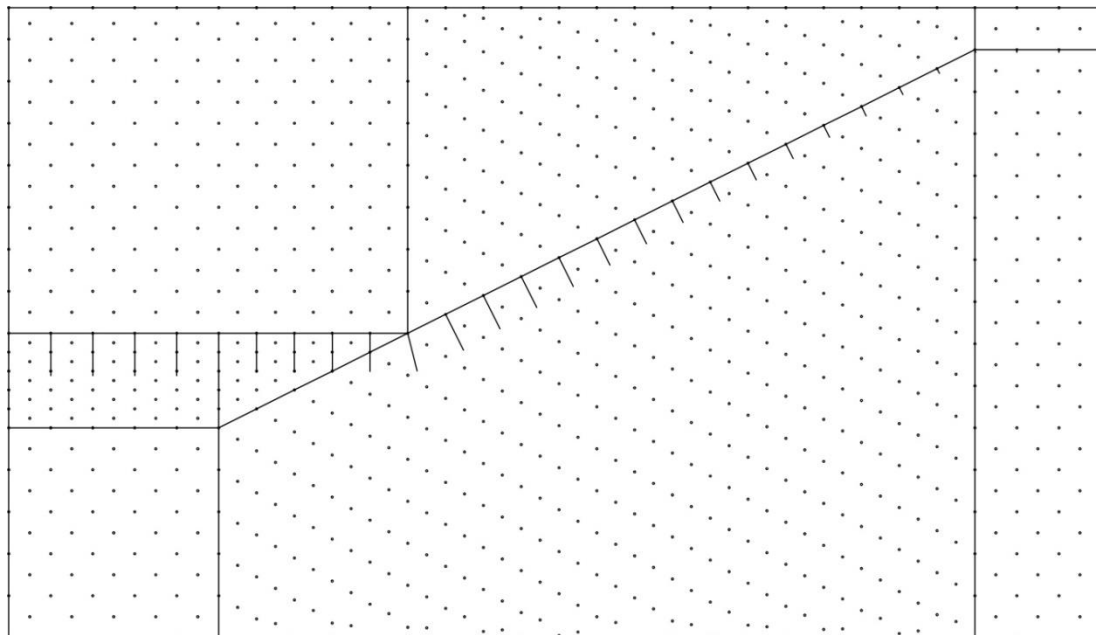
Finally, from figure 4.19, different forms of energy transitions can be distinguished. It shows the changes of the relevant forms of energy as a function of time, starting at the begin of dredging. The change of the potential energy in soil hardly decreases till about 1 sec. Thereafter the decrease rate transits from gradual to progressive, at about 1.5 sec and subsequently reaching about 107 kNm (per unit of length in the direction normal to the plane of deformation) after 2 sec, at the end of the calculations. After about 1.5 sec the soil slope failure seems to initiate liquefaction, having passed the state of undrained instability. However, it should be noted that this represents the global instability of the system; locally the instability within the elements might have started earlier.

Overall, initially two major contributing factors for the reduction of soil potential energy can be seen. The first factor is the absorption of internal energy by the soil, the ratio of mobilized soil potential energy by internal energy of the soil is about 23.87%. The second factor is the follower type of energy due to virtually applied hydrostatic loadings by the hydrostatic pressure on the slope surface. The latter one remains the major absorbing mechanism throughout the complete energy transitions with about 51.76% mobilization of potential energy of soil. Finally it can be seen from figure 4.19 that as soon as the slope state crosses passes its undrained instability, i.e. at about 1.5 sec, the kinetic energy becomes increasingly larger, indicating that the transition of the slope system has reached its dynamic phase. At the end of the calculation the contribution of the kinetic energy with respect to the mobilization of the soil potential energy is about 22.58%. The sum of all the energies percentage contributions indicate that about 1.8% of mobilized soil potential energy have been lost to numerical accuracy.

Moreover, with little movement in the dredged water region and the water pressures remaining constant, the observed water's combined potential energy line, internal stress strain energy line and kinetic energy line remain practically zero. This implies that the energy absorbed by these forms of water energies is negligible.

4.3 Case B results: New mesh with restrained fluid blocks

4.3.1 Phase 1(B): Initial K0 state



MESH OF 4 TRIANGLES PER SQUARE

NODAL LOAD BY FOLLOWER TYPE OF TRACTION AND APPLIED LOAD

MAGNIFICATION FACTOR ON PAPER:1.0E+00

NODAL VECTORS

MAXIMUM VECTOR LENGTH:5.7E+02

REAL-SCALED MAGNIFICATION:2.8E+02

Figure 4.20: Follower type of nodal loads (assumed water level + soil level) for phase 1(B)

Similar to Case A, firstly, figure 4.20 shows the nodal load distribution of virtually applied follower type of combined loadings (intergranular soil load + hydrostatic pressure head) as downward loading vectors, due to assumed overlaying soil mass and hydrostatic water conditions like in section 3.6.1. Comparing this figure with figure 4.1 of Case A, it can be observed that both load distribution patterns are similar along the slope, as expected. However, here due to the uniform mesh at the toe of the soil-slope, the nodal load distribution also appears to be uniform with the maximum value of -570 kN. It can be noted that this value is lower than the maximum observed value in case A, which can be understood to be due to the new mesh having more nodes at the bottom surface and for mesh being composed of uniform elements (refer to, figure 3.4). Further, the minimum nodal load experienced was on the upper right side node of the soil surface namely -19.62 kN, which is lower than in Case A.

It is worth mentioning here, that both the old and new meshes have different element sizes and distributions. Therefore they cannot be exactly compared on the basis of the follower type of nodal load distribution only. The results of the in-plane effective stress tensors, normal effective stresses and pore water pressures from figure 4.21 to 4.23 respectively give more clear insights into the outcomes of the current phase and thus a proper comparison with Case A.

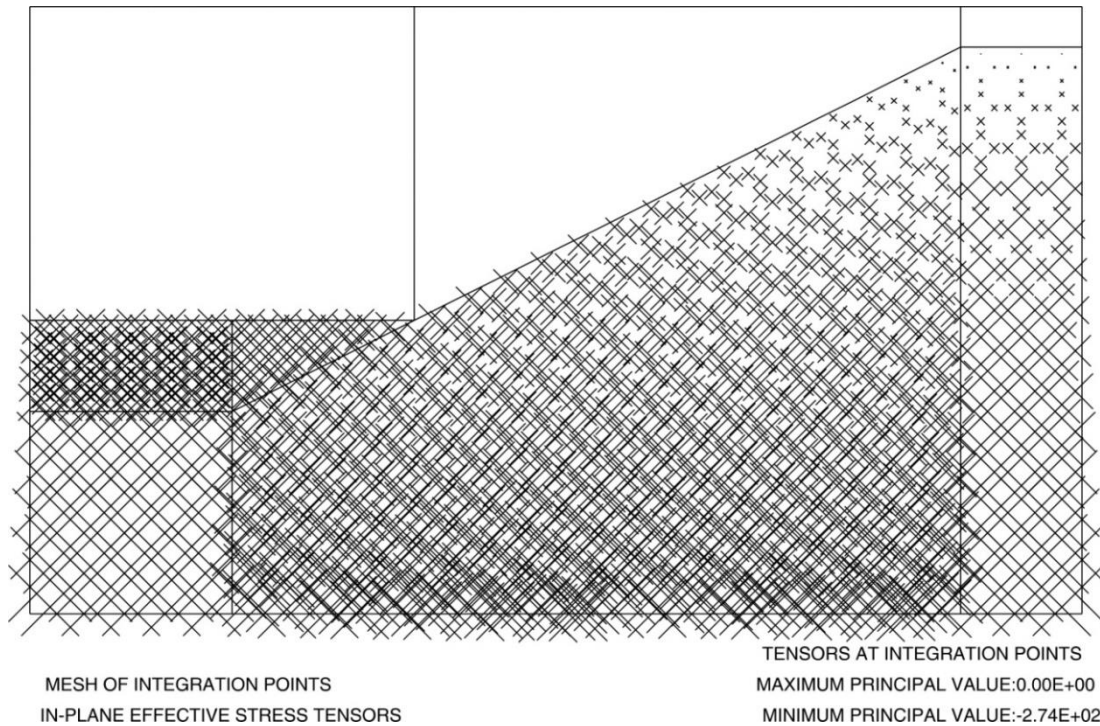


Figure 4.21: In-plane effective stress tensor for phase 1(B)

Figures 4.21 and 4.22, depict the in-plane effective stress tensors and the normal effective stresses respectively. Comparing it with figure 4.2 and figure 4.3, it can be observed that the effective stress state obtained for the current phase is quite similar to that in Case A. Apparently, the strange contour jumps observed near the soil-slope surface in figure 4.22 are due to the mesh coarseness and thus can be ignored. The stresses show the expected pattern of lowest values at the top and highest stresses at the bottom. Moreover the maximum in-plane effective stress tensor observed here is -274 kPa, which is more accurate and closer to the analytical solution as mentioned before in section 4.2.1. This value along with the slightly higher observed normal effective stress value in figure 4.22 (-280 kPa approx.) than in Case A, can again be reasoned to be due to smaller, more uniform and larger number of mesh elements at the bottom regions, thus also resulting in more accurate outcomes there.

The same reasoning can also be given for the more densely distribution of the in-plane stress tensors in the bottom region in figure 4.21. However, Case A has a more dense distribution of in-plane stress tensors along the slope region (refer to figure 4.2), where the defined element sizes are much smaller than in the current case and also uniform (see figure 3.3), which thus produces more precise static calculations at those zone.

Further, similar to case A, figure 4.21, shows that the in-plane effective stresses in both principal axes are equal owing to isotropic conditions with $K_0 = 1$. This result along with the straight line pattern observed in figure 4.22 of normal effective stresses, as expected, also indicate that the K_0 condition is maintained just like in Case A.

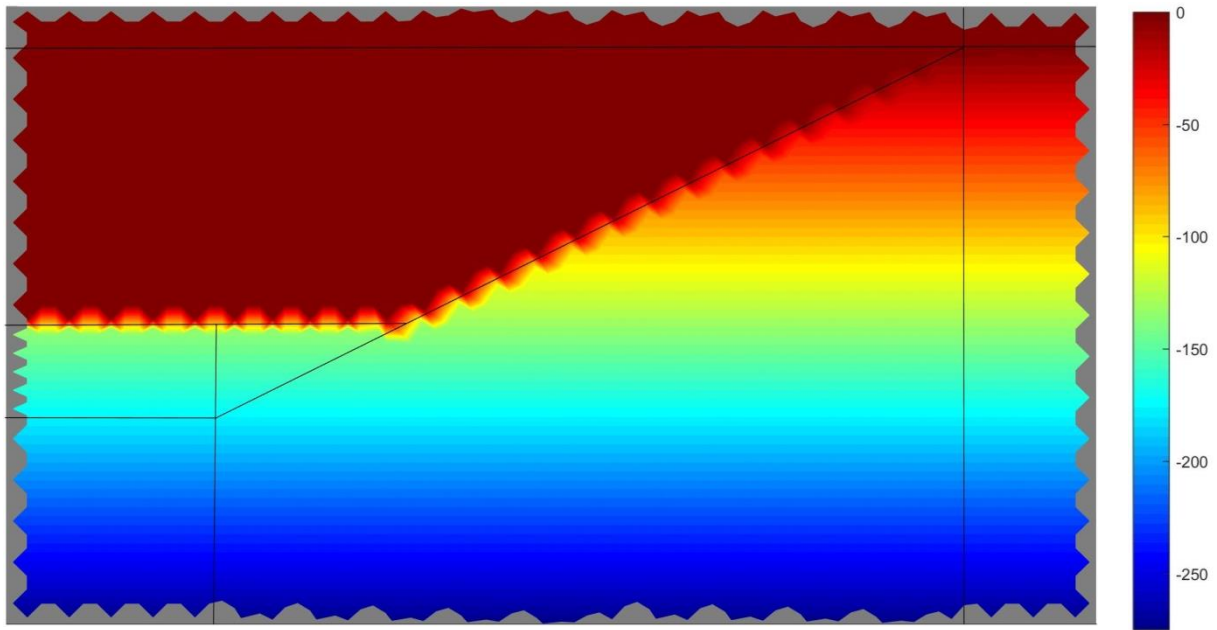


Figure 4.22: Normal effective stress on plane of deformation for phase 1(B) [Value Ranges: -280 kPa to 0 kPa]

Next the, pore water distribution is shown in figure 4.23. Again the straight line pattern observed here suggests that the hydrostatic conditions are maintained. Moreover, the pressure goes from lowest to highest at the bottom with the maximum value of -300 kPa at 30 meters of depth, thus accurately matching the analytical solution.

These outcomes suggest that the calculations are comparable and consistent with Case A and also slightly more precise in the bottom regions, owing to the smaller and uniform elements. However, due to the same reason the results produced along the soil-slope in Case A will be more accurate.

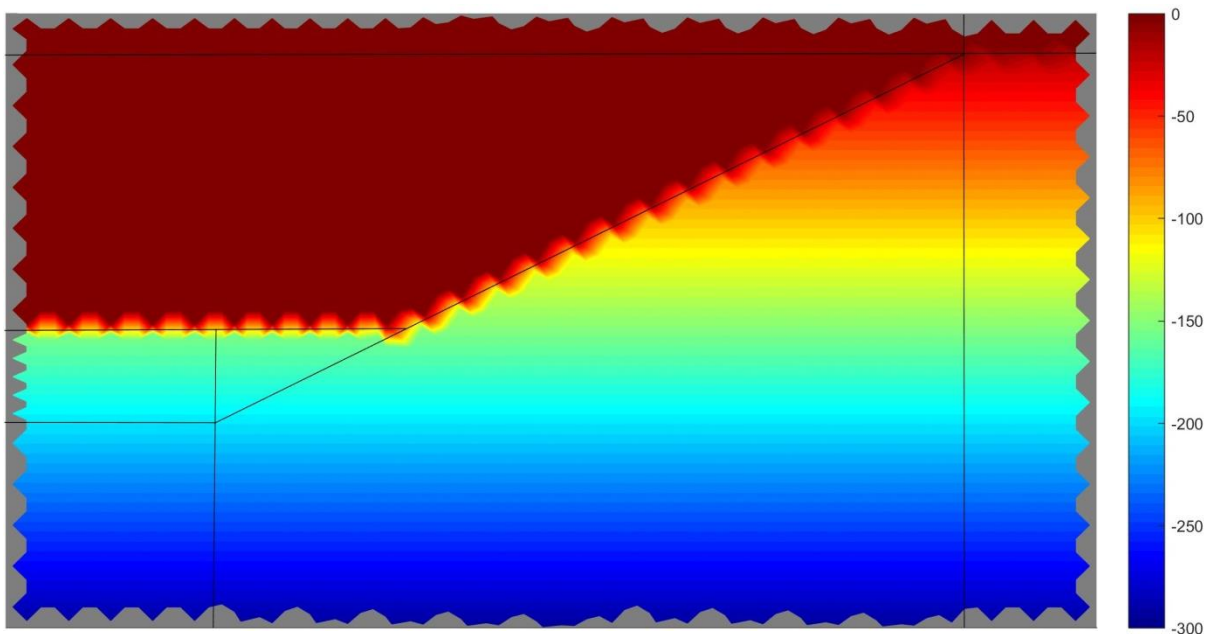
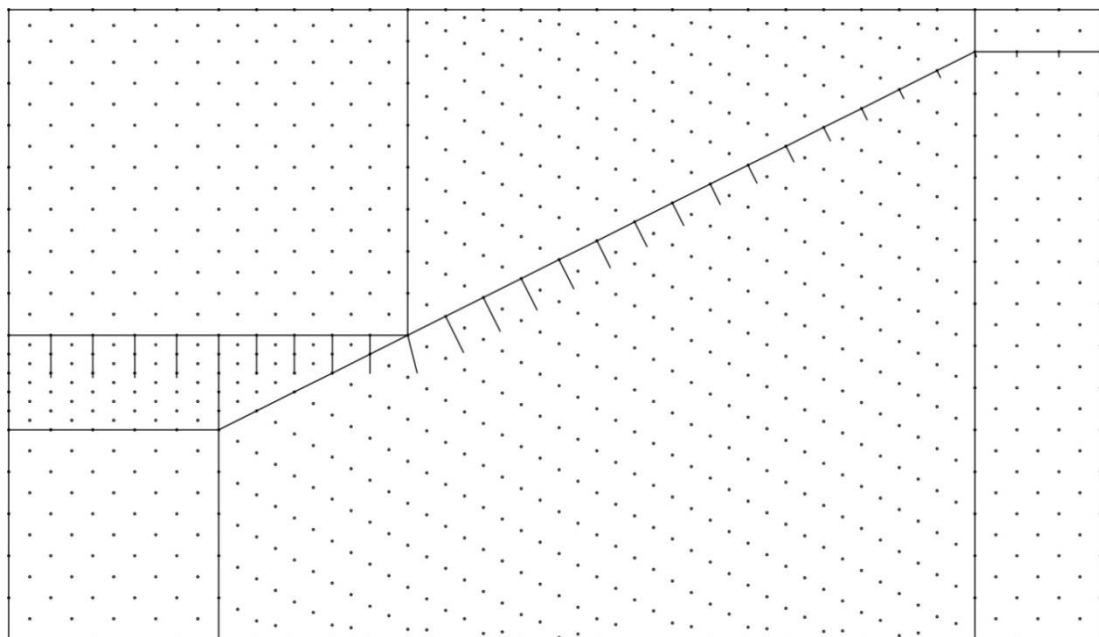


Figure 4.23: Pore water pressure for phase 1(B) [Value Ranges: -300 kPa to 0 kPa]

4.3.2 Phase 2(B): Initial state with drained unloading

This section presents the results of the unloading phase of the new mesh due to the removal of the virtually applied overlaying mass of the buoyant soil weight. Figure 4.24, shows the finally remaining nodal loads after the unloading. The maximum nodal load, remaining at the bottom of the soil-slope surface, has a longest vector length of 300 kN. Other than that, the pattern of the nodal loads remains consistent with Case A (see figure, 4.5).

Next, in figure 4.25 and 4.26 the in-plane effective stress tensors and the normal effective stress distribution are depicted. Similar to Case A, the overall effective stress of the soil has been reduced, especially near to the upper slope surface region. Figure 4.27, indicates the deformation mode of the soil slope with the crest settling with maximum magnitude, the mid-slope region moving towards the toe and the toe region swelling upward with minimum magnitude. Moreover the rotations of principal in-plane effective stress tensors also suggest that the unloading and displacement have led to the generation and accumulation of shear stresses. The normal effective stress contours in figure 4.26 along with the obtained maximum values of stress tensors and normal effective stresses i.e. -263 kPa and -252 kPa, can be considered as analogues to Case A results. It can be observed that due to the uniform distribution of mesh elements and their smaller sizes in this case, on the contrary to Case A, less irregularity effects can be observed near the right bottom corner of the soil region in both figures. Instead the rotations in figure 4.25 and contours in figure 4.26, in comparison to Case A, appear to be smoother.



MESH OF 4 TRIANGLES PER SQUARE

NODAL LOAD BY FOLLOWER TYPE OF TRACTION AND APPLIED LOAD

MAGNIFICATION FACTOR ON PAPER:1.0E+00

NODAL VECTORS

MAXIMUM VECTOR LENGTH:3.0E+02

REAL-SCALED MAGNIFICATION:1.5E+02

Figure 4.24: Follower type of nodal loads (assumed water level only) for phase 2(B)

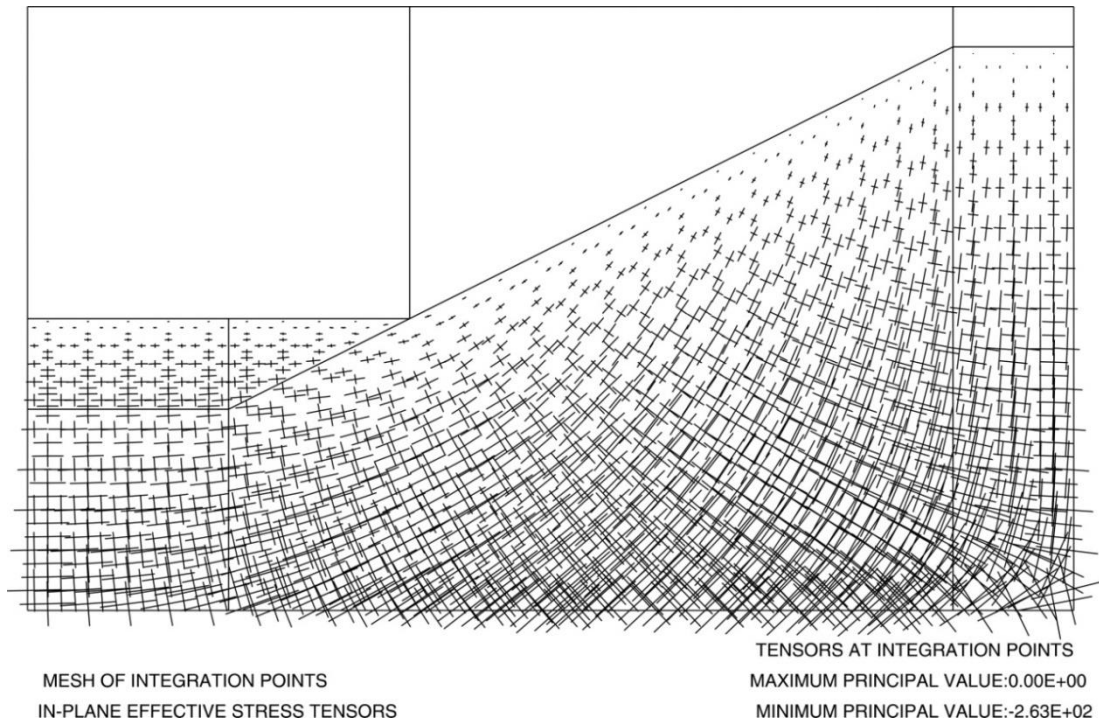


Figure 4.25: In-plane effective stress tensor for phase 2(B)

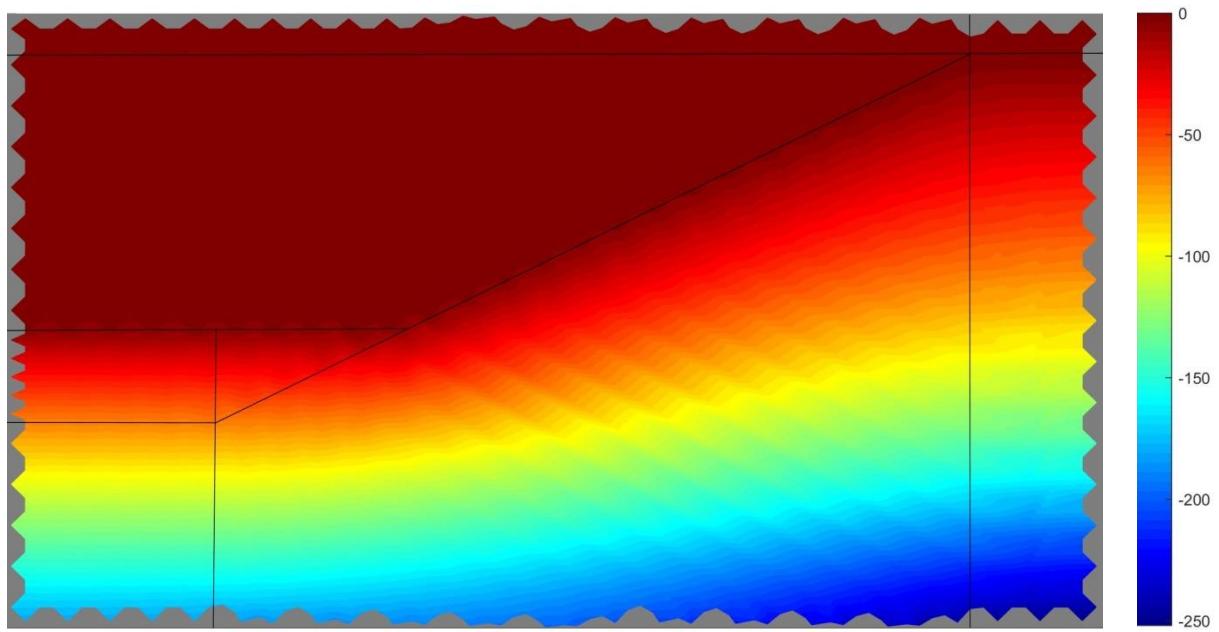
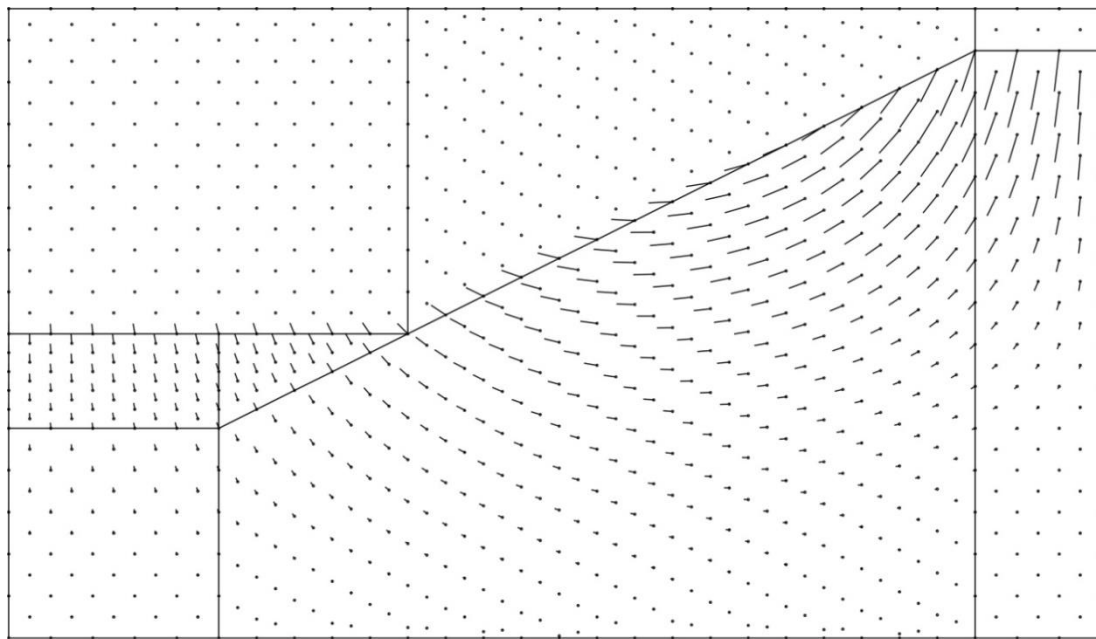


Figure 4.26: Normal effective stress on plane of deformation for phase 2(B) [Value Ranges: -252 kPa to 0 kPa]



MESH OF 4 TRIANGLES PER SQUARE

NODAL DISPLACEMENTS IN LOADING PHASE

MAGNIFICATION FACTOR ON PAPER:1.0E+00

NODAL VECTORS

MAXIMUM VECTOR LENGTH:5.7E-02

REAL-SCALED MAGNIFICATION:2.8E-02

Figure 4.27: Nodal displacements Phase 2(B)

Next, comparing the nodal displacements of the current phase from figure 4.27 with the corresponding figure 4.8 of Case A, exactly the same pattern of soil movement can be observed. The soil seems to slip in a circular fashion along the slope, with relative downward movement at the top surface of the soil slope and outward towards the mid and bottom surfaces of soil- slope. Moreover the highest displacement observed here is 5.7 cm which again is very much comparable to Case A, where the maximum displacement was 5.4 cm.

Further, as expected the pore water pressure observed in this phase in figure 4.28 is similar to figure 4.9 of phase 1 (A). Since, as stated in Case A, this unloading phase is run under drained conditions, the hydrostatic conditions are maintained here.

Overall from the above observations, it can be said for the current drained unloading phase, that the new mesh results are similar and quite consistent to the old mesh (Case A) results.

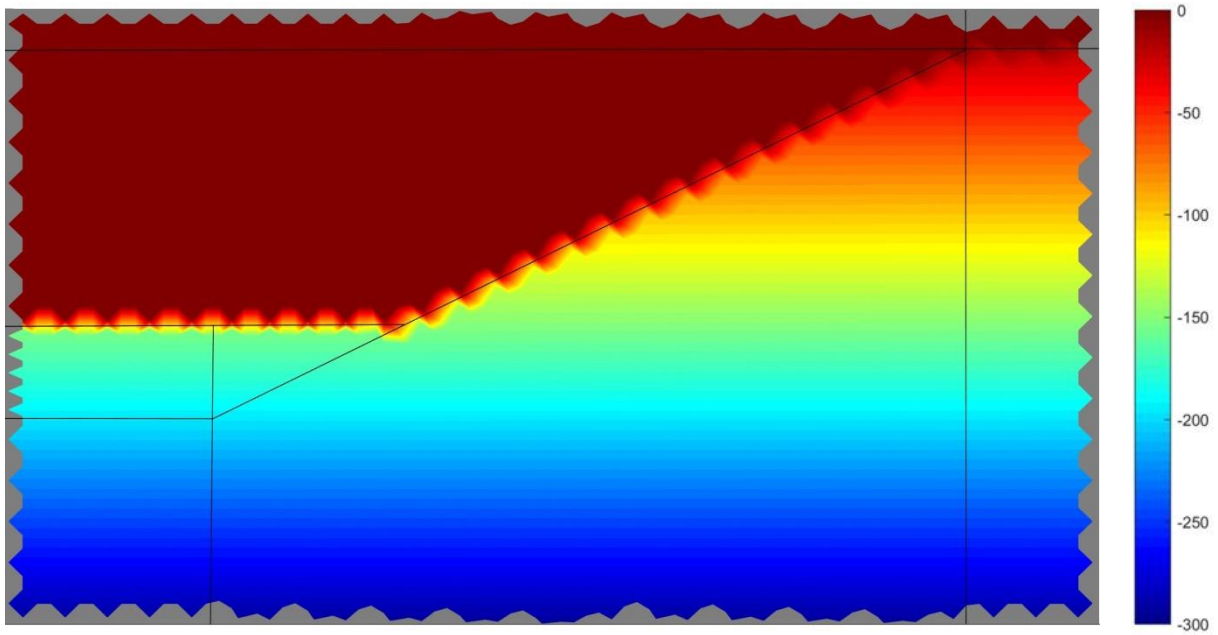
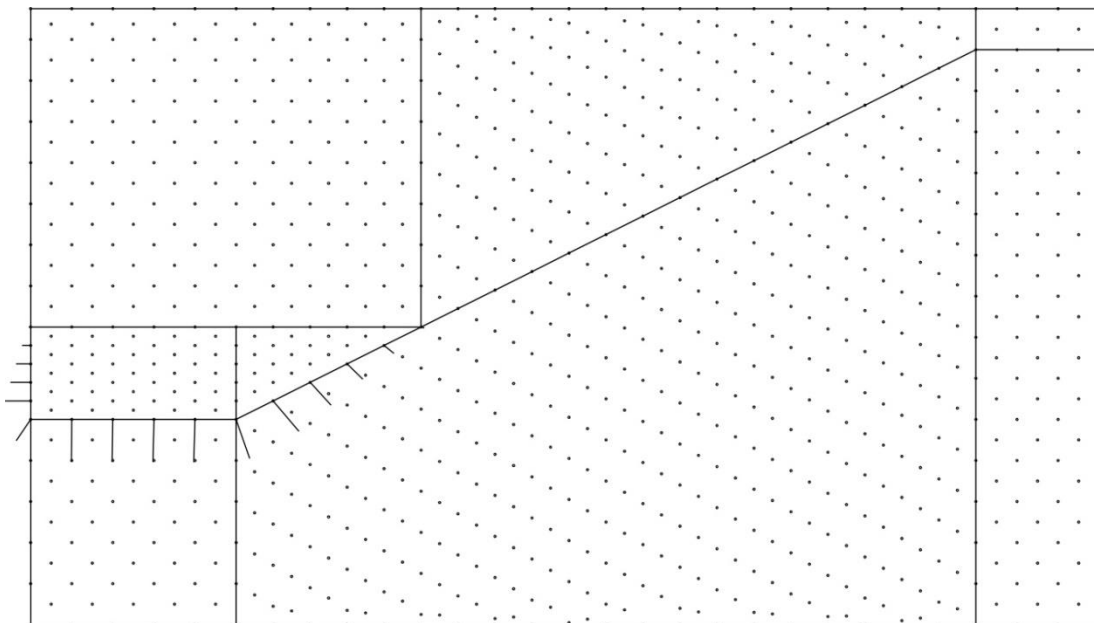


Figure 4.28: Pore pressure Phase 2(B) [Value Ranges: -300 kPa to 0 kPa]

4.3.3 Phase 3(B): Hydrostatic transition and simulation of dredging

The results presented in this section are most critical for evaluating the difference due to the new mesh implementation, since in this section undrained instability and post-stability dynamic behavior occur.



MESH OF 4 TRIANGLES PER SQUARE
 COMBINED LOAD DUE TO DREDGING
 MAGNIFICATION FACTOR ON PAPER:1.0E+00

NODAL VECTORS
 MAXIMUM VECTOR LENGTH:8.9E+01
 REAL-SCALED MAGNIFICATION:4.3E+01

Figure 4.29: Combined nodal loads due to dredged part of soil on non-dredge boundaries; phase 3(B)

From figure 4.29 the distribution of the applied virtual nodal loads due to intergranular traction force on the non-dredged soil surface can be observed for the new mesh. The maximum nodal load can be seen to be calculated at the lower interfacial soil surface, with a value of 89 kN.

Further, figure 4.30 presents the horizontal displacement of a node approximately midway of the sloping surface (node 612, see figure 3.4). From the above figure, it can be clearly seen that the slope passes its instability state and starts to fail at about 1.4 seconds after the start of dredging, which is slightly earlier as compared to case A, for which the failure occurred at about 1.5 sec. Further, similar to case A, the program stops the analysis at about 1.9 sec due to the time step restriction set by eq. (3.114).

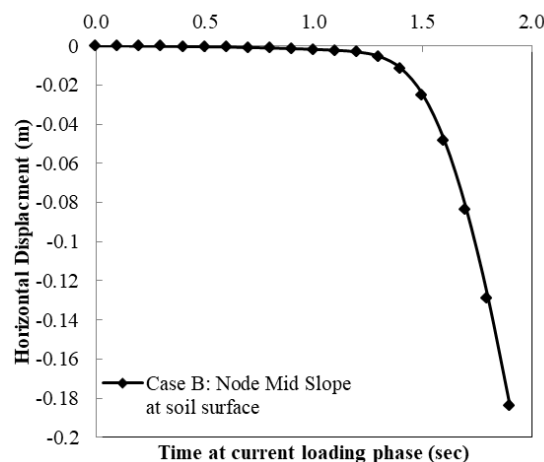


Figure 4.30: Horizontal displacement at a node midway to the slope surface for phase 3(B)

Next, in figures 4.31, 4.32 and 4.33, the in-plane effective stress tensors, normal effective stress and ratio of mobilized deviatoric stress respectively at the end of the calculation are shown. Altogether, these figures provide an indication of the extent of the slope failure and liquefaction. Figures 4.31 and 4.32 together show the severe reduction of the mean effective stresses in the soil around the slips-shear zone due to the activation of liquefaction, similar to Case A. Figure 4.33, clearly indicates that the complete strength has been lost around the slope surface region. In this figure the % value of the ratio of mobilized deviator stress indicates the degree of loss of soil strength. Furthermore, figure 4.31 and 4.33 show that a wide slip-shear cone has developed (indicating translational type of flow failure), typical for the liquefaction in flow failure of saturated loose fine granular materials (e.g. De Jager, 2018)

Further, the maximum principal stress tensor and deviatoric stress states remaining post failure can be observed in figures 4.31 and 4.32, the values obtained i.e. -262 kPa and -252 kPa remain comparable to Case A results. Moreover the rotational pattern of the principal effective stress tensors and the reduction pattern of the deviatoric effective stresses again seem to be analogues to Case A.

The differences between the two cases (A & B) as seen from a comparison of figures 4.33 and 4.15 are only minor, e.g. in figure 4.15 a small partially mobilized strength patch occurs and is missing from figure 4.33. However, the extent of failure in case A from figure 4.15 can be seen to be slightly larger than in figure 4.33, as the rupture zone spreads slightly more, both to the toe edge and towards the upper most slope surface. Additionally on the other hand, with reference to the same figures, Case B mid slope rupture zone seems to be deeper than the Case A. Clearly at this phase, these differences

can be held responsible to the fact that both cases have different mesh distributions. Taking account of case A (refer to figures 4.15 and 3.3), due to its comparatively finer mesh along and near to the soil surface (after dredging), the result obtained near the sloping surface are more accurate since the shear wave propagations are more accurately simulated under transient quasi-static elasto-plastic state conditions, but not under the post-instability dynamic conditions. Thus this may explain the partially mobilized patch along the mid-slope surface and also the slightly different extent of slip-zone.

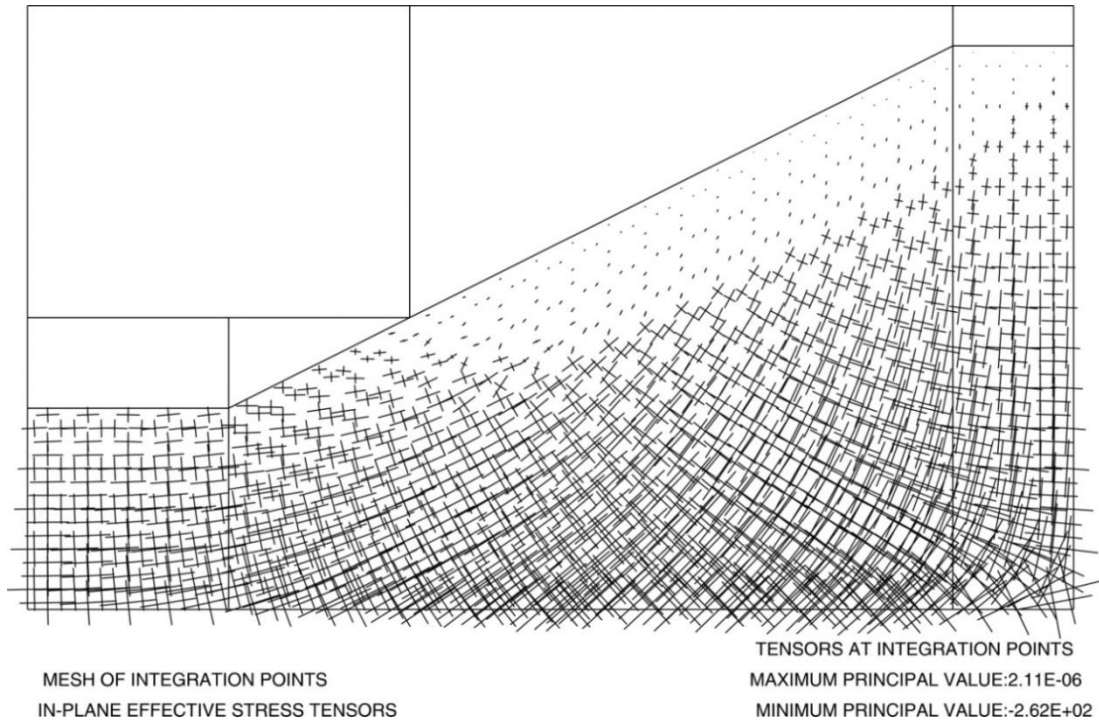


Figure 4.31: In-plane effective stress tensor for phase 3(B)

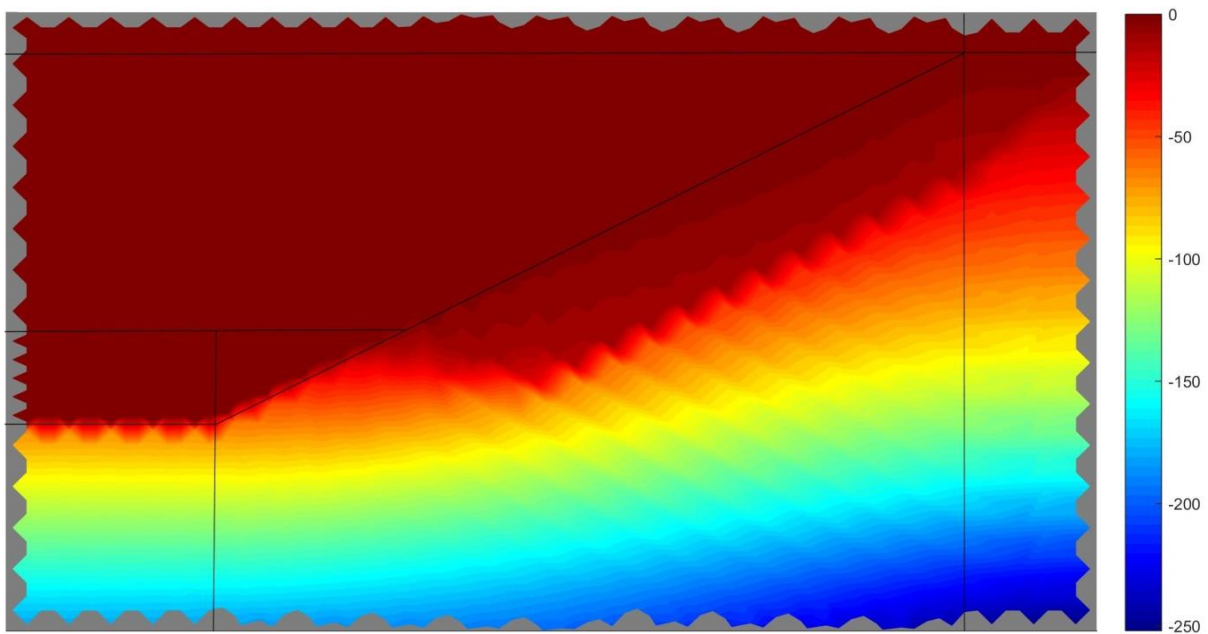


Figure 4.32: Normal effective stress on plane of deformation for phase 3(B) [Value Ranges: -252 kPa to 0 kPa]

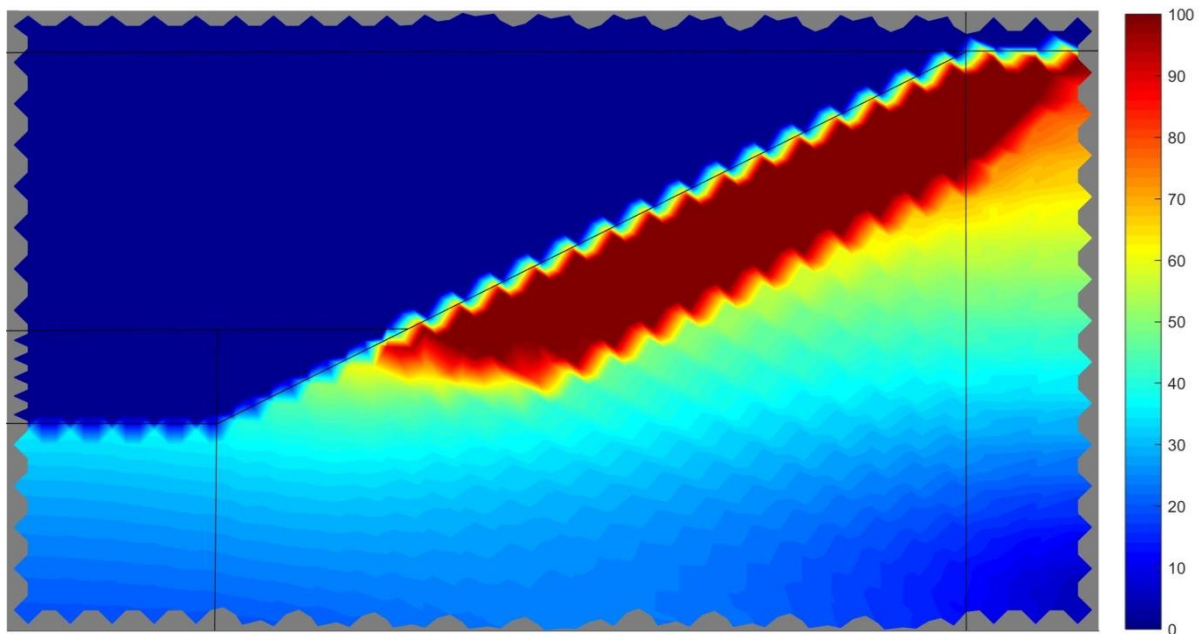


Figure 4.33: Ratio of mobilized and failure deviatoric stress Phase 3(B) [Value Ranges: 0% to 100%]

Figure 4.34, shows the distribution of the excess pore pressure accumulated in this phase. With the obtained maximum excess compressive pore pressure of -190 kPa, it can be observed that it is less than Case A. Further the maximum compressive value appeared to be at the upper portion of the slope (at region represented by dense blue contours in figure 4.34), instead of at the bottom toe as in Case A. The maximum value of the excess pore water pressure in tension observed is 120 kPa, lower than that of in Case A, which appears at both upper and lower ends of the slope represented by dense red contours.

However similar to Case A, here too negative excess pore pressure contour dominates the positive. Additionally, hour glass effects in the mesh also seem to occur, with every locally large contractive pore pressures and neighboring tensile pore pressures appearing, suggesting localized contraction and dilation within the adjacent elements.

However, noting that the outcomes of Case B for all the parameters other than excess pore pressures (EPP) indicates a good similarity with Case A (including the ones discussed later in this section), it can be reasoned that smoothening/averaging of excess pore pressures fields might lead into similar results in both the cases, with average behavior being contractive. Further then, considering this the current difference observed in EPP between the two cases can be attributed to the different mesh refinements along the slope used by both the cases. This thus indicates that for the particular type of elemental arrangement opted i.e. bilinear quadrilaterals divided into four 3-node triangular elements, the hour glass effect becomes more prominent in cases of non-uniformly refined meshes (i.e. in Case A) along the slope, for such liquefied slope failures.

Apart from this, the lower regions of the problem geometry more or less remained unaffected with some slightly compressive pore pressure accumulations around the right lower region.

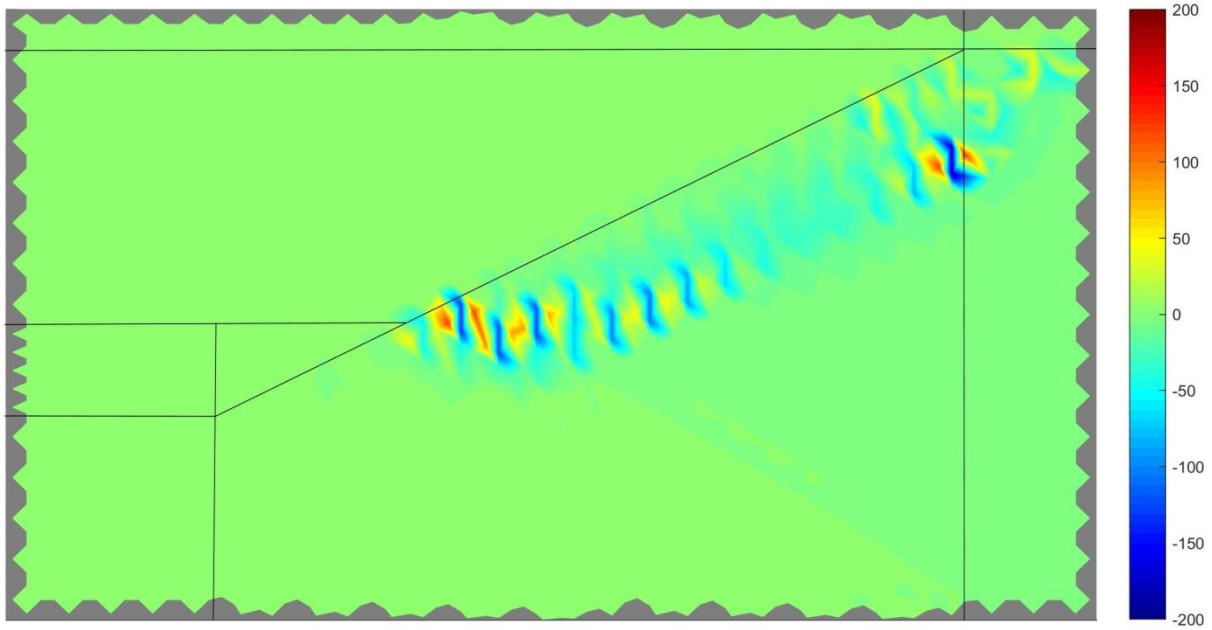


Figure 4.34: Excess pore pressure Phase 3(B) [Value Ranges: -190 kPa to 120 kPa]

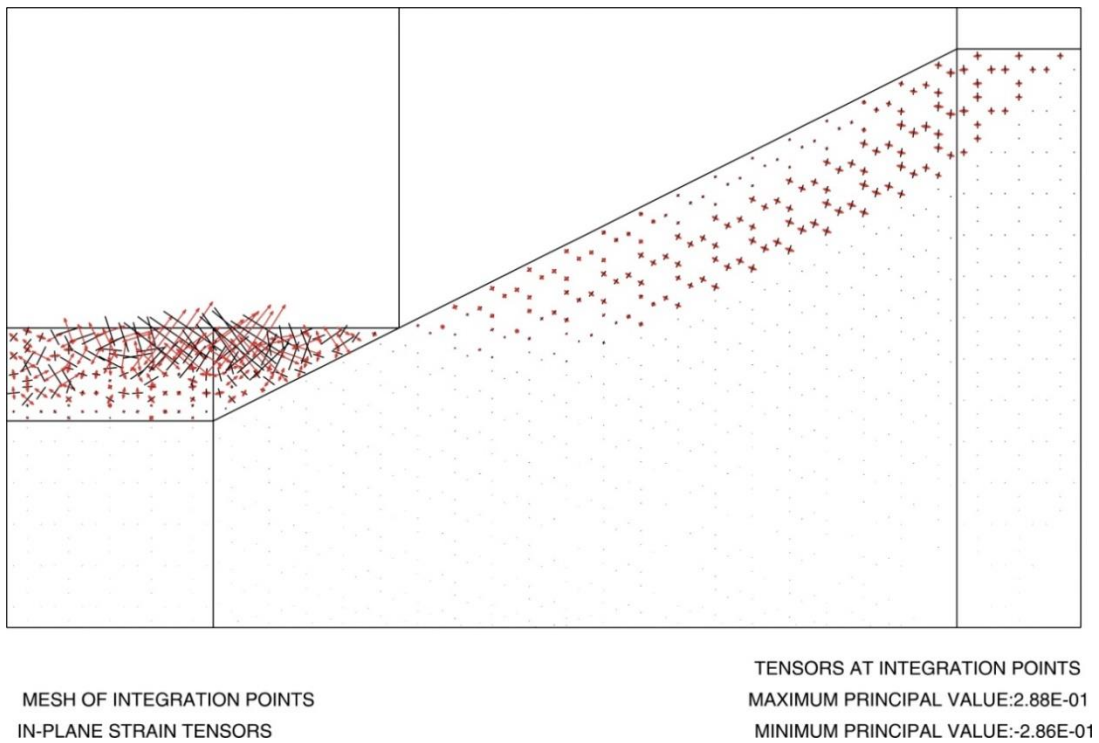


Figure 4.35: In-plane strain tensors phase 3(B)

Further, figure 4.35 depicts the in-plane strain tensors experienced by the finite elements in the problem geometry. The observation that can be made here is that the dredged water region experiences relatively higher strain tensors than the soil region. Comparing these results to those of the old mesh, i.e. Case A analysis, there hardly any strain tensors have been observed (see figure 4.17). Case B has more uniform and smaller finite elements around the dredged regions. Apparently such uniform meshes become more sensitive to shock wave propagations and thus simulate more strains and

displacements. This fact is also evident from nodal displacements shown in figure 4.37, which shows larger water movement in the dredged region than compared to case A. However, it is important to understand that these strains and displacements in the dredged region are non-conclusive and do not represent the water behavior in the dredged region. The strains and movements in the remaining water are indeed influenced by the dynamic motion of slope failure adjacent to it and the virtually applied hydrostatic pressure heads over them based on the assumed water level as a follower type of loads. Thus the strains illustrated in figure 4.35 and the displacements in figure 4.36 are rather artificial in nature and therefore irrelevant. However, this observation is critical in the sense that it shows the comparative importance of using the new mesh over the old one in order to simulate proper shock wave propagation considering Case C analysis with activated fluid layers.

For comparison with Case A, figures 4.35 and 4.37 are re-plotted for the soil region exclusively, leading to 4.36 for strain tensors and to figure 4.38 for the nodal displacements of the soil.

In figure 4.36 the maximum and minimum principal strain tensor values are of the order 0.033 and - 0.0342 which are comparable with the observed strain tensors of Case A, figure 4.17, but are slightly lower. The general pattern of strain tensors along the slope observed is similar to that of Case A i.e. relatively large strain tensors can be observed along the rupture zone, decreasing from there up towards the slope surface

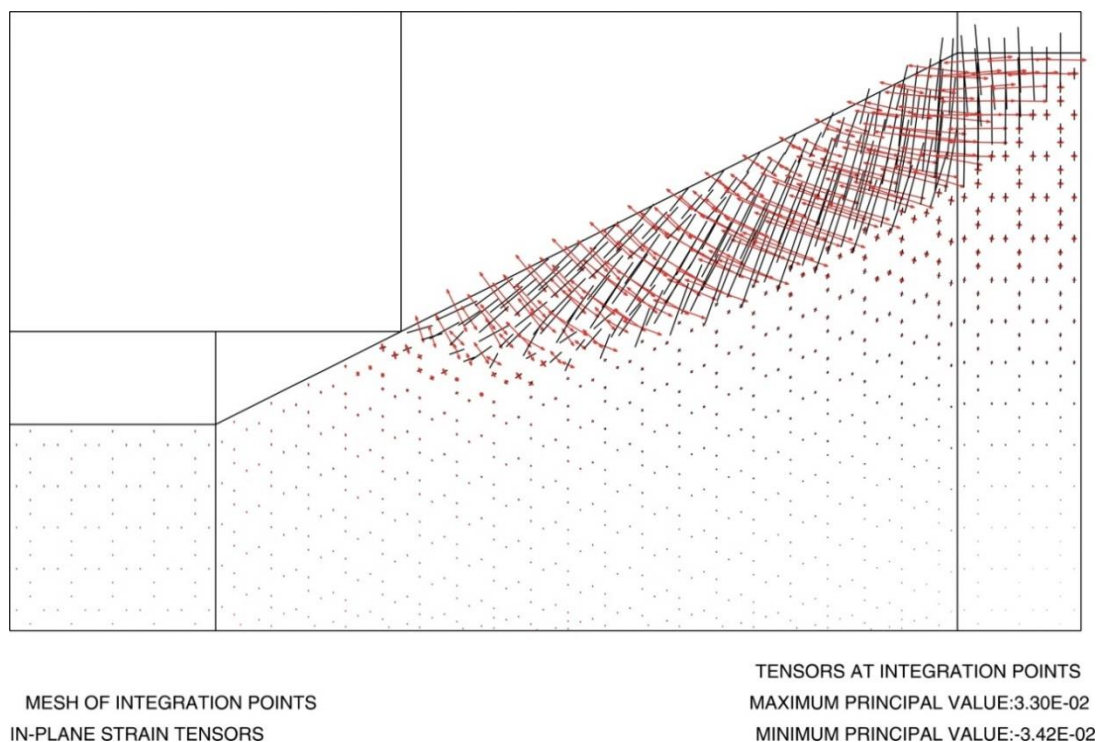
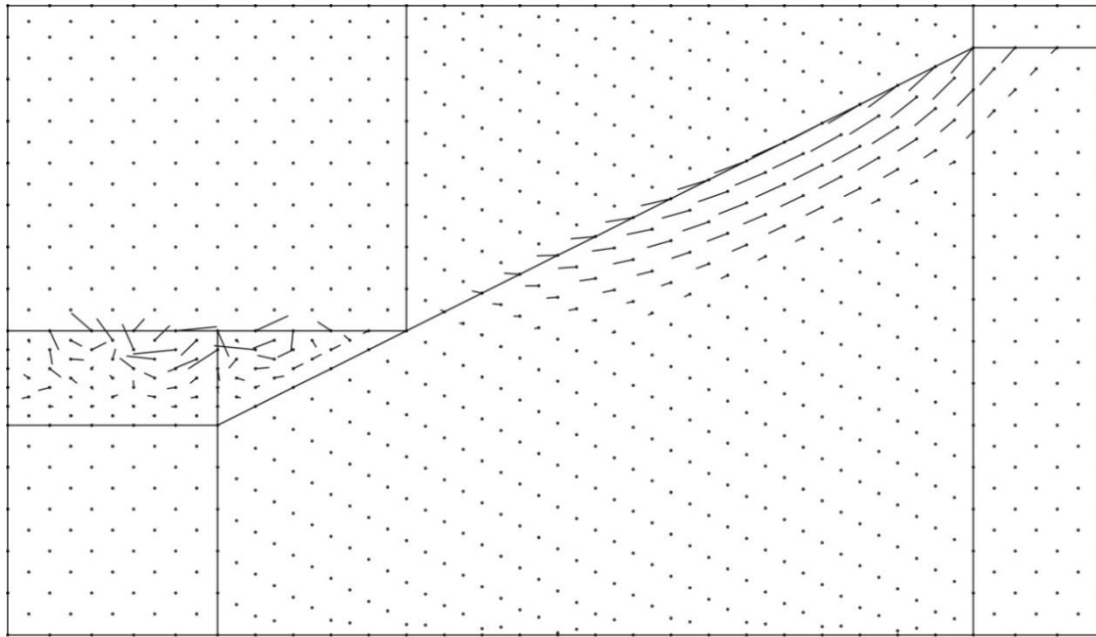


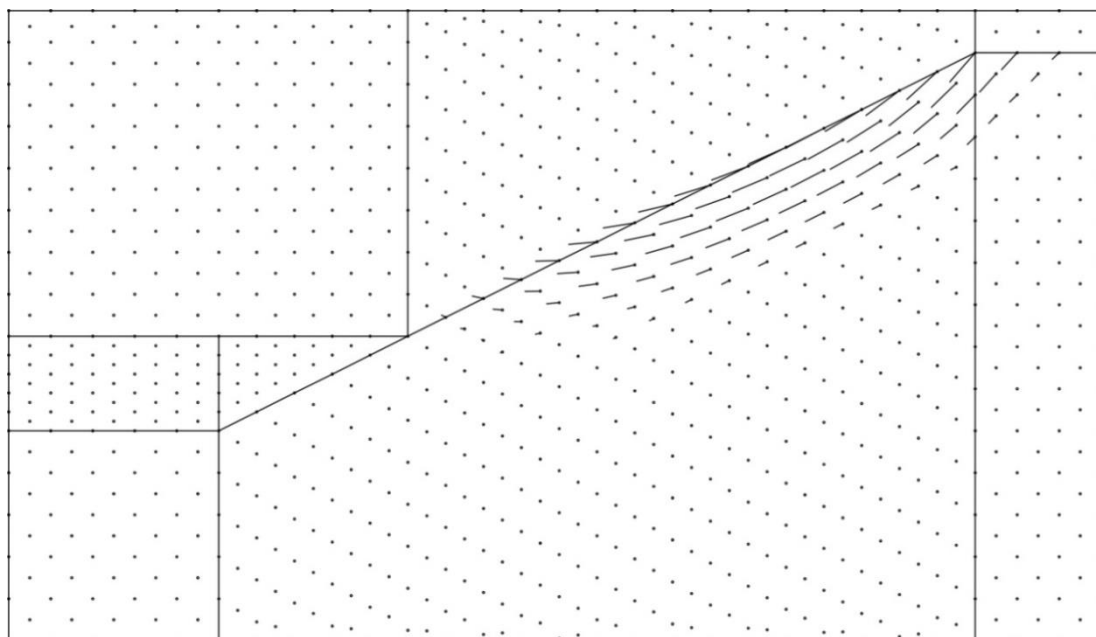
Figure 4.36: In-plane strain tensors phase 3(B), only soil region



MESH OF 4 TRIANGLES PER SQUARE
 NODAL DISPLACEMENTS IN LOADING PHASE
 MAGNIFICATION FACTOR ON PAPER:1.0E+00

NODAL VECTORS
 MAXIMUM VECTOR LENGTH:2.5E-01
 REAL-SCALED MAGNIFICATION:1.2E-01

Figure 4.37: Nodal displacements Phase 3(B)



MESH OF 4 TRIANGLES PER SQUARE
 NODAL DISPLACEMENTS IN LOADING PHASE
 MAGNIFICATION FACTOR ON PAPER:1.0E+00

NODAL VECTORS
 MAXIMUM VECTOR LENGTH:2.2E-01
 REAL-SCALED MAGNIFICATION:1.1E-01

Figure 4.38: Nodal displacements Phase 3(B), only soil region

The nodal displacement vectors for the soil region are indicated in the figure 4.38. At first look, the general shear zone and pattern look rather similar to what has been observed for Case A.

Even the maximum displacement observed here is 22 cm, which is closely comparable to the results of the corresponding Case A; namely a nodal displacements of about 20 cm. However, the shear zone at the mid-slope is slightly deeper and the extent of its reach at the left edge near the toe and to the right top edge is relatively smaller than in Case A.

Finally, different energy forms and their transitions can be observed from figure 4.39. The results for this phase seem closely comparable to the corresponding figure of Case A i.e. figure 4.19, with a few slight variations. Here again the potential energy line of the soil shows a drastic reduction once the liquefaction of soil is initiated at about 1.4 sec. Also the combined soil and water potential energy line practically coincides with that of the soil, thus indicating negligible energy absorption due to the water potential energy. Further the initial main contributing energies and their percentage ratio of mobilized soil potential energy remains comparable to that of Case A, namely: a) internal energy of soil, which mobilizes 23.28% of the soil potential energy and b) follower type of energy due to applied virtual hydrostatic loadings on the slope surface, which mobilizes about 47.4% of the soil potential energy. Moreover, similar to case A, here too, soil's kinetic energy with 23.36% mobilization of soil potential energy becomes a prominent contributor in energy transitions once the slope instability state is crossed and the slope liquefies completely and dynamic motion gets activated.

The main distinguishing factor in the comparison to case A, are the marginal contributions by the dredged water region's internal and kinetic energies. This was expected considering the previous observations made regarding the artificial and arbitrary water nodal movements and strain tensors of the dredged regions. With the potential energy of soil mobilized up to 3.20% by internal water energy and 1.51% by water's kinetic energy, the marginal contribution of internal stress-strain energy of water can be observed to be slightly more. Moreover the energy loss in numerical accuracy in terms of mobilized soil potential energy is calculated to be 1.2%, which is about 0.6% less than in Case A.

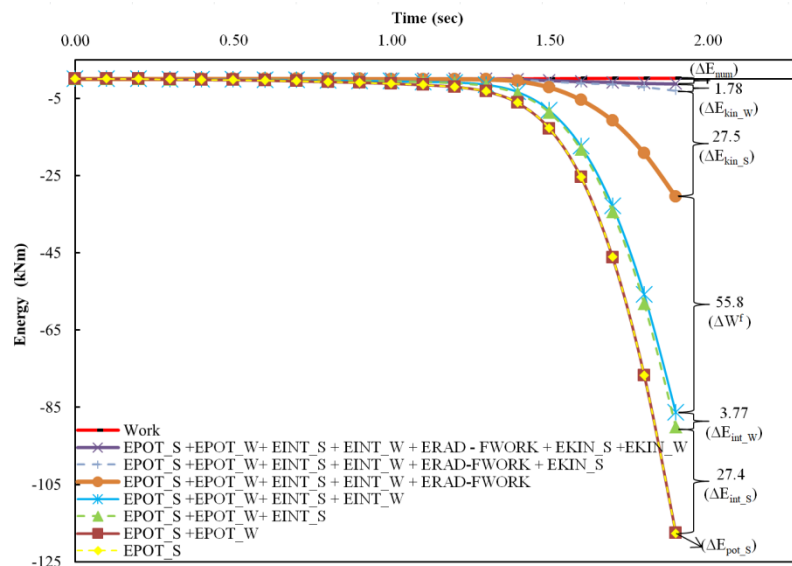


Figure 4.39: Energy transitions Phase 3(B)

Overall with all the observations made under the current phase analysis, it shows the importance of the Case B analysis in order to prepare for the Case C analysis. It can be noted, that although the results of this case might provide consistency with the Case A, they are still different in some critical aspects such as dredged water motion, failure shear zone and thus generated strain tensors and displacements. Thus this phase can provide the basis of more conclusive comparisons than Case A, in the instance of coupled hydrodynamic analysis, run under the Case C scenario.

4.4 Case C results: New mesh with activated fluid blocks

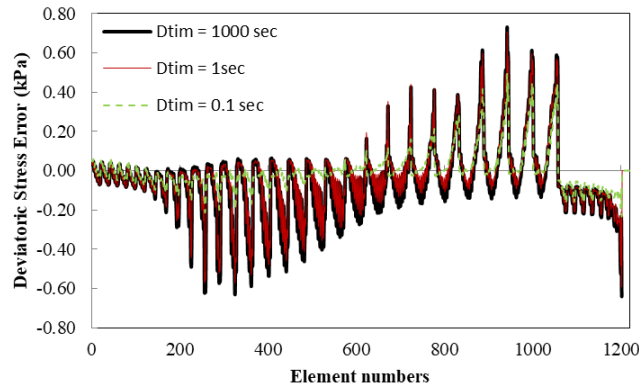
4.4.1 Phase 2(C): Fluid blocks activation and optimization

As stated before in section 3.6.3, this is a fluid activation state with equilibrium conditions. Therefore, time step and time of loading used were kept same. Additionally, as mentioned in an earlier section, the time step and time of loading opted for this are 10^5 seconds, which was earlier considered sufficiently large enough for the inertial mass of the system and the viscosity of water to have negligible contributions in the calculation. Thus in this way static equilibrium condition is practically maintained throughout the problem geometry. However, on running the analysis it was observed that with the aforementioned time interval sets, the calculation did not converge in the above defined single step. Moreover, it was observed that due to the relatively large unbalance owing to the numerical inaccuracy from the previous calculation phase, displacements or strains obtained were beyond the allowable limits for 1 step convergence. From eq. (3.22) it can be observed that with large time steps the contributions due to the mass matrix and the viscosity matrix remain negligible. Therefore the global tangent stiffness matrix remains small in comparison to the equating residual unbalance forces. Hence the calculated displacement increases. One way to resolve the issue is to further reduce the allowable error from 0.001 to an extent, where the residual unbalance forces become negligible. However doing so will lead to large computation times thus it has been avoided.

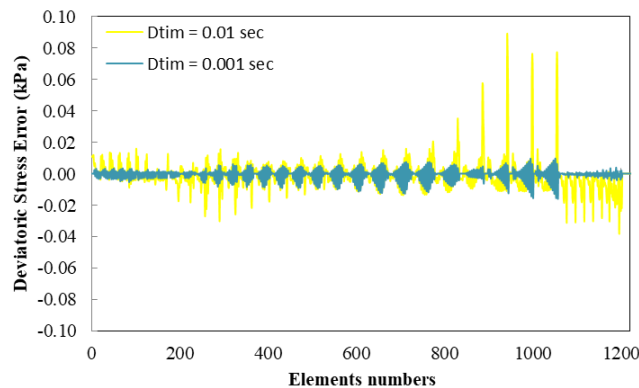
Instead, the time step and time interval were optimized such that the achieved displacements in the system were practically negligible and the obtained stress state in the soil domain remained identical to the previous phase conditions. To this end, it was attempted to produce a solution with minimum contributions of the inertial mass matrix and viscosity matrix. It is worth mentioning, that the attempt here is to increase the contribution by the global stiffness matrix by increasing the factors of the inertial mass matrix and shear viscosity matrix factors so that under MNR accuracy eq. (3.22), the nodal incremental displacements can be decreased in the system. For this six different time intervals and loading times were analyzed ranging from 1000 sec – 0.001 sec. For optimization of the results three primarily governing parameters were set: 1) maximum nodal displacements achieved in current phase, 2) Onset of slope instability time in Phase 3(c) i.e. dredged unloading phase and 3) Difference (error) of deviatoric stresses in soil domain from previous phase i.e. 2(B) to current phase 2(C). Table 4.2 can be referred to for the former two parameters and figure 4.40 for the latter one.

Table 4.2: Time sets vs calculated maximum nodal displacements in Phase 2(C) and time of failure in Phase 3(C)

Time of loading and time step for Phase 2(C)	Maximum nodal displacements in Phase 2(C)	Onset of slope instability time in Phase 3(C)
1000 sec	2.7e-3 m	11.6 sec
1 sec	2.2e-3 m	9.6 sec
0.1	2.3e-4 m	1.3 sec
0.01	1.3 e-5 m	1 sec
0.001	5e-7 m	1 sec



(a) Time intervals and loadings used: 1000 sec, 1 sec, 0.1 sec (*larger scale)



(b) Time intervals and loadings used: 0.01 sec, 0.001 sec (*smaller scale)

Figure 4.40: Deviatoric stress state difference in soil domain between phase 2(B) and 2(C).

From the above table 4.2 and figure 4.40, the general observation that can be made is that larger time sets, lead to larger displacements and higher order of relative stress state discrepancies in the soil domain with respect to previous phase. Moreover, from the 3rd column of table 4.2, an additional fact can be observed, namely that the change in stress-state of the soil domain in the current phase with higher time sets is such that it strengthens the slope as it delays the occurrence of failure during subsequent dredging.

Thus observing the results, times sets with 1000 and 1 seconds were straight away rejected as the displacements produce by them were in order of 10^{-3} m and the maximum relative deviatoric stress state error of 0.7 kPa (approx.), which were relatively quite large. Moreover the slope failure obtained in the subsequent phase of dredged unloading, considering aforementioned time steps in current phase was very high as compared to the corresponding Phase 3(B) with restrained fluid layer mesh, thus these sets are deemed unrealistic.

Moving on, the maximum displacement produced by 0.1 sec time sets was still reasonable and also the additionally time to reach failure in consecutive phase 3(C) with respect to phase 3(B) seemed comparable (refer to table 4.2). However, even though the difference in deviatoric stress (refer to figure 4.40) for major part of soil domain been considerably reduced than the 1000 and 1 seconds time sets, but the maximum still reaches up to 0.5 kPa.

On the other hand it can be observed that for time sets 0.01 and 0.001 the maximum displacement has been considerably reduced and also the deviatoric stress error in the soil domain is well below 0.09 kPa, therefore the 0.1 time step has been rejected as well. Next, comparing the results for the time sets 0.01 and 0.001 seconds it can be observed that the maximum displacement in both

cases is comparable and almost negligible as well. Although there is a considerable difference between the two sets in terms for deviatoric stress error, this does not affect the failure time of phase 3(C) due to dredged unloading. Table 4.2 indicates that for both time set values the slopes fails at 1 seconds, which still is comparable to phase 3(B). It can be concluded, that for the 0.01 seconds time set the deviatoric stress error becomes sufficiently low to affect the subsequent dredged unloading phase results. Therefore with these observation finally, 0.01 seconds time interval and time of loading was opted for this phase analysis. Also by preferring 0.01 seconds over 0.001, the further involvement of inertial mass and shear viscosity of water (refer to eq. 3.22) remained limited.

Moreover, the results of nodal displacements and ratio of mobilized and failure deviatoric stress for dredged unloading in phase 3(C) in scenario of 0.001 seconds time set can be referred to from appendix E and thereby compared with corresponding results in case of 0.01 seconds from figures 4.48 and 4.53. This comparison further suggests that the results hardly get affected for smaller time steps than the 0.01 seconds time set, thus supporting the reasoning to choose the 0.01s time set for current phase analysis.

Next, it is important to note that even though the chosen time set of 0.01 seconds fulfills the two main objectives i.e. giving the same stress state in the soil as in the previous phase with negligible displacements in the system, further analyses were required, namely to evaluate the influences of inertia, compressibility and viscous shear of the submerging water on the current phase results and thereby in dredged unloading phase 3(C). Considering this, firstly the influence of the increase in viscous shear due to a lowered time of loading and interval was analysed. It was expected that the water region would show an increase in the effective stresses. Hence, it was observed that the normal viscous shear stress in water region changes from the order of 10^{-24} to 10^{-12} kPa (approx.), while changing the time sets from 1000 to 0.01 seconds. From this observation it can be said that even though the difference in relative terms is quite large, the obtained stresses in the water regions for the 0.01 seconds of time set are still small enough to cause any considerable impact on the dredged unloading phase 3(C). Thus, this increase was considered acceptable and thereby ignored.

Secondly, suspecting the influence of change in time sets on the inertia related factors, outcome of parameter such as nodal velocity was noted. From the results it was observed that while changing time options from 1000 to 0.01 seconds, the maximum nodal velocities changes from the order of 10^{-5} to 10^{-3} m/s (approx.). Considering this change to possibly influence the outcome of subsequent dredge phase, the phase 3(C) analysis was re-ran while putting zero nodal velocities in the restart file “.rin” obtained from current activation phase analysis. The nodal displacements and ratio of mobilized and failure deviatoric stress outcome of this analysis are presented in appendix E. Further, comparing these results with the actual un-altered nodal velocity scenario shown later in figure 4.48 and 4.53, it was observed that the results are exactly same. Thus, indicating that the obtained nodal velocity in this phase at 0.01 seconds time option was small enough to cause any interference with the dredged unloading phase 3(C). This observation also implies that the outcome in the phase 3(C) is more prone to the stress-state of the soil obtained in previous phase than nodal velocities.

Hence, all the aforementioned analysis suggests that using time of loading and time interval 0.01 seconds is the safe and correct option so to make conclusive comparison between Phase 3(B) with restrained fluid blocks to Phase 3(C) unrestrained fluid blocks. Therefore, further with this opted option the results of in-plane effective stress tensors, normal effective stresses, nodal displacements and pore-pressures can be referred to figures 4.41 to 4.44, respectively.

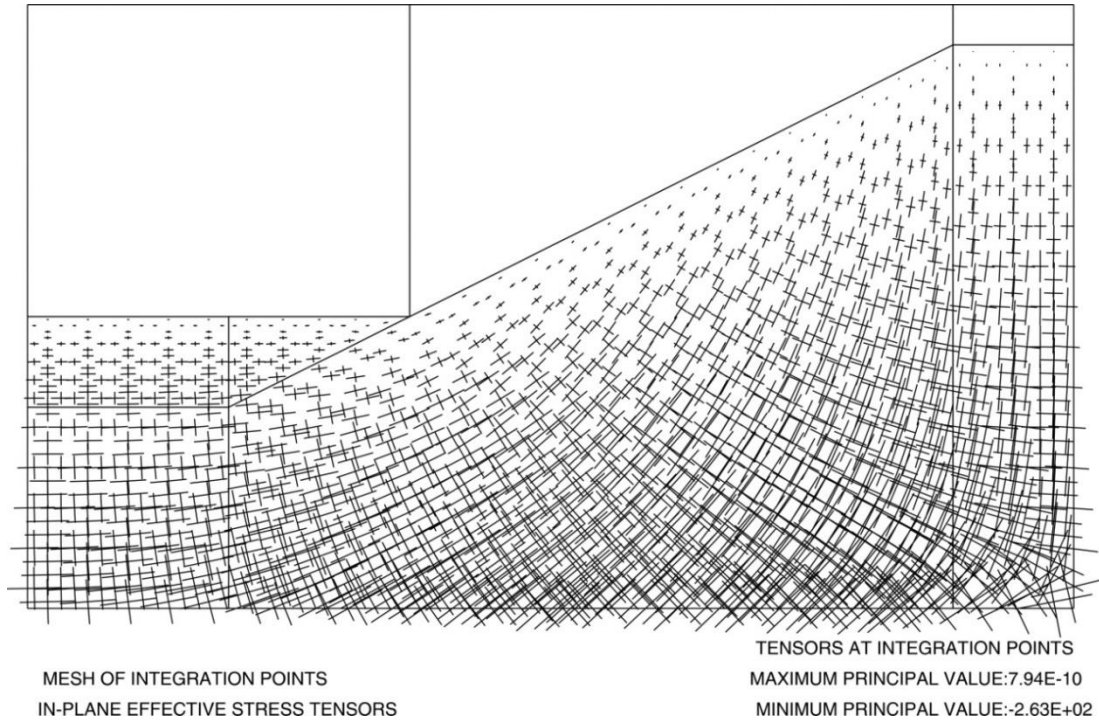


Figure 4.41: In plane effective stress tensor for phase 2(C)

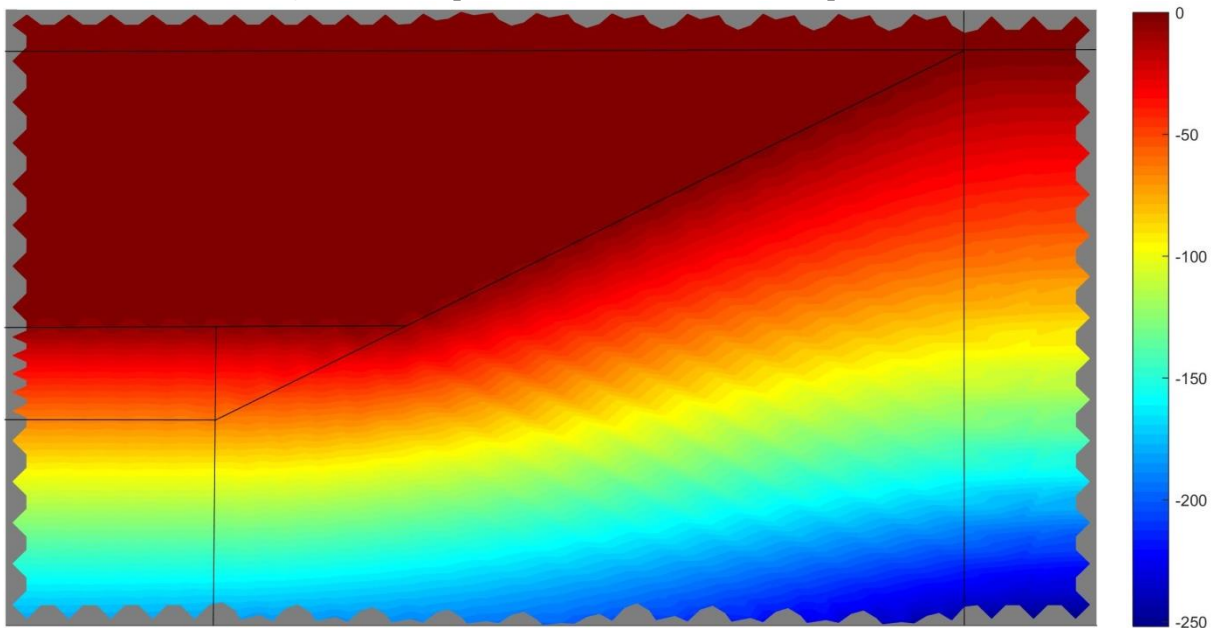
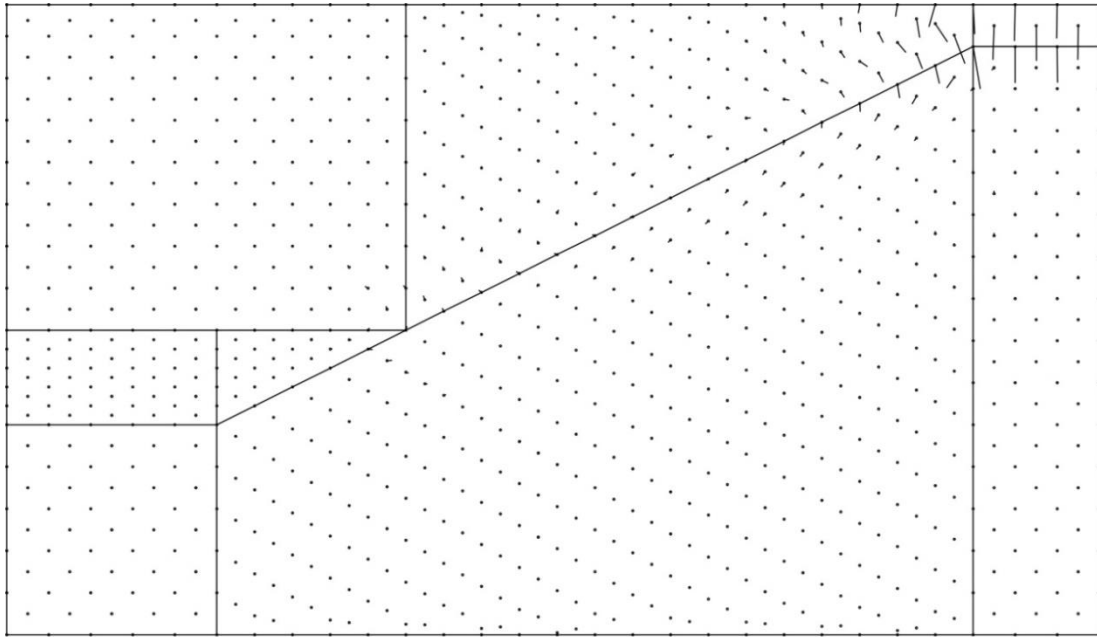


Figure 4.42: Normal effective stress on plane of deformation for phase 2(C) [Value Ranges: -252 kPa to 0 kPa]

It can be clearly observed from figures 4.41 and 4.42 of in-plane effective stress tensors and the normal effective stresses that the stress state obtained at this phase in the soil domain after the fluid blocks activation remains quite identical to the Phase 2(B), which is the precursor of this phase and where the unloading of the assumed overlaying soil took place. Moreover the maximum compressive principal stress value of -263 kPa and maximum normal effective stress of -252 kPa here are also similar to what has been obtained in Phase 2(B). Further, it can be seen that the viscous stresses obtained in fluid blocks are negligible enough to be shown in the figure 4.41 of effective stress tensors and also it has been represented by zero contour lines in figure 4.42 of normal effective stress.

Next, from figure 4.43 of nodal displacements with maximum observed displacement value of $1.3E-5$, it can be said that indeed the system does not experiences any kind of movement and thus remains mainly static. Additionally, the direction of displacements in the fluid blocks and over all in the system remains mainly in accord to the nodal displacements observed in pre-cursing phase 2(B). Since, it can be seen that the highest displacements are downward in the fluid blocks appearing along and above the slope's top surface, which is the same location where the highest displacement in the soil have been observed in Phase 2(B) (refer to figure 4.27).



MESH OF 4 TRIANGLES PER SQUARE
 NODAL DISPLACEMENTS IN LOADING PHASE
 MAGNIFICATION FACTOR ON PAPER:1.0E+00

NODAL VECTORS
 MAXIMUM VECTOR LENGTH:1.3E-05
 REAL-SCALED MAGNIFICATION:6.3E-06

Figure 4.43: Nodal displacements Phase 2(C)

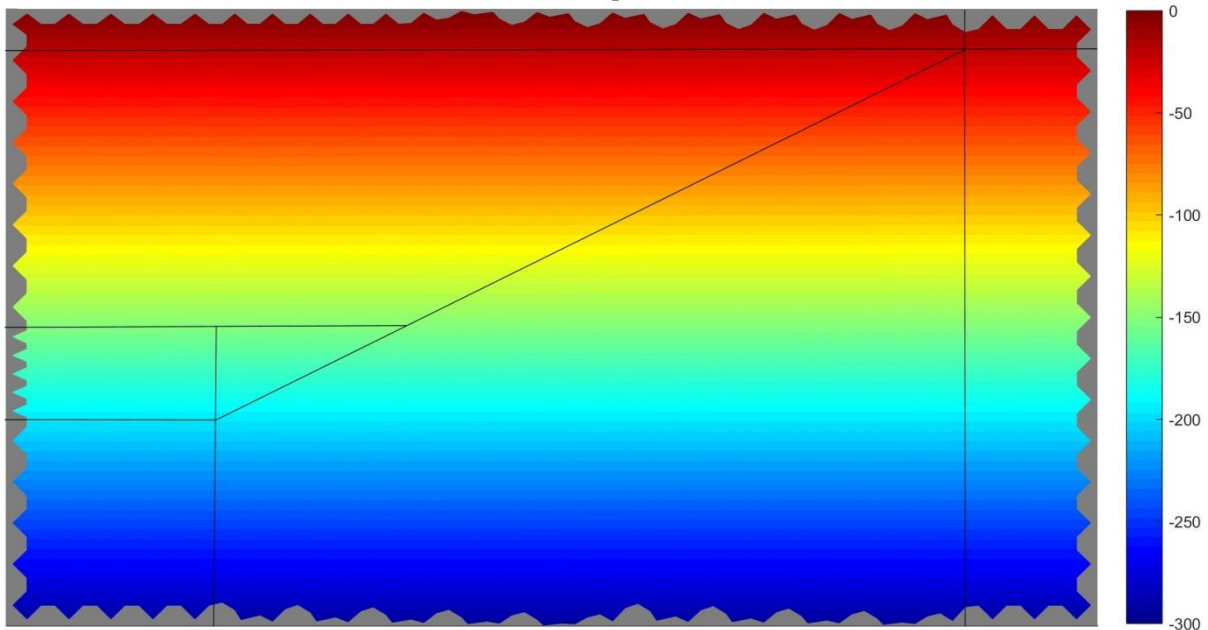


Figure 4.44: Pore pressure Phase 2(C) [Value Ranges: -300 kPa to 0 kPa]

Finally, observing the pore pressure results from above figure 4.44, the results obtained were as expected. The straight line contours represent a drained condition with zero pore pressure accumulations. Moreover, the pore pressures in soil domain remain exactly identical to what observed in corresponding figure 4.28 of Phase 2(B). Further, it is to be noted that the same plot in the fluid blocks the hydrostatic water pressures is shown, which again can clearly be seen to duplicate the expected analytical solution in this case. Additionally, as expected, the same pressure contours are being continued from soil into water regions through straight lines.

4.4.2 Phase 3(C): Hydrostatic transition and simulation of dredging

Finally the collective impact on slope failure and overlaying water mass movement due to hydro-dynamic coupling can be evaluated through the results presented in this section. It should be noted that since both mesh and loading mechanism remain the same as for case B, therefore the combined applied virtual dredged loading on the non-dredged surface remains identical (refer to figure 4.29) and thus it shall not be discussed here.

Next similar to phase 3(B), figure 4.45 depicts the mid slope surface nodal horizontal displacement with respect to time. From this figure it can be clearly seen that the slope fails after about 1 second of time, as the node gets displaced drastically, past that mark. Further it can be observed that this failure time, is less than what was observed in the restrained fluid Case B's corresponding result, where the slope failed at 1.4 sec. It may be suspected that this difference probably might have occurred due to the interaction between slope and overlaying water mass. However given the sensitivity of the outcomes observed in pre-cursing phase analysis, other possible cause might be due to the induced numerically inaccuracy in the previous Phase 2(C) (fluid activation) calculations.

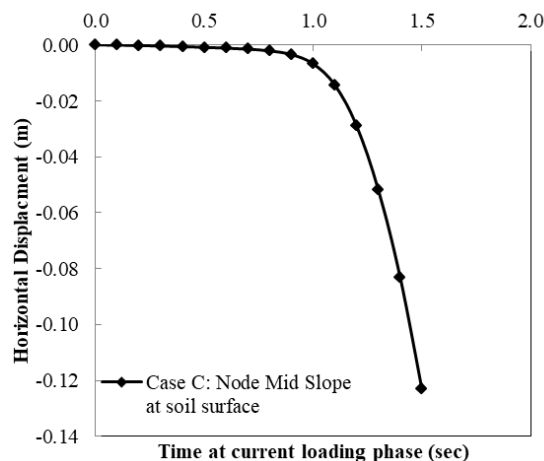


Figure 4.45: Horizontal displacement at a node midway to the slope surface for phase 3(C)

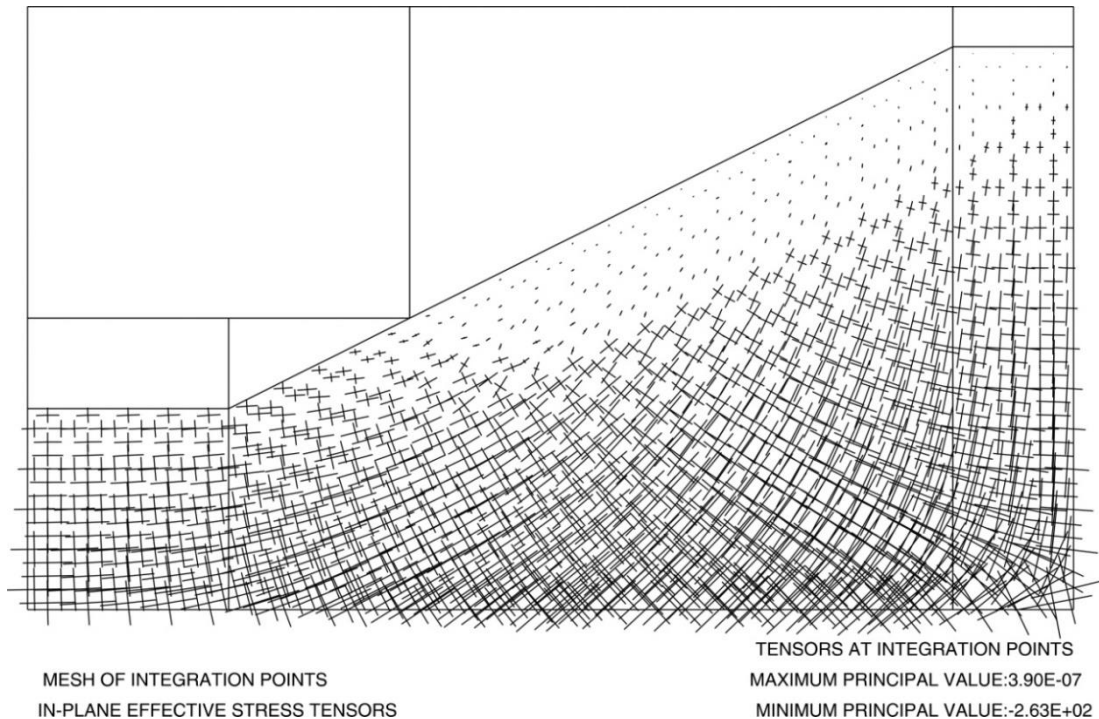


Figure 4.46: In-plane effective stress tensor for phase 3(C)

Moving on, figures 4.46 and 4.47 illustrate in-plane effective stress tensors and normal effective stress contours in the system. It can be observed that the stress in soil drastically reduces along and around the slip-shear zone just like in corresponding phase of Case B (restrained fluid case). However a slight distinction can be made concerning the slip-shear zone, with normal effective stress plots in the figure 4.32. As it can be observed that the soil retains some effective stresses just below the region of the mid-slope surface, whereas in case B this region completely loses its stresses within the same zone. This observation is also evident in the ratio of mobilized and failure deviatoric stress figure 4.48, where this region is marked by a partially mobilized stress contours patch, varying from 95% to 77%, other than this a clear slip-shear zone can be seen near the slope, where the soil has completely lost its strength and thus has been liquefied.

It is to be noted that the time difference post slope instability after which the program stops is same in all three cases i.e. 0.5 s. Thus considering this the variation observed here in comparison to Case B, i.e. formation of the partially mobilized strength patch, may be attributed to the fact that the post slope instability the overall interaction forces from submerging water on the liquefying slope may reduce the rate of liquefaction or flow itself. This is also evident from later figure 4.52 of nodal displacements which shows maximum soil displacement of 14 cm against 22 cm of Case B.

Apart from this discrepancy, all the other aspects of the stress state such as: the maximum compressive principal effective tensor value (-263 kPa), the maximum compressive normal effective stress (-252 kPa), the principal effective stress tensors rotational pattern, the normal effective stress contours and, the extent and shape of slip-shear zone observed via the ratio of mobilized strength according to figure 4.48 remain identical to the corresponding features of restrained fluid blocks Case B's phase 3(B) (refer to figures 4.31 to 4.33). Moreover from figures 4.46 and 4.47, it can be clearly observed that the viscous stresses, rotation and change of principal stresses developed in water regions due to its very low shear viscosity are insignificant.

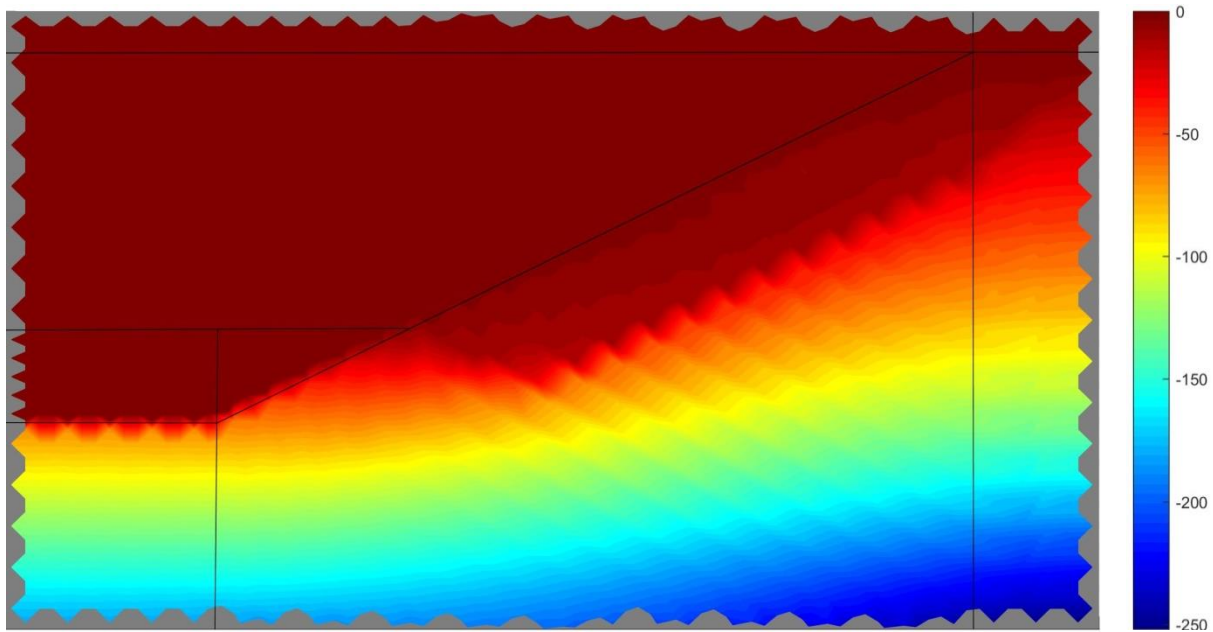


Figure 4.47: Normal effective stress on plane of deformation for phase 3(C) [Value Ranges: -252 kPa to 0 kPa]

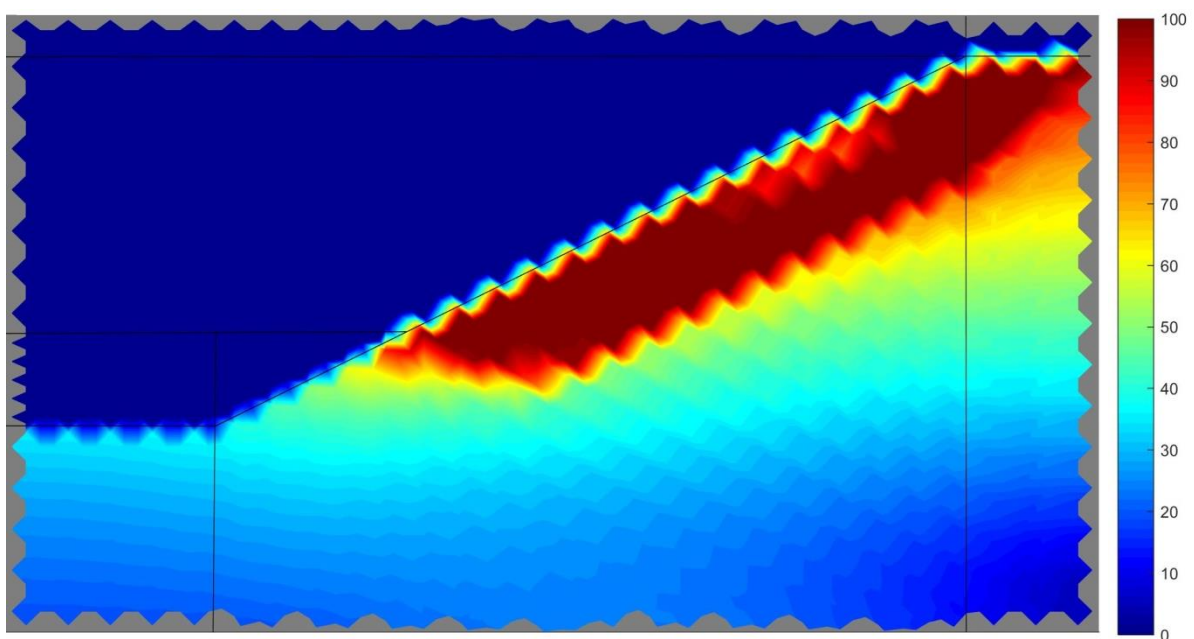


Figure 4.48: Ratio of mobilized and failure deviatoric stress Phase 3(C) [Value Ranges: 0% to 100%]

Apart from the stress state, the excess pore pressure (EPP) outcomes can be observed from figure 4.49. From the preliminary observations of the excess pore pressure contours, it can be seen that the large excessive pore pressures are accumulated in the shear zone near the slip-shear surface. Further, the appeared pattern although with few variations, seems to be rather similar to the corresponding pattern figure in Case B's phase 3(B) (refer to figure (4.34)). Moreover both the maximum limit of excess pore pressure observed, i.e. in compression (-160kPa) and in tension due to hour glass locking effects in the mesh (130 kPa), seems quite comparable to the limits observed in Phase 3(B) of Case B. Further, similar to Case B, a dominating negative excess pore pressure contours

can be observed here. Thus an overall contractive pore pressure behavior can be expected after smoothing of the excess pore pressure field in the current case C.

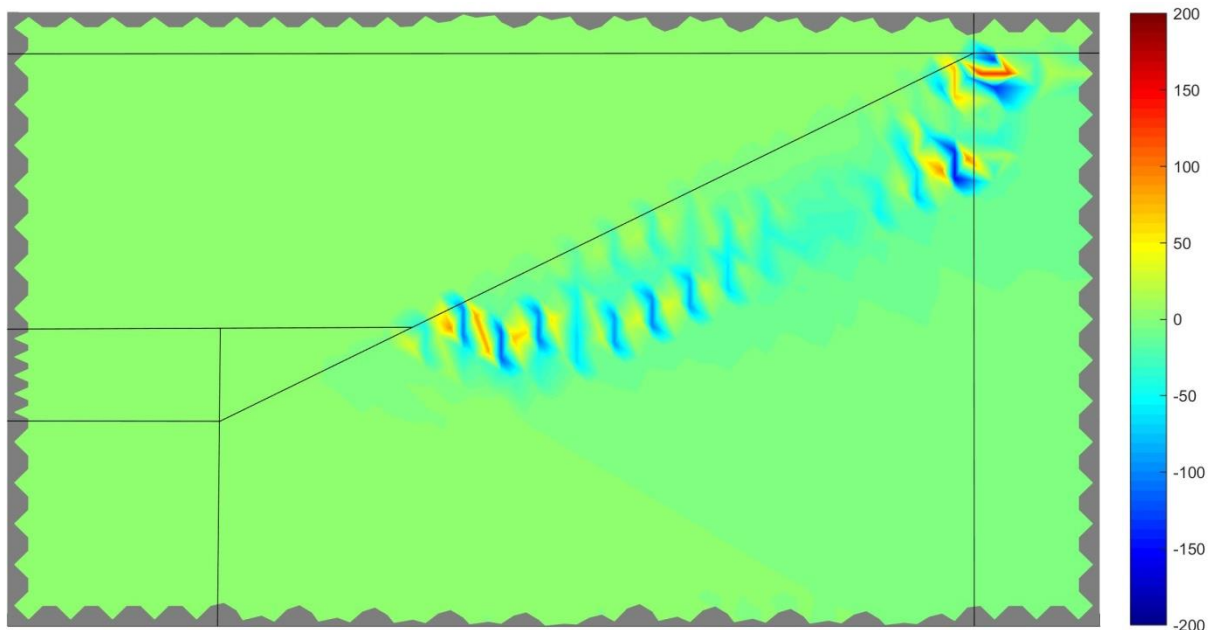
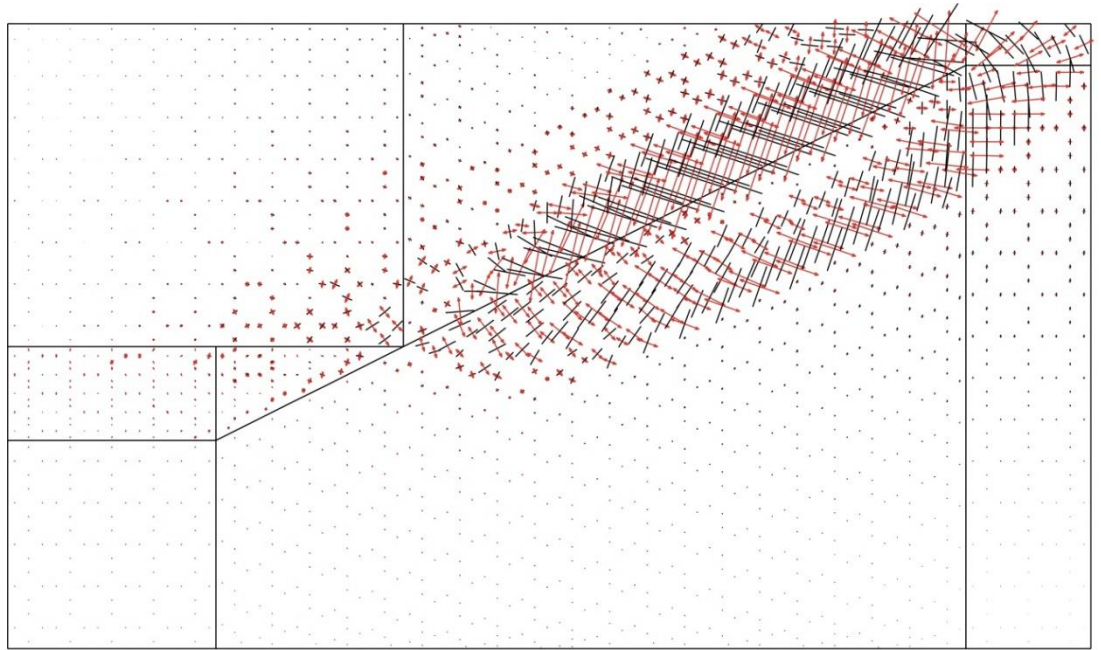


Figure 4.49: Excess pore pressure Phase 3(C) [Value Ranges: -160 kPa to 130 kPa]

Figure 4.50 illustrates the in-plane strain tensors generated within the elements in the slope and the submerging water. In the figure the strain pattern produced within the soil shows similarity to Case A, as expected large strain tensors were produced along the lower rupture zone as these elements experienced relatively large deformations considering they lie within the zone with the larger shear strain and flow. The strain decreases from there up towards the slope surface where the elements collectively move with little shear or any relative movement at all. Moreover similar to Case A, no strain tensors were experienced within the small patch of partially mobilized strength as depicted in figure 4.48, which again signifies that the elements experience negligible deformation, implying zero relative movements or shear.

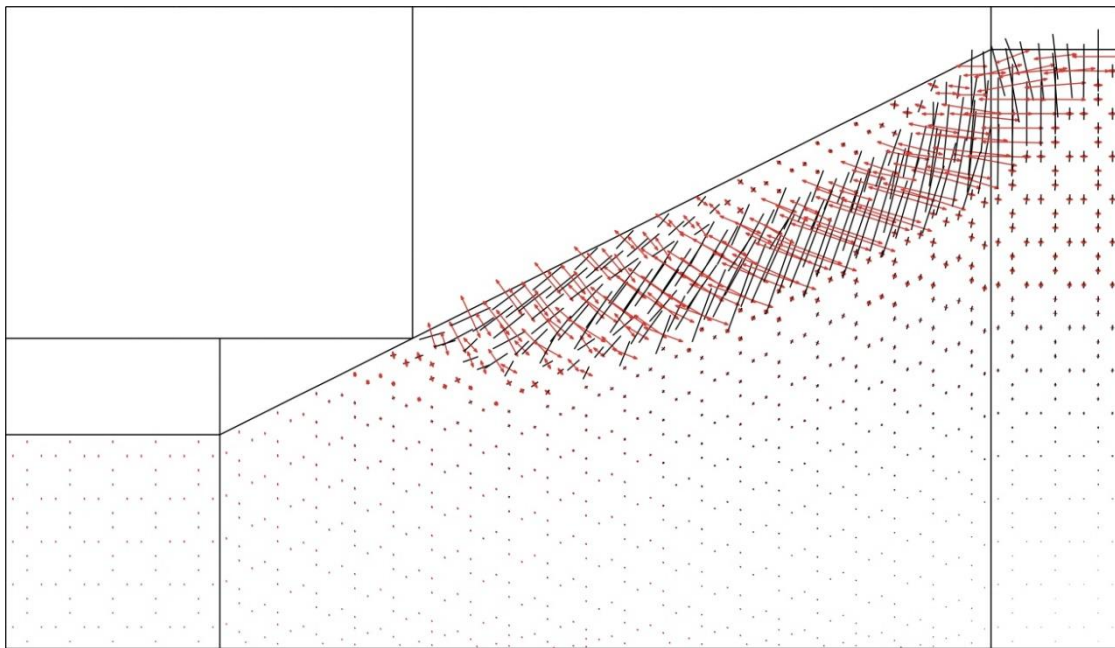
Apart from resemblances with Case A, similarities between this case and Case B can also be drawn. From figure 4.51, it can be observed that apart from the patch with near zero strain the pattern is identical to Case B corresponding to figure 4.36. Even the maximum and minimum principal values here i.e. 0.0317 and (-) 0.0326 are quite closely comparable to the limits obtained in Case B.



MESH OF INTEGRATION POINTS
IN-PLANE STRAIN TENSORS

TENSORS AT INTEGRATION POINTS
MAXIMUM PRINCIPAL VALUE:5.84E-02
MINIMUM PRINCIPAL VALUE:-5.84E-02

Figure 4.50: In-plane strain tensors phase 3(C) (*without excessive strained point)



MESH OF INTEGRATION POINTS
IN-PLANE STRAIN TENSORS

TENSORS AT INTEGRATION POINTS
MAXIMUM PRINCIPAL VALUE:3.17E-02
MINIMUM PRINCIPAL VALUE:-3.26E-02

Figure 4.51: In-plane strain tensors phase 3(C), only soil region

Further, an important and interesting aspect in figure 4.50, is the strain tensors in the water region along the slope interface. As can be seen, large strain tensors have been developed just above the slope interface. This signifies the deformation of the element and relative movements within them.

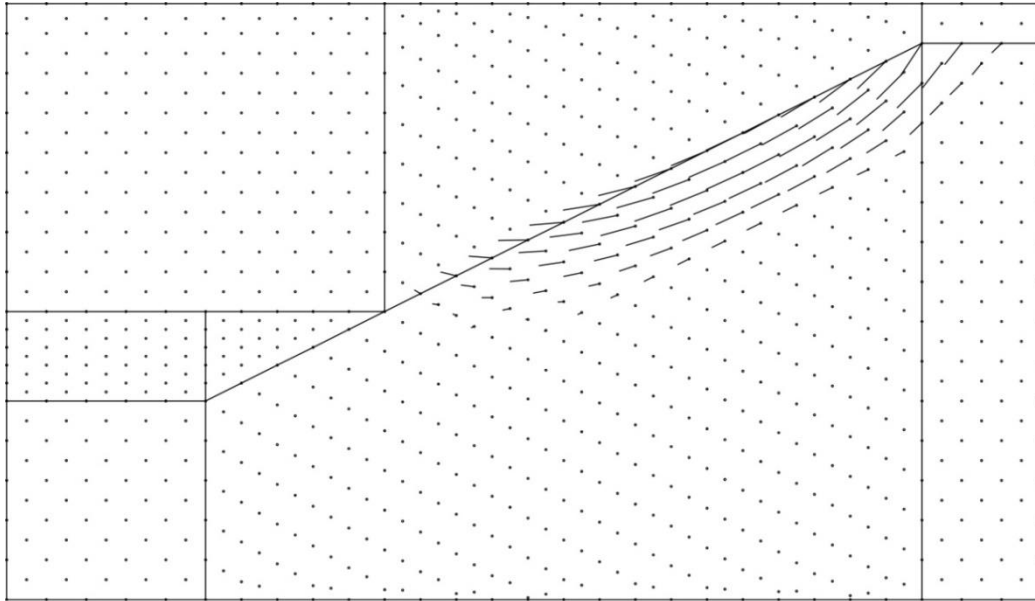
Further this was expected, since in an element that consists of interface nodes and fluid material nodes, the extent by which the interface nodes gets displaced are higher than by which the fluid material nodes do. This happens because only normal displacement component (not the shear) of interface will cause resulting motion in water just above it, considering very low shear viscosity of water.

Apart from this area between the interface and the water layer just above it, large strain tensors are also clearly evident in fluid regions above it. A clear thick strain tensor zone can be observed which reaches up towards the upper slope surface. The main contributing factor for these strain tensors are the two fluid circulation type formations and therefore overall differential nodal movements of the elements around them, figure 4.53 can be referred to for observing these circular water motions.

It can also be observed that the strain tensors in the fluid layer reduce strongly in size towards the water surface or left portions of the problem geometry, as here the elements collectively move in same direction thus they experience relatively less shear deformation. Additionally, within the dredged region some strain tensors can also be observed as the fluid elements within this region experience some relative movement too. However, the intensity of these deformations is fairly low, since the overall nodal displacements in this region remain quite low, as can be seen in figure 4.53. This result is in sharp contrast with the restrained results in the fluid block of Case B's corresponding figure 4.35 and further strengthens the argument stated earlier in that section namely that in the restrained case the observed strains and displacements in the dredged part are arbitrary and non-conclusive.

It shall also be noted that, in the above figure 4.50 deliberately one strain tensor value at the integration point in the triangular element just next to the toe of the slope in the dredged volume has been omitted. The obtained strain in that element was excessively large (about -15) and therefore it would shade off all other strains plotted in the figure. Appendix F, figure F1 is referred to for the strain tensors including the omitted point. The reason for such high strain experienced within the element is because it is positioned between the interface and fluid region, such that the fluid nodal parts of that element gets displaced more in comparison to negligible movements in interface nodes, as the interface still holds its position due to the remaining artificial loading. Figure F2 in Appendix F can be referred to for the magnified view on nodal displacement in the dredged part. It can be observed that the fluid part of the mentioned element shows right upward movement against the sloping direction, influenced by fluid motion from beneath. The whole occurrence of the fluid motion within the dredged part is due to artificial loading mechanism; replacing the complete dredged region with water, making these displacements and strains in the dredged region artificial. Consequently this might not occur in practical scenarios, where the removal of the dredged region will be done layer by layer.

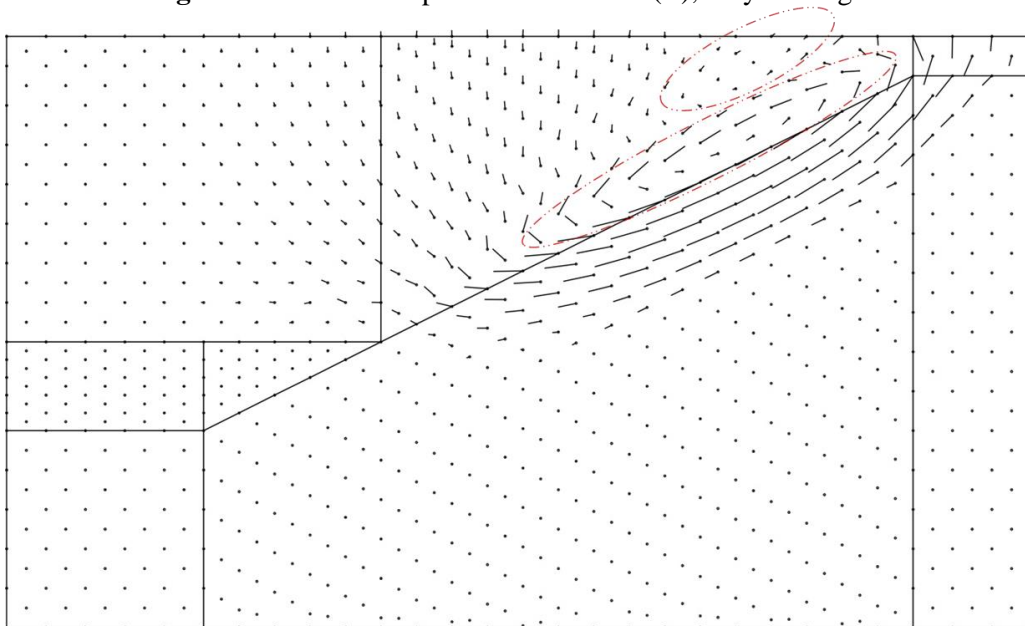
Next the nodal displacements within the soil region are illustrated by figure 4.52 while figure 4.53 shows the same for the complete problem geometry. Looking at figure 4.52 it can be observed that the shear zone pattern is almost identical to what was observed in the corresponding figure 4.38 of Phase 3(B). However the maximum achieved displacement in this case is 14 cm which is lower than what was observed in the restrained fluid Phase 3(B), which was 22 cm. As stated before this lower value than Case B, might be the result of dynamic interaction of submerging water on the slope interface which thereby slows the rate of liquefied flow.



MESH OF 4 TRIANGLES PER SQUARE
 NODAL DISPLACEMENTS IN LOADING PHASE
 MAGNIFICATION FACTOR ON PAPER:1.0E+00

NODAL VECTORS
 MAXIMUM VECTOR LENGTH:1.4E-01
 REAL-SCALED MAGNIFICATION:6.7E-02

Figure 4.52: Nodal displacements Phase 3(C), only soil region



MESH OF 4 TRIANGLES PER SQUARE
 NODAL DISPLACEMENTS IN LOADING PHASE
 MAGNIFICATION FACTOR ON PAPER:1.0E+00

NODAL VECTORS
 MAXIMUM VECTOR LENGTH:1.4E-01
 REAL-SCALED MAGNIFICATION:6.7E-02

Figure 4.53: Nodal displacements Phase 3(C) with marked circular formations

Furthermore, figure 4.53 gives an insight into the overlaying fluid mass movements due to soil-slope failure, thus also ensuring successful hydrodynamic coupling of the model. In total three main types of motion in the fluid can be observed due to pressure wave propagation from the failing soil slope into the overlaying fluid mass. The first type starting from the top of the slope surface, is the immediate downward movement of the fluid as the slope fails and moves down. The second type is near the toe, where the soil motion along the slope surface transits from outward and slightly

downward to horizontally outward and finally to outward and upward directions. This soil motion initiates a collective fluid movement in upward direction with mostly going outwards towards left of the problem geometry.

Apart from this, the dredged fluid region nodal movements are directly influenced by the aforementioned movements of nodes just above the dredged block. However as stated earlier this fluid region occurs due to the artificial loading mechanism, where the dredged block is completely replaced by water first and then the intergranular loading on the interfaces are applied artificially. Thus it is safe to say that the displacements generated in nodes within the dredged region are tailored to the current loading application and thereby can be deemed as artificial, which may not represent actual practical conditions. One way to resolve this issue and to bring the dredged region outcomes more closely to realistic situation, as mentioned earlier in section 3.6.4, is to perform layer by layer dredging. This can be achieved easily from this model in later works by simply subdividing the dredged part into several layers and thus applying similar load mechanism one after the other. However, for the current study this has not been considered for simplicity.

Moving on, finally the third major type of motion in the fluid and also the most interesting one to observe is the formation of the two fluid circulations and the motion of fluids within them, as marked in figure 4.53. Out of these two circularity formations the primary one, which is longest and occurs throughout along the rupture zone surface of the slope, is most probably formed due to the typical feature of translational flow slide. That is, rapid down leftward movement of soil particles at top regions of the rupture surface (crest of the slope in this case), whereas up and leftward movement of soil particles at the end regions of the rupture surface. On the other hand the secondary circular motion is the clear outcome of the interaction of primary circular motion and the shallow water levels.

It is to be noted that a similar circular motion of water above the slope has also been observed by Jiang et. al., (2015) in their work, where they too simulated a submarine flow slide coupled with a hydrodynamic model, which was shown in section 2.13 and figure 2.21. This similarity in the pattern thus asserts the occurrence of the primary circular fluid motion in the current case. Further, another secondary circular motion is formed at the top surface of free water due to interaction between the primary circulatory motion and shallow water levels, which thereby influences the surface impulse waves.

This particular development in fluid motion distinguishes this computational model from most of the conventional practices, both experimental and computational, where the submarine landslide based tsunamis are simulated or predicted based on using rigid or viscous sliding blocks, as discussed in section 2.2. Further, comparing the results with the conventional studies (refer to figures 2.32 and 2.33), where no such circular motions are formed during the generation phase of impulse waves, re-assures the fact that indeed the shape of the soil rupture zone affects the water movements. Moreover, this observation further asserts the claim that the conventional studies may still predict close results of tsunami genic waves, for subaerial or partial submerged rock block slides or even granular slides over the submarine slope. However their prediction might remain conservative for the flow liquefaction based translational submarine landslides at the initial stages of failure. Since, due to the fact that they do not apply or produce realistic slope failure rupture zones in case of a translational flow slide, especially the sloping edges at both ends of the rupture surface, they usually fail to simulate the fluid circular motion shown in figure 4.53. Thus this may lead to the over-estimation of the height of the impulse wave formations. Here the reduction of potential energy in soil is directly observed by the increase in crest or trough of the impulse wave, whereas in case of circulatory formation the energy is

observed partially by the circular motion of water and thus the impulse wave produced in such scenario is of lower amplitude.

Furthermore, the impulse wave generated on the water surface throughout the time can be observed through figure 4.53. From the figure looking at the final stage impulse waves at $t = 1.5$ s and also the nodal displacement on the surface shown in figure 4.53, certain level of similarities in the pattern can be observed with what was produced through the conventional methods and studies. In a broader sense, the obtained nodal displacement pattern on the surface from figure 4.53 can be compared with figure 2.28, at $t = 0.75$ sec. From this it can be observed, that similar to the literature work result, the surface nodal displacements represent one major elongated crest towards the left and a downward motion of the slope and one deep crest towards the top right due to the downward movement of the slope (refer to figure F3 in Appendix F, for magnified view on nodal displacements). However, in case of literature work (ex. figure 2.28), the surface shape occurs when the rigid wedge has already passed the wave generation phase and in mid run-up position as compared to here, where the observation occurs during the generation phase. This difference can mainly be attributed to the fact that the slope here is completely submerged 2m down the water, where in the case of the wedge it moves right from the surface of the water. Therefore in the literature case the trough is fully formed only once the wedge has moved down to certain depth, as compared to here where both the trough and crest are immediately formed as soon as the slope fails; this is also evident in figure 4.54.

Additionally, looking at the final form of the impulse wave more closely through figure 4.54 at $T = 1.5$ s, it can be observed that in total two waves have been formed, out of which the smallest amplitude crest and trough in between the elongated heightened crest and deepest trough is formed due to the secondary circular motion of water on the surface as marked in figure 4.53. Nonetheless this initial wave pattern is still comparable to graphs produced by several literature works discussed in section 2.2.2. While ignoring the pulsation formed by circular water motion on the surface, thus observing the elongated crest and deep trough in figure 4.54, it can be observed that the pattern of 1st (primary) wave formed in figure 2.27 at $t = 1$ sec and in figure 2.28 at $t = 0.75$ sec closely follow to what is produced in here.

However as mentioned before in the literature works these comparable wave patterns are formed when the wedge is in the run-up phase and within certain depth, thus in these figures a secondary wave is also formed as discussed in chapter 2. On the contrary, here the pattern is formed in the wave generation phase thus no such secondary wave is observed.

Moreover, besides this comparison, observing the impulse wave buildup throughout time in figure 4.54, it can be seen that up until 1 sec mark, the rate by which waves developed was limited. However once crossing this marks as the soil starts to fail and becomes dynamic, the wave build up shows an exponential increment with the highest increment observed at $t = 1.5$ sec. By this time the soil-slope has mostly liquefied and the motion has become highly dynamic, thus displacing more water per time increment. Further as discussed earlier, the initiation of the waves takes place simultaneously. However observing the trough formation between 44 and 52 m i.e. the position of top right water surface, it can be observed that the nodes within 50m and 52 m show drastic downward movements relatively late, effectively after 1.3 s. This can be reasoned as follows: The rupture zone progressively develops with short duration of time, thereby affecting the time at which the corresponding surface nodes get triggered. Again it should be noted that such progressive rupture development with time cannot be replicated by rigid block sliding and although possible with viscous slides but still it might be at least difficult to control the rate for which another constraint for realistic landslide and impulse wave developments would be needed. On the other hand with this model, with the geotechnically

backed slope model in coupling with the free water hydrodynamics this phenomenon is more realistically simulated.

Apart from this, the surface wave reaches the maximum crest of 23.67 mm and trough of about -82.64 mm at the end of the calculation, which are relatively low. However, given the size of the liquefied mass it is fair to expect that the waves at the current stage of calculation are under developed and may grow further in case of a full propagation of the landslide is modeled. Moreover, looking at the maximums in both trough and crest throughout the time period it can be said that the waves are moving towards the left of the problem geometry. This was expected as literature suggests that underwater landslide produces both near-field and far-field wave energy directivity along its axis of failure (Watts, 2001).

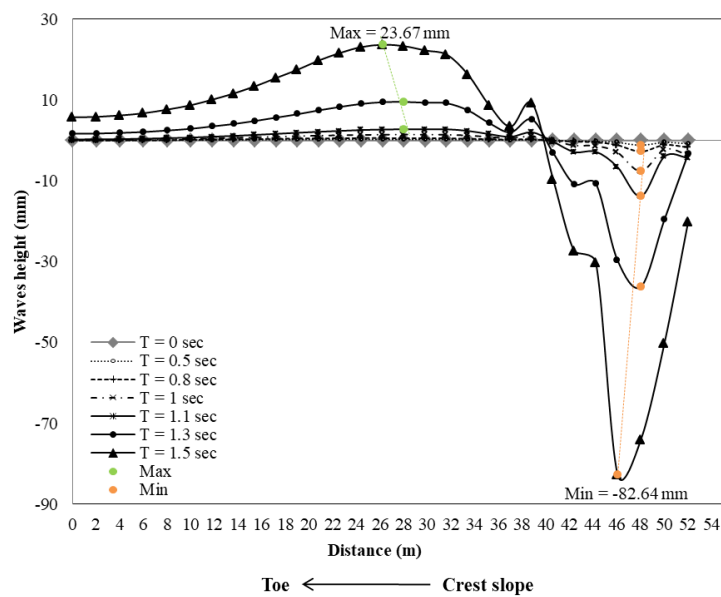


Figure 4.54: Impulse wave generation with time for Phase 3(C)

Figure 4.55 can be referred to in order to view the normal component of free water surface displacement with respect to normal component of interface displacement at $t = 1.5$ s. It is to be noted that considering the motion of submerging water is governed by a pressure wave, thus the normal component of interface displacements were opted to draw the co-relation. It can be seen that at the shallow water range between 52 to 33m, the surface wave mostly follows and reflects the interface displacements. However, it can be observed that the peak normal displacements values of interface are higher i.e. 43.92 mm and -109.34 mm, than in comparison to surface water i.e. 23.67mm and -82.63mm. Additionally, the free surface water motion is more disperse than the slope interface itself. These differences are understandable, since the normal component of interface displacement not only influences the vertical motion of the submerging water but also the horizontal one.

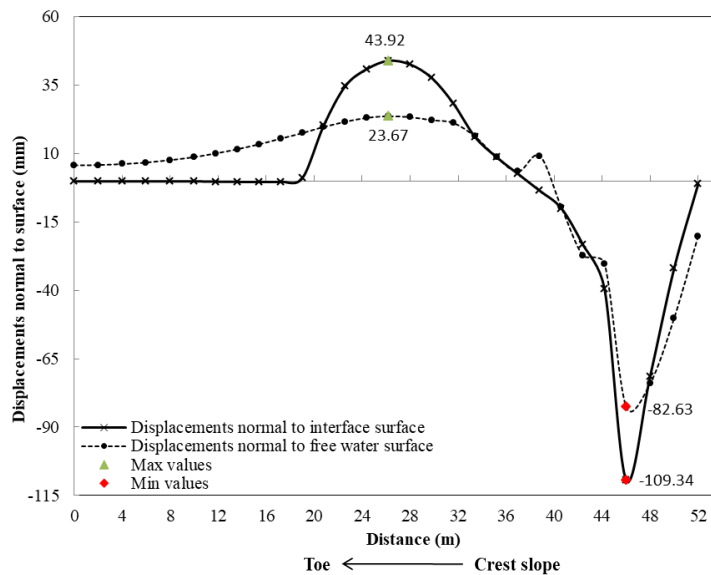


Figure 4.55: Displacement normal to interface surface vs displacements normal to free water surface, at $t = 1.5s$.

Next, figure 4.56 can be referred to in order to compare the change in ‘*elevation*’ pressure head at the soil interface due to the relative change in the levels of the free water surface and the interface, at the time of instability ($T = 1s$) and at the end of the analysis ($T = 1.5s$). At the time of instability i.e. at $T = 1s$, the figure indicates some level of change in elevation heads around the slope crest. However, with change in elevation heads ranging between 4.54 mm and -3.27 mm, the overall change can be considered to be marginal. This therefore suggests that at the initiation of instability, the contribution of submerging water in terms of change in elevation pressure head at the interface is negligible.

On the other hand, at the end of analysis i.e. at $T = 1.5s$, figure 4.56 indicates relatively significant changes. It can be observed that at the range of horizontal locations around 52 – 47m, which concerns the upper surface of the slope, the elevation head decreases from its initial rest position at ($t = 0s$). The minimum change observed to be of -19 mm at 52m of horizontal distance. However, the elevation head rises after about a horizontal distance of 47 m up-till 0 m, while reaching a maximum of about 71.6 mm at around 39 m of horizontal distance. Observing this elevation head change pattern, it can be considered to be one of the factors affecting the liquefaction rate (post-instability) in the current scenario Case C as compared to Case B.

Apart from the change in submerging water elevation heads, it is important to note that the *inertial loads* due to the submerging water motion at the interface may also play a role during both; the initiation of instability ($T = 1s$) and post instability liquefied flow ($T > 1s$). However at the current level of work from the processed outcomes, it is difficult to present an exclusive comparison for the same.

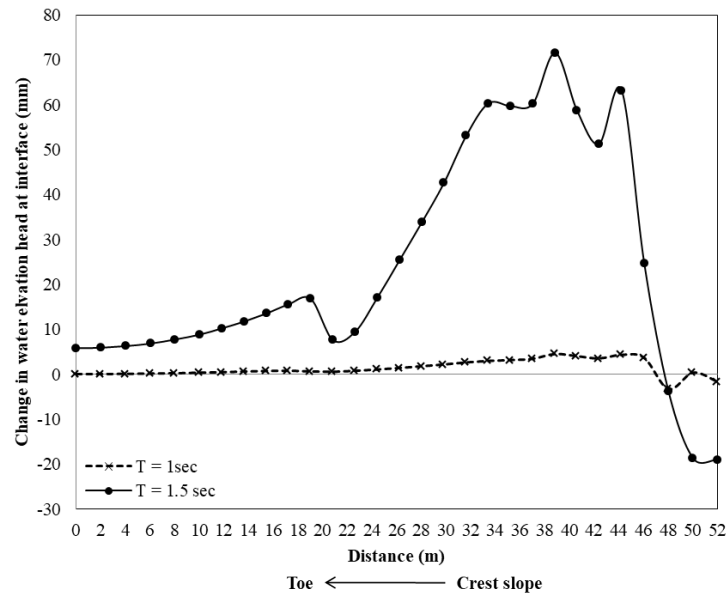
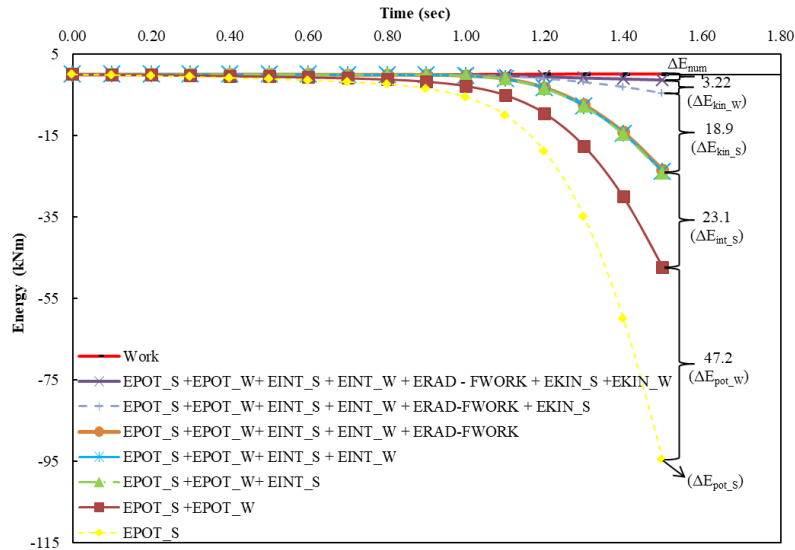


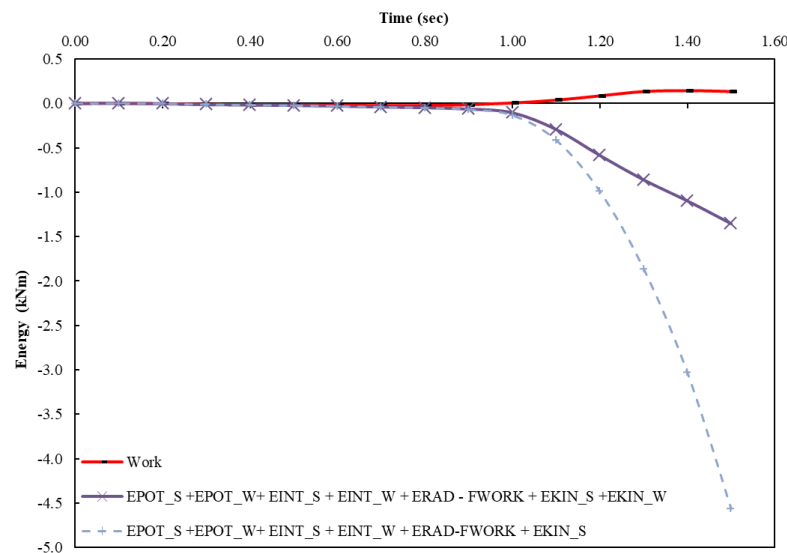
Figure 4.56: Change in water elevation head at the interface w.r.t initial rest position.

Finally, different forms of energy transitions in the system till the end of this analysis can be looked upon through figure 4.57(a). Here, similar to the restrained fluid block Case B, it can be observed that the reduction in soil potential energy starts to increase drastically at about $t = 1$ sec, when the soil slope fails and liquefies. However the extent of this reduction is slightly smaller than what was observed in case B i.e. 94.5 kNm per unit of the length normal to the plane of deformation. This might be because the dynamic interaction of the submerging water might provide some resistance to liquefied flow. Furthermore, a more distinguishing factor here is the larger soil potential absorption by the potential energy of water, as the calculated percentage ratio of mobilized soil potential energy by the water potential is about 49.9 % (note: it is an energy stored by whole water mass, not to be confused by wave energy). This is comparable with the previous Case B's contribution of the follower type of loading (due to assumed constant water level) in the mobilization of the potential energy of the soil. This also indicates here that the major part of the contribution by the follower type of loading in the previous case has been replaced by the potential energy of water. The contribution of the internal stress-strain energy of soil in the reduction of the soil potential is calculated to be 23.36%, which again is comparable to the previous Case B's corresponding parameter. With this observation, consequently it can be said that in this case the initial contributing factors in the reduction of the potential energy of the soil are the potential energy of water and the internal energy of soil.

Next, in this case the observed internal stress-strain energy of water is quite negligible, as it can be seen in the plot that the corresponding energy curve almost coincides with the curve of the combined potential energy of the soil, water and internal energy of soil. Further, also as expected since in this case the follower type of loading is zero, no contribution exists.



(a)



(b)

Figure 4.57: Energy transitions Phase 3(C); a) all forms of energy contribution, b) magnified plot for kinetic energies contribution

Moving on, similar to Case B, here as well once the slope’s instability state is crossed; kinetic energies get triggered and become more and more prominent progressively as the soil liquefaction increases and the system becomes increasingly more dynamic. Again forming analogy to previous Case B here it can also be observed that the third major contributing factor to reduction of soil potential energy is kinetic energy in soil. The calculations shows about 19.96% of the potential energy mobilization by the kinetic energy of soil, which is slightly lower than Case B, as here some portion of soil along the slope does not completely liquefy which is evident in figure 4.48. Next, the calculation shows about 3.4% contribution of the kinetic energy by water in mobilizing the potential energy of soil in this case, which is slightly more than in Case B, as expected due to fluid blocks activation. Lastly, with all the percentages contribution of energies in mobilizing potential energy of soil, the loss in numerical accuracy is calculated to be 2.2%, which is 1% higher than in Case B.

Finally with above observations, it can be said that in this case the follower type of loading energies from Case B, have been completely replaced by the combination of potential energy (major contribution) and kinetic energy of water (marginal contribution).

Moving on, apart from the different forms of energy transitions, it can be noted from the figure 4.57(b), that the contribution of kinetic energy by water practically initiates only after the initiation of instability at $t = 1s$. Considering that the kinetic energy reflects inertial material forces, this observation therefore indicates that at the initiation of instability the contribution of inertial loads due to the submerging water motion at the interface should be negligible. Thus this observation along with the earlier remark from the figure 4.56 (at $t = 1s$), ultimately suggests that the cause of a difference in occurrence of instability between current Case C and Case B is most probably due to the induced numerically inaccuracy in the previous Phase 2(C) (fluid activation) calculations.

5

Conclusion

5.1 Primary research conclusions: Effect of submerging water on liquefying slope

- a) The preliminary comparison of undrained soil response in terms of *occurrence of instability* from figures 4.30 and 4.45, between Case B (at $t = 1.4s$, a case with constant hydrostatic pressure heads due to assumed water level) and Case C (at $t = 1s$, a case with fully coupled hydrodynamic interaction between submerging water and the soil) suggests that the fully coupled submarine slope models might experience an earlier failure than the uncoupled scenarios. However, the closer investigation of Case C results (refer figure 4.56 and 4.57 (b)), suggests an insignificant change in elevations heads and inertial forces at the interface due to submerging water mass at the occurrence of instability. This hence indicates that the difference in occurrence of instability has mainly risen due to the induced numerical inaccuracy of the fluid activation Phase, which therefore clearly needs further investigations. Nonetheless, the above observation may still suggest that the use of an uncoupled approach such as in Case B may still lead to a reasonable outcome for the occurrence of instability by liquefaction of submarine slopes.
- b) The *post-instability* comparison between the fully coupled model (Case C) vs uncoupled model (Case B) in terms of results such as: normal effective stress on plane (see figures 4.32 and 4.47), mobilized deviatoric strength (see figures 4.33 and 4.48), extent of nodal displacements (see figures 4.38 and 4.52), total reduction of potential energy of soil at the end of calculation (see figures 4.39 and 4.57), all suggest that in case of the fully coupled model the rate of liquefied flow decreases relatively. However the results of the final in-plane effective stress tensors (see figures 4.31 and 4.46) and excess pore pressures (see figures 4.34 and 4.49) achieved in soil were quite comparable between the two scenarios and thus no conclusive argument could be made through them.

One of the probable factors affecting the liquefaction flow rate might be the changing submerging water elevation head at the interface (see figure 4.56), post-instability. The change in elevation head pattern at the end of the analysis shows a decreasing trend at the upper surface of the slope and an increasing trend along the slope. At this stage of work an exclusive contribution of inertial loads of submerging water on soil, which may also influence the liquefaction flow, could not be processed. Therefore this topic needs more attention in future works.

- c) The *energy transition* comparison indicates that in case of fully coupled model (Case C) (see figure 4.57 (a)) the calculated potential energy and kinetic energy of water consumes similar proportions of soil potential energy as compared to that of follower type of energy due to constant hydrostatic loading in uncoupled model (Case B) (see figure 4.39). The percentage of mobilization of the potential energy of the soil by other forms of soil energies such as internal energy and kinetic energy remains quite similar in both the scenarios.

Moreover, the fully coupled Case C suggests that about 50% of the loss in the potential energy of soil is consumed by the potential energy of water at the very initial stages of post-instability and that the contribution of kinetic energy by water amounts to mere 3.4%. However it is important to note that this factor of absorption by potential energy of water is only valid for the initial stages of failure. As it is known that as the slide progresses the kinetic energies in water and soil will become more prominent and eventually heat will start to play role. At that time the absorption ratio of potential energy of soil by potential energy of water is expected to drop (Jager 2018).

5.2 Secondary research conclusions: Submerging water motion due to liquefying slope

- a) The results of the fully coupled scenario (Case C) (see figure 4.53) show that in response to the submarine liquefied slope failure the *submerging water motion* gets actively dispersed. This induces an almost simultaneous surface level change throughout the length of the considered geometry, leading to a full length wave formation at the same time (see figure 4.54). The main highlight of the submerging water motion is the formation of two circular fluid motions (refer to figure 4.53), thereby showing a visible influence on the surface wave (see figure 4.54) as a bulge or pulsation. The probable cause of the formation of such circular fluid motion along the slope is considered to be the effect of the shape of the flow mechanism of the collective motion of liquefied soil.

Further, it was observed that the undulations of the impulse wave closely reflect the movements of the normal displacements of the slope interface (see figure 4.55). At the end of calculation, i.e. at $t= 1.5s$, in total two waves are formed at the free water surface, where the highest elongated crest of 23.67 mm and the deepest trough of -82.64 mm were observed in response to the peak normal displacements of the slope interface, being 43.92 mm and -109.34 mm respectively. Considering the size of the soil mass failure, it is speculated that the observed peak surface elevations at the end of the calculation are pre-mature and may further increase if the case of a full extent of slope deformation would be simulated. Moreover, based on the progression of the impulse wave throughout time it was concluded that the direction of impulse wave movement was along the direction of the slope failure, which literature such as Watts (2001) suggests as well.

- b) Comparing the submerging water motion of the *current model with the literature*, incorporating conventional methods of landslides simulation such as: rigid or viscous sliding wedges for wave modelling, the main difference is the presence of circular fluid motion along the slope (just above the interface) in the current model. A Similar pattern of circular fluid motion was reported in the fully coupled study done by Jiang et. al., (2015) on submarine liquefaction flow slides, thus supporting its formation in the current model. Considering, that such difference in motion is caused by the more realistic shape of the liquefied flow mechanism and its absence from most of the conventional methods of study, indicates an advantage of fully coupled modeling. The absence of such circular fluid motion along the interface in conventional studies might also indicate an overestimation of surface wave elevation at the very initial phase of wedge sliding, since these motions partially consume the loss of potential energy of the soil failure mechanism. Some of the key characteristics, that this model incorporates in order to simulate more realistic liquefied flow than conventional sliding wedge studies (e.g., Heinrich, 1992, Abadie et al., 2008) or experimental granular slides (e.g., Rzadkiewicz et. al., 1997), are as follows:

- Distributions of the density and effective stress state of the soil.

- Loading history of the soil, potentially inducing heterogeneity, including historic slip surfaces, which could be reactivated.

Furthermore, the calculated surface (impulse) wave pattern (see figure 4.53 and 4.54) suggests that the formation of in total two waves were mainly due to the intermediate bulging or pulsation which formed because of the secondary circular fluid motion as a result of the interaction between the primary circular motion along the slope and the shallow water level. However keeping this bulging aside, the undulations in the surface indicate one elongated heightened crest formation along the slope failure and one shortened deep trough at the upper surface of slope failure. This observation was consistent with the results of the early stage landslide induced general wave patterns reported in literatures such as: Heinrich (1992) and Cremonesi et. al., (2011).

5.3 Tertiary research conclusions: Limitation and recommendations

Having critically evaluated the performance of the current model; the following limitations of the model have been encountered, enabling the following recommendations and future scope of the work:

- *Dredging mechanism* – The current modified approach to the dredging mechanism was to replace the dredged material with water first and apply virtually the equilibrating intergranular traction forces around dredged boundary, which than uniformly are reduced to simulate unloading. This modification in current research was initially implemented in order to avoid the concern of the previous work model (Molenkamp, 1999), where the material is dredged by reducing the buoyant weight of the soil uniformly. The main disadvantage of that previous model approach observed was that the numerically dredged soil could reach an ill-defined effective stress state, while converting into water as the remaining buoyant weight of the soil approaches zero. The current approach avoids this potential numerical problem due to ill-defined effective stresses. However, observing the huge difference in time of occurrence of instability between the pilot test i.e. Case A (at $t = 1.5$ s) and the previous model (at $t = 22$ s), raises the question of underestimating of the soil strength by the current approach. The probable cause of such early failure in the current model is identified to be the uniformly unloading of a large block of dredged material in one long unloading period. Thus it is recommended for future works, in order to remain more realistic, that the dredged region should be sub-divided into smaller layers, which subsequently should be removed layer after layer.
- *Hour glass effect and mesh refinements* – Literature such as Pastor et. al., (1999) suggests that the elemental arrangement implemented in the current model i.e. bilinear quadrilaterals, divided into four 3-node triangular elements, avoid shear locking. However, the results of excess pore pressure fields (see figures 4.16, 4.34, 4.49) show another type of numerical shortcoming, a like the hour glass effect (see Appendix G), namely leading to the alternate contraction and dilation of the neighboring triangular elements. This is a common problem in computational soil mechanics; Appendix G can further be referred to for the additional details on the characteristics of hour-glass eigenmodes of the opted finite elemental arrangement. One approximate solution to it in the current scenario is to average the values of the 4 triangular elements of each bilinear quadrilateral. Such process is referred to as smoothening of the numerical solution and could be used in future works for better pore pressure field visualization.

Another better, but much more fundamental approach involves the development and application of quadrilateral analytical finite elements, satisfying the equilibrium conditions of the effective stress field throughout the whole finite element. The analytical solution in terms of a

series of displacement functions enables to express the continuous stress tensor field for a particular constitutive elasto-plastic model like Mohr-Coulumb. Rohe (2013) was able to practically finish the analytical formulation and its numerical implementation, but did not reach the level of application. It is recommended to finish and apply the analytical description in FE-analysis in order to avoid local hour-glass effects for future applications.

Other than this while comparing the excess pore pressure field of Case A and Case B (see figures 4.16 and 4.34), which mainly differs in terms of applied mesh refinements, it was observed that in case A, where the mesh is more refined though elements are non-uniformly arranged along the interface, shows more prominent effect of hour glass locking than Case B (a uniform and relatively coarser mesh along slope). This therefore needs further attention in case of future work. It is suspected that this mainly occurs due to the non-uniform element size distribution within the bilinear quadrilaterals in Case A (see figure 3.3). Apart from this, most of the results between Case A and Case B were quite comparable. In general Case A shows 0.1s of delay in total running time of the program and also in the occurrence of slope instability, as compared to Case B. Thus Case A indicates higher accuracy due to refined mesh along the slope. Overall it can be recommended from these observations that for future work, element distribution should be kept uniform and finer than Case B, in order to improve accuracy.

- *Shake down effect* – From the pilot test Case A results (see figure 4.12 and appendix figure D1) it was observed that the numerical error induced due to the shake down effect in Phase 2 (initial state with drained unloading phase), effects the soil stress state in terms of early occurrence of instability in subsequent dredging phase (difference of about 2.5s observed). Additionally, it is suspected to be the probable cause for the sensitivity of the fluid activation phase 2(C). Thus to increase accuracy this effect has to be reduced in future works. Although, it is to be noted that this factor alone does not affect the research outcomes, as it's a commonly induced numerical error in soil initial effective stress state for all the implemented cases and since the research work is mainly a comparative type of study.
- *Fluid activation phase* – The analysis carried out in the fluid activation phase i.e. Phase 2(C) suggests that the effective stress-state of the dredging phase in the fully coupled scenario (Case C) are highly sensitive towards the time set options (i.e. time of loading and time step) opted for Phase 2(C). This therefore raises the doubt that the induced numerical inaccuracy in the fluid activation phase might also be the contributing factor to the differences observed between fully coupled Case C and uncoupled Case B. Thus, this phase needs further attention in future work to scale down any additional numerical discrepancies/inaccuracies accumulating under this phase calculation and hence to have more conclusiveness from the outcomes.
- *Fluid numerical model* – From the fluid tank test in section 3.8, it was observed that for the current studied range of time limits the model will produce reasonable results. However, it was observed that the numerical model shows excitation for later periods of pressure wave propagation. Thus, this model needs improvement to avoid such excitation, in case a full scale of large continuous flow of submarine landslide is simulated in future. Probable solution that might work will be the mesh refinements and smaller time steps. Nevertheless, the cause of numerical excitation needs further investigation
- *Slope-water interface* – Considering the coarseness of the mesh used in case C along the interface in fluid region, the effect of shear slip could not be simulated. One possible way to properly simulate this affect would be by implementing repetitive mesh refinement near the interface in the submerging water region, till the effect of shear slip becomes ineffective with respect to the refinements. The outcomes of the approach can then be compared to the current model results. It is

expected that the shear slip will have little effect on the overall fluid motion presented in the results (refer to figure 4.53).

- *Advanced numerical approach* – As the current model is bounded in terms of time limit restriction based on the element size, mesh refinement in future work can also increase the extent of liquefied flow. However, to evaluate the full extent of submarine landslide it is important to implement an advance computational approach which uses re-meshing algorithms such as ALE and MPM. Apart from this, it is also important to update the model in order to simulate phenomena such as consolidation and turbidity (Jager, 2018) especially during the post liquefaction flows.
- *Experimental evaluation*, of the model is needed; physical modelling such as in large liquefaction tank can be performed, in future.

References

1. Abadie. S., Grilli. S. and Glockner. S., (2006), “*A Coupled Numerical Model For Tsunamis Generated By Subaerial And Submarine Mass Failures*”, Coastal Engineering 2006: pp. 1420-1430.
2. Abadie. S., Morichon. D., Grilli. S. and Glockner. S., (2008), “VOF/Navier-Stokes Numerical Modelling of Surface Waves Generated by Subaerial Landslide”, La Houille Blanche, (1), pp: 21-26.
3. Abadie. S., Morichon. D., Grilli. S. and Glockner. S., (2010), “*Numerical Simulation of Waves Generated by Landslides Using a Multiple-Fluid Navier-stokes model*”, Coastal Engineering, (57), pp: 779-794.
4. Andersen. K. H. and Schjetne. K., (2012), “*Database of Friction Angles of Sand and Consolidation Characteristics of Sand, Silt and Clay*”, Journal of Geotechnical and Geoenvironmental Engineering, ASCE (139 – 7), pp: 1140–1145.
5. Aghajani. H. F., Salehzadeh. H. and Shahnazari. H., (2015), “*Stability Analysis of Sandy Slope Considering Anisotropy Effect in Friction Angle*”, Sadhana, Indian Academy of Science, (40-6), pp: 1955-1974.
6. Atigh E., Byrne P.M., (2003), “*Flow Liquefaction Failure of Submarine Slopes Due to Monotonic Loadings — An Effective Stress Approach*”, In: Locat J., Mienert J., Boisvert L. (eds) Submarine Mass Movements and Their Consequences. Advances in Natural and Technological Hazards Research, vol 19. Springer, Dordrecht
7. Azizian A., Popescu R., (2005), “*Finite element simulation of seismically induced retrogressive failure of submarine slopes*”, Canadian Geotechnical Journal, Vol. 42(6):1532-1547. <https://doi.org/10.1139/t05-032>
8. Babuška, I., (1973). “*The finite element method with Lagrangian multipliers*”. Numerische Mathematik, Vol. 20(3), 179-192.
9. Brezzi, F., (1974). “*On the existence, uniqueness and approximation of saddle-point problems arising from Lagrangian multipliers*”. RAIRD, Vol. 8(R2), 129-151.
10. Byrne. P. M., Puebla. H., Chan. D. H., Soroush. A., Morgenstern. N.R., Cathro. D. C., Gu. W. H., Pullips. R., Robertson. P. K., Hofmann. B. A., Wride. C. E., Sego. D. C., Plewes. H. D., List. B. R. and Tan. S., (2000), “*CANLEX Full-Scale Experiment and Modelling*”, Can. Geotech. J., (37), pp: 543-562.
11. Berg. J. H. Van Den., Gelder. A. Van. and Mastbergen. D. R., (2002), “*The Importance of Breaching as a Mechanism of Subaqueous Slope Failure in Fine Sand*”, Sedimentology, (49), pp: 81 – 95.
12. Boldini. D., Wang. F. W., Sassa. K., and Tommasi. P., (2005), “*Mechanism of landslide causing the December 2002 tsunami at Stromboli volcano, in Landslide: Risk Analysis and Sustainable Disaster Management*”, edited by K. Sassa et al., pp. 173 – 180, Springer, New York.
13. Burkardt. J., (2010), “*triangulation_order3_contour*”, matlab code, licensed by GNU LGPL.
14. Beinssen. K., Neil. D.T. and Mastbergen. D. R., (2014), “*Field Observations of Retrogressive Breach Failure at the Two Tidal Inlets in Queensland*”, Australia, Australian Geomechanics49(3): 55–64
15. Bandara. S. and Soga. K., (2015), “*Coupling of Soil Deformation and Pore Fluid Flow using Material Point Method*”, Computers and Geotechnics, (63), pp: 199-214.
16. Beddoe. R. A. and Take. W. A., (2015), “*Influence of Slope Inclination on the Triggering and Distal Reach of Hydraulically-Induced Flow Slides*”, Engineering Geology, (187), pp: 170-182

17. Bhandari. T., Hamad. F., Moorman. C., Sharma. K.G. and Westrich. B., (2016), “*Numerical Modelling of Seismic Slope Failure using MPM*”, Computers and Geotechnics, (75), pp: 126-134.
18. Peelen. G., (2016), “*Breach Flow Slides*”, MSc Thesis, Delft University of Technology (Delft, The Netherlands),
19. Castro. G., (1969), “*Liquefaction of Sands*”, Ph.D. thesis, Harvard University, Cambridge, Massacutes.
20. Chiocci. F. L., Romagnoli. C., Tommasi. P., and Bosman. A., (2008), “*The Stromboli 2002 Tsunamigenic Submarine slide: Characteristics and Possible Failure Mechanisms*”, Journal of Geophysical Research (113- B10102).
21. Cremonesi. M., Frangi. A. and Perego. U., (2011), “*A Lagrangian finite element approach for the simulation of water-waves induced by landslides*”, Computer & Structures (89), Issues 11-12, pp: 1086-1093.
22. Chu. J., Wanatowski. D., Loke. W.L. and Leong. W.K., (2015), “*Pre-Failure Instability of Sand Under Dilatancy Rate Controlled Conditions*”, Soils and Foundations, (55-2), pp: 414-424.
23. Davim. J. P., (2017), “*Computational Methods and Production Engineering Research and Development*”, The Officers’ mess Business Center, Royston Road, Duxford, CB22 4QH, United Kingdom, Woodhead Publication, Elsevier.
24. Edgars. L. and Karlsrud. K., (1982), “*Soil Flows Generated by Submarine Slides – Case Studies and Consequences*”, Nor. Geotech. Inst. Bull 143 (1982): 1-11.
25. Eckersley. D., (1990), “*Instrumented Laboratory Flowslide*”, Geotechnique, Issue (40 -3), pp: 489-502
26. Fryer. G. J. and Watts. P., (2001), “*Motion of the Ugamak Slide, Probable Source of the 1 April 1946*”, ITS 2001 Proceedings, Session 6, Number 6-6, pp: 683-694.
27. Fritz. H. M., (2002), “*Initial Phase of Landslide Generated Impulse Waves*”, Doctor of Technical Science at ETH Zurich, Switzerland.
28. Fine. I.V., Rabinovich. A.B., Bornhold. B.D., Thomson. R.E. and Kulikov. E.A., (2005), “*The Grand Banks landslide-generated tsunami of November 18, 1929: preliminary analysis and numerical modeling*”, Marine Geology (215), Issues 1-2, pp: 45-57.
29. Gregersen. O., (1981), “*The Quick Clay Landslide in Rissa, Norway; The sliding Process and Discussion of Failure modes*”, Norwegian Geotechnical Institute, Publication No. 135, Oslo.
30. Guzman, A. A., Leonards, G. A. & Chameau, J. L., (1988), “*Undrained monotonic and cyclic strength of sands*”, Journal of Geotechnical Engineering Am. Sot. Civ. Engrs, (114 – 10), pp:1089-1 109.
31. Gadala. M. S. and Wang. J., (1998), “*ALE Formulation and its Application in Solid Mechanics*”, Comput. Methods Appl. MEch, Engrg. (167), pp: 33-55
32. Grilli. S.T. and Watts. P., (2005), “*Tsunami Generation by Submarine Mass Failure. I: Modeling, Experimental Validation, and Sensitivity Analyses*”, Journal of Waterway, Port, Coastal, and Ocean Engineering (131), Issue 6.
33. Groot. M. De., Lindenbergh. J., Mastbergen. D. and Ham. G. Van den.,(2018), “*Liquefaction Flow Slide in Large Flumes*”, International Journal of Physical Modelling in Geotechnics, ICE- Institution of Civil Engineers.
34. Heinrich. P., (1992), “*Nonlinear Water Waves Generated by Submarine and Aerial Landslides*”, Journal of Waterway, Port, Coastal and Ocean Engineering, (118 – 3), pp: 249 – 266.

-
35. Hicks, M.A, (1995), “*MONICA, A computer algorithm for solving boundary value problems using double strain-hardening constitutive law Monot. part 2. Algorithm validation*”. International Journal Numerical Analytics Methods in Geomechanics (19), pp: 29-57.
 36. Hampton. M. A., Lee. H. J. and Locat. J., (1996), “*Submarine Landslides*”, Reviews of Geophysics (34, 1), pp: 33-59, copyright by American Geophysical Union.
 37. Hunter. G. and Fell. R., (2001), “*Rapid Failure of Soil Slopes*”, UNICIV Report No. R-400, The University of New South Wales Sydney 2052 Australia, ISSN0077-880X, ISBN: 85841 367 1.
 38. Hicks. M.A. and Onisiphorou. C., (2005). “*Stochastic evaluation of static liquefaction in a predominantly dilative sand fill*”. Géotechnique 55(2), pp: 123–133.
 39. Harbitz. C. B., Løvholt. F., Pedersen. G. and Masson. D.G., (2006), “*Mechanisms of tsunami generation by submarine landslides: a short review*”, Norwegian Journal of Geology, (86), pp. 255-264. Trondheim 2006. ISSN 029-196X.
 40. Jiang L. and LeBlond. P. H., (1992), “*The coupling of a Submarine Slide and the Surface Waves Which it Generates*”, Journal of Geophysical Research (97 – C8), pp: 12,731 -12,744.
 41. Jiang. M., Sun. C., Crosta. G. B., Zhang. W., (2015), “*A Study of Submarine Steep Slope Failures Triggered by Thermal Dissociation of Methane Hydrates using a Coupled CFD-DEM Approach*”, Engineering Geology, (190), pp: 1 – 16.
 42. Jafarian, Y., Ghorbani, A., Salamatpoor, S. et al., (2013), “*Monotonic triaxial experiments to evaluate steady-state and liquefaction susceptibility of Babolsar sand*”, J. Zhejiang Univ. Sci. A (2013) 14: 739. <https://doi.org/10.1631/jzus.A1300032>
 43. Jager. R. de. (2018), “*Assessing Liquefaction Flow Slides: Beyond Empiricism*”, Doctor of Philosophy, Delft University of Technology. DOI: 10.4233/uuid:51df13ed-6ba0-49ba-99d7-1c14f8fd022e.
 44. Koppejan. A., van Wamelen. B. and Weinberg. L., (1948), “*Coastal Flow Slides in Micaceous Sands*”, in Proceedings of the 2nd International Conference on Soil Mechanics and Foundation Engineering, (5) (Rotterdam, the Netherlands, 1948), pp: 89-96
 45. Kramer. S. L. and Seed. H. B., (1988), “*Initiation of Soil Liquefaction Under Static Loading Conditions*”, Journal of Geotechnical Engineering. (114- 4), pp:412 – 430.
 46. Kajjura, K., (1990), “*Tsunamis*”, Ocean Engineering Science 9A, Eds. LeMéhauté, B., Hanes, D.M.; John Wiley, New York.
 47. Kraft. L. M. Jr., Gavin. T. M. and Bruton. J. C., (1992), “*Submarine Flow Slide in Puetget Sound*”, Journal of Geotechnical Engineering, (118 – 10), pp: 1577 – 1591.
 48. Konkol J., (2014), “*Numerical solutions for large deformation problems in geotechnical engineering*”. PhD Interdisciplinary Journal”, 2014:49– 55
 49. Locat. J., (2000), “*Instabilities along Ocean Margins: A Geomorphological and Geotechnical Perspective*”, Marine and Petroleum Geology (18), pp: 503-512.
 50. Lade. P. and Yamamuro., (2011), “*Evaluation of Static liquefaction potential of silty sand slope*”, Canadian Geotechnical Journal (48), pp:247-264.
 51. Løvholt. F., Bondevik. S., Laberg. J. S., Kim. J. and Boylan. N., (2017), “*Some Giant Submarine Landslides Do Not Produce Large Tsunamis*”, Geophysical Research Letters, 44(16), 8463–8472. <https://doi.org/10.1002/2017GL074062>.
 52. Løvholt. F., Schulten. I., Mosher. D., Harbitz., C. and Krastel. S., (2018), “*Modelling the 1929 Grand Banks Slump and Landslide Tsunami*”, In D. G. Lintern, D. C. Mosher, L. G. Moscardelli, P. T. Bobrowsky, C. Campbell, J. D. Chaytor, J. J. Clague, A. Georgiopolou, P. Lajeunesse, A. Normandeau, D. J. W. Piper, M. Scherwath, C. Stacey, & D. Turmel (Eds.),
-

- Subaqueous mass movements (p. 477). London: Geological Society London Special Publications. <https://doi.org/10.1144/SP477.28>.
53. Molenkamp. F., (1980), “*Elasto-Plastic double hardening model Monot*, Report of *Laboratorium voor Grondmechanica*”, Delft, CO-218595, Second revision 1983.
54. Molenkamp. F., (1986), “*Limits of Jauman stress rate*”, International journal of numerical and analytical methods in Geomechanics. (10), pp: 151-176
55. Molenkamp. F. and Os. R. Van., (1987), “*Liquefaction Test in the Brutus Tank*”, Tech. Rep. COSE- 690504.2 (Delft Geotechnics, Delft, The Netherlands)
56. Molenkamp. F., Kidger. D. J., Smith. I. M., (1992), “*Accuracy of four-node standard finite element*”, Int. J. Numer. Anal. Meth. Geomech., (16), pp: 323-333.
57. Molenkamp. F., (1998), “*Dynamics of Large Deformation Elasto-Visco-Plasticity*”, Research Report, University of Manchester Institute of Science & Technology.
58. Molenkamp. F., (1999), “*Collapse Due to Static Liquefaction Analyzed Using Large Deformation Elasto-Visco-Plastic Dynamics*”, Numerical models in Geomechanics- NUMOG VII, Pande, Pietruszczak & Schweiger (eds), CRC Press/Balkema, Rotterdam, Netherlands, pp: 527-533.
59. Molenkamp. F., Sellmeijer. E. B., Sharma. C. B., Lewis E. B., (2000a), “*Explanation of locking of four-node plane element by considering it as elastic Dirichlet-type boundary value problem*”, Int. J. Numer. Anal. Meth. Geomech., (24-14), pp: 1013-1048.
60. Molenkamp. F., Lewis. E. B., Sharma. C. B., Sellmeijer. E. B., (2000b), “*Fractal approach applied to calculate hour-glass eigenvalue of elastic square 4-node quad*”, Int. J. Numer. Anal. Meth. Geomech., (24-14), pp: 1049-1060.
61. Mienert. J., (2009), “*Methane Hydrate and Submarine Slides, Encyclopedia of Ocean Science (2nd Edition)*”, pp: 790-798.
62. Molenkamp. F., (2009), “*Chapter 12: Some integral equation for finite element*”, updated version of lecture note on Continuum Mechanics
63. Mohammadi. S., (2013), “*Large Deformation Analysis of Slope and Embankments*”, Doctor of Philosophy, University of New South Wales, Australia.
64. Maghsoudloo. A., Galavi. V, Hicks. M. A. & Askarinejad. A., (2017). “*Finite element simulation of static liquefaction of submerged sand slopes using a multilaminar model*”. In Proceedings of the 19th International Conference on Soil Mechanics and Geotechnical Engineering (pp. 801-804). Seoul, South Korea.
65. Molenkamp. F., (2017), “*Lagrangian and Eulerian forms of Navier-Stokes equations*”, Dated: 10/10/2017.
66. Molenkamp. F., (2018), “*Procedures and program MESH_GEN3.F95 for generation of a rough mesh of the water-submerged slope in the liquefaction tank*”, TU Delft University, intermediate version, 28/4/2018.
67. Nasser, N. S. and Takahashi, K. (1984). “*Liquefaction and fabric of sand*”, Journal of Geotechnical Engineering, ASCE, (110-9), 1291-1306.
68. Pastor. M., Li. T., Liu. X. and Zienkiewicz. O.C., (1999), “*Stabilized low-order finite elements for failure and localization problems in undrained soils and foundations*”, Computer methods in applied mechanics and engineering (174), pp: 219-234.
69. Pruijn. N. S., (2016), “*The improvement of the material point method by increasing efficiency and accuracy*”, Doctor of Philosophy, Delft University of Technology.

-
70. Qiu. G., Henke. S., Grabe. J., (2011), “*Application of a Coupled Eulerian-Lagrangian Approach on Geomechanics Problems Involving Large Deformation*”, Computers and Geotechnics, (38), pp: 30-39.
71. Rzadkiewicz. S. A., Mariotti. C. and Heinrich. P., (1997), “*Numerical simulations of submarine landslides and their hydraulic effects*”, J. Waterway, Port, Coastal, and Ocean Engrg., ASCE, (123- 4), pp: 149-157.
72. Rohe. A., (2013), “*Towards parameter limits of displacement boundary value problems for Mohr-Coulomb models*”, Doctor of Philosophy, Delft University of Technology.
<https://doi.org/10.4233/uuid:640567ea-dfba-4f01-8b13-b11c8cc8e42f>.
73. Sterling. G. H. and Strohbeck. G. E., (1975), “*The Failure of South Pass 70B Platform in Hurricane Camille*”, Journal Petroleum Technology, pp: 263–268.
74. Sulsky. D., Chen. Z. and Schreyer. H.L., (1993), “*A particle method for history-dependent materials - technical report sand93-7044*”, Technical report, Albuquerque, New Mexico, United States.
75. Steinmetz. M., and Muller. E., (1993), “*On the Capabilities and Limits of Smoothed Particle Hydrodynamics*”, Astronomy and Astrophysics, (268), pp: 391-410.
76. Synolakis. C. E., Bardet. J. P., Borrero. J. C., Davies. H. L., Okal. E. A., Silver. E. A., Sweet. S. and Tappin. D. R., (2002), “*The Slump Origin of the 1988 Papua New Guinea Tsunami*”, Proc. R. Soc. Lond. A 2002, (458), pp: 763 – 789.
77. Smith. I.M. and Griffiths. D.V., (2004), “*Programming the finite element method*”, John Wiley & Sons, 4-th ed.
78. Sorensen. R.M., (2006), “*Basic Coastal Engineering*”, Springer US, 3rd edition.
doi:10.1007/b101261
79. Sun E.Q., (2006), “*Shear locking and hourglassing in MSC Nastran, ABAQUS, and ANSYS*”. In: MSC Software Corporation’s 2006 Americas virtual product development conference: evolution to enterprise, Simulation.
80. Tappin. D. R., Matsumoto. T., Watts. P., Satake. K., Mcurtry. G. M., Matsuyama. Y., Lafoy. Y., Tsuji. Y., Kanamatsu. T., Lus. W., Iwabuchi. Y., Yeh. H., Matsumotu. Y., Nakamura. M., Mahoi. M., Hill. P., Crook. K., Anton. L., and Walsh. J. P., (1999), “*Sediment Slump Likely Caused 1998 Papua New Guinea Tsunami*”, EOS, Trans. Am. Geophys. U., (80), pp: 329–340.
81. Tappin. D.R., Grilli. S.T., Harris. J.C., Geller. R.J., Materlark. T., Kirby. J.T., Shi. F., Ma. G., Thingbaijam. K.K.S. and Mai. P.M., (2014), “*Did a submarine landslide contribute to the 2011 Tohoku tsunami?*” Marine Geology (357), pp: 344-361.
82. Tappin. D.R., (2017), “*Tsunamis from Submarine Landslides*”, Geology today (33), Issue 5.
83. USGS: fact sheet- 2004-3072, (2004), U.S. Department of the Interior and U.S. Geological Survey.
84. Varma. K. K., (2014), “*Finite amplitude waves- waves with peaked crests and broad troughs*”. Resonance 19(11) 1047-1057.
85. Vardon. P., Wang. B, Hicks. M. A., (2017), “*Slope Failure Simulations with MPM*”, Science Direct-Journal of Hydrodynamics, (29-3), pp: 445-451.
86. Watts. P., (2001), “*Some opportunities of the landslide tsunami hypothesis*”, Sci. Tsunami Hazards, 19(3), 126–149.
87. Watts. P., Grilli. S. T., Kirby. J. T., Fryer. G. J. and Tappin. D. R., (2003), “*Landslide Tsunami Case Studies using a Boussinesq Model and a Fully Nonlinear Tsunami Generation Model*”, Natural Hazards and Earth System Sciences, (3), pp: 391 – 402.
-

88. Wanatowski. D. , Chu. J. and Lo. R. S. -C., (2010), “*New types of failure mechanisms for flowslide*”, *Geomechanics and Geoengineering*, (5: 1), pp: 3 — 13
89. Wang. B., (2017), “*Slope failure analysis using the material point method*”, TU Delft repository, DOI: 10.4233/uuid:f24a64b0-ef93- 42d7-81a0-a5d34a4eb3dc
90. Yalciner. A.C., Pelinovsky. E.N., Okal. E. and Synolakis. C.E., (2001), “*Submarine Landslides and Tsunamis*”, published by Springer Science + Business Media, B.V., Proceedings of the NATO Advanced Research Workshop on Underwater Ground Failure on Tsunami Generation, Modeling, Risk and Mitigation, Istanbul, Turkey, May 23-26, 2001.
91. Zienkiewicz. O.C. and Taylor. R.L., (1991), “*The finite element method*”, McGraw-Hill, Vol. 2, Solid and fluid mechanics. Dynamics and non-linearity.
92. Tsunami Taro, Iwate, Japan, Image source:
<http://www.sciencemag.org/news/2014/09/underwater-landslide-may-have-doubled-2011-japanese-tsunami>

Appendix (A) – Overview of structure F.E program

MODIFIED_DYN_MLK4.95

```

PROGRAM MODIFIED_DYN_MLK4
!-----
! Plane strain / axisymmetric dynamics (ramp/cyclic loading)
! Constitutive models: elastic, mises, coulomb, monot, monot2, alternat
! Modified-Newton-Raphson iteration with Unbalance Load
! Global stiffness matrix: elastic, symmetric/non-symmetric elasto-plastic
! Connections/ties of freedoms
! Restart facility
! Capability to simulate subsequent construction phases with extending mesh
! Large displacement with polar decomposition and Updated Lagrange.
! Minimization of band-width using frontal method
!-----
USE MYKIND ! portable definitions of precision
USE MAIN_F95 ! f95 library by prof smith (+ mykind, adapted by mlk)
USE COMCONST ! common constitutive subroutines; requires module mykind
USE MLK_LB1 ! f.e. subroutines by molenkamp (+mykind,comconst,main_f95)
USE MISES ! enhanced von-mises model; requires modules mykind+comconst
USE COULOMB ! mohr-coulomb vertex model; requires modules mykind+comconst
USE MONOT ! monot model; requires modules mykind+comconst
USE MONOT2 ! monot2 model; requires modules mykind+comconst
USE ALTERNAT ! alternat model; requires modules mykind+comconst
IMPLICIT NONE
!-----
!declarations (30)
!input of mesh and data and allocation of storage (193)
!compose nodal freedom matrix (739)
!read loading details (953)
IF(STEP0>0)THEN !read state at start of calculation phase from restart file
!restart file with input data (1091)
END IF
!calculate quantities at start of current calculation phase (1193)
!take account of type of change of soil and water in current calculation phase
SELECT CASE(TYPCHANG) !elaborate for current type of change (1229)
.CASE(0) !no change of soil and water
.CASE(1) !define initial state due to uniform total stress
.CASE(2) !define initial state due to total stress by weight
.CASE(3) !raise soil, assumed drained behaviour in raised layers
.CASE(4) !Hydrostatic transition of Dredge Block and excavation
.CASE(5) !change water level, weight changes, ....
.CASE(6) !Fluid blocks activation and removal of virtual assumed hydrostatic pressures from slope surface
END SELECT
!check equilibrium at start of current calculation phase (2390)
!load vector due to transmitting boundary at start of current phase (2483)
!specification of types of global matrix and loading (2557)
SELECT CASE(LOADTYP) !elaboration for type of loading (2648)
.CASE(1) !ramp loading (2649)
..Do IEL = 1, NELS
...IF((CMODEL(LL)>=0 .AND. CMODEL(LL)<=5 .AND. TYPCHANG/=4) .OR. &
...&(TYPCHANG==4 .AND. NEWLAY(LL)/=1 .AND. CMODEL(LL) <= 5))THEN
...! out of layers choosing soil layer and checking if not empty (2657)
...SELECT CASE (CMODEL(LL)) !LL=3 for monot (2665)
.....!Check input time step (DTMIN) for shear wave propagation and element size (2670)
.... END SELECT (2763)
...END IF (2764)
..END DO (2765)
.CASE(2) !cyclic loading (2771)
END SELECT (2867)
!output at start of current calculation phase (2870)
!-----
DO IY=STEP0+1,STEP0+STEP,1 !load increment loop (2955)
.DO IMATRIX=1,MAX_IMATRIX,1 !loop for repeating calculation because of lack of.
...!convergence with adapted time step and new global matrix (2960)
..IF(IY==STEP0+1 .OR. GLOBMAT>=1 .OR. NEWDTIM==1)THEN !generation and..
...!decomposition of global matrix (2968)

```

```

...DO IEL=1,NELS,1 !elements_3: stiffness integration for f.e. mesh (3009)
...IF(CMODEL(LL)>=0) THEN ! Checking element is not empty (3012)
.....DO I=1,NIP,1 !gauss_pts_2: integration per f.e. element (3020)
..... IF((TYPCHANG/=4 .AND. CMODEL(LL)<=5 ).OR. (TYPCHANG==4 .AND. NEWLAY(LL)/=1 .AND. ....&
CMODEL(LL)<=5))THEN ! non dredge material and non-water layers (3022)
.....!compose soil elastic/elasto-plastic constitutive matrix (monot model) (3064)
.....Else !dredged material or Fluid material layers (3178)
.....!Compose linear elastic water matrix and linear viscous water matrix (3182)
.....END IF !non-dredged/soil else:dredged material/water (3185)
.....!compose stiffness matrix (3188)
.....!compose viscous matrix (3206)
.....!compose mass matrix (3210)
.....END DO !gauss_pts_2: integration per f.e. element (3231)
.....!compose global matrix (3233)
...END IF !element is not empty (3248)
...END DO !elements_3: stiffness integration for f.e. mesh (3250)
...!transmitting (viscous) boundary matrix (3252)
...!decompose equations (3292)
..END IF !generation and decomposition of global matrix (3304)
..!-----
..!Modified-Newton-Raphson-iteration to reduce unbalance vector (3307)
..!unbalance at begin and end of increment (3309)
..DO ITERS=1,ITS,1 !M-N-R iteration loop (3434)
...!compose unbalance vector for current M-N-R-iteration step (3484)
...DO IEL=1,NELS,1 !elements_4: integrate for f.e. mesh (3486)
...IF(CMODEL(LL)>=0)THEN ! element is not empty (3489)
.....DO I=1,NIP,1 !gauss_points_3: integration per f.e. element (3507)
.....!calculate incremental strain (3519)
.....IF ((TYPCHANG/=4 .AND. CMODEL(LL)<= 5) .OR. &(TYPCHANG == 4 .AND. NEWLAY(LL)/=1 .....& .AND.
CMODEL(LL)<= 5))THEN !not dredged, else: water (3556)
.....!calculate incremental rotation and stretch (3559)
.....!Check max allowable strain (3561)
.....!Apply Soil constitutive subroutine (3581)
.....!calculate new pore pressure (3665)
.....!calculate soil stress (3690)
.....ELSE ! dredge or water layers (3707)
.....!Apply water constitutive subroutine (3710)
.....!calculate stress tensors in water (3713)
.....END IF !not dredged, else: water (3730)
.....!compose inertial force (3734)
.....!compose weight force (3738)
.....END DO !gauss_points_3: integration per f.e. element (3740)
.....!calculate incremental energy terms 1st part(3746)
.....!compose inertial load and load due to total stress (3762)
.....!calculate incremental energy terms 1st part(3771)
...ELSE
.....!maintain effective stress in empty elements (3804)
.....END IF !element is not empty, else empty (3809)
...END DO !elements_4: integrate for f.e. mesh (3810)
...!compose viscous damping force of transmitting boundary (3816)
...!compose unbalance at begin and end of increment (3905)
...!calculate global incremental energy terms (3913)
...!check convergence (3930)
..END DO !M-N_R iteration loop (3984)
..!modify time step if convergence is slow or strain increment is large (3986)
..END DO !DO IMATRX=1,MAX_IMATRX,1 !loop for repeating calculation because..
..!of lack of convergence with adapted time step and new global matrix (4030)
..!update for next load increment (4083)
..!Check probable increase in time for ramp loading if acceptable for M-N-R iteration (4171)
..IF(CONVERGED)THEN
..!output results to restart file: DYN_MLK4.REX (4244)
..END IF
..!calculate nodal forces in direct contact elements (4328)
..!store energy parameters (4426)
..!check for termination of time stepping (4458)

```

```
END DO !load increment loop (4507)
!-----
!prepare output of main results (4510)
!write updated deformed mesh: DYN_MLK4.RMS (4531)
!refill file with integration points: DYN_MLK4.DIP (4550)
!output results to restart file: DYN_MLK4.REX (4571)
!file with type of material behaviour and material restraint at i.p.(4728)
!output results at end of calculation phase (4741)
END PROGRAM MODIFIED_DYN_MLK4
```

TYPES OF OUTPUT AT END OF CALCULATION PHASE:

- time of loading phase
- global energy parameters
- surface nodal displacements
- nodal weight
- nodal load in equilibrium with total stress
- nodal load due to inertia
- nodal load transmitting vibrations through boundary
- nodal unbalance vectors
- accumulated nodal displacements
- nodal displacements in loading phase
- modulus of nodal displacements in loading phase
- last nodal displacement increments
- nodal velocities
- nodal accelerations
- in-plane strain tensors
- lode angle of strain
- in-plane strain tensors in loading phase
- deviator strain in loading phase
- volumetric strain in loading phase
- in-plane effective stress tensors
- normal effective stress on plane of deformation
- deviator stress
- mean effective stress
- lode angle of stress
- pore pressure
- excess pore pressure in loading phase
- mobilized mohr-coulomb friction angle
- ratio of mobilized and failure deviatoric stresses

Appendix (B) – Link to program related data files

In order to refer program related various data files listed in table B1, follow the Link:
<https://github.com/abhishekguptacib19/Submarine-landsilde-model?files=1>

Table B1: Program related various data files list

Case A	Phase 1(A): Initial, K0 state	dyn_mlk4_1(A).DAT
		dyn_mlk4_1(A).MSH
		dyn_mlk4_1(A).res
	Phase 2(A)*: Initial state with drained unloading	dyn_mlk4_2(A).DAT
		dyn_mlk4_2(A).res
		dyn_mlk4_2(A).mat
	Phase 3(A): Hydrostatic transition and simulation of dredging	dyn_mlk4_3(A).dat
		dyn_mlk4_3(A).msh
		dyn_mlk4_3(A).res
Case B	Phase1(B): Initial, K0 state	dyn_mlk4_1(B).dat
		dyn_mlk4_1(B).msh
		dyn_mlk4_1(B).res
	Phase2(B)*: Initial state with drained unloading	dyn_mlk4_2(B).DAT
		dyn_mlk4_2(B).res
	Phase3(B): Hydrostatic transition and simulation of dredging	dyn_mlk4_3(B).dat
		dyn_mlk4_3(B).MSH
		dyn_mlk4_3(B).res
	Case C	Phase2(C)†: Fluid blocks activation and optimization
dyn_mlk4_2(C).res		
Phase3(C): Hydrostatic transition and simulation of dredging		dyn_mlk4_3(C).DAT
		dyn_mlk4_3(C).MSH
		dyn_mlk4_3(C).res
Fluid tank test	Phase 1(FT)	Fluid_bheviour_test_M.dat
		Fluid_bheviour_test_M.msh
		Fluid_bheviour_test_M.res
	Phase 2(FT)_1*	Fluid_bheviour_test_M2.dat
		Fluid_bheviour_test_M2.res

*Phase 2 '.msh' file is same as Phase 1 '.msh' file

†Phase2(C) '.msh' file is same as Phase 2(B) '.msh' file.

Appendix (C) – Discretization of saturated soil

In soil mechanics two sets of equations are expressed in Lagrangian form for the linear momentum conservation of the saturated soil mass: a) for the soil skeleton (eq.1), b) for the pore fluid (eq.2) in index format.

$$\sigma_{ji,j}^* + (1-n)p_{,j} + (1-n)\rho_s b_i - (1-n)\rho_s \ddot{u}_i + nR_i = 0 \quad (1)$$

$$np_{,j} + n\rho_f b_i - n\rho_f (\ddot{u}_i + \dot{v}_i|_{\dot{u}}) - nR_i = 0 \quad (2)$$

in which the following quantities occur:

ρ_s - average density of the minerals composing the grains

ρ_f - average density of the fluid filling the pores, namely for air-saturated dry soil it is pore air and for saturated soil it is water.

n - porosity of solid skeleton.

\ddot{u}_i - average acceleration vector of the soil skeleton

$\dot{v}_i|_{\dot{u}}$ - relative average velocity vector of the pore fluid with respect to the soil skeleton

$\sigma_{ji,j}^*$ - average intergranular stress tensor (continuum mechanics: tension positive).

p - average pore fluid stress (continuum mechanics: tension positive).

b_i - body force vector per unit of mass ($b = -g\delta_{iv}$) due to gravity

R_i - hydrodynamic interaction force vector between soil skeleton and pore fluid due to the pore fluid flow.

Adding the aforementioned expressions of conservation of the linear momentum i.e. eq. (1) and (2), gives the conservation expression of the linear momentum of the “bulk” of the saturated soil, which can be expressed in index format as:

$$\begin{aligned} \sigma_{ji,j}^* + p_{,j} + \rho b_i - (1-n)\rho_s \ddot{u}_i - n\rho_f (\ddot{u}_i + \dot{v}_i|_{\dot{u}}) &= 0 \\ \Rightarrow \sigma_{ji,j} + \rho b_i - \rho \ddot{u}_i - n\rho_f \dot{v}_i|_{\dot{u}} &= 0 \end{aligned} \quad (3)$$

in which the “bulk” density of the saturated soil $\rho = (1-n)\rho_s + n\rho_f$, and total stress tensor

$$\sigma_{ji,j} = \sigma_{ji,j}^* + p_{,j}$$

Next, considering undrained dynamic analysis of a soil, the relative average velocity vector of pore fluid with respect to soil skeleton is taken zero ($\dot{v}_i|_{\dot{u}} = 0$ in eq. 2). This represents zero volume change in the soil system, if both the pore water and the granular minerals would be incompressible. Further undrained conditions eq. (3) can be re-written as:

$$\sigma_{ji,j} + \rho b_i - \rho \ddot{u}_i = 0 \quad (4)$$

Weak formulation and numerical boundary conditions:

The following boundary conditions can be applied to eq. (4) for undrained saturated soil conditions:

- at the part of the co-moving boundary surface s_j of the solid skeleton with outward normal unit vector \mathbf{n} and prescribed traction vector $\bar{\tau}^{(n)}(t)$:

$$\tau_i^{(n)} - \bar{\tau}_i^{(n)} = n_j \sigma_{ji} - \bar{\tau}_i^{(n)} = 0 \quad (5)$$

- at the complementary part of the boundary surface $s_u = s - s_\tau$ with prescribed displacement vector $\bar{u}_i(t)$:

$$u_i - \bar{u}_i = 0 \quad (6)$$

- at the part of the boundary surface s_v with prescribed viscous transmitting boundary traction $T_i(t)$

$$T_i = C_{ji} \dot{u}_i \quad (7)$$

where, C is a viscous damping matrix (refer, Molenkamp - 1998)

Next, similar to the step involved in weak formulation of fluid model in section 3.5.2 (refer, eq. 3.36), eq. (8) represents the first of 3 steps combined, in order to arrive at weak formulation using Galerkin's approach. The field equations (4) and the boundary conditions (5) to (7) were first multiplied by dimensionless weight functions $N^p(x)$ and $M^p(x)$ respectively and subsequently integrated over new state volume v and surface s of the new state for which they are valid. Finally, they were added together while equating the sum to be zero.

$$\int_v N^p (\sigma_{ji,j} + \rho b_i - \rho \ddot{u}_i) dv + \int_{s_\tau} M^p (n_j \sigma_{ji,j} - \bar{\tau}_i^{(n)}) ds + \int_{s_u} M^p \eta (u_i - \bar{u}_i) ds + \int_{s_v} M^p C_{ji} \dot{u}_i ds = 0 \quad (8)$$

where η has been used just to equalize the dimensions of all terms, which will be eliminated in later steps.

Next, applying the divergence theorem to the stress term σ_{ij} gives:

$$\int_v (N^p \sigma_{ji})_{,j} dv = \int_v N^p \sigma_{ji,j} dv + \int_v N^p_{,j} \sigma_{ji} dv = \int_s \int N^p \sigma_{ji} n_j ds \quad (9)$$

where, vector n_j is the outward unit normal vector on the boundary surface s .

Rearranging the term of eq. (8), substituting eq. (9) and subsequently replacing, $M^p(x) = -N^p(x)$ gives:

$$\begin{aligned} & \int_v N^p \sigma_{ji,j} dv + \int_{s_\tau} M^p (n_j \sigma_{ji}) ds + \int_v N^p (-\rho \ddot{u}_i + \rho b_i) dv + \int_{s_u} M^p \eta (u_i - \bar{u}_i) ds \\ & - \int_{s_\tau} M^p \bar{\tau}_i^{(n)} ds + \int_{s_v} M^p C_{ji} \dot{u}_i ds = 0 \end{aligned} \quad (10)$$

$$\begin{aligned} \Rightarrow & - \int_v N^p_{,j} \sigma_{ji} dv + \int_s \int N^p \sigma_{ji} n_j ds - \int_{s_\tau} N^p (n_j \sigma_{ji}) ds + \int_v N^p (-\rho \ddot{u}_i + \rho b_i) dv - \int_{s_u} N^p \eta (u_i - \bar{u}_i) ds \\ & + \int_{s_\tau} N^p \bar{\tau}_i^{(n)} ds - \int_{s_v} N^p C_{ji} \dot{u}_i ds = 0 \end{aligned} \quad (11)$$

$$\begin{aligned} \Rightarrow & - \int_v N^p_{,j} \sigma_{ji} dv + \int_{s_u} N^p \sigma_{ji} n_j ds + \int_v N^p (-\rho \ddot{u}_i + \rho b_i) dv - \int_{s_u} N^p \eta (u_i - \bar{u}_i) ds + \int_{s_r} N^p \bar{\tau}_i^{(n)} ds \\ & - \int_{s_v} N^p C_{ji} \dot{u}_i ds = 0 \end{aligned} \quad (12)$$

Further similar to section 3.5.2 (see, eq. 3.41), to discretize the above equation, the local displacement vector u can be replaced by the local displacement as the sum of the weighted nodal displacement i.e. $u_i = N^q \hat{u}_i^q$. Thus, in this case the boundary condition of (12) on the boundary surface S_u with prescribed displacement \bar{u}_i will be satisfied automatically, by which the integral with the unknown scalar η can be omitted. Consequently, on boundary surface S_u no further solution will be needed and therefore the integral with traction $\sigma_{ji} n_j$ can also be omitted, thereby reducing (12) to:

$$- \int_v N^p_{,j} \sigma_{ji} dv + \int_v N^p (-\rho \ddot{u}_i + \rho b_i) dv + \int_{s_r} N^p \bar{\tau}_i^{(n)} ds - \int_{s_v} N^p C_{ji} \dot{u}_i ds = 0 \quad (13)$$

Reversing the sign the (13) can be rewritten as:

$$\int_v N^p_{,j} \sigma_{ji} dv - \int_v N^p (-\rho \ddot{u}_i + \rho b_i) dv - \int_{s_r} N^p \bar{\tau}_i^{(n)} ds + \int_{s_v} N^p C_{ji} \dot{u}_i ds = 0 \quad (14)$$

Now, to transform the integration limits in expression (14) from unknown new state quantities to known current state i.e. volume v to V_0 and boundary surface s to S_0 , incremental deformation gradients: \hat{F} and \hat{G} are used as shown below in (15). Equation (3.3) can be used for further referral on gradients.

$$\int_{V_0} N^p_{,j} \sigma_{ji} \left| \hat{F} \right| dv - \int_{V_0} N^p (-\rho \ddot{u}_i + \rho b_i) \left| \hat{F} \right| dv - \int_{s_{0r}} N^p \bar{\tau}_i^{(n)} \left| \hat{G} \right| ds + \int_{s_{0v}} N^p C_{ji} \dot{u}_i \left| \hat{G} \right| ds = 0 \quad (15)$$

Where, $s \rightarrow s_0$, $s_r \rightarrow s_{0r}$, $s_v \rightarrow s_{0v}$ $dv \rightarrow \left| \hat{F} \right| dv$ and $ds \rightarrow \left| \hat{G} \right| ds$.

Further multiplication of (15) by δ_{ki} enables the subsequent substitution of eq. (3.44), introducing the strain-nodal displacement components B_{kij}^p :

$$\int_{V_0} B_{kij}^p \sigma_{ji} \left| \hat{F} \right| dv - \int_{V_0} N^p (-\rho \ddot{u}_k + \rho b_k) \left| \hat{F} \right| dv - \int_{s_{0r}} N^p \bar{\tau}_k^{(n)} \left| \hat{G} \right| ds + \int_{s_{0v}} N^p C_{jk} \dot{u}_k \left| \hat{G} \right| ds = 0 \quad (16)$$

Next the total stress σ_{ji} at the new state can be expressed in terms of total stress σ_{kl}^0 at the current state, components of co-rotational stress increment $\Delta \tilde{\sigma}_{kl}$ and incremental material rotation rate \hat{R}_{jk} (Molenkamp, 1986). Therefore with this the expression (16) can be rewritten as:

$$\begin{aligned}
 & \int_{V_0} B_{kij}^p \hat{R}_{jk}^{rT} (\sigma_{kl}^o + \Delta \tilde{\sigma}_{kl}^c) \hat{R}_{li}^r |\hat{F}| dv - \int_{V_0} N^p (-\rho \dot{u}_k + \rho b_k) |\hat{F}| dv - \int_{s_{0r}} N^p \bar{\tau}_k^{(n)} |\hat{G}| ds \\
 & + \int_{s_{0v}} N^p C_{jk} \dot{u}_k |\hat{G}| ds = 0
 \end{aligned} \tag{17}$$

It is to be noted that in the first term of the above equation, the co-rotational total stress increment is the sum of the respective products of the stiffness of intergranular soil and stiffness of pore fluid with incremental time (Δt). The stiffness of the intergranular soil is a non-linear function of the loading history and depends upon the soil constitutive model and its governing parameters. However, for undrained condition, pore water bulk stiffness is kept constant and equals 4.E6 kN/m².

Finally replacing local displacement u_k in nodal terms by introducing shape function as $u_k = N^q \hat{u}_k^q$, the above expression of linear momentum of conservation can be expressed in residual nodal vector term f_k^p as:

$$\begin{aligned}
 f_k^p &= \int_{V_0} B_{kij}^p R_{jk}^{rT} (\sigma_{kl}^o + \Delta \tilde{\sigma}_{kl}^c) R_{li}^r |\hat{F}| dv + \int_{V_0} N^p \rho N^q |\hat{F}| dv \ddot{u}_k - \int_{V_0} N^p \rho b_k |\hat{F}| dv \\
 & - \int_{s_{0r}} N^p \bar{\tau}_k^{(n)} |\hat{G}| ds + \int_{s_{0v}} N^p C_{jk} N^q |\hat{G}| ds \hat{u}_k \approx 0
 \end{aligned} \tag{18}$$

Reversing the sign and rearranging the order in above gives:

$$\begin{aligned}
 f_k^p &= \int_{s_{0r}} N^p \bar{\tau}_k^{(n)} |\hat{G}| ds + \int_{V_0} N^p \rho b_k |\hat{F}| dv - \int_{V_0} B_{kij}^p R_{jk}^{rT} (\sigma_{kl}^o + \Delta \tilde{\sigma}_{kl}^c) R_{li}^r |\hat{F}| dv \\
 & - \int_{s_{0v}} N^p C_{jk} N^q |\hat{G}| ds \hat{u}_k - \int_{V_0} N^p \rho N^q |\hat{F}| dv \ddot{u}_k \approx 0
 \end{aligned} \tag{19}$$

Appendix (D) – Phase 2(A) shake down effect on Phase 3(A)

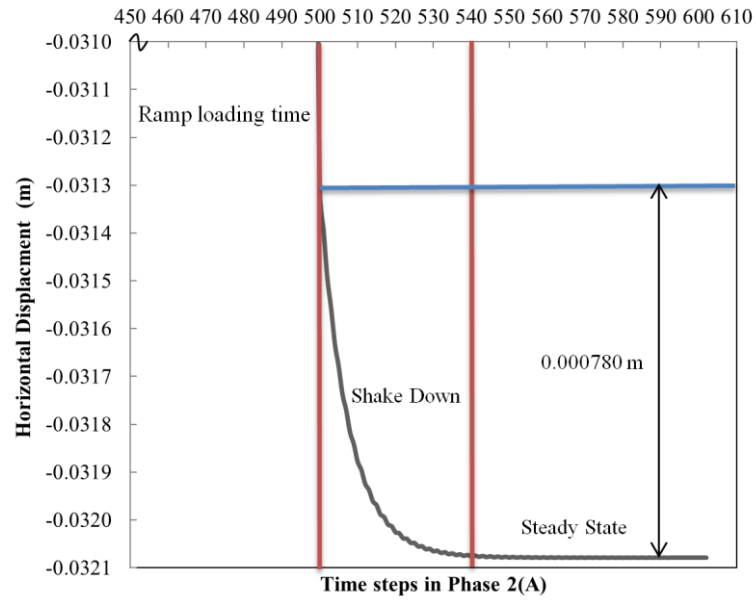
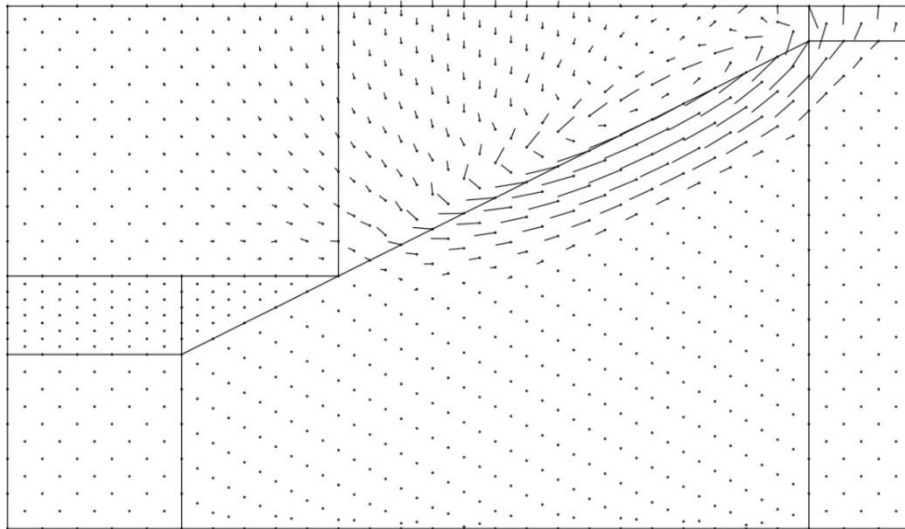


Figure D1: Shake down affect in Phase 2(A), for horizontal displacement in mid-slope surface node

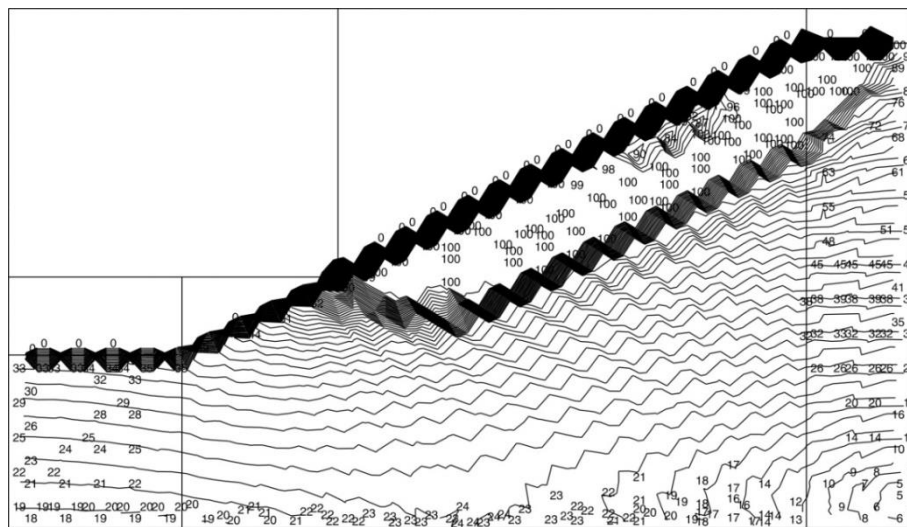
Appendix (E) – Phase 2(C): Activation of fluid material blocks optimization



MESH OF 4 TRIANGLES PER SQUARE
 NODAL DISPLACEMENTS IN LOADING PHASE
 MAGNIFICATION FACTOR ON PAPER:1.0E+00

NODAL VECTORS
 MAXIMUM VECTOR LENGTH:1.4E-01
 REAL-SCALED MAGNIFICATION:6.8E-02

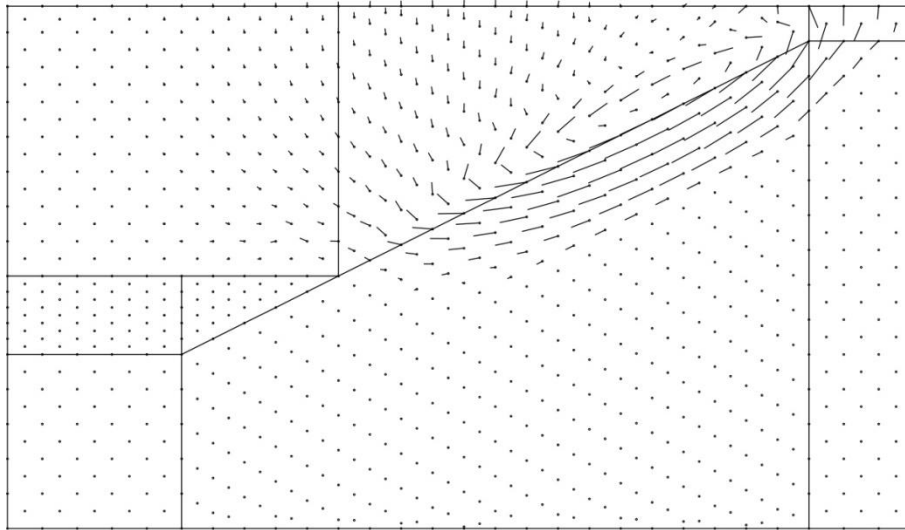
Figure E1: Nodal displacements phase 3(C) for 0.001 s time sets in phase 2(C)



MESH OF INTEGRATION POINTS
 RATIO OF MOBILIZED AND FAILURE DEVIATORIC STRESSES

CONTOUR LINES OF SCALARS AT INTEGRATION POINTS
 PLOTTED SCALARS MUST BE MULTIPLIED BY:1.00E-02
 CONTOUR INTERVAL OF PLOTTED SCALARS: 2
 MINIMUM: 0
 MAXIMUM:100

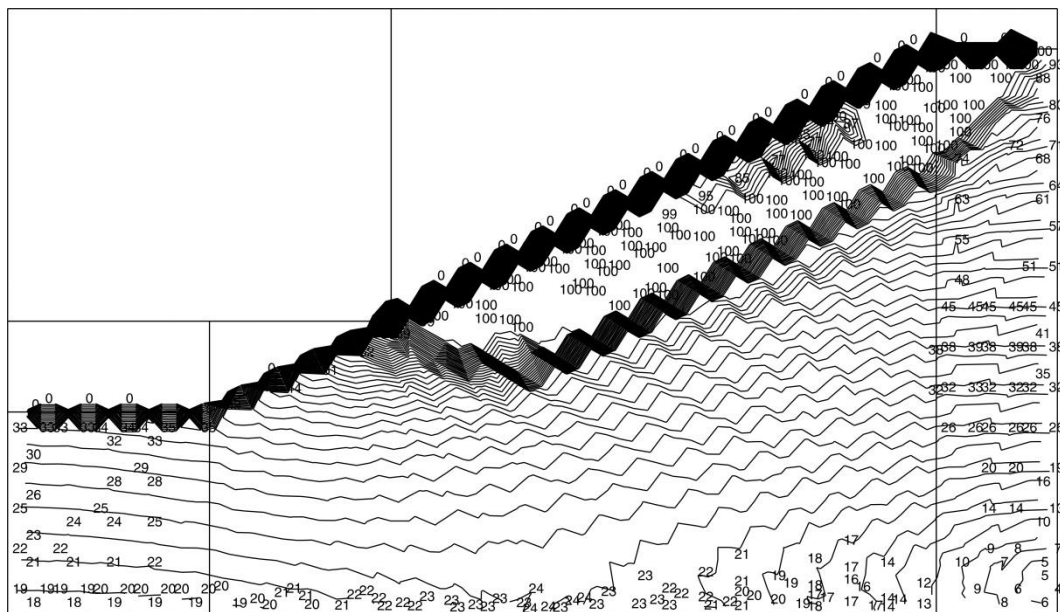
Figure E2: Mobilized strength phase 3(C) for 0.001 s time sets in phase 2(C)



MESH OF 4 TRIANGLES PER SQUARE
 NODAL DISPLACEMENTS IN LOADING PHASE
 MAGNIFICATION FACTOR ON PAPER:1.0E+00

NODAL VECTORS
 MAXIMUM VECTOR LENGTH:1.4E-01
 REAL-SCALED MAGNIFICATION:6.7E-02

Figure E3: Nodal displacements phase 3(C) for 0.01 s time with zero initial nodal velocities



MESH OF INTEGRATION POINTS
 RATIO OF MOBILIZED AND FAILURE DEVIATORIC STRESSES

CONTOUR LINES OF SCALARS AT INTEGRATION POINTS
 PLOTTED SCALARS MUST BE MULTIPLIED BY:1.00E-02
 CONTOUR INTERVAL OF PLOTTED SCALARS: 2
 MINIMUM: 0
 MAXIMUM: 100

Figure E4: Mobilized strength phase 3(C) for 0.001 s time with zero initial nodal velocities

Appendix (F) – Phase 3(C): Other Results

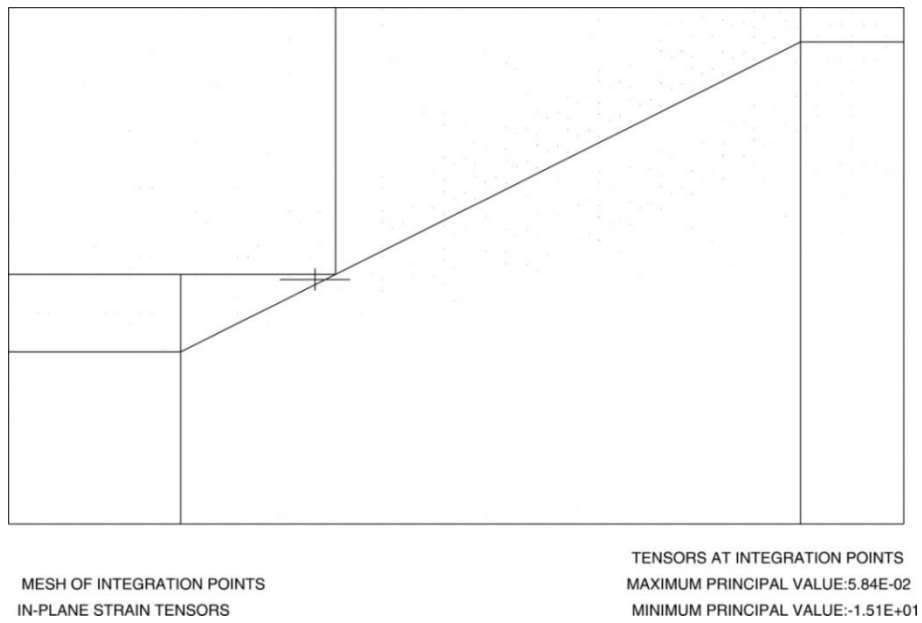


Figure F1: In Plain Strain tensors with excessively high strain point for Phase 3(C)

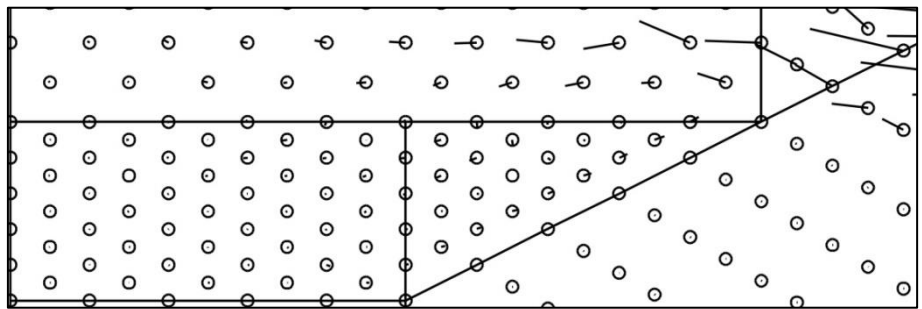
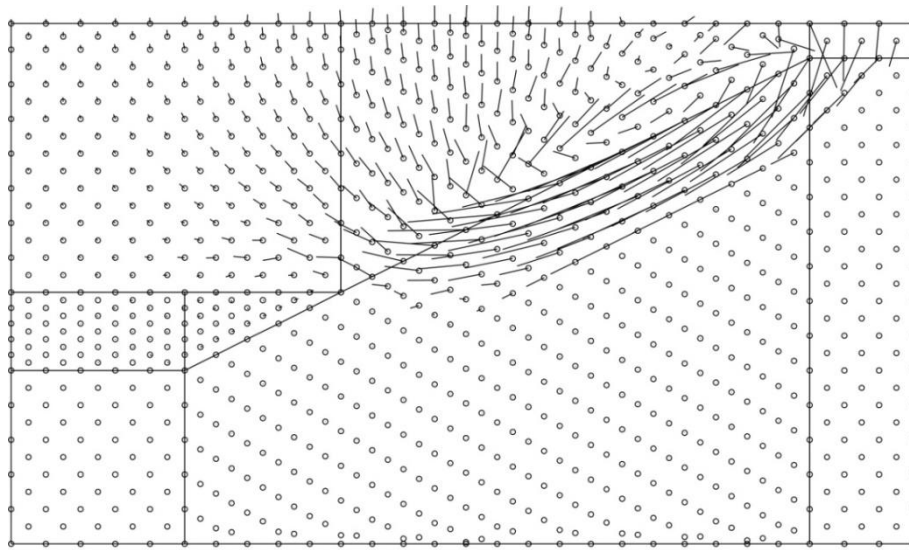


Figure F2: Nodal displacement at dredged soil region filled with water for Phase 3(C)



MESH OF 4 TRIANGLES PER SQUARE
NODAL DISPLACEMENTS IN LOADING PHASE
MAGNIFICATION FACTOR ON PAPER:3.0E+00

NODAL VECTORS
MAXIMUM VECTOR LENGTH:1.4E-01
REAL-SCALED MAGNIFICATION:6.7E-02

Figure F3: Magnified Nodal displacement for Phase 3(C)

Appendix (G) - Some characteristics of hour-glass eigenmodes of plane 4-node finite elements

The 4-node bilinear finite element for plane deformation has 8 eigenmodes (Molenkamp, Kidger, Smith, 1992), namely:

- a) 3 for rigid displacement
- b) 3 for uniform deformation
- c) 2 for hour-glass modes

For full numerical integration 4 integration points would be needed, causing the two hour-glass eigenmodes to become extremely stiff for elastic materials with a large bulk modulus. For elasto-plastic materials with a large bulk modulus for stress states approaching failure by the deviatoric stress passing its upper limit the two hour-glass eigenmodes become extremely stiff. This characteristic is known as “locking” and also “shear-locking”. (Molenkamp, Sellmeijer, Sharma, Lewis, 2000a, Molenkamp, Lewis, Sharma, Sellmeijer, 2000b).

For reduced numerical integration 1 integration points would be needed, causing the two hour-glass eigenmodes to become extremely flexible. For elasto-plastic materials for stress states approaching failure by the deviatoric stress approaching its upper limit the two hour-glass eigenmodes become extremely flexible. At this phase the hour-glass modes can increase in a non-controlled way, governing the calculated deformation pattern. This characteristic is known as the occurrence of “spurious hour-glass modes”. This pattern is illustrated in figure J1.

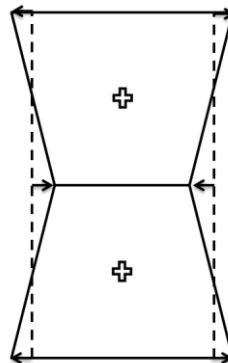


Figure J1: Illustration of two 4-node elements with spurious hour-glass eigenmodes (interpreted from Molenkamp et. al., 2000a).

In pragmatic attempts to avoid these problems plane quadrilateral 8-node finite elements have been applied, also causing similar shortcomings as “locking” for full (9-point) numerical integration and spurious modes for reduced (4-point) numerical integration.

Subdividing a 4-node finite element for plane deformation into 4 triangles by introducing a fifth central node at its center causes the element to get 10 eigenmodes. Note, that each triangular finite element with one central integration point for full numerical integration has 6 eigenmodes, namely:

- a) 3 for rigid displacement
- b) 3 for uniform deformation

The characteristics of this 4-node finite element (with a fifth central node) are: no “shear-locking” and no “spurious modes”

Nevertheless this research demonstrates that for elasto-plastic materials with dilative (and contractive) characteristics for stress states approaching failure by the deviatoric stress passing its

upper limit the 5-th central node can move away from the center, causing two opposite triangular finite elements to dilate and contract respectively, which is illustrated in figure J2. This is a numerical shortcoming, which could be indicated as an hour-glass related numerical shortcoming.

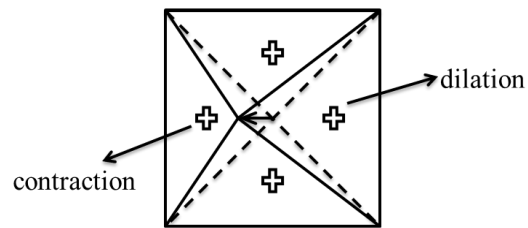


Figure J2: Illustration of 4-node element with fifth central node, showing the hour-glass related eigenmodes (interpreted from Molenkamp et. al., 2000a).

